

UNIVERSITY OF CALIFORNIA

Los Angeles

**Combustion and Magnetohydrodynamic Processes
in Advanced Pulse Detonation Rocket Engines**

A dissertation submitted in partial satisfaction
of the requirements for the degree
Doctor of Philosophy in Aerospace Engineering

by

Lord Kahil Cole

2012

© Copyright by
Lord Kahil Cole
2012

ABSTRACT OF THE DISSERTATION

Combustion and Magnetohydrodynamic Processes in Advanced Pulse Detonation Rocket Engines

by

Lord Kahil Cole

Doctor of Philosophy in Aerospace Engineering

University of California, Los Angeles, 2012

Professor Ann Karagozian, Chair

A number of promising alternative rocket propulsion concepts have been developed over the past two decades that take advantage of unsteady combustion waves in order to produce thrust. These concepts include the Pulse Detonation Rocket Engine (PDRE), in which repetitive ignition, propagation, and reflection of detonations and shocks can create a high pressure chamber from which gases may be exhausted in a controlled manner. The Pulse Detonation Rocket Induced Magnetohydrodynamic Ejector (PDRIME) is a modification of the basic PDRE concept, developed by Cambier (1998), which has the potential for performance improvements based on magnetohydrodynamic (MHD) thrust augmentation. The PDRIME has the advantage of both low combustion chamber seeding pressure, per the PDRE concept, and efficient energy distribution in the system, per the rocket-induced MHD ejector (RIME) concept of Cole, et al. (1995).

In the initial part of this thesis, we explore flow and performance characteristics of different configurations of the PDRIME, assuming quasi-one-dimensional transient

flow and global representations of the effects of MHD phenomena on the gas dynamics. By utilizing high-order accurate solvers, we thus are able to investigate the fundamental physical processes associated with the PDRIME and PDRE concepts and identify potentially promising operating regimes.

In the second part of this investigation, the detailed coupling of detonations and electric and magnetic fields are explored. First, a one-dimensional spark-ignited detonation with complex reaction kinetics is fully evaluated and the mechanisms for the different instabilities are analyzed. It is found that complex kinetics in addition to sufficient spatial resolution are required to be able to quantify high frequency as well as low frequency detonation instability modes. Armed with this quantitative understanding, we then examine the interaction of a propagating detonation and the applied MHD, both in one-dimensional and two-dimensional transient simulations. The dynamics of the detonation are found to be affected by the application of magnetic and electric fields. We find that the regularity of one-dimensional cesium-seeded detonations can be significantly altered by reasonable applied magnetic fields ($B_z \leq 8T$), but that it takes a stronger applied field ($B_z > 16T$) to significantly alter the cellular structure and detonation velocity of a two-dimensional detonation in the time in which these phenomena were observed. This observation is likely attributed to the additional coupling of the two-dimensional detonation with the transverse waves, which are not captured in the one-dimensional simulations. Future studies involving full ionization kinetics including collisional-radiative processes, will be used to examine these processes in further detail.

The dissertation of Lord Kahil Cole is approved.

Owen Smith

Chris Anderson

Xiaolin Zhong

Jean-Luc Cambier

Ann Karagozian, Committee Chair

University of California, Los Angeles

2012

To my mother, Linda, the enduring memory of my father, Otha, and my fiancée,
Kendra.

TABLE OF CONTENTS

Nomenclature	1
1 Introduction	5
1.1 Background on Detonation Engine Concepts	5
1.1.1 Engine Impulse and Efficiency	7
1.1.2 Pulse Detonation Engines	8
1.1.3 AJAX and RIME concepts for thrust augmentation	9
1.2 Plasma Flows	10
1.2.1 The Lorentz Force	10
1.2.2 Plasmas and Cesium Ionization	11
1.3 Pulse Detonation Rocket Induced Magnetohydrodynamic Ejectors and other Alternative Configurations	13
1.3.1 PDRIME	14
1.3.2 Cambier’s Quasi-1D Model and Verification	16
1.4 Detonation Waves and MHD Effects	18
1.5 Goals of the Present Studies	20
2 Governing Equations and Physical Phenomena	27
2.1 Conservative Formulation	27
2.1.1 Single-Temperature(1T) Hydrodynamic Formulation	28

2.1.2	Single-Temperature(1T) Ideal MHD Formulation ($Re_m \rightarrow \infty$)	29
2.1.3	Two-Temperature(2T) Formulation	30
2.2	Overview of Source Terms for Governing Equations	32
2.2.1	Combustion and Ionization Reaction Kinetics	32
2.2.2	MHD Transport	33
2.3	Kinetics	34
2.3.1	Combustion Kinetics	35
2.3.2	Ionization Kinetics	38
2.3.3	Two-Temperature(2T) Relaxation	39
2.4	MHD Transport	40
3	Numerical Methods	44
3.1	Operator Splitting	44
3.2	Time Step Restrictions	45
3.2.1	Convection	45
3.2.2	Kinetics Resolution	46
3.2.3	Diffusion	47
3.3	Explicit Runge Kutta Scheme	47
3.4	Hyperbolic Solvers – Approximate Riemann Solvers	48
3.4.1	Weighted Essentially Non-Oscillatory (WENO) Schemes	50
3.4.2	Monotonicity Preserving (MP) Schemes	53
3.4.3	Advection-Diffusion-Reaction (ADER) Schemes	55

3.5	Point-Implicit Euler	57
3.6	Spatial-Implicit Euler	58
4	Verification of Numerical Schemes	65
4.1	Inviscid Hydrodynamics	65
4.1.1	Sod’s Shock Tube	66
4.1.2	Hydrodynamical Interacting Blast Wave Problem	66
4.1.3	Shock-Entropy Wave Interaction	67
4.1.4	Shock Diffraction Down a Backward Facing Step	68
4.1.5	Rayleigh-Taylor Hydrodynamic Instability	68
4.2	Ideal Magnetohydrodynamics(MHD)	69
4.2.1	1D MHD Shock Tube Problems	69
4.2.2	Orszag-Tang Problem	70
4.2.3	Balsara’s Rotor Problem	71
4.2.4	Rayleigh Taylor MHD Instability	71
4.3	Two-Temperature(2T) Model	73
5	Simplified Approach for PDRIME Simulations	100
5.1	PDRIME with Bypass Configurations	102
5.2	Temporal/Temperature Controllers of the Magnetic Field	103
5.3	PDRIME with 2D Bypass Configuration	106
6	Detonation Stability Phenomena	121

6.1	Ignition and Instabilities	121
6.2	Simplified Model	128
6.3	Discussion	131
7	Magnetic Field and Detonation Interactions	147
7.1	Detonation Instabilities with Applied Magnetic Fields	147
7.2	Detonation Instabilities with MHD	150
7.3	2D Cellular Detonation in an Applied Magnetic Field	152
7.3.1	Enhanced Kinetics	154
7.3.2	Strong Applied Fields	155
7.4	Conclusions	156
8	Conclusions and Future Work	198
A	Reaction Mechanism	201
A.1	H_2 -Air Reaction Mechanism	201
A.2	Cesium Reaction Mechanism	202
B	Eigenvector Matrices	203
B.1	Governing Equation	203
B.2	Roe Averaged Weighting	204
B.3	Eigensystem and Flux Jacobian Matrix	204
B.3.1	Right Eigenvectors	205

B.3.2	Left Eigenvectors	207
B.3.3	Riemann ‘Jump’ conditions	209
C	MHD Divergence Cleaning for General Coordinate Systems	211
D	Jacobians and Transforms	212
D.1	Chemical Jacobian	212
D.2	Chemical Jacobian($\frac{\partial \dot{\Omega}}{\partial Q}$) Derivation	213
E	Steady State Detonation	214
F	Iterative & Direct Solvers	215
F.1	Thomas’ Algorithm	215
F.2	Black-Red Gauss-Seidel	216
G	Message Passing Interface (MPI) Implementation	219
G.1	Grid Connectivity	219
	References	221

LIST OF FIGURES

1.1	Generic PDE Cycle	22
1.2	PDRE flight configuration.	23
1.3	Pulse Detonation Rocket Engine with MHD nozzle generation flight configuration.	23
1.4	Pulse Detonation Rocket Induced MHD Ejector.	24
1.5	Pulse Detonation Rocket Engine with Chamber Magnetic Piston. . .	24
1.6	Pulse Detonation Rocket Induced MHD Ejector with Chamber Mag- netic Piston.	25
1.7	Orientation of Electromagnetic Fields and associated Forces.	26
2.1	Induction delay vs Initial Temperature	43
3.1	Basic Operator Splitting	62
3.2	Strang Splitting	63
3.3	ENO/WENO Stencil	63
3.4	Strang Time Splitting	64
4.1	Density distribution for 1D Sod’s Shock Tube problem.	75
4.2	Density distribution for 1D Blastwave problem.	76
4.3	Density distribution of contact discontinuities for 1D Blastwave problem.	77
4.4	Density distribution for 1D Shock-Entropy Wave Interaction problem.	78
4.5	Mach 2.4 flow over backward facing step: MW5	79

4.6	Density distribution for hydrodynamic Rayleigh Taylor Instability: $t = 0.75s$	80
4.7	Density distribution for hydrodynamic Rayleigh Taylor Instability: $t = 1.50s$	81
4.8	Density distribution for hydrodynamic Rayleigh Taylor Instability: $t = 2.25s$	82
4.9	Density distribution for hydrodynamic Rayleigh Taylor Instability: $t = 3.00s$	83
4.10	Density distribution for 1D Brio-Wu problem.	84
4.11	Density distribution for 1D Brio-Wu problem – compound wave and contact discontinuity.	85
4.12	u_x distributions for 1D Brio-Wu problem.	86
4.13	u_y distribution for 1D Brio-Wu problem.	87
4.14	Pressure distribution for 1D Brio-Wu problem.	88
4.15	B_y distribution for 1D Brio-Wu problem.	89
4.16	Density distributions for Orszag-Tang problem.	90
4.17	Balsara’s Rotor Problem (MW5): $t = 0.295s$	91
4.18	Balsara’s Rotor Problem (MP5): $t = 0.295s$	92
4.19	Balsara’s Rotor Problem (AW5): $t = 0.295s$	93
4.20	Density distribution for MHD Rayleigh Taylor Instability: $t = 2s$	94
4.21	MHD Rayleigh Taylor Instability Growth (MW5): $t = 2s$	95
4.22	MHD Rayleigh Taylor Instability Growth (MP5): $t = 2s$	96

4.23	MHD Rayleigh Taylor Instability suppression via a normal magnetic field (MW5): $t = 2s$	97
4.24	MHD Rayleigh Taylor Instability suppression via a normal magnetic field (MP5): $t = 2s$	98
4.25	Mach 10 Argon Shock with/without T_e Relaxation	99
5.1	Variation In Impulse For A PDRE	108
5.2	Quasi 1D Computational Domain	109
5.3	Quasi 1D Performance: Impulse Loss in Nozzle Energy Generation . .	110
5.4	Quasi 1D Component Performance: Bypass vs. Nozzle Impulse . . .	111
5.5	Magnetic Field Strength vs. Time, $\Pi(t)$	112
5.6	PDRIME: Effects of Flight Mach number, $B(t) \sim t^2$	113
5.7	PDRIME: Effects of Flight Mach number, B(T)	114
5.8	PDRIME: Effects of Flight Mach number, B(T)	115
5.9	PDRIME: Effects of Flight Mach number, B(T)	116
5.10	PDRIME: Effects of Flight Mach number, B(T)	117
5.11	PDRIME 2D Results: altitude = 20 km	118
5.12	PDRIME 2D Results: altitude = 25 km	119
5.13	PDRIME 2D Results: altitude = 30 km	120
6.1	Detonation Pressure Contour - MP5	134
6.2	Peak Pressure trace ($\Delta x = 2.5\mu m$ & $12.5\mu m$)	135
6.3	Peak Pressure Trace: High Frequency(HF) Mode	136

6.4	Peak Pressure Trace: High Amplitude(HA) Mode	137
6.5	Peak Pressure Trace: Post-“re-explosion”	138
6.6	Induction Length Trace: Post-“re-explosion”	139
6.7	Time to re-explosion vs Grid Resolution	140
6.8	Fourier Transform of Typical Peak Pressure Traces	141
6.9	Induction Zone in Detonation Reference Frame	142
6.10	Simplified model of the peak Pressure Cycle	142
6.11	High Frequency(HF) Mode Peak Pressure Cycle (phase 1 of 2)	143
6.12	High Amplitude(HA) Mode Peak Pressure Cycle (phase 1 of 2)	144
6.13	High Frequency(HF) Mode Peak Pressure Cycle (phase 2 of 2)	145
6.14	High Amplitude(HA) Mode Peak Pressure Cycle (phase 2 of 2)	146
7.1	Peak Pressure Traces with Cesium Addition	159
7.2	Configuration of Magnetic Field	160
7.3	Peak Pressure Traces with various applied magnetic fields (%Cs = 1)	161
7.4	Peak Pressure Traces with various applied magnetic fields (%Cs = 5)	162
7.5	Peak Pressure Traces with various applied magnetic fields (%Cs = 10)	163
7.6	Peak Pressure Traces with various applied electric and magnetic fields (%Cs = 1)	164
7.7	Peak Pressure Traces with various applied electric and magnetic fields (%Cs = 5)	165

7.8	Peak Pressure Traces with various applied electric and magnetic fields (%Cs = 10)	166
7.9	Time trace comparisons of $B_z = 0, 3,$ and 8 T 1D detonations in the accelerator and generator configuration	167
7.10	Numerical setup for 2D detonation simulations	168
7.11	Schlieren-type plot of cellular detonation	169
7.12	Stoichiometric $H_2 - Air$ detonation	170
7.13	Stoichiometric $H_2 - Air - 1\% Cs$ detonation	171
7.14	Stoichiometric $H_2 - Air - 5\% Cs$ detonation	172
7.15	Stoichiometric $H_2 - Air - 10\% Cs$ detonation	173
7.16	X-t plot: no MHD/generator/accelerator with 1% Cs	174
7.17	X-t plot: no MHD/generator/accelerator with 5% Cs	175
7.18	X-t plot: no MHD/generator/accelerator with 10% Cs	176
7.19	Peak pressure trace: no MHD/generator/accelerator with 1% Cs . . .	177
7.20	Peak pressure trace: no MHD/generator/accelerator with 5% Cs . . .	178
7.21	Peak pressure trace: no MHD/generator/accelerator with 10% Cs . .	179
7.22	Centerline pressure and conductivity profiles: accelerator & generator configurations $B_z = 8T, t = 75\mu s$	180
7.23	Conductivity distribution in a 2D detonation with a linear color map overlaid with Schlieren-type plot using density gradients of the deto- nation front with varying EK in the generator configuration	181

7.24	Conductivity distribution in a 2D detonation with a linear color map overlaid with Schlieren-type plot using density gradients of the detonation front with varying EK in the accelerator configuration	182
7.25	Centerline peak pressure trace: accelerator configuration with 10% Cs with various EK	183
7.26	Centerline peak pressure trace: generator configuration with 10% Cs with various EK	184
7.27	X-t plot: no MHD/generator/accelerator with 10% Cs with $EK = 100$	185
7.28	Centerline peak pressure trace: accelerator configuration with 10% Cs and various B_z	186
7.29	Centerline peak pressure trace: generator configuration with 10% Cs and various B_z	187
7.30	X-t plot: generator configuration with 10% Cs and various B_z	188
7.31	X-velocity profiles at different times: generator configuration with 10% Cs and various B_z	189
7.32	Conductivity profiles at different times: generator configuration with 10% Cs and various B_z	190
7.33	Pressure profiles at different times: generator configuration with 10% Cs and various B_z	191
7.34	Temperature profiles at different times: generator configuration with 10% Cs and various B_z	192
7.35	Detonation history: no MHD with 10% Cs	193

7.36 Detonation history: Accelerator configuration with $B_z = 8T$ and 10% Cs	194
7.37 Detonation history: Accelerator configuration with $B_z = 16T$ and 10% Cs	195
7.38 Detonation history: Accelerator configuration with $B_z = 32T$ and 10% Cs	196
7.39 X-t plot: accelerator configuration with 10% Cs and various B_z	197
F.1 Grid Cell Checkerboard Pattern	218
G.1 Domain and subdomains	220
G.2 Domain-to-domain Connection Example	220

LIST OF TABLES

2.1	Simplified $H_2 - O_2$ Reaction Thermodynamic Properties	42
2.2	Ionization Temperatures	42
3.1	WENO Coefficients	62
4.1	RTI problem hydrodynamic initial conditions	74
4.2	Balsara's rotor problem initial conditions	74
7.1	Detonation Velocity with Cesium	158
G.1	Generic Memory Window List	220

ACKNOWLEDGMENTS

I would like to acknowledge the many people who helped make this dissertation possible. I would like to first thank Professor Ann Karagozian for her great insight, patience, and her infectious drive and energy. I would like to thank my mentor, Dr. Jean-Luc Cambier, for encouraging me to explore the physics deeply and tackle the hard questions. I gratefully acknowledge Professor Owen Smith for his numerous helpful ideas and insight throughout the course of this work. I would also like to thank the members of my committee, Professor Xiaolin Zhong and Professor Chris Anderson, for their guidance.

I would like to thank my current and past labmates, Chris, Hai, Cory, Dan, Sophonias, and Jeff, and classmates, Naveen, Patrick, Pilbum, Morad, Clifton, and Ladan, at UCLA for their support and enjoyable discussions. I also gratefully acknowledge the good folks at the In-Space Propulsion Branch of the Air Force Research Laboratory: Carrie, Kooj, Rob, Carl, and David, for their helpful ideas and technical assistance.

I would particularly like to thank my parents and siblings, Otha and Khalila, for their inspiration and support. Specifically, to my dad, for not giving into the pressures of my bored siblings and prematurely leaving the theater playing *Apollo 13*. Thank you, dad, for nurturing the spark which led to the pursuit of this current work. And finally, and most importantly, I would like to thank my fiancée, Kendra, for her unwavering support and encouragement.

Financial support for this project has come from the U.S. Air Force Office of

Scientific Research under the Space Power and Propulsion program managed by Dr. Mitat Birkan under grants FA9550-07-1-0156 and FA9550-07-1-0368, ERC Inc. under Subcontract RS100226, the AFRL Co-op Program, and the UCLA Cota-Robles Fellowship program. This support is gratefully acknowledged.

VITA

- 2005 B.S. (Physics), United States Naval Academy.
- 2005–2007 United States Naval Officer.
- 2008 M.S. (Aerospace Engineering), UCLA, Los Angeles, California.
- 2008–2009 Teaching Assistant, Mechanical and Aerospace Engineering
Department, UCLA. Taught Aircraft Propulsion Section
- 2010–present Research Co-Op, Air Force Research Laboratory, Propulsion
Directorate, Edwards AFB, CA.

PUBLICATIONS AND PRESENTATIONS

Le, H., Cambier, J.-L., and Cole, L.K., “GPU-based flow simulation with detailed chemical kinetics,” to appear in *Computer Physics Communications*.

Cole, L.K., Karagozian, A.R., and Cambier, J.-L., “Stability of Flame-Shock Coupling in Detonation Waves: 1D Dynamics,” *Combustion Science & Technology*, Vol. 184, Issue 10-11, pp. 1502-1525, 2012.

Zeineh, C.F., Cole, L.K., Roth, T., Karagozian, A.R., and Cambier J.-L., “Magnetohydrodynamic

Thrust Augmentation of Pulse Detonation Rocket Engines,” *Journal of Propulsion and Power*, Vol. 28, No. 1, pp. 146-159, 2012.

Cole, L.K. and A. Karagozian, A.R., “Numerical Simulations of Detonation Wave - Magnetic Field Interactions” presented at the 65th APS/DFD Meeting, San Diego, CA, November 2012.

Cole, L.K., Le, H., J.-L. Cambier, and A. Karagozian, A.R., “Numerical Simulations of Detonation Instabilities and Magnetic Field Interaction” presented at the 64th APS/DFD Meeting, Baltimore, MD, November 2011.

Cole, L.K., Karagozian, A.R., and Cambier J.-L., “Stability of Flame-Shock coupling in Detonation Waves: 1D Dynamics,” presented at 23rd International Colloquium on Dynamics of Explosions and Reactive Systems, Irvine, CA, July 2011.

Cole, L.K., Cambier J.-L., and Karagozian, A.R., “Simulation of a Detonation in Transverse Magnetic Fields” presented at the 63rd APS/DFD Meeting, Long Beach, CA, November 2010.

Cole, L.K., Roth, T., Zeineh, C.F., and Karagozian, A.R., “Magnetohydrodynamic Augmentation of Pulse Detonation Engines: Simplified Modeling and Performance Estimates” presented at 3rd Southern California Symposium on Flow Physics, 2009.

Nomenclature

\tilde{A}	Jacobian Matrix
AR	Exit-to-throat nozzle area ratio
\mathbf{B}	Magnetic field, $\{B_x, B_y, B_z\}$
c_i	Mass fraction of species i
c_p	Specific heat capacity at constant pressure
c_v	Specific heat capacity at constant volume
D	Detonation speed
D_{CJ}	Chapman-Jouget detonation velocity
\mathbf{D}	Displacement Field
e	Internal energy per unit mass
e_0	Internal energy of formation per unit mass
\hat{E}	Total energy per unit volume
\mathbf{E}	Electric field, $\{E_x, E_y, E_z\}$
EK	Enhanced kinetics factor
f	Overdrive factor ($f \equiv (D/D_{CJ})^2$)
f_{loss}	Bypass pressure loss factor

\mathcal{F}	Thrust
\mathbf{g}	Gravitational acceleration
h	Enthalpy per unit mass
\mathbf{H}	Magnetizing Field
I	Impulse
I_{tot}	Total impulse
I_{sp}	Specific impulse ($I_{sp} \equiv I/\rho V g$)
\mathbf{j}	current density
k	Boltzmann's constant
k_b	Backward reaction coefficient
k_f	Forward reaction coefficient
K	Reaction-rate multiplier
\mathbf{K}	Loading factor, $\{K_x, K_y\}$
L	Cellular detonation cell length
M	Mach Number
M_i	Molar mass of species i

n_i	Number density of species i
N	Total number density
P	Static pressure
P^*	Static and Magnetic pressure
q	Heat release per unit mass
P_{ref}	Reference pressure
Q_{rs}	Elastic collision cross-section of the r^{th} and s^{th} species
R_u	Universal gas constant
R_{prod}	Specific gas constant (products)
R_{reac}	Specific gas constant (reactants)
Re_m	Magnetic Reynolds Number
\hat{s}_e	Specific electron entropy
S_e	Electron entropy per unit volume
T	Temperature
T_A	Activation temperature
T_f	Peak flame temperature

\mathbf{u}	Fluid velocity
V	Specific volume ($V \equiv 1/\rho$)
σ	Electrical conductivity
γ	Specific heat ratio ($\gamma \equiv c_p/c_v$)
λ	Cellular detonation cell size (height)
$\nu_{i,j}$	Stoichiometric coefficient for species i at reaction j
ρ	Mass density
$\dot{\omega}$	Reaction source term (see equation (2.22))
Θ	Characteristic Temperature
ϵ_0	Permittivity of free space
μ_0	Permeability of free space
$()_i$	i^{th} numerical grid cell
\vec{q}	$(\dots, q_{i-1}, q_i, q_{i+1}, \dots)^T$
\mathbf{q}	$\{q_x, q_y, q_z\}$

CHAPTER 1

Introduction

1.1 Background on Detonation Engine Concepts

The chemical rocket can be considered the oldest technical development in jet propulsion. In a solid propellant rocket, for example, the exit plane momentum is due to the flow of a hot gas created by the rapid burning of solid fuel composed of a mixture of a fuel and oxidizer. Gun powder emerged in China around AD 850 as the result of accidental discovery by Chinese alchemist. For centuries after this discover, little was done in the advancement of rocket propulsion, until in 1903, a Russian school teacher by the name of Konstantin Tsoikowsky[1] published the paper ‘The Investigation of Outer Space by Means of Reaction Apparatus’. In this paper, Tsoikowsky postulated that man could escape the clutches of earth’s gravity with rockets. His calculations led him to the idea of multi-staging. Subsequently, he went on to discuss the use of liquid oxygen and liquid hydrogen for those purposes. Piggy-backing off of these ideas, the American physicist, Robert Goddard, designed constant pressure rocket combustion chamber nozzles and propellant feed systems. Goddard[2] went on to lead the advancement of liquid fueled rockets and in 1919 published, ‘A Method of Reaching Extreme Altitudes’, which not only provided the mathematical analysis for achieving high altitudes, but also to reach the moon. He devoted much

of his effort to thrust chamber development and to the turbo-machinery needed for pumping the liquid propellants [3].

Still today, almost a century later, the modern aerospace community finds itself facing the same challenges as the founding fathers of modern rocketry. These challenges include, but are not limited to, developing lighter and more efficient propulsion systems and more efficient multi-staging techniques. The present studies focus on exploring potential rocket propulsion systems that take advantage of magnetohydrodynamics(MHD) phenomena.

In 1998, Dr. Jean-Luc Cambier proposed a novel combined cycle propulsive concept, the Pulse Detonation Rocket-Induced Magnetohydrodynamic Ejector (PDRIME)[4]. The PDRIME is one of many MHD thrust augmentation ideas that shows promise for application in advanced propulsion systems. Taking advantage of the unsteady wave engine concept of the constant volume Pulse Detonation Engine (PDE), the PDRIME utilizes temporal periodic energy divergence into a seeded air stream, then MHD acceleration for thrust augmentation. Because of the nature of the unsteady waves in the PDE, the PDRIME does not need heavy turbo-machinery to pump liquid propellants. With the elimination of heavy turbo-machinery, paired with the energy augmentation of the MHD accelerator in the bypass air stream, the PDRIME could potentially be able to achieve the velocities necessary for Single-Stage-to-Orbit (SSTO) flight, thus breaking with the expensive tradition of complicated, expensive multistage propulsive systems.

Another concept developed by Cambier in [5] is the ‘Magnetic Piston’. This concept involves energy extraction from the expansion portion of the nozzle, energy reintroduction into the combustion chamber, followed by acceleration of the com-

bustion products from the combustion chamber. The ‘Magnetic Piston’ builds upon the PDE and the PDRIME, but also gains some advantages of traditional constant pressure rocket propulsion systems. These and other alternative rocket propulsion concepts will be explored in this dissertation. The present chapter provides the technical background for these concepts.

1.1.1 Engine Impulse and Efficiency

Before we can compare the properties and advantages of various propulsion systems, we must first have a quantitative means of expressing various properties. Impulse and efficiency are the properties we are most interested in. Impulse is defined as the integral of thrust, \mathcal{F} , over a given time period:

$$I \equiv \int_0^t \mathcal{F}(\tau) d\tau \quad (1.1)$$

Efficiency in a propulsion system is quantified by the specific impulse, I_{sp} , which is defined as $I_{sp} \equiv \frac{I}{M_p g}$, where $M_p g$ is the weight of the propellant used. A typical rocket engine uses a converging-diverging (Laval) nozzle to convert high pressure and temperature propellant into thrust. The larger the area ratio (AR), ratio of nozzle exit area to nozzle throat area, of the nozzle the faster the exit velocity of the propellant, u_e , and lower the exit pressure, P_e . The thrust generated by rockets is typically expressed as:

$$\mathcal{F} = \dot{m} u_e + (P_e - P_{atm}) A_e \quad (1.2)$$

where \dot{m} is the mass flux of gas exiting the nozzle and A_e is the area of the nozzle exit plane. For optimal thrust, P_e is equal to the ambient pressure, P_{atm} , when this is achieved, a nozzle is said to be ‘perfectly’ expanded. When traveling in altitudes which range from sea level to the edge of space (the Von Karman line, or 100 km),

there is a large variation in the ambient pressures, so that most often $P_e \neq P_{atm}$. These variations in ambient pressure lead to significant losses in nozzle efficiency.

1.1.2 Pulse Detonation Engines

The Pulse Detonation Engines (PDE) in simple terms is an engine that utilizes detonation waves to derive its thrust. The PDE operates in a cycle, shown schematically in Figure 1.1. In this simple configuration, a stoichiometric mixture of reactants is placed in a long tube with an open and closed end (i.e., thrust wall). The mixture is then ignited from the thrust wall (a). This results in a shock and deflagration wave (subsonic flame) quickly coalescing into a detonation wave (supersonic flame – see section 1.4) propagating into the reactant mixture (b). The high pressure region behind the wave imparts force on the thrust wall. When the detonation wave reaches the open end of the tube (c), it will be reflected back into the tube as an expansion wave (d). The expansion wave propagates into the tube, while at the same time purging the combustion products from the tube (e). The expansion wave will then reflect off of the thrust wall, and at that time the lowered pressure will draw fresh reactants into the tube (f). The expansion wave will propagate into the tube, then reflect back from the open end as a compression wave (h). This compression wave will propagate through the re-introduced reactants (i), after which it will reflect of the thrust wall as a shock (j) and a new cycle will begin. There are many advantages to the PDE over conventional rockets propulsion systems. The conventional rocket engines have to pump reactants at very high pressures into a combustion chamber, requiring heavy turbo machinery, while the PDE does not need heavy turbo machinery, but rather naturally introduces the reactants into the combustion chamber

at much lower pressures. The simplicity of the concept is quite attractive, and the PDE's have been tested extensively over the years [22]. PDE's have even been tested as the sole source of propulsion on an experimental aircraft, the Scaled Composites Long E-Z[24], which used an abundance of off-the-shelf parts.

1.1.3 AJAX and RIME concepts for thrust augmentation

Ejectors have been considered for years as a viable method of thrust augmentation for various aerospace propulsion systems. Ejectors rely on the transfer of energy from one stream (primary) to another stream (secondary). Higher thrust can be achieved if the primary stream has a high specific energy and the secondary has a high mass flow rate. A generic Rocket Induced Magnetohydrodynamic Ejector (RIME) [25] consist of 3 parts, each consisting of variable area stream-tubes; (1) the generator, (2) the accelerator, and (3) the mixer. The streams can be described by different power plants, for example a rocket stream, a bypass tube, and the mixer. In the RIME described by [25], the “rocket stream” serves as the MHD generator while the “mixer” is the MHD accelerator. The MHD generator transforms the internal energy of a fluid into electrical power. The fluid itself is a conductor of electricity, the motion of this fluid through a magnetic field gives rise to electromotive force (drag) and flow current in accordance with Faraday's law of inductance. An MHD accelerator uses the same principles, but in this particular case electrical energy is applied to the system resulting in an electromotive force (thrust). In the AJAX system, energy is diverted from the inlet flow via MHD generation, it is then re-applied after the fluid passes through the combustor via MHD generation[26].

1.2 Plasma Flows

1.2.1 The Lorentz Force

The various advanced rocket engine configurations explored and reviewed in this dissertation utilize electromotive forces (Lorentz forces) generated by a moving charge to augment thrust. The Lorentz Force is defined as the Coulombic attractive/repulsive force between single or collection of charged particle(s) moving through an electromagnetic field:

$$\mathbf{F} = \mathbf{j} \times \mathbf{B} \quad (1.3)$$

where \mathbf{F} is the Lorentz force, \mathbf{j} is the current density, and \mathbf{B} is the applied magnetic field. The current density is defined by Ohm's law:

$$\mathbf{j} = \sigma(\mathbf{E} + \mathbf{u} \times \mathbf{B}) \quad (1.4)$$

where σ is the conductivity, \mathbf{E} is the electric field, and \mathbf{u} is the fluid velocity. Expressing the electric field using Ohm's law and using vector identities, the total rate of energy deposition into the fluid can be expressed as :

$$\mathbf{j} \cdot \mathbf{E} = \mathbf{j} \cdot \left(\frac{\mathbf{j}}{\sigma} - \mathbf{u} \times \mathbf{B} \right) = \frac{\mathbf{j}^2}{\sigma} + \mathbf{u} \cdot (\mathbf{j} \times \mathbf{B}) \quad (1.5)$$

where the first term on the right side is the heating of the fluid (dissipation) and the second term on the right side is the mechanical power obtained from the Lorentz force (non-dissipative). The separation of the different forms of power expended in the fluid becomes important as we evaluate efficiency later in this document [4].

1.2.2 Plasmas and Cesium Ionization

A plasma is defined as a collection of charged particles where the long-range Coulombic force is a factor in determining the statistical properties, but where the collection of particles is low enough in density so that the forces exerted by a particles nearest-neighbor is less than the long-range Coulombic force exerted by the particle's many neighbors. Thus, the study of plasma often coincides with the study of low-density ionized gases. An ion is a molecule or atom which acquires enough energy to liberate a valence, outer shell, electron from the respective molecule/atom. A collection of ions, liberated electrons, and neutral particle's form a plasma. In a weakly ionized plasma, which we shall investigate throughout the remainder of this study, the ion remains in close proximity with a liberated electron, thus the plasma as a whole can be thought of as charge neutral, but locally charged [27].

One of the necessary properties of the configurations discussed earlier in this document, the AJAX, the RIME, and other advanced configurations, is the ability for the working fluid to conduct electricity. In order for a fluid to conduct electricity it must be at least partially ionized. These advanced configurations achieved ionization through thermal ionization. Thermal ionization follows mass action laws like any chemical reaction. The heat of ionization, when expressed in Kelvin is referred to as the characteristic temperature of ionization, $\Theta_i \equiv H_{ionization}/k$, where k is Boltzmann's constant. Most common gases and combustion products, i.e., air, CO, CO_2 , and noble gases, have high characteristic temperatures, so they do not thermally ionize until temperatures in excess of 4000K are reached. However, if an alkali metal, which has a low characteristic temperature of ionization, is added in small amounts (on the order of 1 part in 100 or less) thermal ionization can be achieved

at temperatures as low as 2000K. This process, referred to as *seeding*, changes the working fluid into a plasma and allows the previously mentioned configurations to conduct electricity under realistic operating temperatures [28].

A plasma will often take on different characteristics, depending on the temperature, conductivity, and mean velocity, to name a few. Before we delve into the various regimes in which the plasma being studied will exist, we must first look to Maxwell's equations for free charge[29]:

$$\begin{aligned}
\nabla \times \mathbf{H} &= \frac{\partial \mathbf{D}}{\partial t} + \mathbf{j} \\
\nabla \times \mathbf{E} &= -\frac{\partial \mathbf{B}}{\partial t} \\
\nabla \cdot \mathbf{B} &= 0 \\
\nabla \cdot \mathbf{E} &= \frac{e(n_i - n_e)}{\epsilon_0}
\end{aligned}
\tag{1.6}$$

where n_e is the number density of electrons, ϵ_0 is the permittivity of free space, \mathbf{H} is the magnetic field, \mathbf{D} is the electric displacement field, and e is the charge of an electron. As an example, if a one-dimensional gas were to flow perpendicularly to a magnetic field, the induced electric field could be expressed as $E_y \approx \frac{1}{2}u_x B_z$, which can be shown as follows for the idealize case, $\mathbf{j}/\sigma \rightarrow 0$:

$$\begin{aligned}
\mathbf{j} &= \sigma (\mathbf{E} + \mathbf{u} \times \mathbf{B}) \\
\mathbf{E} &\approx -\mathbf{u} \times \mathbf{B} \\
E_y &\approx u_x B_z
\end{aligned}
\tag{1.7}$$

The work done by a unit volume of this gas moving a length, L , oriented perpendicularly to the magnetic field, \mathbf{B} , using Equations 1.3 and 1.6, would produce the following[28]:

$$FL = \frac{1}{2}\sigma_g u B^2 L
\tag{1.8}$$

The energy stored in a magnetic field per unit volume is $\frac{B^2}{2\mu_0}$, which is often referred to as the magnetic pressure. The ratio of these is

$$\frac{\text{Work done by the gas}}{\text{Energy stored in the field}} = \mu_0 \sigma_g u L = Re_m \quad (1.9)$$

The Magnetic Reynolds number, Re_m , is a good measure of the degree in which a field induced by gas motion compares to the original magnetic field. This parameter plays a very important role in determining the performance of the MHD accelerator and generator.

1.3 Pulse Detonation Rocket Induced Magnetohydrodynamic Ejectors and other Alternative Configurations

Spawned from the concept of AJAX [26] and RIME [25], Pulse Detonation Rocket Induced Magnetohydrodynamic Ejectors (PDRIME) and other alternative configurations are meant to push the bounds of MHD thrust augmentation. The Pulse Detonation Rocket Engine (PDRE) is the core of the various alternative engine configuration currently under review. The PDRE is composed of two major components: a combustion chamber and a converging-diverging nozzle shown in Figure 1.2. The combustion chamber introduces reactants on the front end, while the downstream end connects to the converging-diverging nozzle. The converging end of the nozzle has an extremely short length and a high exit-to-throat area ratio, $AR \sim 16$, the significance of which will be explained momentarily. A typical PDRE cycle is at the core a PDE cycle, where reactants are introduced to the combustion chamber and the reactants are ignited at the front end. A detonation wave is formed and propagates downstream, but unlike the PDE cycle previously mentioned, the detonation

wave will reflect off of the high area ratio converging section nozzle and reflect back as a shock wave. The reflected detonation will raise the chamber temperature and pressure so rapidly that the expelled gases can be thought of as started from this high pressure or ‘blow down’ state [30]. The fluid is then accelerated out of the nozzle where more thrust is derived. Over a cycle, the pressure of the chamber will decrease as more products are being expelled. The chamber will then reach a critical pressure in which reactants will be introduced at relatively low pressure, and a new cycle will commence.

1.3.1 PDRIME

The PDRIME is actual a composite of some of the systems previously discussed, that is, the AJAX, the RIME, and PDRE. The PDRIME is physically composed of PDRE (the combustion chamber and nozzle), a bypass tube that sits directly on top of the PDRE and magnets which are placed around the nozzle as well as around the bypass tube which is illustrated in Figure 1.3 and 1.4. The effect of the strengths of these magnetics will be explored later in this dissertation. In a PDRIME cycle, reactants as well as a gas of low ionization energy, e.g., cesium, are introduced into the combustion chamber and a PDRE cycle will commence. The fluid in the combustion chamber will be heated sufficiently to ionize the seeded cesium. During this process, hot products and ions will be expelled out of the nozzle. As the fluid expands through the nozzle, the MHD generator in the nozzle will be engaged. The generator will extract energy from the fluid moving at high velocities and reduce the Mach number, $M = u/a$, to approximately unity at the nozzle exit. With $M \approx 1$ at the nozzle exit, an unsteady shock will migrate from the nozzle exit into the

bypass tube. The front entrance of the bypass tube is seeded with cesium, and as the unsteady shock migrates upstream, the cesium will also pass through the shock and be ionized. From there, the MHD accelerators in the bypass will be employed and will utilize the Lorentz force to accelerate the fluid out of the bypass tube. The aim of this configuration is to take energy out of the nozzle and more effectively utilize it in the bypass tube in order to increase thrust and thus gain more impulse and efficiency.

The PDRE has many good performance characteristics, e.g., low seeding pressure, but one characteristic that we wish to improve is the nature of the unsteady pressure throughout the PDRE cycle. As previously described, the pressure in the chamber is quickly increased with the chemical reactions and subsequent reflection of detonation waves, then gas is expelled from the combustion chamber and expanded through the nozzle. As more combustion products are purged from the combustion chamber, the pressure in the combustion chamber drops drastically with time. In a PDRIME configuration, this drastic drop in pressure severely handicaps the effectiveness of the MHD accelerator in the bypass tube. This impairment works as follows: as the pressure drops in the chamber and nozzle, the back pressure driving the nozzle flow drops. This dropping of pressure driving the nozzle correlates to a drop in pressure entering the bypass tube exit. The pressure at the end of the bypass tube supports the unsteady shock wave in the tube, so as this pressure drops, so does the strength of the unsteady shock heating the fluid in the bypass. As the strength of the unsteady shock dies down in strength, the temperature jump across shock is reduced, therefore less ionization takes place. Less ionization leads to lower conductivity, and with lower conductivity the MHD accelerator is less effective.

In order to prevent the negative effects of the unsteady pressure drop through-

out the cycle, MHD forces can be utilized in the combustion chamber to drive the heated fluid out of the combustion chamber at a more constant pressure. This configuration, with applications of energy extracted from the nozzle into the chamber, for a “magnetic chamber piston” configuration, would then possess the advantages of low seeding pressure demonstrated in the aforementioned PDRE [31] as well as the property of constant pressure possessed by a conventional rocket engine [5]. For the basic PDRIME configuration, this combustion chamber has chemical reactions, ionization of seeding ionizable gas, and reflection of detonation waves. But unlike the PDRIME cycle, with a “chamber piston”, after the chamber is sufficiently heated, a MHD accelerator is placed around the combustion chamber to create the piston forces fluid out of the chamber using the Lorentz force. The ‘magnetic piston’ concept is illustrated in Figure 1.5, and the PDRIME with the ‘magnetic piston’ is illustrated in Figure 1.6. The concept of a ‘magnetic piston’ was first introduced by Kolb in 1957[32]. In his experimentation of magnetic shock tubes, Kolb found by applying a magnetic field to a plasma, that the shock waves produced were stronger than that produced in the absence of the magnetic field. The fundamental interaction of a magnetic field with shocks and detonations will be explored in the present studies.

1.3.2 Cambier’s Quasi-1D Model and Verification

Cambier has performed analysis and numerical simulations of various PDRE configurations; i.e., the PDRIME and the PDRE with a ‘magnetic piston’. The assumptions that are part of the analysis are as follows. In his preliminary studies, Cambier selected a simple configuration where the fluid velocity, electric field, and magnetic field form a right hand coordinate system shown in Figure 1.7, indicating generator

(decelerator) and accelerator configurations. The current density from Equation 1.4 can now be expressed as:

$$j_y = \sigma(E_y - u_x B_z) \approx \sigma u_x B_z (K_y - 1) \quad (1.10)$$

where \mathbf{K} is the loading parameter, i.e., the ratio of the applied electric field to the induced field: $K_y = \frac{E_y}{u_x B_z}$. This is an important parameter in Cambier’s simplified modeling of MHD interaction [4]. When $u_x > 0$ and $0 < K_y < 1$, energy is extracted from the fluid, the Lorentz force is negative, as is j_y , and the device acts as a “generator”, shown in Figure 1.7(a). When $K_y > 1$, a positive application of energy takes place, the Lorentz force is positive, as is j_y , and the device acts as an “accelerator”, shown in Figure 1.7(b). It is the generator configuration that allows energy extraction as shown in Figure 1.3, with energy input to accelerate the flow, as shown in Figures 1.4–1.6. In the present studies we use $K_y = 0.5$ for the generator and $K_y = 1.5$ for the accelerator. The ideal case of no ohmic heating, $\mathbf{j}^2/\sigma \approx 0$, is of particular interest, because it forms a very simple analytical expression, but it is not always valid. In order to neglect the ohmic heating as compared to the mechanical work, the following condition must be satisfied:

$$\left| \frac{\mathbf{j}^2/\sigma}{\mathbf{u} \cdot (\mathbf{j} \times \mathbf{B})} \right| = \left| \frac{j_y}{\sigma u_x B_z} \right| = \left| \frac{E_y - u_x B_z}{u_x B_z} \right| = |K_y - 1| \ll 1 \quad (1.11)$$

Cambier also assumes a constant magnetic field as well as a sufficiently low Re_m . In the case of a highly conducting plasma ($\sigma \approx 1000$ mhos/m), which can be seen in the combustion chamber, the constant magnetic field assumption is only valid if the loading factor is small, which also leads to the low dissipation approximation[4].

1.4 Detonation Waves and MHD Effects

The foregoing discussion pertains to the proposed ability of magnetohydrodynamics (MHD) to affect reactive processes via seeding the flow with potentially ionizing species such as cesium. While this notion will be explored in a global sense for the PDRIME and alternative detonation-based engine configurations in Chapter 5, the ability of magnetic and electric fields to influence combustion processes requires a more detailed examination, in particular, including the effect of complex reaction kinetics. Hence a fundamental understanding of transient detonation processes, and the ultimate impact of MHD on these processes, is required and will also be examined in this thesis.

The study of detonation waves dates back to the late 19th century, where Chapman[6] and Jouguet[7] modeled detonations as a shock wave supported by the heat release of the combustible material in an infinitely thin zone, where all chemistry and diffusive transport takes place. Later Zel'dovich[8], Von Neumann[9], and Doering[10] independently represented the detonation as a confluence of a one-dimensional shock wave moving at a detonation velocity, followed by a chemical reaction zone of finite length; this came to be known as the ZND model for a detonation wave.

While the true structure of detonation waves inevitably calls for representation of multi-dimensional effects with complex reaction kinetics, the simple one-dimensional detonation structure provides a rich spectrum of dynamical features which are worthy of detailed exploration and which have relevance to multi-dimensional phenomena, e.g., cellular detonations [11]. Even with single step Arrhenius kinetics [12, 13, 14, 15], pulsations or instabilities associated with a 1D overdriven ZND detonation may be explored in detail, with important physical features and computational requirements

established. For a rapidly initiated, spark-induced detonation, where the detonation decays from an over-driven state toward the self-sustaining Chapman-Jouguet limit cycle, one obtains a sequence of different modes of physical oscillation between the flame and shock front. The numerical analysis of this effect has been explored previously by Cambier[16] using complex H_2 -air detonation kinetics and highly-resolved numerical simulations, but with only a spatially and temporally second-order convergence rate shock capturing scheme. The initiation of evolving 1D detonation instability modes is also observed in calculations by Leung et al.[17] using a two-step chain-branching reaction model [18] and a Roe scheme, with an overdriven ZND detonation as the initial condition. Similar calculations with a second-order accurate slope-limited centered scheme and a 7-step reduced chemical mechanism for acetylene-oxygen detonations [19] have allowed exploration of the stabilizing effect of dilution of the mixture with argon.

In the present study (Chapters 6 and 7), we combine higher-order numerical methods and complex reaction kinetics for the detailed analysis of the non-linear dynamics associated with a spark-induced detonation. While simplified one-step and two-step chemistry models have provided useful guidance in elucidating the dynamics of detonation instability, it is important to understand the influence of the complexity of a realistic reaction mechanism, since energy release and unsteadiness in the coupling of the wave front and induction zone can affect detonation initiation or failure [20]. Moreover, important physical processes associated with deflagration to detonation transition (DDT) require an understanding of the formation and amplification of localized explosion centers and positive-feedback flame acceleration mechanisms [21, 22, 23]. These phenomena are often easier to understand through dimensionality reduction, while preserving some of the complexity of the physics (i.e.

reaction kinetics). The use of high-order numerical methods can also be a powerful tool in the analysis of such complex flows, but we need to understand the interaction of numerical (spatial accuracy) and physical (chemical) length scales. This must be done before adding other effects such as species diffusion and viscosity; hence our study is limited to reactive Euler flow. Since the use of high-order numerical methods can become a powerful tool in studying the non-linear detonation dynamics, it is also important to gain a good understanding of the effect of the non-linear algorithms on the flow dynamics. In a similar fashion to many previous studies of detonation dynamics, the objective of the present work is not to provide realistic detonation simulations, but to systematically investigate these dynamics through the addition of increasing complexity in the models. We expect of course that adding physical diffusion will eliminate some characteristic length scales of instability, an effect which can be investigated in the future.

1.5 Goals of the Present Studies

Among the goals of the present research is first to explore alternative configurations of the PDRIME to achieve optimal performance from the MHD augmentation. The various engine configurations used in our research took on a multitude of forms, these forms are shown in figures 1.2 through 1.6. While the present studies described in Chapter 5 focused on quasi-one dimensional simulations, these results, together with those in Zeineh [33], were published in a complete study[34].

Inherent to the ability of the PDRIME and its modified configurations to operate is the ability of an applied magnetic field to affect a chemical reaction. Hence in the present study we have separately studied the propagation of a detonation wave

with complex kinetics, including its inherent instabilities (Chapter 6), and then to examine the effects of the cesium seeding and an applied magnetic field on the dynamics of the detonation (Chapter 7). Thus both aspects of this dissertation, the simplified modeling and the detailed detonation simulations, may be used to validate the PDRIME and related MHD propulsion concepts.

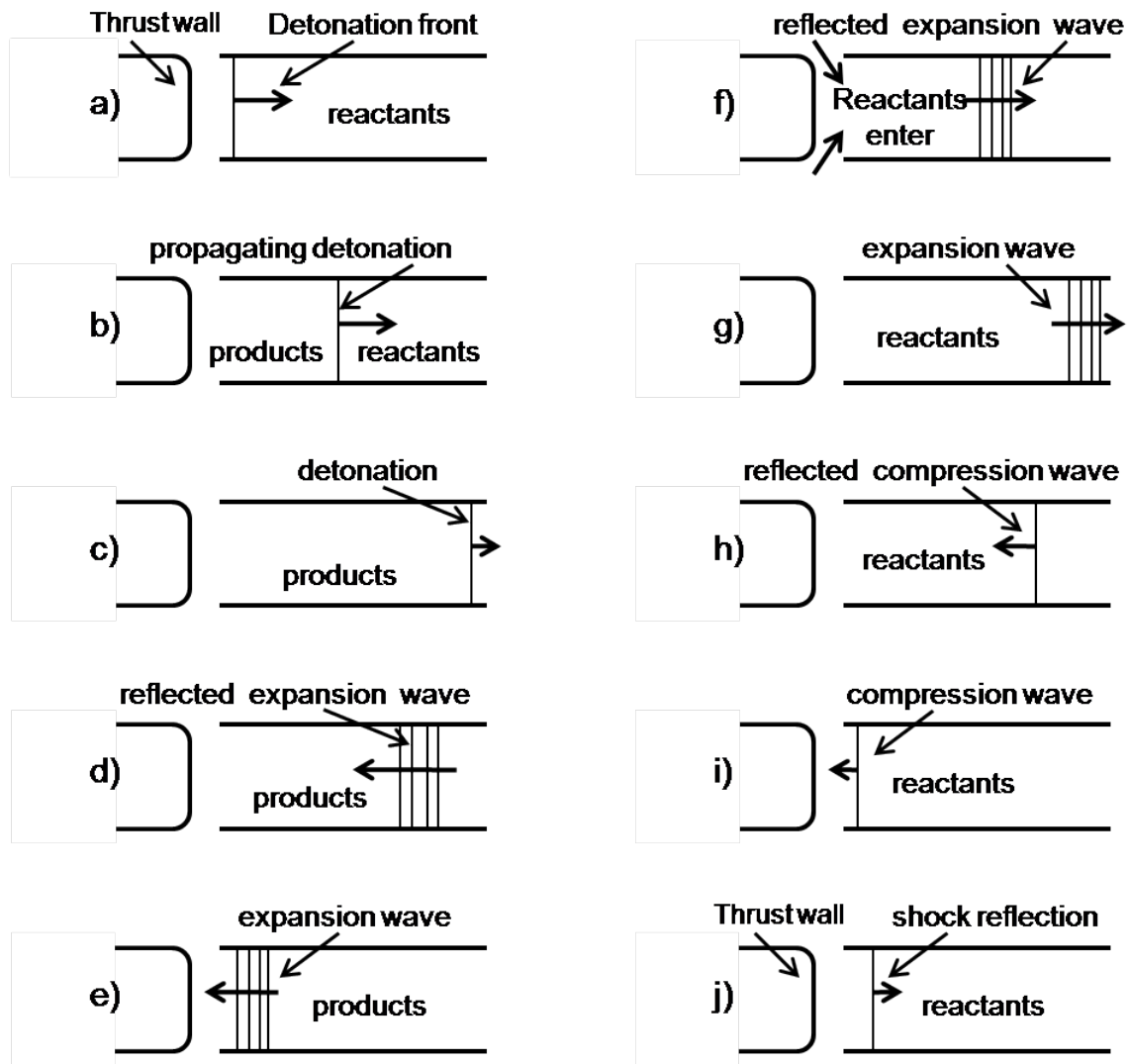


Figure 1.1: The generic pulse detonation cycle. (a)-(c) represent ignition and detonation wave propagation. (d)-(g) represents reflection of an expansion wave from the tube opening to the thrust wall and back to the tube opening. (h)-(j) represents the reflection of compression waves which eventually leads to the re-ignition of the reactants which are drawn into the tube at stage (f).

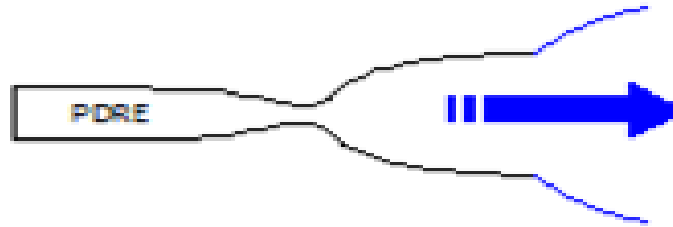


Figure 1.2: PDRE Pulse Detonation Rocket Engine

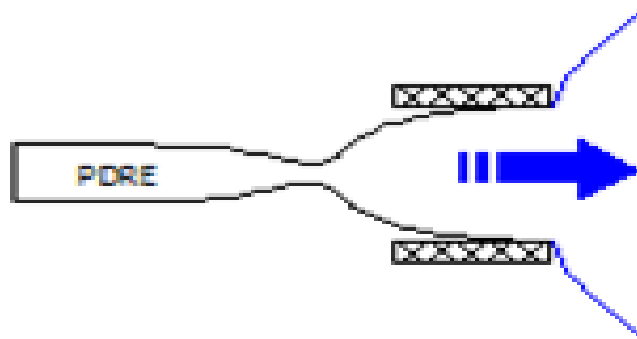


Figure 1.3: Pulse Detonation Rocket Engine with with Nozzle Generator (NG) with MHD nozzle generation flight configuration

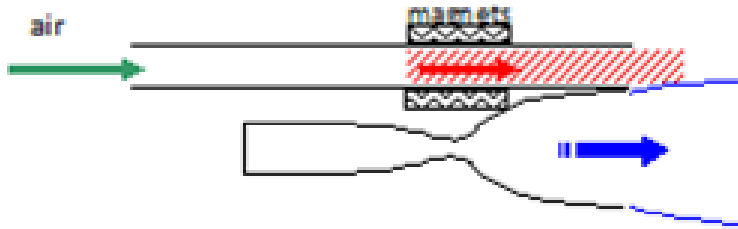


Figure 1.4: Pulse Detonation Rocket Induced MHD Ejector (PDRIME), the MHD accelerator is located in the Bypass Section

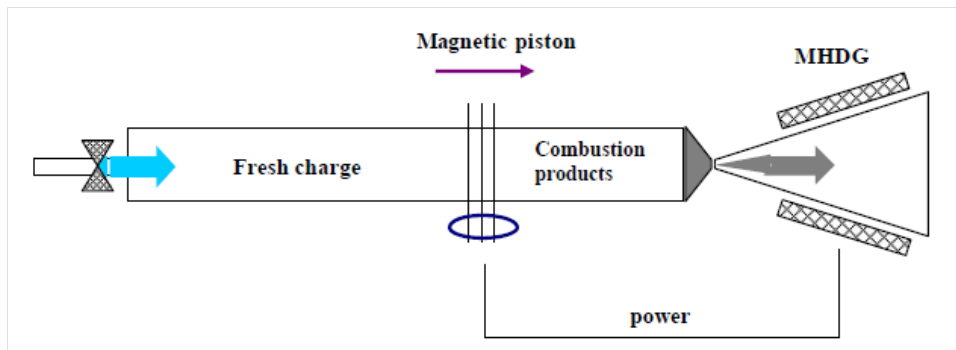


Figure 1.5: Pulse Detonation Rocket Engine with Chamber Magnetic Piston (CP) (from Cambier[5])

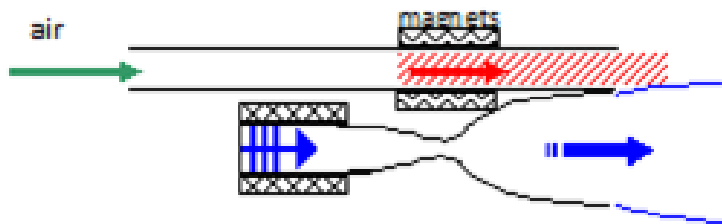


Figure 1.6: Pulse Detonation Rocket Induced MHD Ejector with Chamber Magnetic Piston

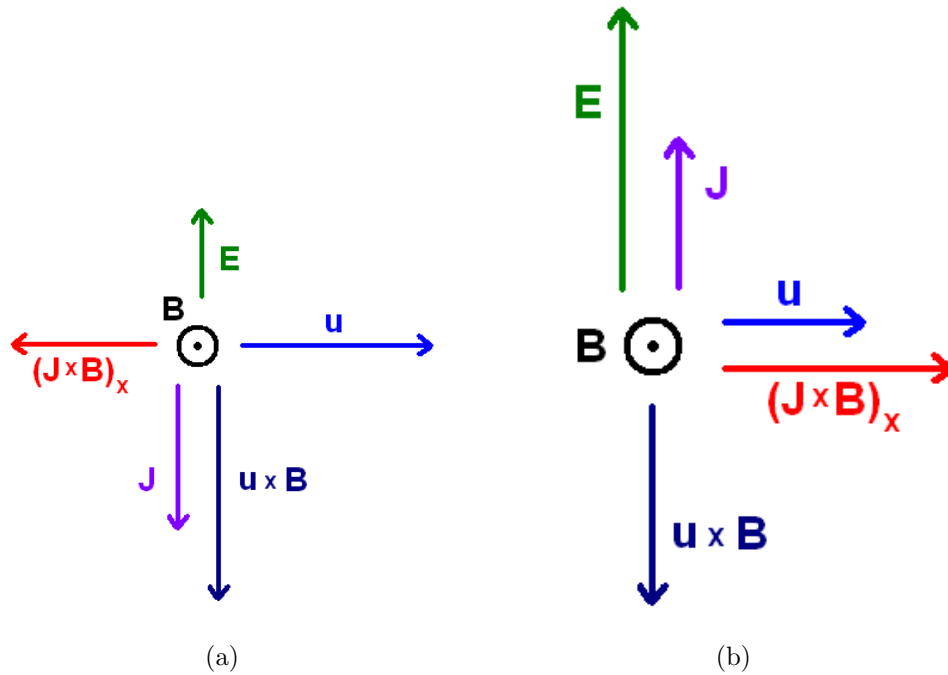


Figure 1.7: Lorentz Force $(\mathbf{J} \times \mathbf{B})_x$ when (a) the MHD generator is on, with fluid moving in the positive x-direction, applied magnetic field in the positive z-direction, and current flowing in the negative y-direction, and (b) the MHD accelerator is on, with fluid moving in the positive x-direction, applied magnetic field in the positive z-direction, and current flowing in the positive y-direction.

CHAPTER 2

Governing Equations and Physical Phenomena

An accurate description of the governing equations is presented here, describing the flow and evolution of properties associated with detonation and MHD processes.

2.1 Conservative Formulation

The governing equations are presented here in the differential form, but later will be expressed in the integral form, which is necessary for the finite-volume formulation used in some simulations of the PDRIME. The flow equations are expressed as a hyperbolic equation with a source term:

$$\frac{\partial \mathbf{Q}}{\partial t} + \nabla_n \cdot \mathbf{F} = \dot{\mathbf{\Omega}} \quad (2.1)$$

where the \mathbf{Q} , \mathbf{F} , and $\dot{\mathbf{\Omega}}$ are arrays of conserved variables, normal component of the flux density of \mathbf{Q} , and source terms, respectively. In the current study all terms on the left hand side (LHS) of Eqn 2.1 are strictly in the hyperbolic form, while the right hand side (RHS) will express all other terms which will be referred to as source terms. Source terms can describe the diffusion, chemical kinetics, or enforcement of geometric coordinate constraint. Operator splitting, which will be discussed in greater detail in Section 3.1, can be employed to compute the convective contribution,

$$\left. \frac{\partial \mathbf{Q}}{\partial t} \right|_{conv} = -\nabla_n \cdot \mathbf{F} \quad (2.2)$$

as well as various source terms,

$$\left. \frac{\partial \mathbf{Q}}{\partial t} \right|_{mhd} = \dot{\mathbf{Q}}_{mhd}, \quad \left. \frac{\partial \mathbf{Q}}{\partial t} \right|_{kinetics} = \dot{\mathbf{Q}}_{kinetics} \quad (2.3)$$

These terms then can be combined to describe the total change of the conserved variables,

$$\frac{\partial \mathbf{Q}}{\partial t} = \left. \frac{\partial \mathbf{Q}}{\partial t} \right|_{conv} + \left. \frac{\partial \mathbf{Q}}{\partial t} \right|_{mhd} + \left. \frac{\partial \mathbf{Q}}{\partial t} \right|_{kinetics} + \dots \quad (2.4)$$

2.1.1 Single-Temperature(1T) Hydrodynamic Formulation

The hydrodynamic formulation of Eqn. 2.1 is well established and can be used to describe the evolution of the density, velocity, and pressure fields of the fluid where the conserved variables and normal fluxes can be described as such:

$$\mathbf{Q} = \begin{pmatrix} \rho_s \\ \rho \mathbf{u} \\ E \end{pmatrix} \quad \mathbf{F} = \begin{pmatrix} \rho_s u_n \\ \rho \mathbf{u} \cdot u_n + P \mathbf{n} \\ (E + P) u_n \end{pmatrix} \quad (2.5)$$

where the total mixture density $\rho \equiv \sum_s \rho_s$, \mathbf{n} is an arbitrary direction, $u_n = \mathbf{u} \cdot \mathbf{n}$, and the total energy and pressure can be expressed as:

$$E = \sum_s \rho_s e_{int,s} + \frac{1}{2} \rho \mathbf{u}^2 \quad (2.6)$$

$$P = (\gamma - 1) \left(E - \frac{1}{2} \rho \mathbf{u}^2 \right) \quad (2.7)$$

where $e_{int,s}$ is the specific internal energy of the s^{th} species and γ is the adiabatic index. For a calorically perfect gas (constant c_v) the specific internal energy can be expressed as:

$$e_{int,s} = \frac{P}{\gamma - 1} \quad (2.8)$$

For thermally perfect gases, which is of particular interest in the present study, the specific internal energy of a species can be expressed as:

$$e_{int,s} = \int c_{v,s}(T)dT + e_{0,s} \quad (2.9)$$

where $c_{v,s}$ is the specific heat capacity at constant pressure for the s^{th} species and the $e_{0,s}$ is the specific internal energy of formation for the s^{th} species.

2.1.2 Single-Temperature(1T) Ideal MHD Formulation ($Re_m \rightarrow \infty$)

By combining Maxwell's equations and the induction equation, Equations 1.6 and 1.4 respectively, as well as adding a zero charge separation approximation, $n_e - n_i \approx 0$, one can describe the time evolution of the magnetic field as:

$$\frac{\partial \mathbf{B}}{\partial t} = - \underbrace{\frac{1}{\mu_0 \sigma} \nabla \times \nabla \times \mathbf{B}}_{\text{diffusive}} - \underbrace{\nabla \times \mathbf{u} \times \mathbf{B}}_{\text{convective}} \quad (2.10)$$

The time varying \mathbf{B} contains a convective term which behaves as a hyperbolic equation and a diffusive term, which behaves as a parabolic equation. Using the criteria set in previous sections, the convective term will be treated as the LHS, of the form of Eqn. 2.1, and the diffusive term as the source term. If the conductivity were to be extremely large such that $\sigma \rightarrow \infty$, then the diffusive term of Equation 2.10 would become zero, leaving only the convective portion of the equation. When this particular case is cast into the divergence form of Eqn. 2.1 as well as incorporating the

magnetic pressure contribution to the momentum and energy equations, i.e. Lorentz force and Joule heating terms, with hydrodynamic formulation of Equation 2.5, it is referred to as the ideal MHD formulation,

$$\mathbf{Q} = \begin{pmatrix} \rho \\ \rho \mathbf{u} \\ \mathbf{B} \\ E^* \end{pmatrix} \quad \mathbf{F} = \begin{pmatrix} \rho u_n \\ \rho \mathbf{u} u_n + P^* \mathbf{n} - \frac{1}{\mu_0} \mathbf{B} B_n \\ u_n \mathbf{B} - \mathbf{u} B_n \\ (E^* + P^*) u_n - \frac{1}{\mu_0} \mathbf{u} \cdot \mathbf{B} B_n \end{pmatrix} \quad (2.11)$$

where $B_n = \mathbf{B} \cdot \mathbf{n}$, and the total energy and pressure can be expressed as:

$$E^* = \sum_s \rho_s e_{int,s} + \frac{1}{2} \rho \mathbf{u}^2 + \frac{\mathbf{B} \cdot \mathbf{B}}{2\mu_0}$$

$$P^* = P + \frac{\mathbf{B} \cdot \mathbf{B}}{2\mu_0}$$

Where E^* is the total energy, P is the mechanical pressure, and the total pressure is defined as $P^* \equiv P + P_m$. Often, $\frac{\mathbf{B} \cdot \mathbf{B}}{2\mu_0}$ is referred to as the magnetic pressure, P_m . Without the presence of a magnetic field, $\mathbf{B} \cdot \mathbf{B} = 0$, the formulation of Equation 2.11 will reduce to the hydrodynamical formulation of Equation 2.5.

2.1.3 Two-Temperature(2T) Formulation

It has been shown by Cambier[35] that under certain conditions the electrons can be heated adiabatically while the bulk fluid can be heated non-isentropically. Conversely, the electrons can be heated non-adiabatically while the bulk fluid is heated adiabatically. One example of the latter is when a microwave is used to excite the electrons in the fluid. In the case of the former, a fluid may pass through a stationary shock at Mach $M = 10$, but while the electron entropy speed is the same as that of the bulk fluid, the speed of sound of the electron is considerably faster, $c_e = \sqrt{\frac{\gamma P_e}{\rho_e}}$,

where the ratio of molar masses of Nitrogen and the electron is $\frac{MW_{N_2}}{MW_e} \sim 10^5$. In the electron reference frame there is therefore no shock, $M_e \ll 1$. When this occurs, the bulk fluid and the electrons have different temperatures, and these temperatures will relax on time scales proportional to the electron-heavy particle elastic collision frequency. The two-temperature MHD formulation (MHD2T), Equation 2.1, builds from the MHD1T formulation but contains additional terms which describe the evolution of the electron energy. The electron thermal energy is transported as:

$$\frac{dE_e}{dt} + \nabla \cdot (\mathbf{u}E_e) = -P_e \nabla \cdot \mathbf{u} \quad (2.12)$$

Because the electron is convected at \mathbf{u} and $|\mathbf{u}|/c_e \ll 0$, the convection of the electron is subsonic and can be treated isentropically. This allows for the recasting of the electron energy into the electron entropy, S_e , which is a conserved quantity and does not require a special source term for convective transport, where the conserved variables and normal fluxes can be described for the two-temperature formulation:

$$\mathbf{Q} = \begin{pmatrix} \rho \\ \rho \mathbf{u} \\ \mathbf{B} \\ E^* \\ S_e \end{pmatrix} \quad \mathbf{F} = \begin{pmatrix} \rho u_n \\ \rho \mathbf{u} u_n + P^* \mathbf{n} - \frac{1}{\mu_0} \mathbf{B} B_n \\ u_n \mathbf{B} - \mathbf{u} B_n \\ (E^* + P^*) u_n - \frac{1}{\mu_0} \mathbf{u} \cdot \mathbf{B} B_n \\ S_e u_n \end{pmatrix} \quad (2.13)$$

where the electron entropy is defined $S_e \equiv \frac{P_e}{\rho^{\gamma_e}}$ and $\gamma_e \equiv \frac{5}{3}$. The electron energy, total energy and total pressure are defined:

$$E_e = \frac{S_e \rho^{\gamma_e - 1}}{\gamma_e - 1} = \frac{n_e k T_e}{\gamma_e - 1} \quad (2.14)$$

$$E^* = \sum_{s \neq e} \rho_s e_{int,s} + \frac{1}{2} \rho \mathbf{u}^2 + \frac{\mathbf{B} \cdot \mathbf{B}}{2\mu_0} + E_e \quad (2.15)$$

Without the presences of a magnetic field, $\mathbf{B} \cdot \mathbf{B} = 0$, and this formulation will reduce to the two-temperature hydrodynamical formulation (EULER2T).

2.2 Overview of Source Terms for Governing Equations

2.2.1 Combustion and Ionization Reaction Kinetics

In the present study, the kinetic processes which include the chemical reactions of combustion processes, the ionization of the fluid, and the temperature relaxation of the electron must be properly captured. In the case of chemical reactions and ionization, chemical species are not strictly conserved, but particles (chemical elements) and mass are, while in the case of temperature relaxation, energy can be transferred from the heavy particles to the electrons and vice-versa. This source term can be represented in the following way,

$$\mathbf{Q} = \begin{pmatrix} \rho_s \\ \rho \mathbf{u} \\ E \\ S_e \end{pmatrix} \quad \dot{\Omega}_{kinetics} = \begin{pmatrix} \dot{\omega}_s \\ 0 \\ \dot{\omega}_E \\ \dot{S}_e \end{pmatrix} \quad (2.16)$$

where $\dot{\omega}_s$ is the production of the s^{th} species, $\dot{\omega}_E$ is the energy production due to change in formation energy, and \dot{S}_e is the electron entropy production. A more detailed description of these terms will be discussed in the following sections as well as Section 2.3.

2.2.2 MHD Transport

2.2.2.1 Fixed Magnetic Field ($R_m \rightarrow 0$)

In the MHD source formulation that is used to study the PDRIME configurations, and some of the MHD-detonation interactions, there is no conservation law for the magnetic field, but rather the Lorentz force and Joule heating are incorporated into a hydrodynamic formulation of the governing equations. By incorporating the Lorentz force exerted by an applied magnetic field, Eqn. 1.3, as well as the mechanical power obtained from the Lorentz force and the associated Joule heating, Eqn. 1.5, one can recover the following MHD source terms for a fixed magnetic field:

$$\mathbf{Q} = \begin{pmatrix} \rho_s \\ \rho \mathbf{u} \\ E \end{pmatrix} \quad \dot{\mathbf{Q}}_{mhd, fixed} = \begin{pmatrix} 0 \\ \mathbf{j} \times \mathbf{B} \\ \mathbf{j} \cdot \mathbf{E} \end{pmatrix} \quad (2.17)$$

In the present study, when this approximation of MHD is used, Cambier's [4] simplified MHD model will be implemented, which was previously discussed in Section 1.3.2. In that model, the system includes the electric and magnetic fields as orientated in Figure 1.7. In addition, one can simplify the expression for current density with Equation 1.10, such that the x-component of the Lorentz force becomes:

$$(\mathbf{j} \times \mathbf{B})_x \approx \sigma u_x B_z^2 (K_y - 1) \quad (2.18)$$

and the Joule heating term becomes:

$$\mathbf{j} \cdot \mathbf{E} \approx \sigma u_x^2 B_z^2 (K_y - 1) K_y \quad (2.19)$$

This formulation will be employed in the simplified PDRIME simulations and in some of the detonation-MHD studies.

2.2.2.2 Resistive MHD ($Re_m \sim O(1)$)

Seldom do real problems act ideally, as described in the perfectly conducting ideal MHD approximation of Eqn. 2.11 or the perfectly resistive fixed field line approximation of Equation 2.17. Typically, there is a finite conductivity such that the diffusive and convective terms of Eqn. 2.10 are of the same order of magnitude, thus neither can be neglected. The diffusion of magnetic field and magnetic energy can be expressed as the following source term:

$$\dot{\Omega}_{mhd, diffuse} = \begin{pmatrix} 0 \\ 0 \\ \nabla \cdot \left(\frac{1}{\mu_0 \sigma} \nabla \mathbf{B} \right) \\ \mathbf{j} \cdot \mathbf{E} \end{pmatrix} \quad (2.20)$$

where the evolution of the magnetic energy is prescribed by

$$\mathbf{j} \cdot \mathbf{E} = \nabla \cdot \left(\frac{1}{\mu_0 \sigma} \nabla \mathbb{T} \right) \quad (2.21)$$

where the Maxwell stress tensor is defined as $\mathbb{T}^{\alpha\beta} = \frac{|B|^2}{2\mu_0} \delta^{\alpha\beta} - \frac{B^\alpha B^\beta}{\mu_0}$. A more detailed discussion of magnetic field diffusion will be presented in Section 2.4.

2.3 Kinetics

In order to properly resolve the chemical reaction and ionization processes, one must first characterize the plasma and chemical kinetics. Using detailed balancing one can express the rate of species production and destruction in the following manner.

$$\dot{\omega}_s = \sum_r \nu_{rs} k_{fr} \prod_j \rho_j^{\nu'_{rj}} - \sum_r \nu_{rs} k_{br} \prod_j \rho_j^{\nu''_{rj}} \quad (2.22)$$

$$\nu_{rs} = \nu''_{rs} - \nu'_{rs}$$

where ν''_{rk} and ν'_{rk} are the coefficients of s^{th} species in the r^{th} forward and backward reactions, respectively, and k_{fr} and k_{br} and the forward and backward chemical rates of the r^{th} reaction. When the temperature of the fluid is near thermal equilibrium, detailed balancing can be used to determine backward rates:

$$k_b = k_f \exp\left(\sum_s \nu_s \Delta G_s / T\right) \quad (2.23)$$

where ΔG_s is the change in Gibbs free energy of the s^{th} species. In cases where the temperature is far from equilibrium, for example when there is a heavy and electron temperature, detailed balance would not be appropriate to determine the backward rates. The forward reaction rates are given by the modified Arrhenius equation of the form:

$$k = AT^\eta \exp(-\Theta/T) \quad (2.24)$$

Where A is the Arrhenius pre-factor, η is the Arrhenius coefficient, and Θ is the activation temperature. Using the form of Equation 2.16 with Equation 2.22, the energy production due to the internal energy change can be expressed as $\dot{\omega}_E = \sum_s \omega_s e_{0,s}$.

2.3.1 Combustion Kinetics

2.3.1.1 Single Step Kinetics

During preliminary testing, we simulated a single-step $H_2 - O_2$ reaction, reactants H_2 and O_2 form product H_2O



The H_2O production rate takes the Arrhenius form of Equation 2.24 in which $\dot{\omega}_p = K\rho_f e^{-\theta/T}$. In this particular case, ρ_f is the density of a stoichiometric mixture of the fuel, H_2 , and oxidizer, O_2 , and ρ_p is the density of the product, H_2O . The thermodynamic properties of the reactants and product are given in Table 2.1. The differences in the thermodynamic properties between reactants and products found in this table are due to the differences in the molar mass, M , and the degrees of freedom associated with the molecular configuration of each species.

2.3.1.2 Detailed Reaction Kinetics

In the present study, we have primarily focused on detailed kinetics of a simple combustion system ($H_2 - O_2$). Another approach to the single step reaction in Equation 2.25, commonly chosen in fundamental studies of detonation dynamics, is a constant-volume one-step reaction model, in which the entire chemistry is described by the evolution of a single progress variable that follows an exponential relaxation with a characteristic time-scale given by the induction delay. This progress variable is also associated with the fractional amount of heat released into the flow. In that model, the induction delay time, τ_{ind} , follows a simple exponential fit, $t_{ind} \simeq e^{\theta_a/T}$. The delay being essentially caused by the need for a sufficient amount of radicals from chain-branching reactions, and the production of those being an endothermic process, the parameter θ_a in this formulation is an averaged activation energy of the key radical-producing reactions.

This is a reasonable approximation to the chemistry in that region, albeit within limits. To study detonation dynamics more completely, we have used the detailed chemistry to compute and parametrize the induction delay as a function of initial

temperature and pressure, with the mixture held fixed to stoichiometric hydrogen-air. As in a previous study [16], the chemical kinetics of a dilute hydrogen-air mixture were solved here. The chemistry includes eight reacting species, H_2 , O_2 , H , O , OH , HO_2 , H_2O_2 , H_2O , and the non-reacting diluent, N_2 , where a compilation of NASA and JANNAF thermo-chemical data is obtained from [36]. As prescribed by [37], 38 elementary reactions, found in Appendix A, are used in this mechanism and the backward rates are computed from equilibrium constants. As shown in Figure 2.1, the delay does follow an exponential form, $t_i \propto \alpha(P)e^{\beta(P)/T}$, as expected. The parameter β in this formulation is an averaged activation energy of the key radical-producing reactions. However, this approach yields unrealistic profiles of the post-shock region, since the heat release is gradual.

A better description is obtained with a two-step reaction model [38, 39], where the heat release is associated with a second progress variable whose evolution can start only at the end of the induction delay, which now follows a linear time variation. While this two-step model allows a separation between the induction and heat release zones, the model is unsatisfactory in several ways. First, the rate of heat release is assumed independent of temperature, which is unrealistic, as the flow heating accelerates the combustion. Generally speaking, a stiff differential equation for the progress variable can be used to reproduce this non-linear effect, but the dynamics can be different from the real conditions. Second, when the flame is accelerated towards the shock, the two reaction zones (induction and flame) start to merge, even if species diffusion is neglected; the enforcing of two separate zones with a two-step model could thus modify the dynamics of the strongly coupled shock-flame system. It is for these reasons we will utilize detailed reaction kinetics to perform the simulations in the present study, per Equations 2.22 – 2.24 and the full $H_2 - O_2$

combustion mechanism described in Appendix A.

2.3.2 Ionization Kinetics

The existence of plasma in a working fluid is studied via the field of magnetohydrodynamics. If a working fluid's characteristic temperature of first ionization, Θ_i , is high relative to the fluid temperature, it is imperative to seed the fluid with a species with a sufficiently low characteristic temperature to create the flow of ionized gas. The principle components of the working fluids in this study, air, H_2 , O_2 , and H_2O , have high characteristic temperatures relative to the fluid temperature in the scope of the present study. A sampling of ionization temperatures are shown in Table 2.2. As prescribed by Cambier in [40], cesium is chosen as the seeded species due to its low characteristic temperature of ionization. In the modeling of the ionization and recombination of cesium in the working fluid, we start with a simple three-body reaction mechanism:



where M in this particular case represents a third-body species. In the present study, it is extremely important to be able to calculate the conductivity of the plasma in order to correctly simulate MHD. The scalar conductivity, σ , is defined as:

$$\sigma = \frac{n_e e^2}{m_e \nu_m} \quad (2.27)$$

where n_e is the electron number density, m_e is the electron mass, and e is the Coulombic charge where the electron collisional frequency, ν_m is defined as:

$$\nu_m = \underbrace{n_e Q_{ei} \bar{v}_e}_{\nu_{ei}} + \underbrace{N \sum_{s \neq e} \int_0^\infty d\epsilon Q_{es}(\epsilon) v \cdot f(\epsilon)}_{\nu_{en}} \quad (2.28)$$

where \mathcal{Q}_{ei} and ν_{ei} is the electron-ion elastic collisional cross-section and collisional frequency, \mathcal{Q}_{es} and ν_{es} is the electron-neutral elastic collisional cross-section and collisional frequency of the s^{th} species, v_e is the electron thermal velocity, and f is the electron distribution function. Electron-neutral cross-section data are found in [41] while the electron-ion cross-section, commonly referred to as the Coulombic cross-section is given by [42]:

$$\mathcal{Q}_{ei} = \frac{2.87 \times 10^{-14}}{T_{[eV]}^2} \ln \Lambda \quad (2.29)$$

where the Coulombic logarithm is $\ln \Lambda = 13.57 + 1.5 \log T_{[eV]} - 0.5 \log n_e$. In the regime where the fluid is strongly ionized, $\alpha \gtrsim 10^{-4}$, the electron-ion collision term of Equation 2.28 dominates, and the conductivity scales as follows:

$$\sigma \sim T_e^{5/2} \quad (2.30)$$

2.3.3 Two-Temperature(2T) Relaxation

When a plasma is rapidly heated by a shock, radiation, or other process, the heavy particle and the electron temperatures can be altered from equilibrium and must undergo a series of elastic collisions to return them to equilibrium, or thermalize. If the collisional time scale is significantly faster than the fluid time scale, the heavy particles and electrons can be assumed to be in equilibrium. But, when the collisional time scales are much slower than that of the fluid, the temperatures can be treated completely separately. In the event the time scale associated with thermalization is on the order of the fluid time scale, the finite rate of elastic energy relaxation must be taken into account. The relaxation of the electron energy is as follows [42]:

$$\frac{dE_e}{dt} = \nu_m \left(\frac{2m_e}{M} \right) \frac{3}{2} n_e k_b (T_h - T_e) \quad (2.31)$$

where T_h is the translational temperature of the heavy particles. Equation 2.31 can be recast in terms of electron entropy as follows:

$$\dot{S}_e = \frac{dS_e}{dt} = \nu_m \left(\frac{2m_e}{M} \right) \frac{3}{2} n_e k_b (T_h - T_e) (\gamma_e - 1) \rho^{1-\gamma_e} \quad (2.32)$$

2.4 MHD Transport

In order to properly characterize a non-ideal system in the presence of an imposed magnetic field, one must account for both the convective and diffusive transport of the magnetic field. Let us re-examine the formulation of the temporal evolution of the magnetic field expressed in Equation 2.10:

$$\frac{\partial \mathbf{B}}{\partial t} = - \underbrace{\frac{1}{\mu_0 \sigma} \nabla \times \nabla \times \mathbf{B}}_{\text{diffusive}} - \underbrace{\nabla \times \mathbf{u} \times \mathbf{B}}_{\text{convective}}$$

Starting from 2.1 and the description of the source term from Eqn. 2.20, one can define a system which describes the evolution of the magnetic field and magnetic pressure due to diffusive transport in the divergence form as follows:

$$\begin{aligned} \frac{\partial \mathbf{B}}{\partial t} &= \nabla \cdot \frac{1}{\mu_0 \sigma} \nabla \mathbf{B} \\ \frac{\partial P_B}{\partial t} &= \nabla \cdot \frac{1}{\mu_0 \sigma} \nabla \mathbb{T} \end{aligned} \quad (2.33)$$

where P_B is the magnetic pressure which was previously defined as $P_B = \frac{\mathbf{B}^2}{2\mu_0}$. Now let us rewrite Eqn. 2.33 in a flux formulation of the form,

$$\mathbf{Q}_t = \nabla \cdot \mathbf{F}^\nu \quad (2.34)$$

where \mathbf{F}^ν represents the magnetic diffusive flux,

$$\mathbf{Q} = \begin{pmatrix} B_x \\ B_y \\ B_z \\ P_B \end{pmatrix} \quad \mathbf{F}^\nu = \frac{1}{\mu_0 \sigma} \begin{pmatrix} \nabla B_x \\ \nabla B_y \\ \nabla B_z \\ \nabla \mathbb{T} \end{pmatrix} \quad (2.35)$$

This description of MHD diffusive transport is particularly useful when the conductivity of a fluid is finite, as in the problems represented in this thesis. The limits of ideal MHD and perfectly resistive MHD, where $\sigma \rightarrow \infty$ and $\sigma \approx 0$, respectively will also be investigated.

Species	R [$\frac{J}{kg-K}$]	c_v [$\frac{J}{kg-K}$]	e_0 [$\frac{J}{kg}$]
$H_2 - O_2$	692.8	2.425×10^3	0
H_2O	461.9	2.079×10^3	1.344×10^7

Table 2.1: List of thermodynamic properties of a stoichiometric mixture of $H_2 - O_2$, reactant, and H_2O , product, for a simple, single-step reaction.

Species	Θ_i , [K]
Cs	45,141
K	50,364
Na	59,647
Li	62,548
O_2	139,834
H_2O	146,217
O	157,937
CO_2	167,105
H_2	181,030
N_2	181,030
Ar	182,887
He	285,239

Table 2.2: Listing of characteristic temperatures of first ionization of selected species[43].

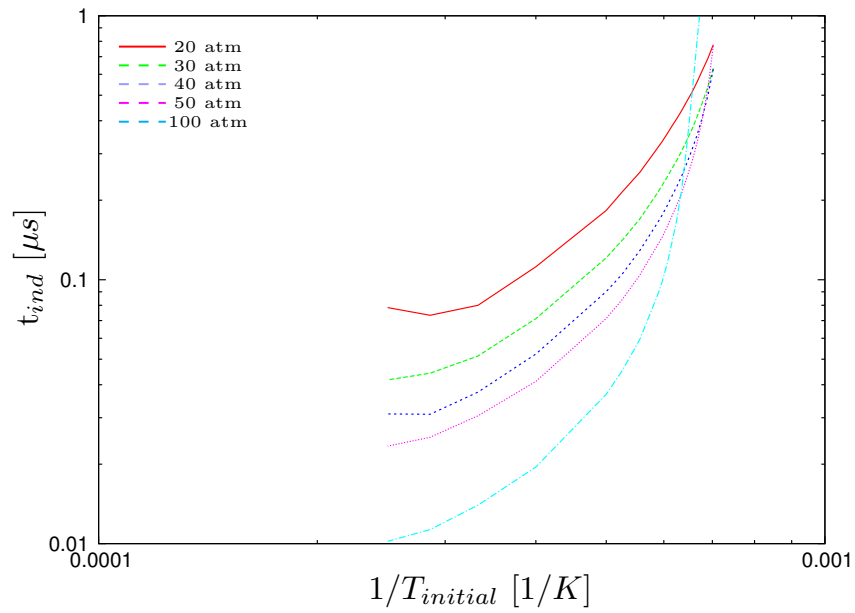


Figure 2.1: Computed induction delay as a function of initial temperature at various pressures P for the stoichiometric H_2 -air reaction with complex kinetics. Curves can be fitted as $t \sim \alpha(P)e^{\frac{\beta(P)}{T}}$.

CHAPTER 3

Numerical Methods

The following chapter will list and describe the numerical methods utilized to solve the governing equations described in the previous section.

3.1 Operator Splitting

As shown in Equation 2.4, it is often necessary to solve the LHS with one solver while solving the various RHS source terms with other solvers. For example, one might wish to solve a problem which involves convection, LHS, as well as chemical kinetics, RHS, and utilize different solvers, or *operators*, \mathcal{L}^{conv} and \mathcal{L}^{chem} , respectively. By utilizing these operators, the solution of \mathbf{Q} at $t = t^{n+1}$, where $t^{n+1} = t_0 + \Delta t$, can be determined as follows:

$$\begin{aligned}\Delta\mathbf{Q}^{chem} &= \mathcal{L}^{chem}\mathbf{Q}^n - \mathbf{Q}^n \\ \Delta\mathbf{Q}^{conv} &= \mathcal{L}^{conv}\mathbf{Q}^n - \mathbf{Q}^n \\ \mathbf{Q}^{n+1} &= \mathbf{Q}^n + \Delta\mathbf{Q}^{chem} + \Delta\mathbf{Q}^{conv}\end{aligned}\tag{3.1}$$

Figure 3.1 illustrates the contribution of the two operators in attaining the solution at $t = t^{n+1}$.

When stronger coupling is needed amongst multiple operators, either for stability or accuracy, Strang splitting[44] can be employed. Strang splitting the convective

and chemical kinetic operator of the previous example would go as follows:

$$\begin{aligned}\tilde{\mathbf{Q}} &= \mathcal{L}^{chem} \mathbf{Q}^n \\ \mathbf{Q}^{n+1} &= \mathcal{L}^{conv} \tilde{\mathbf{Q}}\end{aligned}$$

which can be simply expressed in the compact notation:

$$\mathbf{Q}^{n+1} = \mathcal{L}^{conv} \mathcal{L}^{chem} \mathbf{Q}^n \quad (3.2)$$

Figure 3.2(a) illustrates how the chemical kinetic solver operates on the solution at $t = t^n$, and the convective solver operates on the updated solution in order to obtain the solution at $t = t^{n+1}$. Since Strang splitting is not a commutative operation, the ordering of the operators can indeed yield unique solutions,

$$\mathcal{L}^{chem} \mathcal{L}^{conv} \mathbf{Q}^n \neq \mathcal{L}^{conv} \mathcal{L}^{chem} \mathbf{Q}^n \quad (3.3)$$

Figures 3.2(a) and 3.2(b) illustrate how commuting the operators could yield a different solution.

3.2 Time Step Restrictions

3.2.1 Convection

For linear or linearized hyperbolic equations, the Courant-Friedrich-Levy(CFL) condition ensures that information does not propagate further than one grid cell in a given time step:

$$\Delta t_{conv} \leq \frac{\nu \Delta x}{\lambda} \quad (3.4)$$

where Δt_{conv} represents the convection-limited time step, ν is the Courant number, for linear stability $0 < \nu \leq 1$, Δx is the grid cell size, λ is the wave speed of the

convected information. For a purely convective simulation, where there is no kinetic or diffusive processes, the CFL would be sufficient for stability of the time integration.

3.2.2 Kinetics Resolution

Solving kinetics presents a different challenge in that the reaction time scale must be taken into consideration in order to determine the proper time step restriction. For the simple case of an explicit single step reaction with the form, $\dot{\omega}_p = \rho_f K e^{-\theta/T}$, the time step restriction would be determined as,

$$\Delta t_{chem} \leq |K^{-1} e^{\theta/T}| \quad (3.5)$$

In the case of an explicit complex reaction of the form of Equation 3.41,

$$\Delta t_{chem} \leq \min \left(\frac{\rho_k}{\dot{\omega}_k}, \frac{E_{int}}{\dot{\omega}_E} \right) \quad (3.6)$$

Since the kinetic source term of Equation 2.3 is often extremely stiff and $\Delta t_{chem} \sim 0$ when $\rho_k \sim 0$, an implicit approach will be taken. When a strictly implicit numerical scheme is employed, the time step restrictions for stability of Equation 3.6 are no longer required. But even though restrictions for stability are no longer required, there still exist accuracy considerations. The following *accuracy* time step restriction was introduced in the present study:

$$\Delta t_{chem} = \min \left(\epsilon_c \frac{\rho_k^*}{|\dot{\omega}_k|}, \epsilon_T \frac{E_{int}}{|\dot{\omega}_E|} \right) \quad (3.7)$$

Where ρ_k^* is the greater value of ρ_k and a floor density, ϵ_c is the maximum species creation/destruction fraction, and ϵ_T is the maximum temperature cooling/heating fraction.

3.2.3 Diffusion

When solving diffusive transport problems, which are expressed as parabolic partial differential equations of the form, $u_t = -\mu u_{xx}$, the explicit time step restriction is quite similar to that of the convective transport. The explicit time step restriction is given by,

$$\Delta t_{diff} \leq \frac{0.5\Delta x^2}{\mu} \quad (3.8)$$

where μ represents the “kinematic viscosity”. This time step can become quite constraining with the increase in the diffusivity, μ , or with moderate grid spacing reduction ($\Delta t \sim \Delta x^2$). For these reasons, spatially implicit numerical schemes will be utilized to solve problems of this type.

3.3 Explicit Runge Kutta Scheme

In order to obtain stable high order convergent solutions in time, a TVD Runge-Kutta (RK) time integrator is used. This particular version of the Runge Kutta family was implemented by Shu and Osher in [45]. For 3rd order Runge-Kutta (RK3), $\forall j$

$$\begin{aligned} \mathbf{Q}_j^{(0)} &= \mathbf{Q}_j^n \\ \mathbf{Q}_j^{(1)} &= \mathbf{Q}_j^{(0)} + L_j(\mathbf{Q}_j^{(0)}) \\ \mathbf{Q}_j^{(2)} &= \frac{3}{4}\mathbf{Q}_j^{(0)} + \frac{1}{4}\mathbf{Q}_j^{(1)} + \frac{1}{4}L_j(\mathbf{Q}_j^{(1)}) \\ \mathbf{Q}_j^{n+1} &= \frac{1}{3}\mathbf{Q}_j^{(0)} + \frac{2}{3}\mathbf{Q}_j^{(2)} + \frac{2}{3}L_j(\mathbf{Q}_j^{(2)}) \end{aligned} \quad (3.9)$$

where L_j represents the flux into the j^{th} grid cell and $\mathbf{Q}^{(k)}$ represents the conserved variables of the k^{th} step of the Runge-Kutta integration. Equation 3.9 will serve as the fluid convection operator, \mathcal{L}^{conv} , for the remainder of this study, unless otherwise stated, while the temporally and spatially integrated flux, L_j , will be determined by

Riemann solvers which will be discussed in the next sections.

3.4 Hyperbolic Solvers – Approximate Riemann Solvers

In the present study, it is imperative that the fluid convection solver be able to capture shocks without introducing dispersion or excess dissipation into the solution. Let us now recast the LHS of our governing equation, Equation 2.1, into its integral or conservative form:

$$\frac{\partial}{\partial t} \int \mathbf{Q} dV + \int \mathbf{F} dS = 0 \quad (3.10)$$

We will next assume a given grid cell is uniform in its properties, and can be approximated with its cell-averaged value. Then Equation 3.10 can take the following form:

$$\frac{\partial \mathbf{Q}}{\partial t} + \frac{1}{V} \sum_s \mathbf{F}_s dA_s = 0 \quad (3.11)$$

where \mathbf{F}_s and dA_s are the areas and normal fluxes of the s^{th} face of a given grid cell. As a building block, we will utilize Roe’s scheme[46] to solve for the flux at the face, $\mathbf{F}_{i+1/2}$ as follows:

$$\mathbf{F}_{i+1/2} = \frac{1}{2} (\mathbf{F}_R + \mathbf{F}_L) - \frac{1}{2} \mathbf{R} \tilde{\Lambda} \mathbf{L} (\mathbf{Q}_R - \mathbf{Q}_L) \quad (3.12)$$

where $\mathbf{F}_{R,L}$ and $\mathbf{Q}_{R,L}$ represent the normal fluxes and conserved variables of the right and left side of the face, respectively, \mathbf{L} is the matrix of eigenvector, \mathbf{R} is the inverse of the matrix of eigenvector, and $\tilde{\Lambda}$ are the HLLE[47] conditioned eigenvalues. The eigen-system is discussed in more detail in Appendix B. For the 1st order spatial accuracy convergent Roe scheme, the right fluxes and conserved variables are, \mathbf{F}_{i+1} and \mathbf{Q}_{i+1} , respectively and the left fluxes and conserved variables are, \mathbf{F}_i and \mathbf{Q}_i ,

respectively. In the proceeding sections, the numerical schemes used to calculate high order spatially convergent conserved variable solutions will be discussed.

In order to achieve a spatially high order convergent interpolation of the conserved variables at the cell interface, $\mathbf{Q}_{R,L}$, the governing system of equations, Equation 2.1, must be linearized in the following manner:

$$\begin{aligned}
\mathbf{Q}_t + \mathbf{F}_n &= 0 \\
\mathbf{Q}_t + \mathbf{A}\mathbf{Q}_n &= 0 \\
\mathbf{L}\mathbf{Q}_t + \mathbf{L}\mathbf{R}\mathbf{\Lambda}\mathbf{L}\mathbf{Q}_n &= 0 \\
\mathbf{W}_t + \mathbf{\Lambda}\mathbf{W}_n &= 0
\end{aligned} \tag{3.13}$$

where $()_n$ represents the spatial derivative in an arbitrary direction, the convective flux jacobian is $\mathbf{A} = \frac{\partial \mathbf{F}}{\partial \mathbf{Q}}$ and the characteristic variable array, $\mathbf{W} = (w_1, w_2, \dots)^T$ is defined as the projection of the conserved variables, $\mathbf{W} = \mathbf{L}\mathbf{Q}$, and by definition $\mathbf{L}\mathbf{R} = \mathbf{R}\mathbf{L} = \mathbf{I}$. Now that the governing equations have been linearized with the process shown in Equation 3.13, it can now be expressed as a system of scalar hyperbolic differential equations:

$$w_t + \lambda w_n = 0 \tag{3.14}$$

where the eigenvalues are the diagonal components of the matrix of eigenvalues, $\lambda_i = \Lambda_{i,i}$. After using one of the high order spatially convergent methods, which will be discussed in greater detail in the preceding sections, to approximate the characteristic variable solution at the cell interface, $\mathbf{W}_{R,L}$, the characteristic variables can be projected back to its component form using the following operation:

$$\mathbf{Q}_{R,L} = \mathbf{R}\mathbf{W}_{R,L} \tag{3.15}$$

The updated conserved variables determined from Equation 3.15 are then used to calculate the interface flux, $\mathbf{F}_{R,L}$, as well as construct a new eigensystem.

3.4.1 Weighted Essentially Non-Oscillatory (WENO) Schemes

In Weighted Essentially Non-Oscillatory (WENO) schemes, first introduced by Liu, Osher, & Chan [48], high spatial order of convergence is achieved where the solution is smooth and a spatial convergence of no greater than $O(1)$ near a discontinuity in the solution. In the present study, we utilized a 5th order spatially convergence variant of WENO which weights the contribution of three stencils, illustrated in Figure 3.3. Here we will describe how $w_{L,i+1/2}$ is computed in [48] on the basis of the ENO stencil[49]. For simplicity, the “L” subscript will be dropped. The formula for the right characteristics are symmetric and will only be shown when they vary from the left characteristics.

The r^{th} order ENO scheme chooses the “smoothest” stencil from r candidate stencils to approximate $w_{i+1/2}$. In the case of $r = 3$, the stencil S_k , where $k \in [0, 2]$, shown in Figure 3.3, happens to be chosen as the ENO interpolation stencil, the r^{th} -order ENO approximation of $w_{i+1/2}$ to produce

$$w_k = q_k^r (w_{i+k-r+1}, \dots, w_{i+k}) \quad (3.16)$$

where

$$q_k^r (g_0, \dots, g_{r-1}) = \sum_{l=0}^{r-1} a_{k,l}^r g_l \quad (3.17)$$

Here $a_{k,l}^r$, $0 \leq k, l \leq r - 1$, are constant coefficients, which are provided in Table 3.1. Using the smoothest of the r^{th} stencil would be desirable near a discontinuity, but in smooth regions, information from all stencils can be used in the final solution. Thus, in smooth regions, it would be desirable to combine the ENO stencils in a manner that will generate a higher than r order solution. As shown in [48], one can use all of the r candidate stencils, which all together would contain $(2r - 1)$ grid values of

$w_{i+1/2}$ to give a $(2r - 1)$ th-order approximation of w

$$w_k = q_{r-1}^{2r-1} (w_{i-r+1}, \dots, w_{i+r-1}) \quad (3.18)$$

which is the solution of a $(2r - 1)$ th-order *upstream central scheme*. Since high order upstream central schemes (in space), combined with high order Runge-Kutta methods (in time) are stable and dissipative under appropriate CFL numbers, they are convergent. Using this fact, one can now use the $(2r - 1)$ th-order upstream central scheme in smooth regions and the r^{th} order ENO scheme near discontinuities. As shown in Equation 3.16, each of the stencils can approximate $w_{i+1/2}$. If the stencil is smooth, an r^{th} order approximation of the stencil can be recovered, but if the stencil is discontinuous, a less accurate or inaccurate approximation would be recovered. So WENO assigns a weight, $\hat{\omega}_k$, to each of the candidate stencil S_k , where $k \in [0, r - 1]$, and uses these weights to combine the r different approximations to obtain the final approximation of the solution as:

$$w_{i+1/2} = \sum_{k=0}^{r-1} \hat{\omega}_k q_k^r (w_{i+k-r+1}, \dots, w_{i+k}) \quad (3.19)$$

where q_k^r is defined in Equation 3.17. To achieve essentially non-oscillatory properties, WENO requires that the weights adapt to the relative smoothness of w . Discontinuous stencils contributions should be assigned weights of zero. In the smooth regions the weights should be adjusted so the upstream central scheme, Equation 3.18, is recovered.

In the present study, the 5^{th} order WENO(WENO5) scheme ($r = 3$) is utilized

as prescribed by Jiang and Shu in [45]. The stencils, S_k , are calculated as:

$$\begin{aligned}
S_0(w_{i-2}, w_{i-1}, w_i) &= \frac{1}{6} (2w_{i-2} - 7w_{i-1} + 11w_i) \\
S_1(w_{i-1}, w_i, w_{i+1}) &= \frac{1}{6} (-1w_{i-1} + 5w_i + 2w_{i+1}) \\
S_2(w_i, w_{i+1}, w_{i+2}) &= \frac{1}{6} (2w_i + 5w_{i+1} - 1w_{i+2})
\end{aligned} \tag{3.20}$$

And the right solution is stencils, S_k^R are calculated as:

$$\begin{aligned}
S_0^R(w_{i+3}, w_{i+2}, w_{i+1}) &= \frac{1}{6} (2w_{i+3} - 7w_{i+2} + 11w_{i+1}) \\
S_1^R(w_{i+2}, w_{i+1}, w_i) &= \frac{1}{6} (-1w_{i+2} + 5w_{i+1} + 2w_i) \\
S_2^R(w_{i+1}, w_i, w_{i-1}) &= \frac{1}{6} (2w_{i+1} + 5w_i - 1w_{i-1})
\end{aligned} \tag{3.21}$$

The smoothness of each stencil is then calculated as:

$$\begin{aligned}
IS_0 &= \frac{13}{12} (w_{i-2} - 2w_{i-1} + w_i)^2 + \frac{1}{4} (w_{i-2} - 4w_{i-1} + 3w_i)^2 \\
IS_1 &= \frac{13}{12} (w_{i-1} - 2w_i + w_{i+1})^2 + \frac{1}{4} (w_{i-1} - w_{i+1})^2 \\
IS_2 &= \frac{13}{12} (w_i - 2w_{i+1} + w_{i+2})^2 + \frac{1}{4} (3w_i - 4w_{i+1} + w_{i+2})^2
\end{aligned} \tag{3.22}$$

The smoothness of each stencil for the right solution is then calculated as:

$$\begin{aligned}
IS_0^R &= \frac{13}{12} (w_{i+3} - 2w_{i+2} + w_{i+1})^2 + \frac{1}{4} (w_{i+3} - 4w_{i+2} + 3w_{i+1})^2 \\
IS_1^R &= \frac{13}{12} (w_{i+2} - 2w_{i+1} + w_i)^2 + \frac{1}{4} (w_{i+2} - w_i)^2 \\
IS_2^R &= \frac{13}{12} (w_{i+1} - 2w_i + w_{i-1})^2 + \frac{1}{4} (3w_{i+1} - 4w_i + w_{i-1})^2
\end{aligned} \tag{3.23}$$

We can now calculate the new weights, $\hat{\omega}'_k$, based on the smoothness, IS_k , and the optimal weights, $\hat{\omega}_k^{opt}$, which are defined as $\hat{\omega}^{opt} = (\frac{3}{10}, \frac{6}{10}, \frac{1}{10})$ for approximation of w by using the procedure from [45],

$$\hat{\omega}'_k = \frac{\hat{\omega}_k^{opt}}{(\epsilon + IS^k)^2} \tag{3.24}$$

where $\epsilon = 10^{-6}$ is there to guarantee non-singular behavior. These new weights, $\hat{\omega}'_k$, are then normalized to become the final WENO weights:

$$\hat{\omega}_k = \frac{\hat{\omega}'_k}{\sum_{z=0}^2 \hat{\omega}'_z} \quad (3.25)$$

where $\sum_k \hat{\omega}_k = 1$. The weighted solutions from each stencil are then summed, in the same manner as Equation 3.18, to form our WENO5 approximated solution:

$$w_{i+1/2} = \sum_{k=0}^2 \hat{\omega}_k q_k^5 \quad (3.26)$$

After at characteristics at all of the cell interfaces are calculated, the characteristics are then projected back to real space using Equation 3.15 then the final flux at the cell interface, $\mathbf{F}_{i+1/2}$, is determined by Equation 3.12 using the updated approximations to the conserved variables.

3.4.2 Monotonicity Preserving (MP) Schemes

The Monotonicity Preserving (MP) scheme, first introduced by Suresh & Huynh[50], uses a high order spatially convergent reconstruction of the interface, the original value, then limits this solution in order to obtain the final interface value. We will adopt the notation of the previous section and drop the “L” subscript for solutions at the face. For the 5th order MP scheme (MP5), which will be used throughout the present study, the original value, $w_{i+1/2}^{OR}$, is given as:

$$w_{i+1/2}^{OR} = (2w_{i-2} - 13w_{i-1} + 47w_j + 27w_{i+1} - 3w_{i+2}) / 60 \quad (3.27)$$

To find the MP5 solution, a few constraints must be satisfied. The first constraint is *monotonicity*-preservation, which Suresh & Huynh [50] define as the upper limit,

$$w^{UL} = w_i + \alpha(w_i - w_{i-1}) \quad (3.28)$$

where $\alpha = 2$, represents a parabolic reconstruction. The second constraint, *accuracy*-preserving, is accomplished by bounding the solution with the median and large curvature solutions. The median (denoted by superscript “MD”) value at the interface, $x_{i+1/2}$, is given by

$$w^{MD} = w^{AV} - \frac{1}{2}d_{i+1/2}^{MD} \quad (3.29)$$

While the large curvature (denoted by superscript “LC”) value at the interface is given by

$$w^{LC} = w_i + \frac{1}{2}(w_i - w_{i-1}) + \frac{\beta}{3}d_{i-1/2}^{LC} \quad (3.30)$$

where $\beta = 4$, w^{AV} is the average solution, d_i is the curvature, and $d_{i+1/2}^{LC}$ is the minmod approximation of the curvature at the zone boundary, all of which are defined as follows:

$$\begin{aligned} w^{AV} &= \frac{1}{2}(w_i + w_{i+1}) \\ d_i &= w_{i-1} + w_{i+1} - 2w_i \\ d_{i+1/2}^{MM} &= \text{minmod}(d_i, d_{i+1}) \end{aligned} \quad (3.31)$$

The superscript “MM” indicates the use of a minmod function. Suresh & Huynh[50] recommended the use of a slightly more restrictive curvature measure than $d_{i+1/2}^{MM}$, which is given by:

$$d_{i+1/2}^{M4} = \text{minmod}(4d_i - d_{i+1}, 4d_{i+1} - d_i, d_i, d_{i+1}) \quad (3.32)$$

For the MP5 scheme $d_{i+1/2}^{MD} = d_{i+1/2}^{LC} = d_{i+1/2}^{M4}$. Now that the mechanisms for the two constraints, *monotonicity*-preserving and *accuracy*-preserving, have been stated, the minimum and maximum value of the solution, w^{MIN} and w^{MAX} , respectively, are given by:

$$\begin{aligned} w^{MIN} &= \max [\min(w_i, \min(w_{i+1}, w^{MD})), \min(w_i, \min(w^{UL}, w^{LC}))] \\ w^{MAX} &= \min [\max(w_i, \max(w_{i+1}, w^{MD})), \max(w_i, \max(w^{UL}, w^{LC}))] \end{aligned} \quad (3.33)$$

The solution at the face, $w_{i+1/2}$, can now simply be expressed as:

$$w_{i+1/2} = \text{median} (w_{i+1/2}^{OR}, w^{MIN}, w^{MAX}) \quad (3.34)$$

The 5th order convergent Monotonicity Preserving WENO (MW5) scheme by Balsara & Shu [51], which is based on the MP5 scheme, has the smooth solution of WENO5, but is strictly monotonicity-preserving near discontinuities. Balsara & Shu were able to demonstrate that the solutions to ideal MHD simulations were far superior to that of MP5 and WENO5. The form of the MW5 solution is the same MP5, Equation 3.34, but the key difference is in how MW5 is used to determine the original value, w^{OR} , and the curvature at the median and large curvature values, d^{MD} and d^{LC} , respectively. By using the WENO stencils for $r = 3$, Equation 3.20 with WENO coefficients from Table 3.1, and the optimal weights, the MW5 original value, w^{OR} , is recovered:

$$w^{OR} = (6w_{i-2} - 27w_{i-1} + 65w_i + 17w_{i+1} - w_{i+2}) / 60 \quad (3.35)$$

In an attempt to filter out extremal features with small domains of support, while keeping extremal features with large domains of support intact, $d_{i+1/2}^{MD} = d_{i+1/2}^{LC} = d_{i+1/2}^{MAX}$, where

$$d_{i+1/2}^{MAX} = \text{minmod} (4d_i - d_{i+1}, 4d_{i+1} - d_i, d_i, d_{i+1}, d_{i-1}, d_{i+2}) \quad (3.36)$$

3.4.3 Advection-Diffusion-Reaction (ADER) Schemes

The Advection-Diffusion-Reaction (ADER) schemes of Titarev & Toro [52] utilize high order spatial derivatives calculated by the underlying scheme to generate the

temporal derivatives using the Cauchy-Kovalevskaya procedure:

$$\begin{aligned}
\partial_t w &= -\lambda \partial_x w \\
\partial_{tt} w &= \lambda^2 \partial_{xx} w \\
\partial_{ttt} w &= -\lambda^3 \partial_{xxx} w \\
&\vdots \\
\partial_t^{(k)} w &= (-\lambda)^k \partial_x^{(k)} w
\end{aligned} \tag{3.37}$$

Where λ is the characteristic wave speed. With the high order temporal derivatives generated from Equation 3.37, a simple Taylor series expansion is performed to acquire a higher order temporally and spatially convergent scheme. But first, we must take the temporal series expansion at the interface,

$$w_{i+1/2} = \tilde{w} + \sum_{k=1}^{m-1} \partial_t^{(k)} \tilde{w} \frac{\tau^k}{k!} \tag{3.38}$$

Where τ is the time step size and $\tilde{w} = w(x_{i+1/2}, 0^+)$ is the approximation of the solution at the interface from the underlying scheme. In the present study, we wish to achieve 3^{rd} order convergence in time, so we will start from Equation 3.38 with $m = 3$ to give,

$$w_{i+1/2} = \tilde{w} + \partial_t \tilde{w} \tau + \partial_{tt} \tilde{w} \frac{\tau^2}{2} \tag{3.39}$$

By performing the Cauchy-Kovalevskaya procedure on Equation 3.39, the solution, $w_{i+1/2}$, will become a function of the time step size and spatial derivatives of the approximate solution as follows:

$$w_{i+1/2} = \tilde{w} - \lambda \partial_x \tilde{w} \tau + \lambda^2 \partial_{xx} \tilde{w} \frac{\tau^2}{2} \tag{3.40}$$

Equation 3.40 will serve as the general form of the temporally 3^{rd} order convergent ADER (ADER3) scheme. Since the expensive Runge-Kutta time integration steps

are no longer required, ADER schemes are extremely efficient and well suited for parallel computation.

By combining the 5th order spatially convergent WENO5's reconstruction to calculate the approximate solution and its spatial derivatives, \tilde{w} and $\partial_x^{(k)}\tilde{w}$, respectively, with the 3rd order temporally convergent ADER3, we form the 3rd order temporal and 5th order spatial convergent ADER-WENO (AW5) scheme [53]. At discontinuities, $\partial_x^{(k)}\tilde{w} = 0 \quad \forall \quad k > 1$ is satisfied in order to prevent spurious oscillations.

3.5 Point-Implicit Euler

The finite rate kinetic systems in the present study are extremely stiff. When solving a stiff ODE, it is often beneficial to solve the problem implicitly. The stiff chemical kinetics ODEs will be expressed in the form of Equation 2.3:

$$\frac{d\mathbf{Q}}{dt} = \dot{\mathbf{\Omega}}_{kinetic} \quad (3.41)$$

where \mathbf{Q} and $\dot{\mathbf{\Omega}}_{kinetic}$ are defined by Equation 2.16. The 1st order point-implicit Euler will be utilized to solve problems of this particular form. First, let us discretize the time into uniform intervals of size Δt and denote $t^n = t_0$ and $t^{n+1} = t_0 + \Delta t$. Upon discretization, a Taylor series expansion can be performed on Equation 3.41 and is expressed as follows:

$$\begin{aligned} \frac{\Delta \mathbf{Q}}{\Delta t} &= \dot{\mathbf{\Omega}}^{n+1} \\ \frac{\Delta \mathbf{Q}}{\Delta t} &= \dot{\mathbf{\Omega}}^n + \frac{\partial}{\partial t} \dot{\mathbf{\Omega}}^n \Delta t \\ \frac{\Delta \mathbf{Q}}{\Delta t} &= \dot{\mathbf{\Omega}}^n + \frac{\partial}{\partial \mathbf{Q}} \dot{\mathbf{\Omega}}^n \frac{\partial}{\partial t} \mathbf{Q} \Delta t \\ \frac{\Delta \mathbf{Q}}{\Delta t} &= \dot{\mathbf{\Omega}}^n + \frac{\partial \dot{\mathbf{\Omega}}^n}{\partial \mathbf{Q}} \Delta \mathbf{Q} \end{aligned} \quad (3.42)$$

Then we shall proceed and solve for the change in the conserved variables, $\Delta \mathbf{Q}$, and arrive with the following form:

$$\Delta \mathbf{Q} = \left(\mathbf{I} - \frac{\partial \dot{\mathbf{\Omega}}^n}{\partial \mathbf{Q}} \Delta t \right)^{-1} \dot{\mathbf{\Omega}}^n \Delta t \quad (3.43)$$

From here we arrive at the solution to our implicit formulation as:

$$\mathbf{Q}^{n+1} = \mathbf{Q}^n + \left(\mathbf{I} - \frac{\partial \dot{\mathbf{\Omega}}^n}{\partial \mathbf{Q}} \Delta t \right)^{-1} \dot{\mathbf{\Omega}}^n \Delta t \quad (3.44)$$

This can also be expressed in the operator form: $\mathbf{Q}^{n+1} = \mathcal{L}^{chem} \mathbf{Q}^n$, where the operator is defined as:

$$\mathcal{L}^{chem} = 1 + \left(\mathbf{I} - \frac{\partial \dot{\mathbf{\Omega}}^n}{\partial \mathbf{Q}} \Delta t \right)^{-1} \frac{\partial \dot{\mathbf{\Omega}}^n}{\partial \mathbf{Q}} \Delta t \quad (3.45)$$

3.6 Spatial-Implicit Euler

Diffusive MHD transport will often have much stricter explicit time step restrictions, Equation 3.8, than that of convective transport, Equation 3.4. Since the maximum allowable explicit diffusive time step is determined by $\Delta t \leq 0.5 \Delta x^2 \sigma_{min} \mu_0$, it becomes apparent that as $\sigma \rightarrow 0$ then $\Delta t \rightarrow 0$. This can become quite cost prohibitive, so in order to ensure stability with a non prohibitive time step, an implicit time marching scheme is utilized.

Before we can cast the diffusive MHD transport into an implicit formulation, we must start from the magnetic diffusion flux formulation of the RHS, Equation 2.34, and define the magnetic field diffusion Jacobian, A'' , for the dimensionally split

magnetic diffusion as

$$\frac{\partial \mathbf{Q}}{\partial t} = \frac{\partial}{\partial x} \left(A_x^\nu \frac{\partial \mathbf{Q}}{\partial x} \right) \quad (3.46)$$

where the magnetic field diffusion Jacobian, $A_x^\nu = \frac{\partial \mathbf{F}_x^\nu}{\partial \mathbf{Q}}$,

$$A_x^\nu = \frac{1}{\mu_0 \sigma} \begin{pmatrix} 1 & 0 & 0 & 0 \\ 0 & 1 & 0 & 0 \\ 0 & 0 & 1 & 0 \\ -\frac{B_x}{\mu_0} & 0 & 0 & 1 \end{pmatrix}$$

Assuming a one-dimensional discretization on a uniformly-spaced grid, the spatial derivatives can be approximated by finite-differences and the subscript in A_x^ν will be ignored, thereby reducing the PDE to a system of ODE's,

$$\frac{d\mathbf{Q}_i}{dt} = \frac{1}{\Delta x^2} \left(A_{i+\frac{1}{2}}^\nu \mathbf{Q}_{i+1} - (A_{i+\frac{1}{2}}^\nu + A_{i-\frac{1}{2}}^\nu) \mathbf{Q}_i - A_{i-\frac{1}{2}}^\nu \mathbf{Q}_{i-1} \right) \quad (3.47)$$

the system of equations can be written in matrix notation as

$$\frac{\partial \vec{\mathbf{Q}}}{\partial t} = \tilde{\Phi} \vec{\mathbf{Q}} \quad (3.48)$$

where $\tilde{\Phi}$ is a tridiagonal matrix and $\vec{\mathbf{Q}}$ is the spatial vector of the conserved element array,

$$\tilde{\Phi} = \frac{1}{\Delta x^2} \begin{pmatrix} \ddots & & & & \\ & \ddots & & & \\ & & -A_{i-\frac{1}{2}}^\nu & (1 + A_{i-\frac{1}{2}}^\nu + A_{i+\frac{1}{2}}^\nu) & -A_{i+\frac{1}{2}}^\nu \\ & & \ddots & \ddots & \ddots \\ & & & & \ddots \end{pmatrix}, \quad \vec{\mathbf{Q}} = \begin{pmatrix} \vdots \\ \mathbf{Q}_{i-1} \\ \mathbf{Q}_i \\ \mathbf{Q}_{i+1} \\ \vdots \end{pmatrix} \quad (3.49)$$

Now, we can determine the implicit formulation by evaluating the RHS of Eqn. 3.48 at time $t + \Delta t$,

$$\vec{\mathbf{Q}}^{n+1} = \vec{\mathbf{Q}}^n + \Delta t \tilde{\Phi} \vec{\mathbf{Q}}^{n+1} \quad (3.50)$$

By applying backwards Euler to Equation 3.50, one can recover the operator form, $\vec{\mathbf{Q}}^{n+1} = \mathcal{L}_\alpha^{diff} \vec{\mathbf{Q}}^n$, where the MHD diffusion matrix operator for the α -direction is

$$\mathcal{L}_\alpha^{diff} = \left(1 - \Delta t \tilde{\Phi}_\alpha\right)^{-1} \quad (3.51)$$

In order to apply the diffusive MHD transport in all directions, one might perform the following operation:

$$\mathbf{Q}^{n+1} = \mathcal{L}_x^{diff} \mathcal{L}_y^{diff} \mathcal{L}_z^{diff} \mathbf{Q}^n \quad (3.52)$$

Upon inspection of Equation 3.49, \mathcal{L}^{diff} is merely the inverse of a tridiagonal system of equations. Rather than applying a scheme with a relatively high computation cost, i.e. GMRes or Gaussian Elimination, one can exploit the fact the system is tridiagonal and implement Thomas' Algorithm, which is discussed in more detail in Appendix F.1.

The diffusive MHD operators, $\mathcal{L}_\alpha^{diff}$, use line relaxation to proceed in time. If the grid and fluid properties, i.e. conductivity, grid resolution, etc., are not spatially uniform the diffusive MHD transport will have different time scales for each directional sweep. When this occurs, it becomes necessary to split a given operator, \mathcal{L}_x , in time using the Strang operator splitting technique demonstrated in Section 3.1. The superscript 'diff' has been discarded for the remainder of this section. One permutation of applying multiple spatial operators to a generic 2D diffusive MHD problem would go as follows:

$$\mathbf{Q}^{n+1} = \mathcal{L}_x^{\Delta t/2} \mathcal{L}_y^{\Delta t} \mathcal{L}_x^{\Delta t/2} \mathbf{Q}^n \quad (3.53)$$

which is illustrated in Figure 3.4(a). In order to avoid developing a bias toward a particular direction, after applying Equation 3.53 one should use the following:

$$\mathbf{Q}^{n+2} = \mathcal{L}_y^{\Delta t/2} \mathcal{L}_x^{\Delta t} \mathcal{L}_y^{\Delta t/2} \mathbf{Q}^{n+1} \quad (3.54)$$

which is illustrated in Figure 3.4(b). A similar permutation can be performed when solving a 3-D diffusive MHD problem.

r	k	$l = 0$	$l = 1$	$l = 2$
2	0	-1/2	3/2	
	1	1/2	1/2	
3	0	1/3	-7/6	11/6
	1	-1/6	5/6	1/3
	2	1/3	5/6	-1/3

Table 3.1: WENO Coefficients, $a_{k,l}^r$

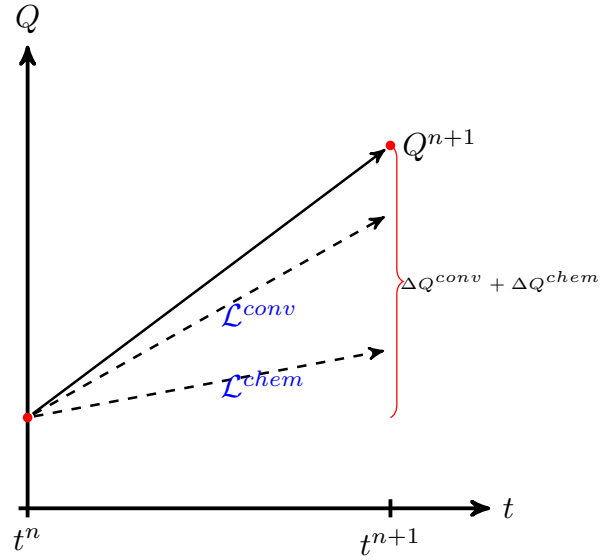


Figure 3.1: Operator splitting of two generic operators, \mathcal{L}^{chem} & \mathcal{L}^{conv} .

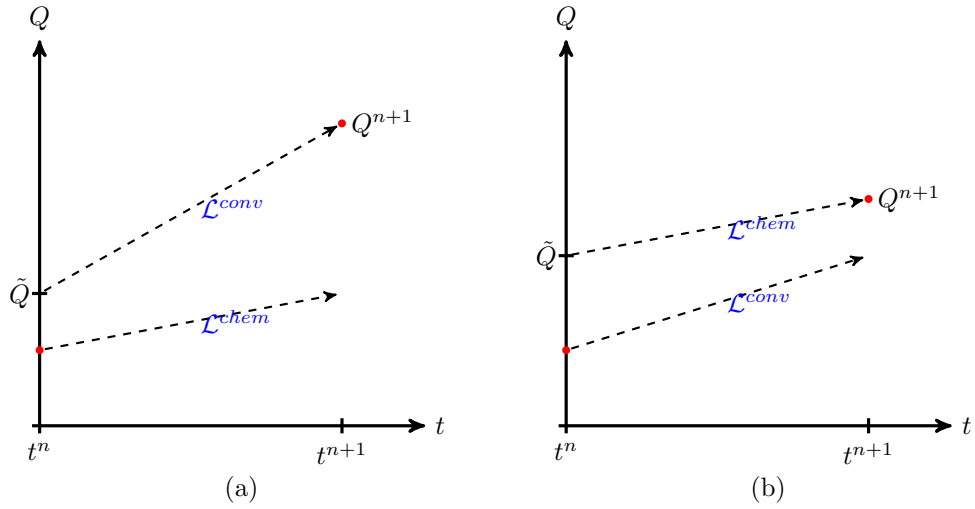


Figure 3.2: Demonstration that with Strang splitting coupled operators, the ordering of the operators can significantly change the solution.

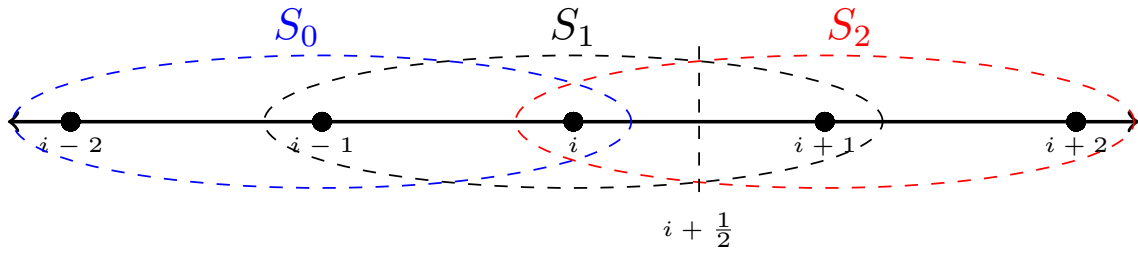


Figure 3.3: WENO stencil for $r = 3$.

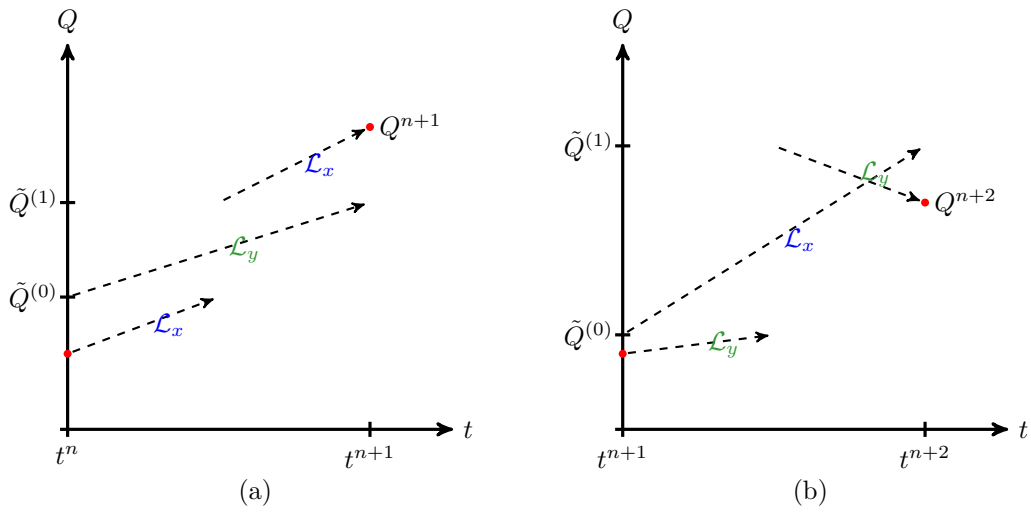


Figure 3.4: Strang operator splitting in time for three operations illustrated with different ordering of the operators, \mathcal{L}_x and \mathcal{L}_y .

CHAPTER 4

Verification of Numerical Schemes

The numerical schemes used in the present study must be validated and verified to ensure their accuracy and proper usage. The 1-dimensional, 2-dimensional, and 3-dimensional forms of the hydrodynamic and magnetohydrodynamic governing equations assume the form of Equation 2.1:

$$\frac{\partial \mathbf{Q}}{\partial t} + \nabla_n \cdot \mathbf{F} = \dot{\mathbf{\Omega}}$$

For the 1-D subset of the governing equations, the variation in the y- and z-dimensions are set to zero, $\frac{\partial}{\partial y} \equiv 0$ and $\frac{\partial}{\partial z} \equiv 0$, respectively. While in the 2-D subset of the governing equations, there is no variation in the z-direction, $\frac{\partial}{\partial z} \equiv 0$.

4.1 Inviscid Hydrodynamics

The hydrodynamic test cases will show that the physical wave (acoustic and entropy) speeds present in the simulation are properly captured and that the approximate Riemann solution matches the proper jump conditions in the event of a shock. In the hydrodynamic limit the conserved variables, \mathbf{Q} , and flux, \mathbf{F} , are expressed as

Equation 2.5:

$$\mathbf{Q} = \begin{pmatrix} \rho \\ \rho \mathbf{u} \\ E \end{pmatrix} \quad \mathbf{F} = \begin{pmatrix} \rho u_n \\ \rho \mathbf{u} \cdot u_n + P \mathbf{n} \\ (E + P) u_n \end{pmatrix}$$

4.1.1 Sod's Shock Tube

There are a few classic test cases performed utilizing our Riemann solvers, in order to test their ability to resolve shocks, contact discontinuities, and rarefactions as well as the interactions of these structures. The first test case was introduced by Sod [54], known presently as Sod's shock tube. We will adopt the same initial and boundary conditions. The left and right states are

$$\begin{aligned} (\rho_L, u_{x,L}, P_L) &= (1 \text{ kg/m}^3, 0 \text{ m/s}, 1 \text{ Pa}) & x < 0 \\ (\rho_R, u_{x,R}, P_R) &= (0.125 \text{ kg/m}^3, 0 \text{ m/s}, 0.1 \text{ Pa}) & x > 0 \end{aligned} \quad (4.1)$$

where the adiabatic index, $\gamma \equiv 1.4$, unless otherwise stated, and over a domain $x \in (-5, 5] \text{ mm}$. Figure 4.1(a) shows the solution for the schemes at $t = 200 \mu\text{s}$ which contains a single shock, contact discontinuity and rarefaction. The figure clearly shows that all of the schemes used resolved the problem reasonably well compared to the exact solution. Figure 4.1(b) illustrates MW5 solution converging to the exact solution at the contact discontinuity as Δx is decreased.

4.1.2 Hydrodynamical Interacting Blast Wave Problem

Blast waves are generally described as strong and rapid release of energy which are often characterized by regions containing drastic temperatures and pressure rises. For the second test of our 1D hydrodynamic test problems, we ran the interacting

blast wave problem which was first proposed by Woodward and Collela [55]. The problem consist of the left, middle, and right initial states, L, M, and R respectively, which are as follows:

$$\begin{aligned}
(\rho_L, u_{x,L}, P_L) &= (1, 0, 10^3) & x < 0.1 \\
(\rho_M, u_{x,M}, P_M) &= (1, 0, 10^{-2}) & 0.1 < x < 0.8 \\
(\rho_R, u_{x,R}, P_R) &= (1, 0, 10^2) & x > 0.8
\end{aligned} \tag{4.2}$$

where $x \in (0, 1]$. Figure 4.2 shows the density profiles at $t = 38$ seconds using the MP5, AW5, and MW5 schemes with greater detail in Figure 4.3. While all of the schemes resolve the shocks at $x \approx 0.65$ & 0.87 reasonably well, the contact discontinuities at $x \approx 0.75$ & 0.8 are slightly better resolved by MP5. None of the schemes used artificial compression methods.

4.1.3 Shock-Entropy Wave Interaction

In the last of our 1-D hydrodynamic test cases, we wish to test our numerical schemes ability to resolve smooth flow disturbances which is of particular interest because of the nature of the problems in the present study. The Shu-Osher problem [56] has been extensively used to simulate a Mach 3 shock wave interacting with an oscillatory density disturbance which generates a flow field with a combination of smooth structures and discontinuities. The initial conditions are given for the left and right state as follows:

$$\begin{aligned}
(\rho_L, u_{x,L}, P_L) &= (3.857143, 2.629369, 10.33333) & x < 0.8 \\
(\rho_R, u_{x,R}, P_R) &= (1 + 0.2\sin(5\pi x), 0, 1) & x > 0.8
\end{aligned} \tag{4.3}$$

where $x \in (-1, 1]m$. From the density profile in Figure 4.4(a) at $t = 360ms$, one can see that three schemes resolved the entropy disturbances quite well. Upon closer

inspection, Figure 4.4(b) clearly shows that while AW5 was slightly diffused and MW5 slightly amplified, MP5 was clearly able to resolve the transient entropy waves the best.

4.1.4 Shock Diffraction Down a Backward Facing Step

The next test problem describes the diffraction of a Mach 2.4 shock down a backward facing step[57]. The strong rarefaction generated by the diffraction at the 90° corner often results in numerical errors described by over-expansion and negative pressure for many Riemann solvers[58]. The problem is simulated using a resolution of $\Delta x = \Delta y = \frac{1}{1024}$ with the MW5 solver. The numerical simulation is shown side-by-side with the experimental images in Figure 4.5. The numerical solution is presented using a Schlieren-type plot as prescribed by [58] which uses density gradients in an analogous way to index of refraction gradients, which makes it ideal for comparison with experimental images. The figure shows that the MW5 scheme was able correctly reproduce the flow features in the region of the rarefaction.

4.1.5 Rayleigh-Taylor Hydrodynamic Instability

In the next test, a heavy fluid is supported by a lighter fluid in a gravitational field, or equivalent, which accelerates the heavier fluid into a lighter fluid. This condition is unstable once the interface between the two fluids is perturbed. The instability is known as the Rayleigh-Taylor(RT) instability. Earlier analytical investigations date back to the detailed analysis given by Chandrasekhar[59].

In the initial configuration, two fluids with a prescribed density ratio ($\rho_L/\rho_U = 2$) are left to evolve between two planes ($y = -1$ m and $y = +1$ m), with gravity oriented

in the upward direction ($\mathbf{g} = \{0, +1\}^T$). The boundaries are adiabatic solid walls. The remainder of the fluid initial conditions above and below the diaphragm, U & L respectively, are found in Table 4.1. The solutions produced by the MP5, AW5, and MW5 scheme were compared for this problem against the test solution at various times in Figures 4.6-4.9. From these figures, it becomes quite clear that sharp features and rolled up vortices in the MW5 solution are far superior to that of the solutions produced by MP5 and AW5.

4.2 Ideal Magnetohydrodynamics(MHD)

The ideal MHD test cases will demonstrate that the physical waves (entropy, fast & slow magneto-acoustic, and Alfvén) are properly captured under various configurations by the present schemes.

4.2.1 1D MHD Shock Tube Problems

The Brio-Wu problem [60] was used to ensure the numerical scheme sufficiently captured all of the important features, ie, a contact discontinuity, fast shock, fast rarefaction, compound wave, and slow shock. The initial conditions are analogous to Sod's shock tube problem where the initial left and the right states are as follows:

$$\begin{aligned} (\rho_l, u_{x,l}, u_{y,l}, u_{z,l}, B_{x,l}, B_{y,l}, B_{z,l}, P_l) &= (0.1, 0, 0, 0, 0.75, -1, 0, 1) & x < 0 \\ (\rho_r, u_{x,r}, u_{y,r}, u_{z,r}, B_{x,r}, B_{y,r}, B_{z,r}, P_r) &= (1, 0, 0, 0, 0.75, +1, 0, 10) & x > 0 \end{aligned} \quad (4.4)$$

where $\gamma \equiv 2$ and $x \in (-1, 1]$. Figure 4.10 - 4.15 show the distributions of various fluid properties at the solution time, $t = 0.1$. Figure 4.11(a) shows a zoom in of the compound wave at $x \approx -0.03m$. From this figure, it is clear that the MW5

scheme is able to resolve the major features (compound wave, fast & slow rarefaction) better than MP5 & AW5. All of the schemes (MP5, AW5, & MW5) resolve the contact discontinuity fairly well, shown in Figure 4.11(b). The undershoot observed in the velocity profile, Figure 4.12(a), at $x \approx 0.35$ m is a well documented feature in literature for higher order MHD schemes at magneto-sonic points; Jiang and Shu [61] suggest performing the test problem in a moving reference frame in order to suppress the oscillations.

4.2.2 Orszag-Tang Problem

Various 2D MHD test cases were performed to ensure that the solver correctly captured all physical waves and to ensure the solution remains divergence free, $\nabla \cdot \mathbf{B} \equiv 0$. The divergence cleaning procedure used when performing MHD simulations is given in Appendix C. The first numerical test case is that of the Orszag-Tang vortex problem, first introduced by Orszag & Tang[62]. This is a well-known model problem for testing the transition to supersonic 2D MHD turbulence. The initial conditions of the problem are given by:

$$(\rho, u_x, u_y, B_x, B_y, P) = (2.778, -\sin(y), \sin(x), -\sin(y)\sqrt{\mu_0}, \sin(2x)\sqrt{\mu_0}, 1.667) \quad (4.5)$$

where $\gamma \equiv \frac{5}{3}$. The problem is set on a periodic domain with the dimensions $x : y \in [0, 2\pi)m : [0, 2\pi)m$. Figure 4.16 shows the temperature distribution of the solutions at $t = 3s$. Although the images illustrated appear similar, upon further inspection the flow features in Figures 4.16(a) & (c) are sharper than those in Figure 4.16(b).

4.2.3 Balsara’s Rotor Problem

The following test, which was originally introduced by Balsara & Spicer[63], consists of the propagation of strong torsional Alfvén waves into an ambient fluid. The problem consists of a dense, rapidly spinning cylinder of fluid (the rotor) surrounded by a light, stationary fluid (ambient fluid). Because there is no diffusive transport in this problem, the two fluids are connected by an initially uniform magnetic field. The rapidly spinning rotor causes torsional Alfvén waves to propagate into the ambient fluid, which will lead to a decrease of angular momentum in the rotor. The magnetic field is strong enough that as it wraps itself around the rotor, the increased magnetic pressure will compress the rotor into an oblong shape. Balsara & Spicer applied a slight taper to the initial density and velocity of the rotor as to avoid generating strong start-up transient from the computational scheme. The computation domain is described by $x : y \in [0, 1] : [0, 1]$ and the initial conditions are described in Table 4.2.

At the solution time, $t = 0.295$ s, MW5 and MP5 shown in Figures 4.17 & 4.18, respectively, agree quite well with the results of Balsara & Spicer[63] using $CFL = 0.3$, while AW5 is unstable at this CFL number. Figure 4.19 illustrates that AW5 can remain stable and resolve Balsara’s rotor problem quite well by reducing the CFL to 0.15.

4.2.4 Rayleigh Taylor MHD Instability

Equally as important as the stability of the chemical processes is that of the stability of the MHD. As previously demonstrated in Section 4.1.5, Rayleigh-Taylor Instabilities (RTI) can arise from infinitesimal disturbances in amplitude and grow because

of the gradient in the applied force, e.g., a buoyant force. In [59], Chandrasekhar analytically demonstrated RTI with a uniform tangential magnetic field in both fluids, where the stability growth rate is:

$$n^2 = gk \frac{\rho_2 - \rho_1}{\rho_2 + \rho_1} - \frac{\mathbf{B}^2 k^2 \cos^2 \theta}{2\pi(\rho_2 + \rho_1)} \quad (4.6)$$

where k is the wave number, n is the growth rate, and θ is the angle between \mathbf{B} and \mathbf{k} . The critical strength of a magnetic field to suppress instability of a mode of wavelength λ is:

$$\mathbf{B}_c = \frac{\sqrt{g\lambda(\rho_2 - \rho_1)}}{\cos \theta} \quad (4.7)$$

Similarly, the critical wavelength for a given strength of a magnetic field can be expressed as:

$$\lambda_c = \frac{\mathbf{B}^2 \cos^2 \theta}{g(\rho_2 - \rho_1)} \quad (4.8)$$

where $\lambda < \lambda_c$ are suppressed.

As specified by Remacle et al.[64], a domain with dimensions $x : y \in [0, 0.25]m : [-0.5, 0.5]m$ is enclosed by reflective, adiabatic walls. The heavy, upper fluid is separated from the light, lower fluid at $y = 0.01\cos(8\pi x)$. The acceleration due to gravity is $\mathbf{g} = \{0, -1\}^T$. The initial conditions of the fluid are listed in Table 4.1. Figures 4.20(a) - (c) show the solution of the density distribution of MW5, MP5, and AW5, respectively, at $t = 2$ s with grid resolution $\Delta x = \Delta y = \frac{1}{400}m$. Due to the lack of rolled up vortices in Figure 4.20(c), AW5 cannot properly resolve the instability of the current problem. Thus, only MW5 and MP5 will be used in the next portion of the test.

The suppression of the instability growth with tangential magnetic field strengths of $B_x = 0, 0.2B_c, 0.5B_c,$ and $0.8B_c$ at $t = 2$ s using MW5 & MP5, respectively, is

illustrated in Figures 4.21 & 4.22 . The illustrations support the well established theory of Chandrasekhar[59] that there is a critical tangential magnetic field that will suppress a perturbations growth in this particular test case. A normal magnetic field with the strengths $B_y = 0.5B_c$, $1.5B_c$, and $2B_c$ are illustrated at $t = 2$ s in Figures 4.23 & 4.24. The normal magnetic field did not have a significant affect on the growth of the instabilities until a larger field was applied relative to the tangential field strength, which is confirmed by Jun et al.[65]. Additionally, Jun et al. show that the growth of the instability in the nonlinear regime is enhanced by the normal field up to a certain field strength.

4.3 Two-Temperature(2T) Model

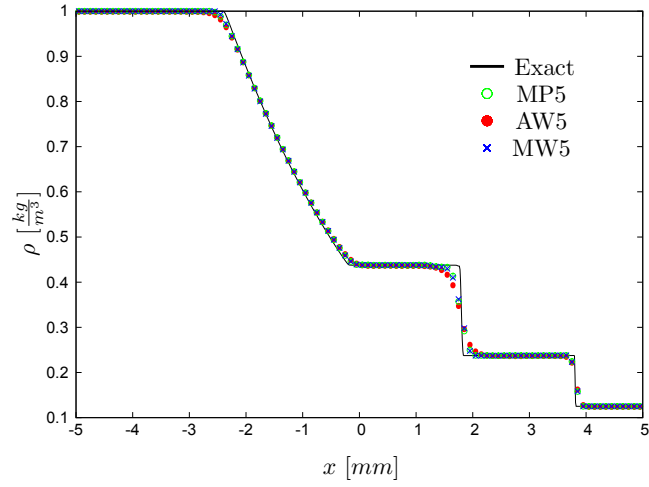
When there is significant ionization due to shocks or non-isentropic processes, the electron temperature, T_e , is adiabatic and must relax to the translational temperature of the heavy particles, T_h . Next, we present a 1D test case of a Mach 10 fully ionized plasma of argon passing through a normal shock. Figure 4.25(a) illustrates the electron and heavy particle temperatures when they are conserved separately and are not allowed to relax toward equilibrium, while Figure 4.25(b) illustrates the electron and heavy particle temperatures relaxing via electron-ion collisions toward equilibrium. In these figures we see that MP5 is able properly conserve electron entropy as well relax to the correct equilibrium temperature, $T_e = T_h = 7800K$.

	upper part	lower part
ρ	2	1
P	$2 - 2y$	$2 - y$
u_x	$\epsilon_x \sin(8\pi x) \cos(\pi y) \sin^{\tau-1}(\pi y)$	same as upper part
u_y	$-\epsilon_y \cos(8\pi x) \sin^\tau(\pi y)$	same as upper part

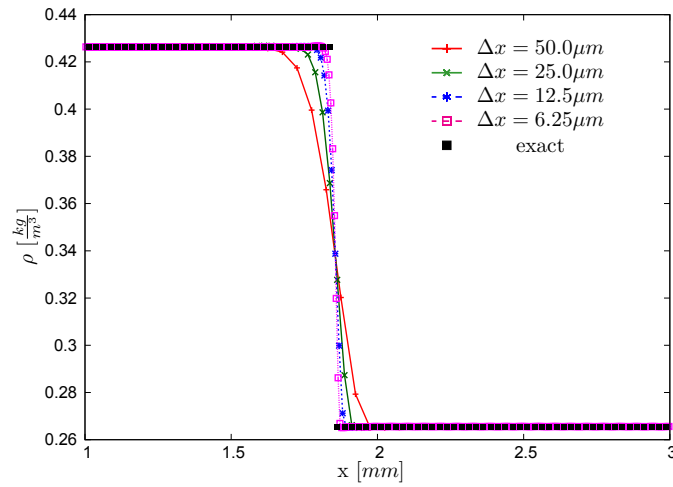
Table 4.1: RTI problem hydrodynamic initial conditions as specified by Remacle et al.[64] where $\tau = 6$, $M_0 = 0.1$, $\epsilon_y = M_0 \sqrt{\gamma/2}$, and $\epsilon_x = -\epsilon_y \tau / 16$.

	$r < r_0$	$r_0 < r < r_1$	$r > r_1$
ρ	10	1	$1 + 9f$
P	0.5	0.5	0.5
u_x	$-\frac{v_0(y-y_0)}{r_0}$	$-f \frac{v_0(y-y_0)}{r_0}$	0
u_y	$\frac{v_0(x-x_0)}{r_0}$	$f \frac{v_0(x-x_0)}{r_0}$	0

Table 4.2: Balsara's rotor problem initial conditions as specified by Tóth[66] with a magnetic field $B_x = 2.5/\mu_0$, where $r_0 = 0.1$, $r_1 = 0.115$, $f = \frac{r_1-r}{r_1-r_0}$, $v_0 = 1$, $(x_0, y_0) = (0.5, 0.5)$, and $\gamma = 5/3$.



(a)



(b)

Figure 4.1: Density distribution of Sod's[54] 1D Shock Tube problem at runtime = 2 s and CFL=0.4, where (a) compares the MP5, AW5, and MW5 solutions with $\Delta x = 100\mu m$ and (b) is an expanded view near the contact discontinuity showing the convergence of MP5 with successively reduced grid size Δx .

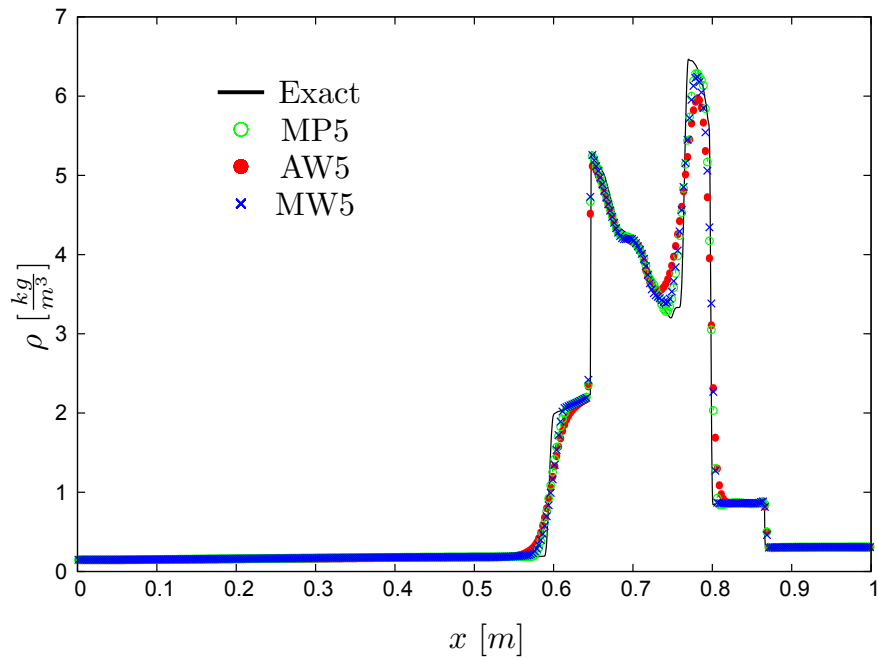
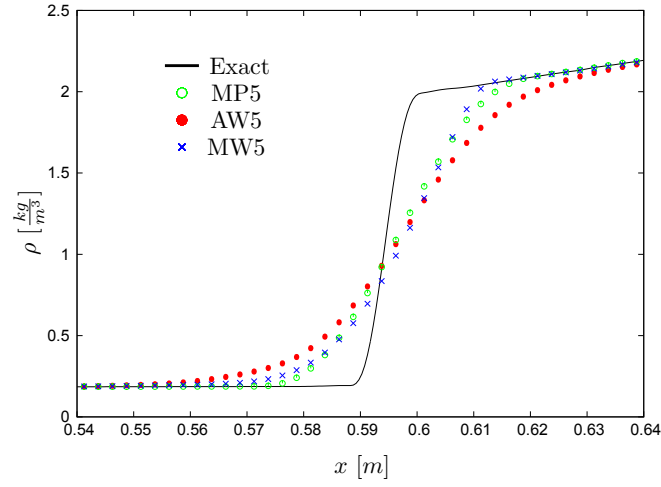
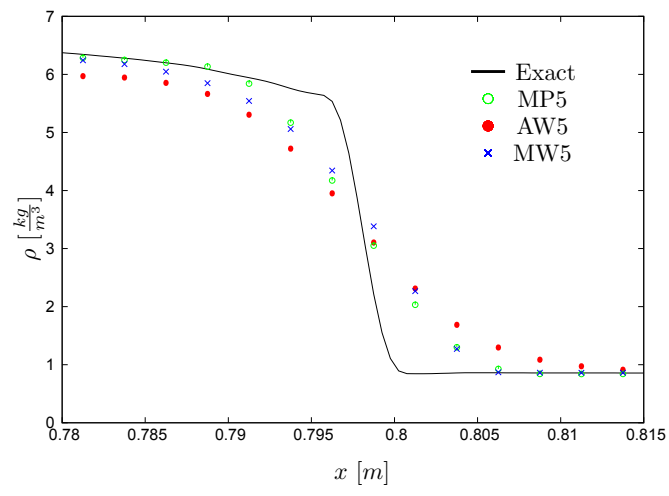


Figure 4.2: Density distribution of Woodward and Collela's[55] 1D Blastwave problem using MP5, AW5, and MW5, $\Delta x = 2.5 \times 10^{-3}m$, CFL = 0.4, runtime = 38ms.

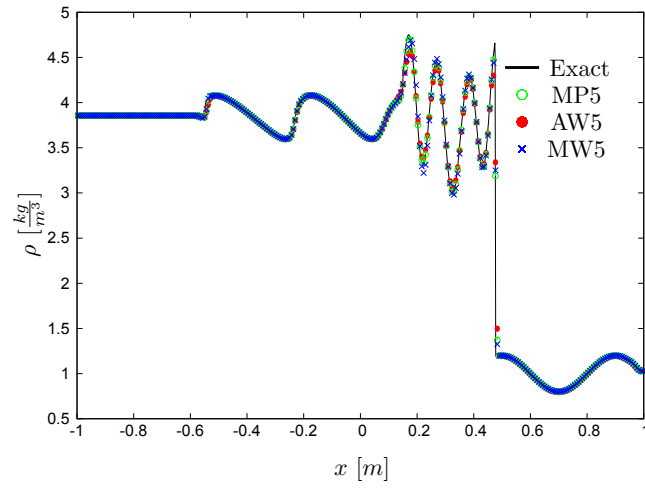


(a)

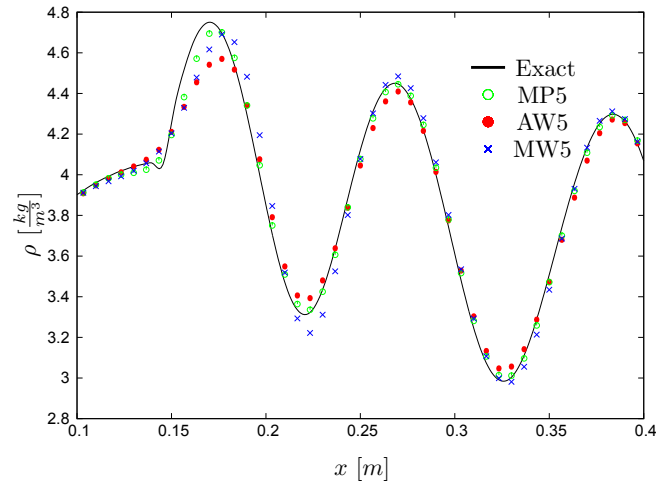


(b)

Figure 4.3: Density distribution of the contact discontinuities for the 1D Blastwave problem [55] using MP5, AW5, and MW5, $\Delta x = 2.5 \times 10^{-3}m$, CFL = 0.4, runtime = 38ms, where (a) and (b) are expanded views near contact discontinuities of Figure 4.2.



(a)



(b)

Figure 4.4: Density distribution of the 1D Shock-Entropy Interaction problem [56] using MP5, AW5, and MW5, $\Delta x = 6.67 \times 10^{-3}m$, CFL = 0.4, runtime = 360ms, where (a) is the wide view and (b) is an expanded view near an entropy disturbance.

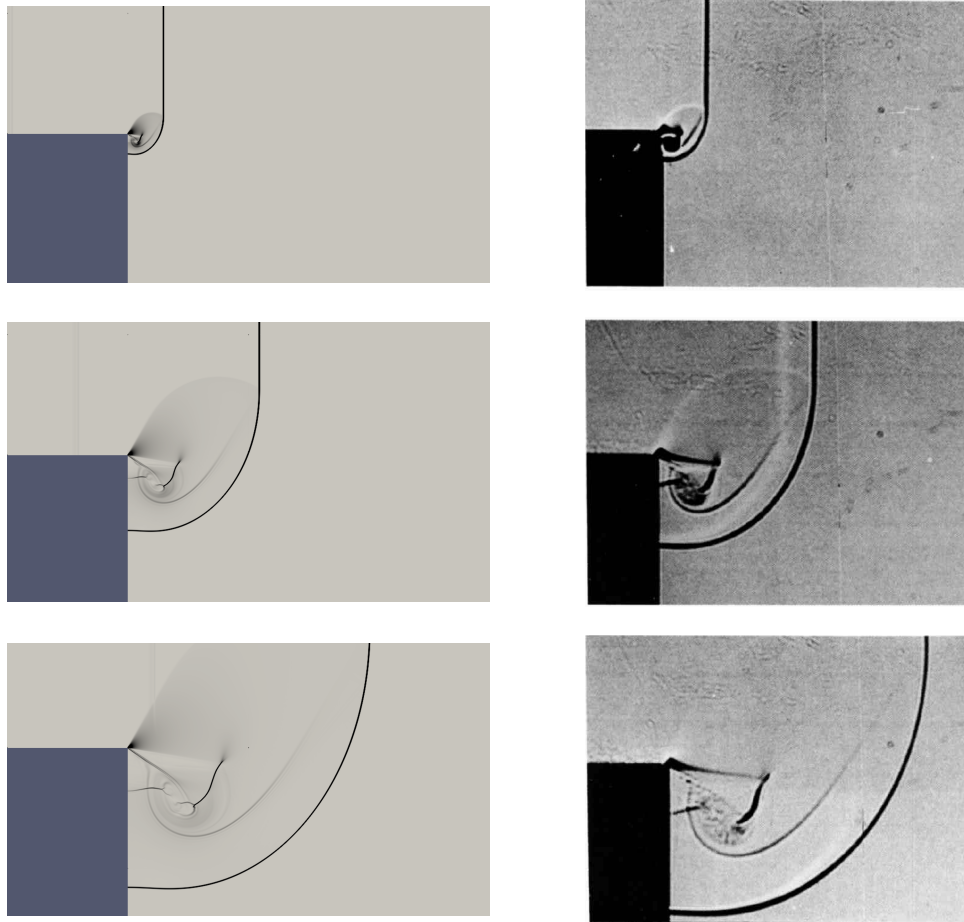


Figure 4.5: Mach 2.4 flow over a backward facing step solution (left) using MW5 with $\Delta x = \Delta y = \frac{1}{1024}m$ compared to the experimental results (right) [57].

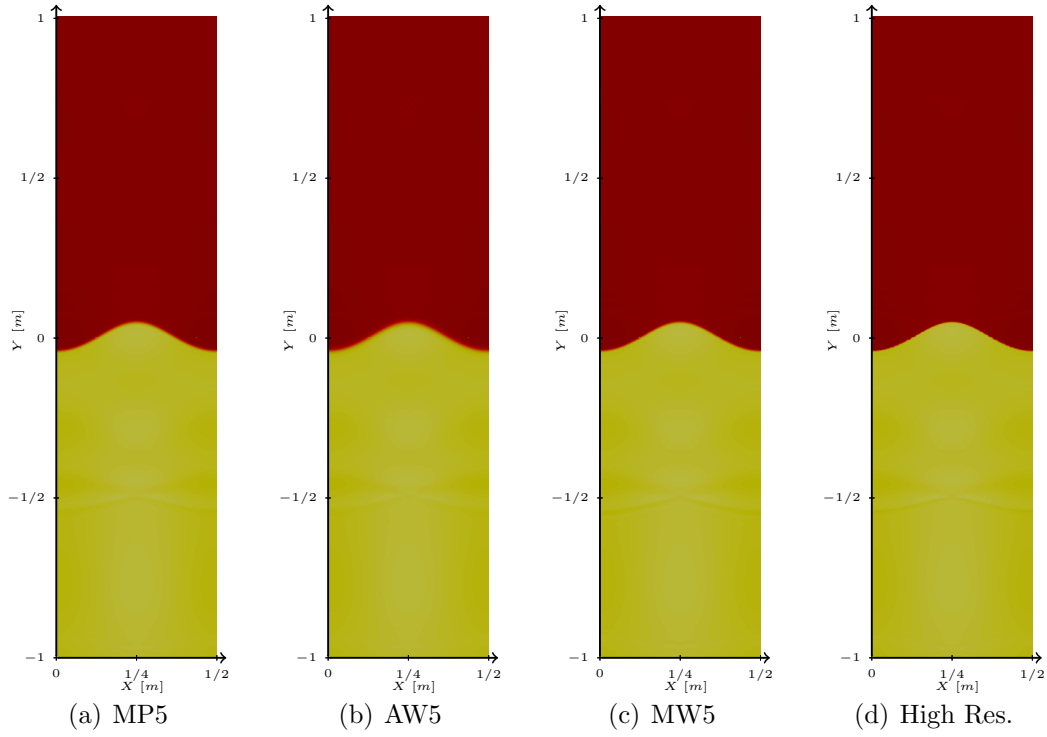



Figure 4.6: Density distribution for hydrodynamic Rayleigh Taylor Instability problem at $t = 0.75s$, where $\Delta x = \Delta y = \frac{1}{800}m$ (For High Resolution, MW5 was used with $\Delta x = \Delta y = 6.25 \times 10^{-4}m$), min  max .

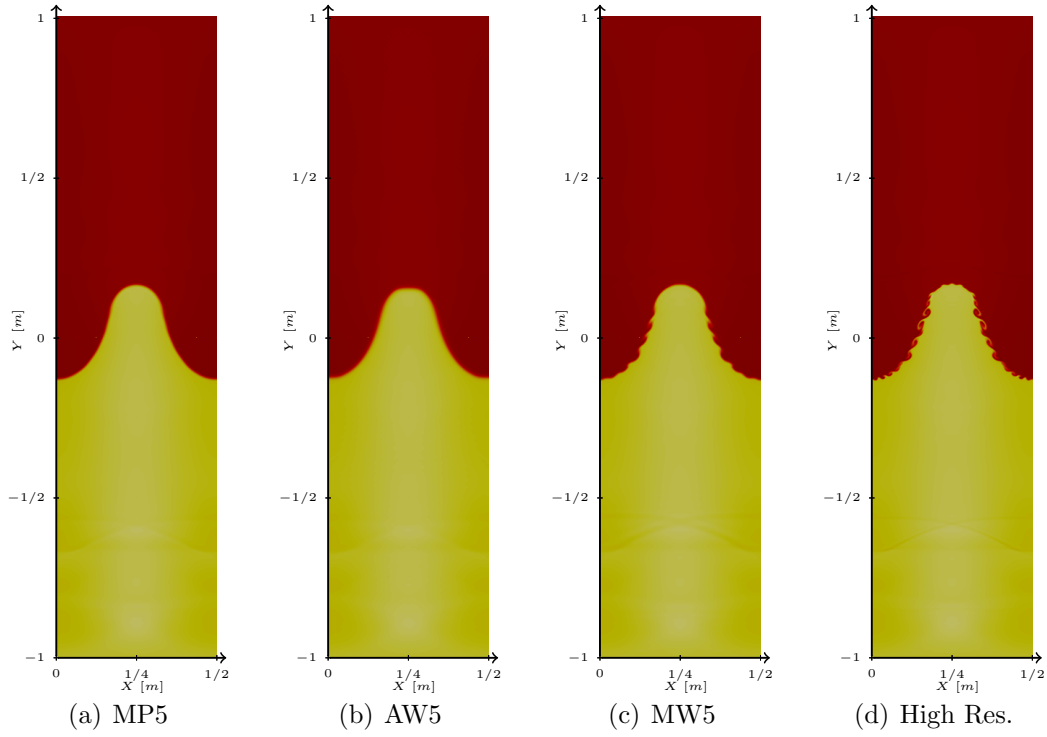



Figure 4.7: Density distribution for hydrodynamic Rayleigh Taylor Instability problem at $t = 1.50s$, where $\Delta x = \Delta y = \frac{1}{800}m$ (For High Resolution, MW5 was used with $\Delta x = \Delta y = 6.25 \times 10^{-4}m$), min  max .

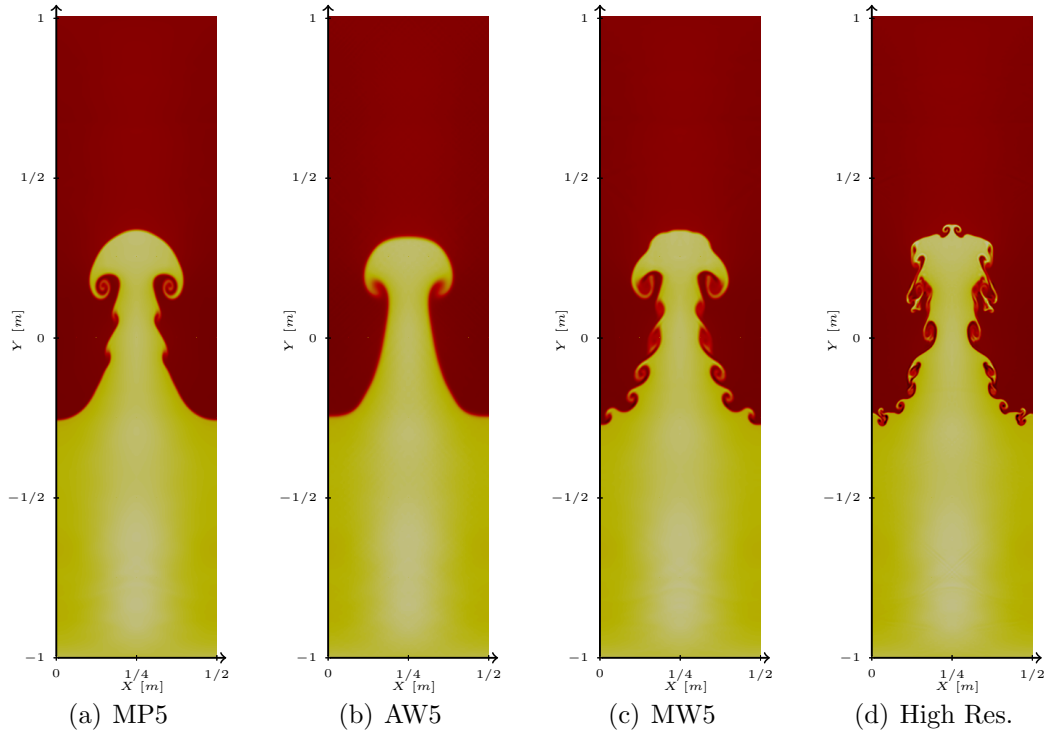



Figure 4.8: Density distribution for hydrodynamic Rayleigh Taylor Instability problem at $t = 2.25s$, where $\Delta x = \Delta y = \frac{1}{800}m$ (For High Resolution, MW5 was used with $\Delta x = \Delta y = 6.25 \times 10^{-4}m$), min  max .

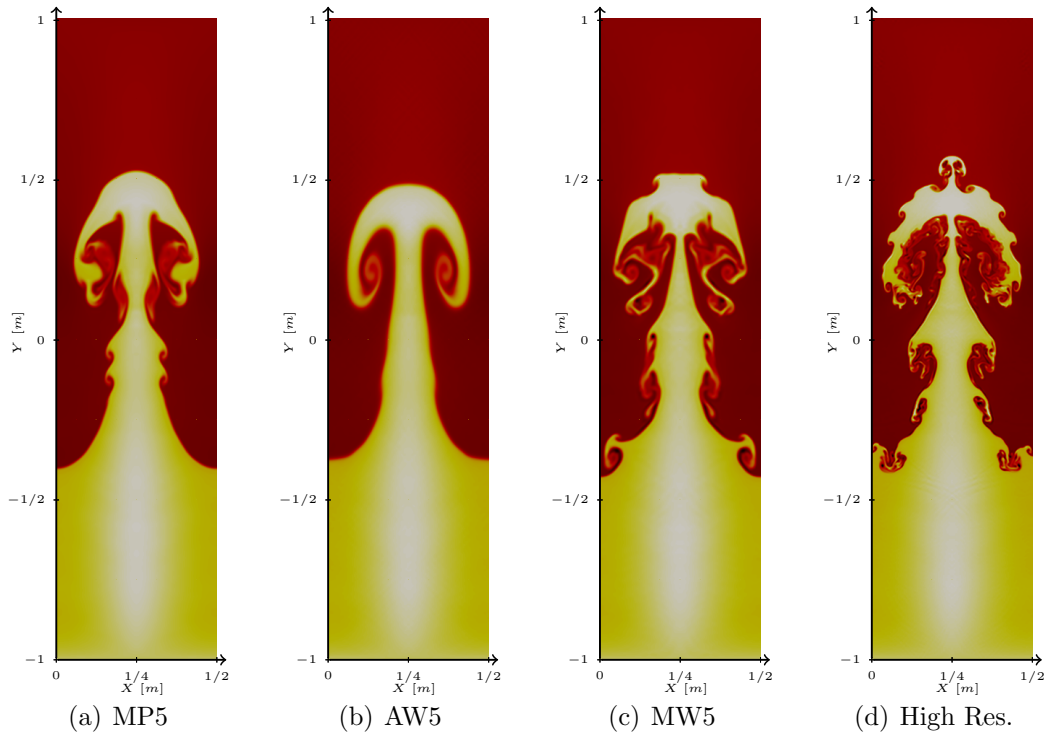


Figure 4.9: Density distribution for hydrodynamic Rayleigh Taylor Instability problem at $t = 3.00s$, where $\Delta x = \Delta y = \frac{1}{800}m$ (For High Resolution, MW5 was used with $\Delta x = \Delta y = 6.25 \times 10^{-4}m$), min max .

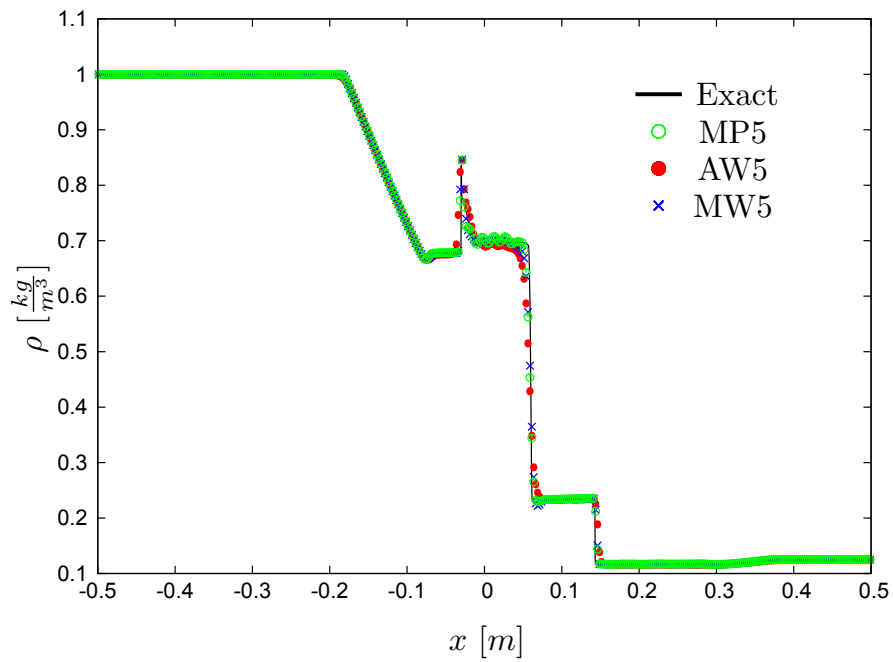
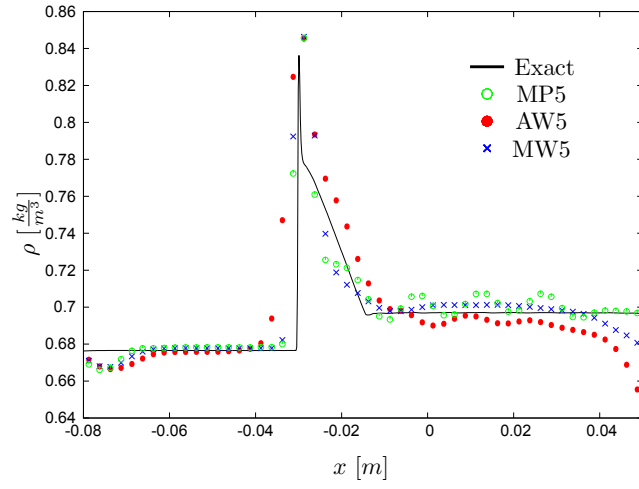
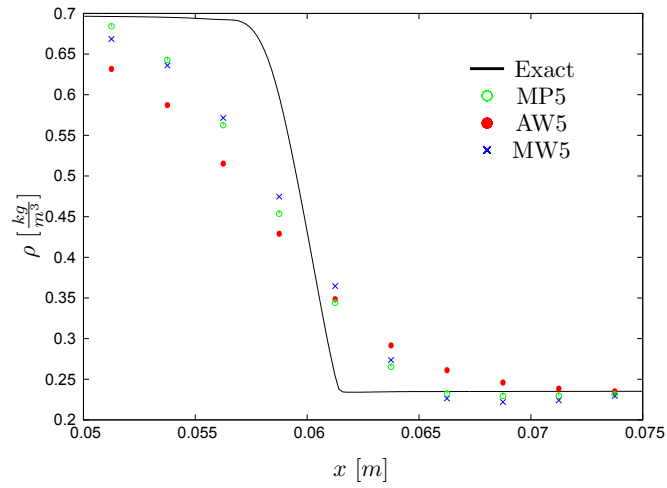


Figure 4.10: Density distribution of the Briou-Wu[60] problem using MP5, AW5 and MW5, $\Delta x = 2.5 \times 10^{-3}m$, CFL = 0.4, runtime = 100ms

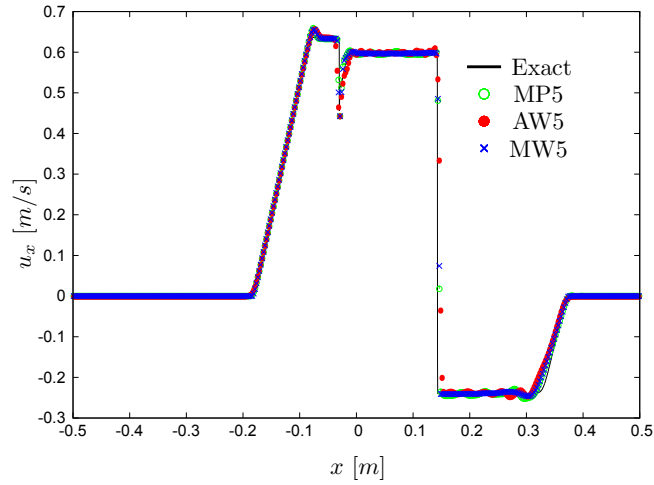


(a)

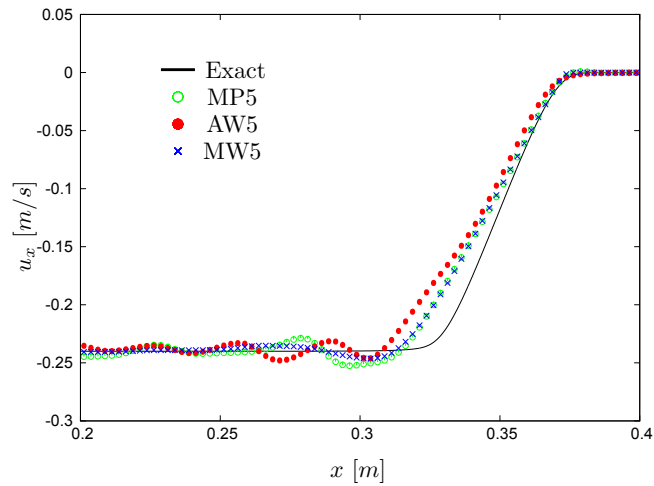


(b)

Figure 4.11: Density distribution for the 1D Brio-Wu[60] problem using MP5, AW5, and MW5, $\Delta x = 2.5 \times 10^{-3}m$, CFL = 0.4, runtime = 100ms, which illustrate the expanded views near the compound wave (a) and contact discontinuity (b) of Figure 4.10.



(a)



(b)

Figure 4.12: Velocity distribution of the x-component for the 1D Brio-Wu[60] problem using MP5, AW5, and MW5, $\Delta x = 2.5 \times 10^{-3} \text{m}$, CFL = 0.4, runtime = 100ms, which (b) illustrates the expanded views near the trailing edge of the fast rarefaction of (a).

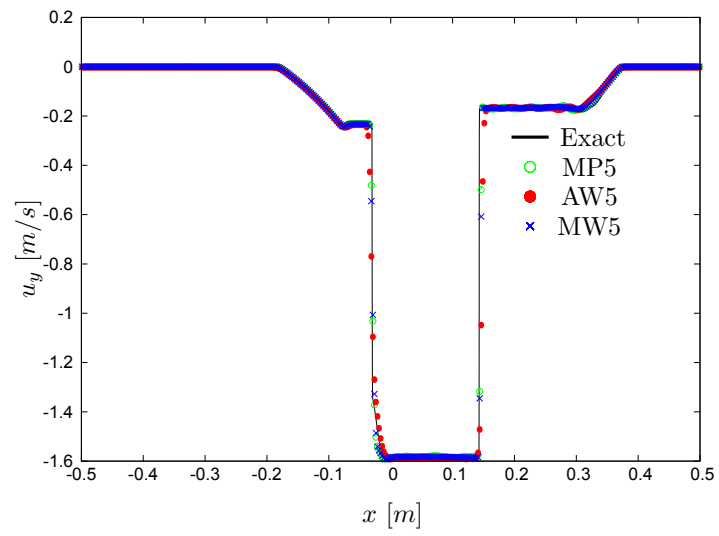


Figure 4.13: Velocity distribution of the y-component for the Brio-Wu[60] problem using MP5, AW5 and MW5, $\Delta x = 2.5 \times 10^{-3}m$, CFL = 0.4, runtime = 100ms

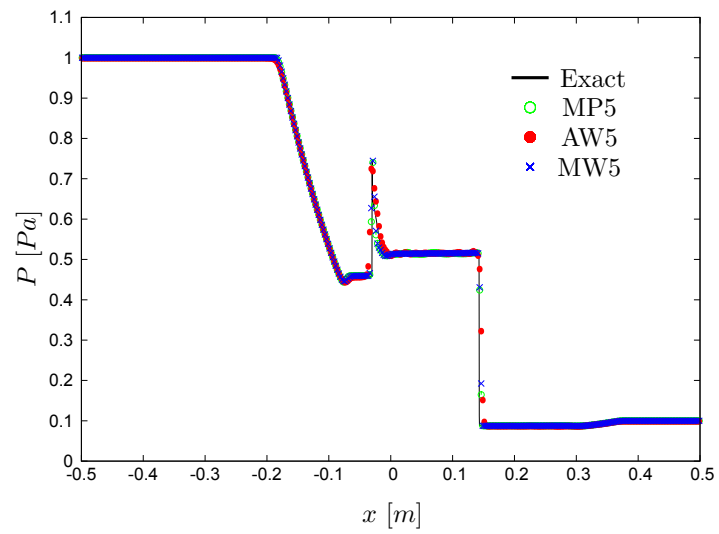


Figure 4.14: Pressure distribution of the Briou-Wu[60] problem using MP5, AW5 and MW5, $\Delta x = 2.5 \times 10^{-3}m$, CFL = 0.4, runtime = 100ms

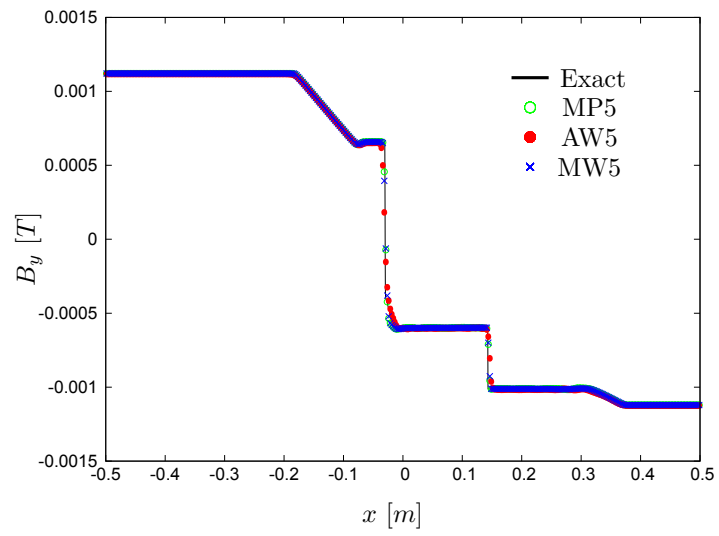


Figure 4.15: B_y distribution of the Brio-Wu[60] problem using MP5, AW5 and MW5, $\Delta x = 2.5 \times 10^{-3}m$, CFL = 0.4, runtime = 100ms

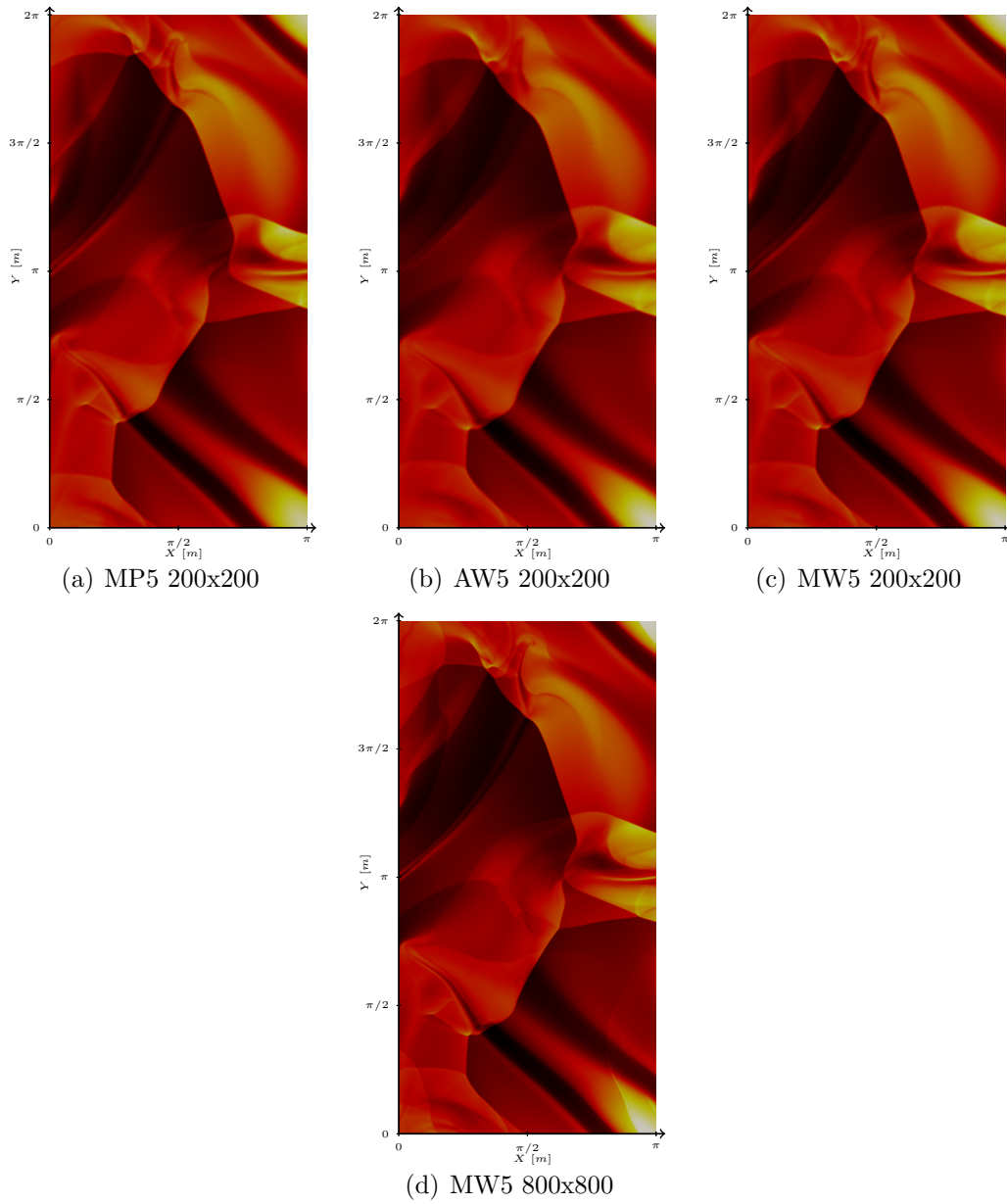



Figure 4.16: Density distribution for Orszag-Tang problem for $x \times y \in [0, \pi]m \times [0, 2\pi]m$ CFL = 0.4, runtime = 3 s, \min  \max .

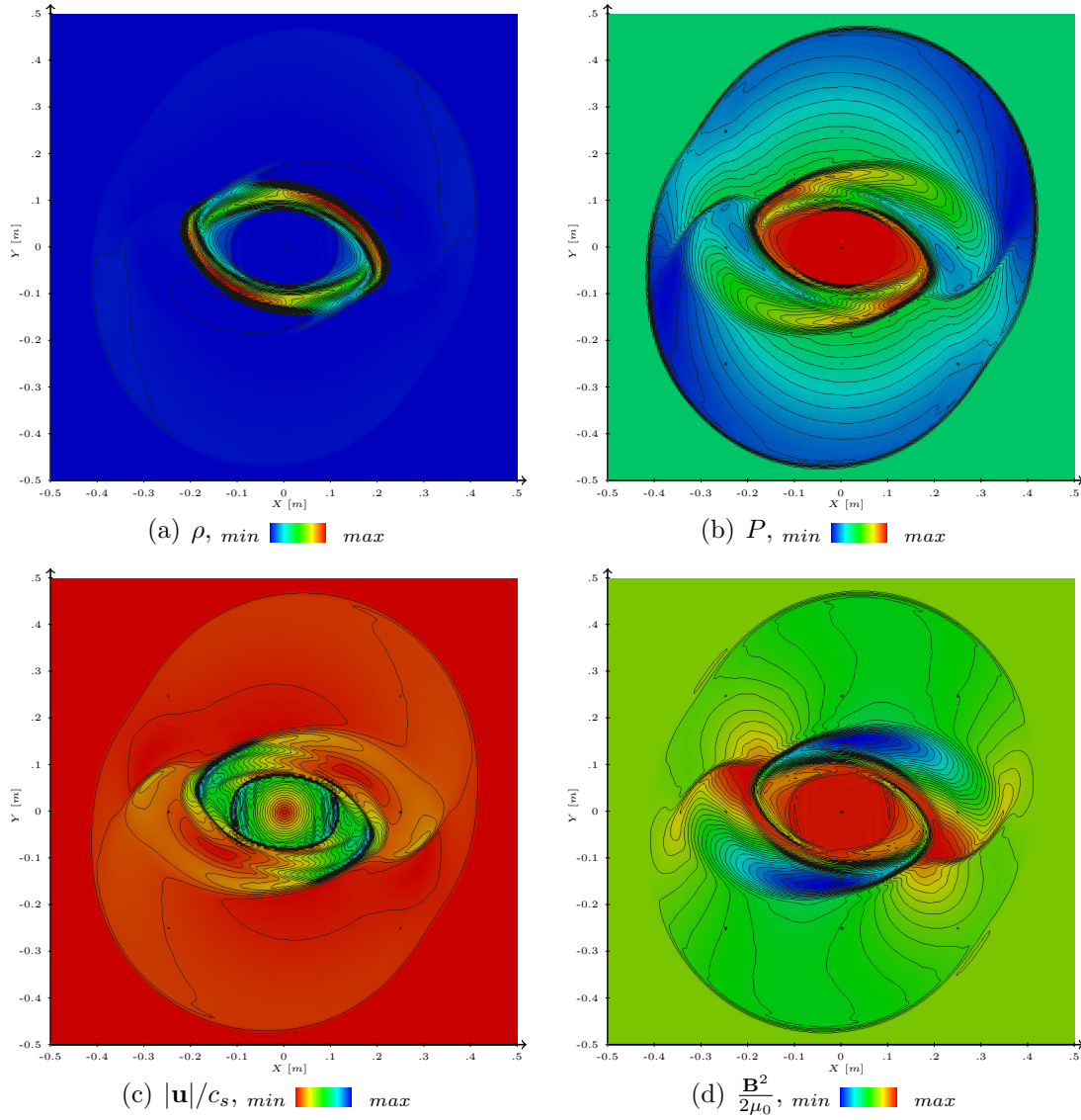


Figure 4.17: The density, thermal pressure, Mach number, and the magnetic pressure distributions at $t = 0.295s$ for Balsara's rotor problem. The solution was obtained using MW5 with a grid resolution of $\Delta x = \Delta y = \frac{1}{400}m$ and $CFL = 0.3$. The 30 contour lines are shown for the ranges $0.532 < \rho < 10.83 \frac{kg}{m^3}$, $.007 < P < 0.702 Pa$, $0 < \frac{|\mathbf{u}|}{c_s} < 3.64$, and $0.007 < \frac{\mathbf{B}^2}{2\mu_0} < 0.702 Pa$, as prescribed by Tóth [66].

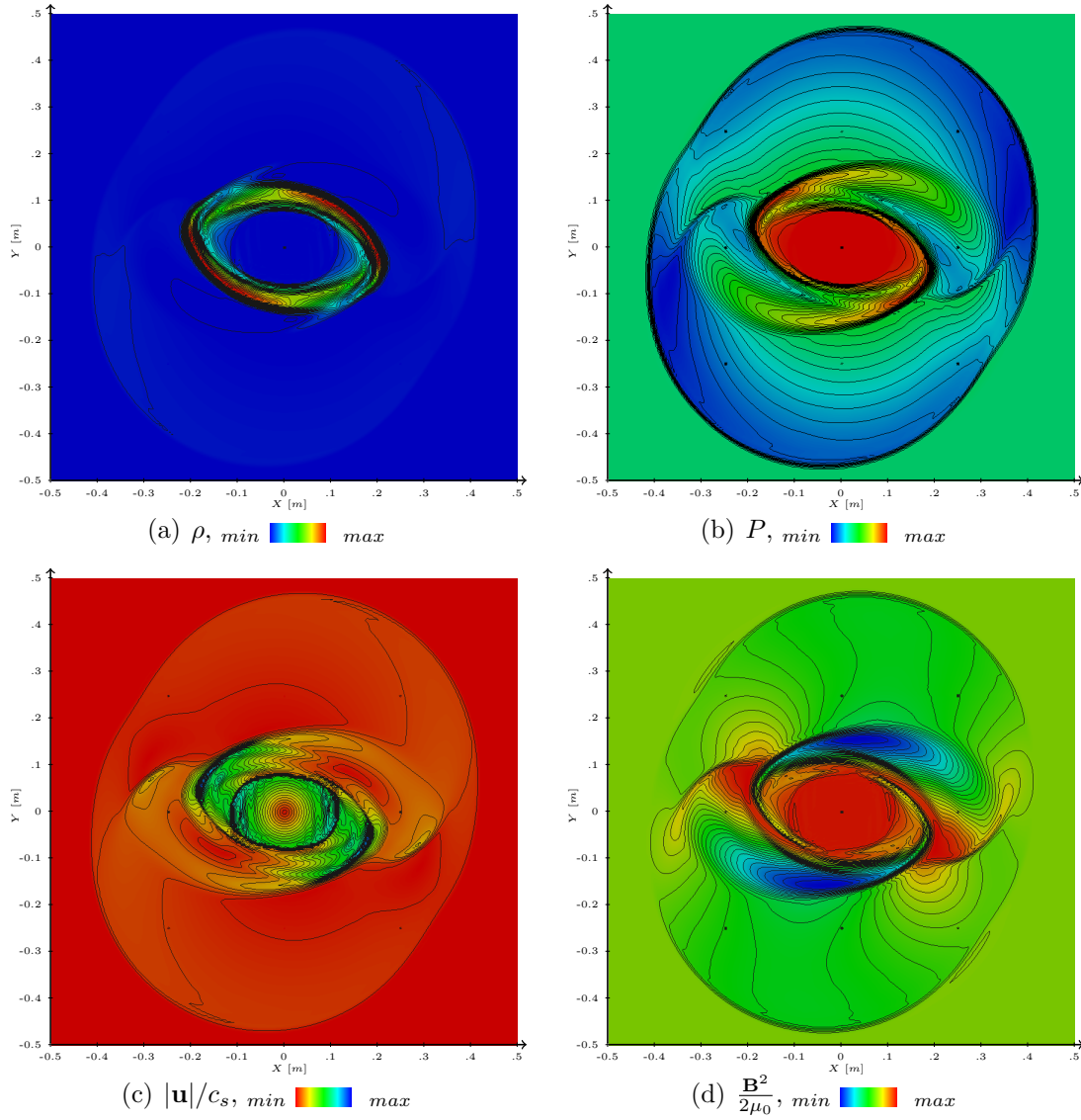


Figure 4.18: The density, thermal pressure, Mach number, and the magnetic pressure distributions at $t = 0.295s$ for Balsara's rotor problem. The solution was obtained using MP5 with a grid resolution of $\Delta x = \Delta y = \frac{1}{400}m$ and $CFL = 0.3$. The 30 contour lines are shown for the ranges $0.532 < \rho < 10.83 \frac{kg}{m^3}$, $.007 < P < 0.702 Pa$, $0 < \frac{|\mathbf{u}|}{c_s} < 3.64$, and $0.007 < \frac{\mathbf{B}^2}{2\mu_0} < 0.702 Pa$, as prescribed by Tóth [66].

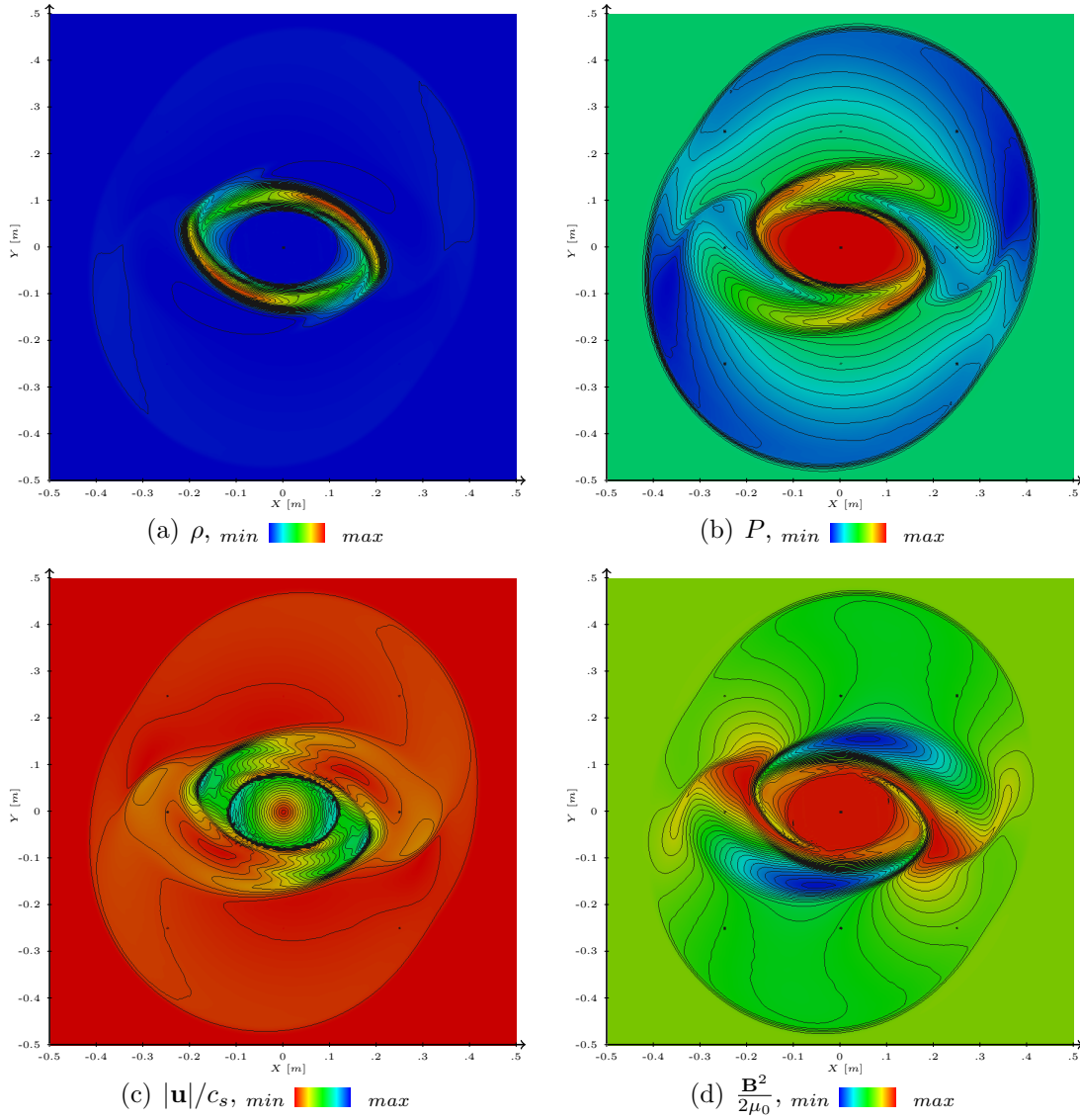


Figure 4.19: The density, thermal pressure, Mach number, and the magnetic pressure distributions at $t = 0.295s$ for Balsara's rotor problem. The solution was obtained using AW5 with a grid resolution of $\Delta x = \Delta y = \frac{1}{400}m$ and $CFL = 0.15$. The 30 contour lines are shown for the ranges $0.532 < \rho < 10.83 \frac{kg}{m^3}$, $.007 < P < 0.702 Pa$, $0 < \frac{|\mathbf{u}|}{c_s} < 3.64$, and $0.007 < \frac{\mathbf{B}^2}{2\mu_0} < 0.702 Pa$, as prescribed by Tóth [66].

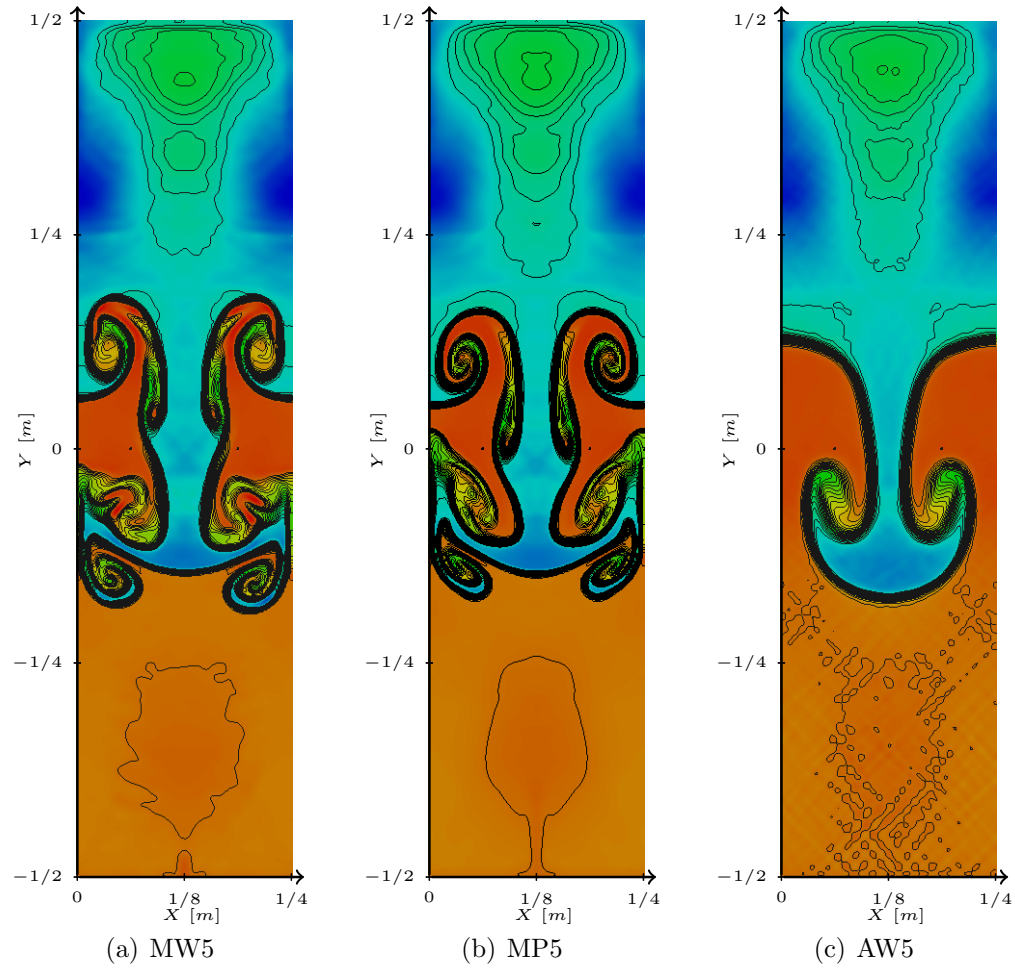


Figure 4.20: Growth of instability without the presence of a magnetic field at $t = 2s$ for MW5, MP5, and AW5 where $\Delta x = \Delta y = \frac{1}{400}m$. Density distribution with 20 density contours between 1 2.

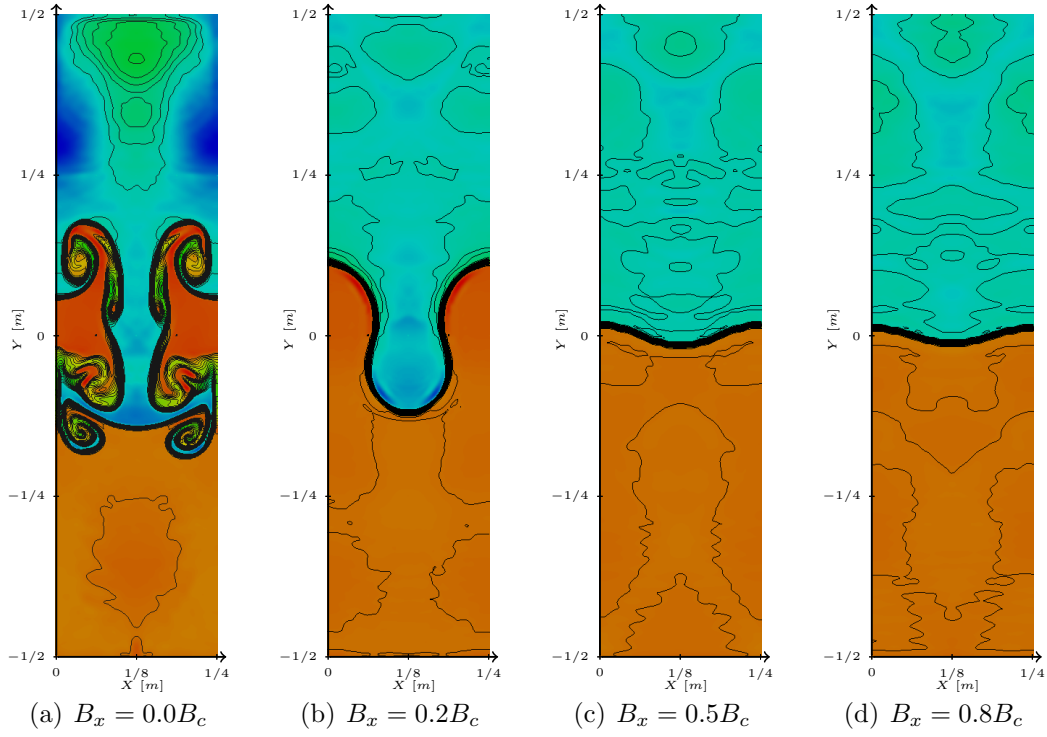



Figure 4.21: The impact of the tangential magnetic field, B_x , on the growth of instabilities at $t = 2s$ where $\Delta x = \Delta y = \frac{1}{400}m$ and $B_c = 0.5T$ using MW5. Density distribution with 20 density contours between 1  2.

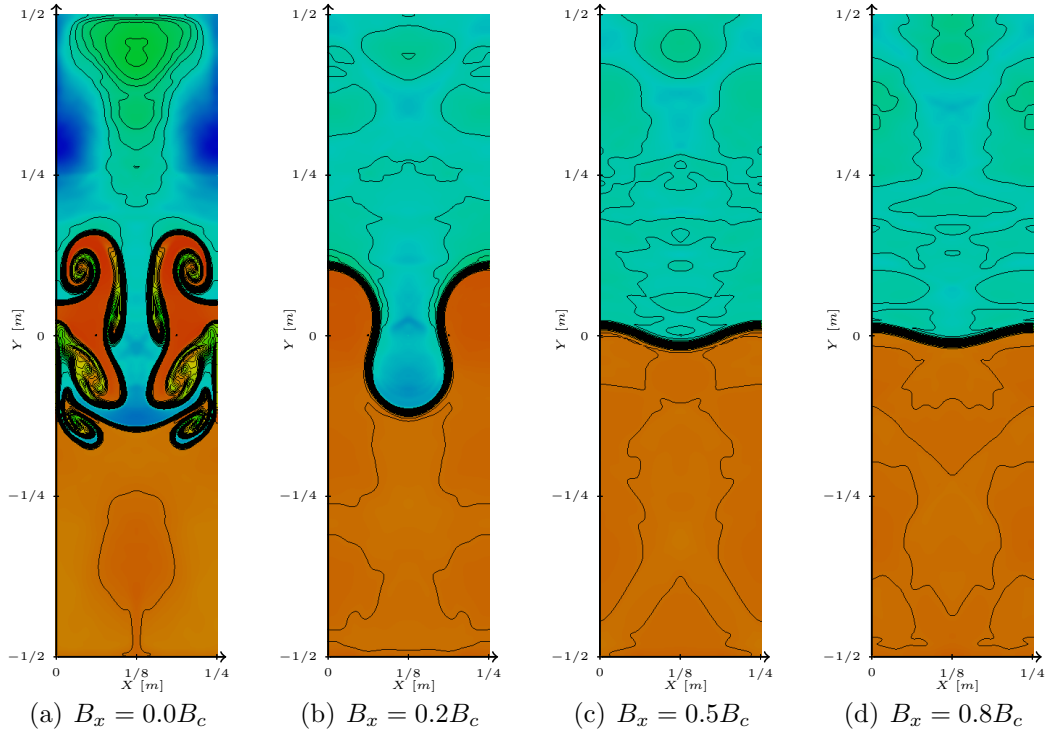



Figure 4.22: The impact of the tangential magnetic field, B_x , on the growth of instabilities at $t = 2s$ where $\Delta x = \Delta y = \frac{1}{400}m$ and $B_c = 0.5T$ using MP5. Density distribution with 20 density contours between 1  2.

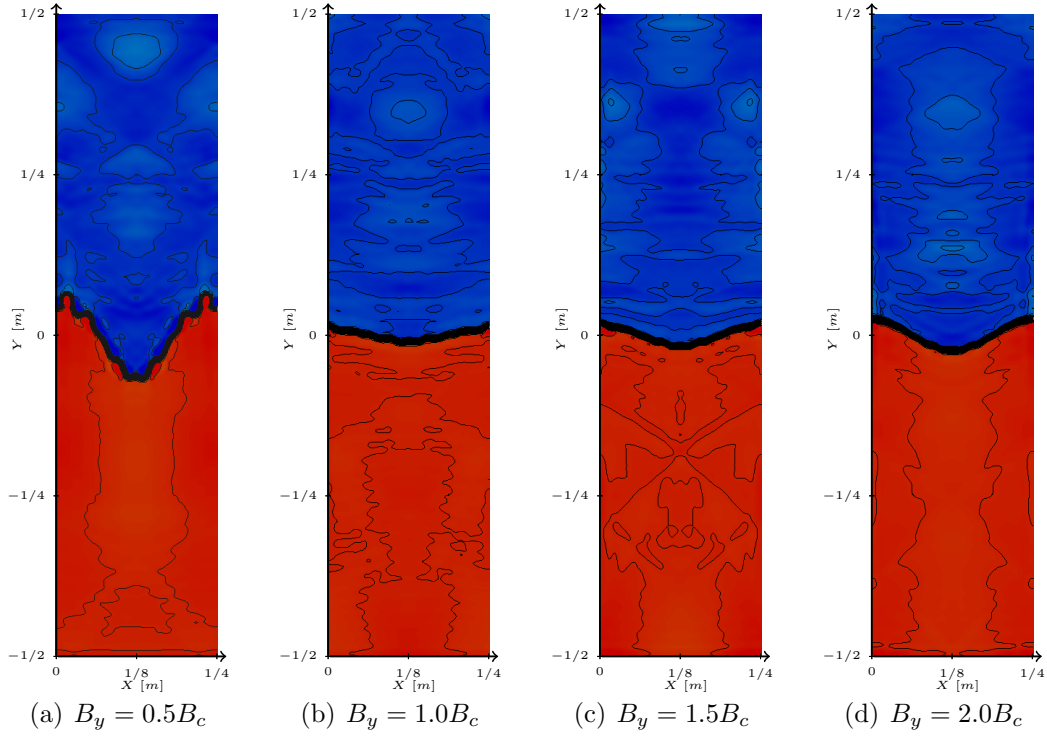



Figure 4.23: The impact of the normal magnetic field, B_x , on the growth of instabilities at $t = 2s$ where $\Delta x = \Delta y = \frac{1}{400}m$ and $B_c = 0.5T$ using MW5. Density distribution with 30 density contours between 1  2.

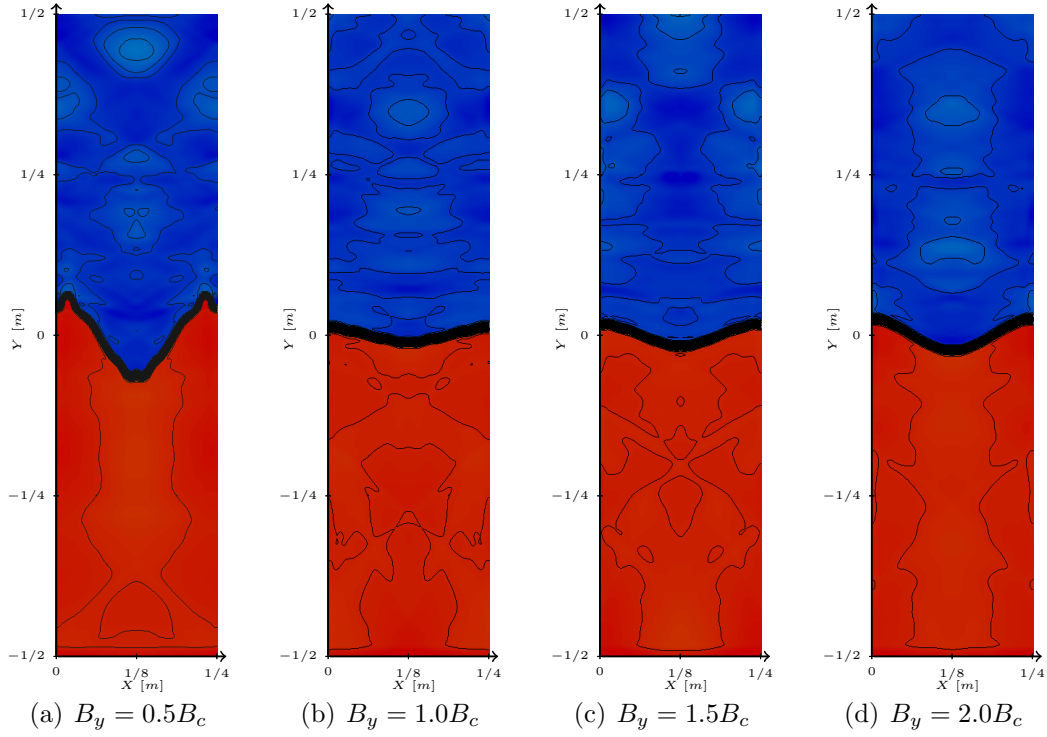

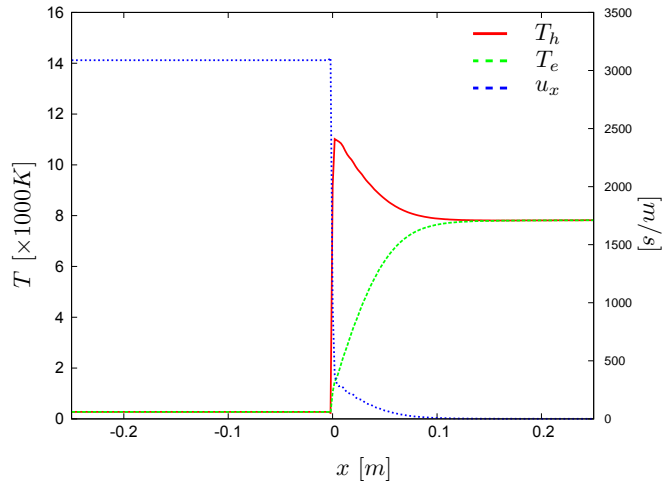
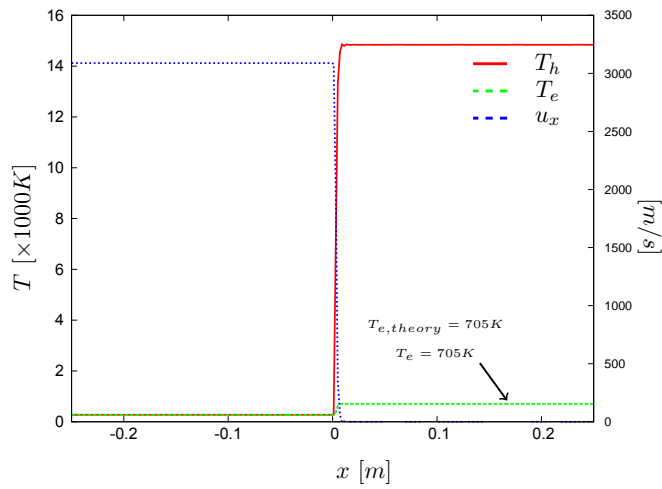


Figure 4.24: The impact of the normal magnetic field, B_x , on the growth of instabilities at $t = 2s$ where $\Delta x = \Delta y = \frac{1}{400}m$ and $B_c = 0.5T$ using MP5. Density distribution with 30 density contours between 1  2.



(a) With T_e relaxation



(b) Without T_e relaxation

Figure 4.25: Mach 10 fully ionized Argon shock in shock reference frame with (a) and without (b) T_e relaxation where $\Delta x = \frac{1}{500}m$ using MP5.

CHAPTER 5

Simplified Approach for PDRIME Simulations

Now that the various numerical schemes have been validated, we first investigate the performance of a PDRE flight configuration, and later the PDRIME, using a simplified non-reactive model, Equation 2.5. In the simplification, we assumed that all reactants (H_2 and O_2) in the combustion chamber have been consumed, leaving just products (H_2O) and the seeded Cesium. We also assumed that the detonation has left the chamber. This model has been shown to replicate blowdown conditions in a rocket nozzle reasonably accurately, as shown in Figure 5.1 from the work by Cambier. Following Cambier’s blowdown model[67], we initialize the combustion chamber with the post-combustion and post-detonation conditions:

$$\begin{cases} \hat{P}_0 &= 100 \text{ atm} \\ \hat{T}_0 &= 3000 \text{ K} \\ \hat{\rho}_0 &= \frac{\hat{P}_0}{R\hat{T}_0} \end{cases}$$

Rather than simulating the combustion chamber, the combustion chamber is modeled as a “reservoir” whose conditions (P_0 , T_0) temporally evolve as prescribed by Cambier’s blowdown equations[67]:

$$P_0 = \hat{P}_0 [f(t)]^{\gamma/(\gamma-1)} \tag{5.1a}$$

$$\rho_0 = \hat{\rho}_0[f(t)]^{1/(\gamma-1)} \quad (5.1b)$$

$$T_0 = \hat{T}_0[f(t)] \quad (5.1c)$$

where $f(t) = \frac{1}{1+\nu t}$ and ν is the blowdown frequency and is equal to 87.5 Hz for this particular case. Now, by using the isentropic relations, we can determine the conditions at the PDRE throat as a function of time. With this simplification, our computational domain no longer needs to include the combustion chamber, this is illustrated in Figure 5.2. Next, we assume that the back pressure, the atmospheric pressure P_{atm} , is sufficiently low, so that there is no back flow into the nozzle. Pressures at the altitudes we are simulating are high enough that even with the expansion in the nozzle, the nozzle exit pressure is greater than the atmospheric pressure, $P_{exit} > P_{atm}$. Because of the extremely high flight altitudes (altitude $\approx 15 - 20$ km), the PDRE performance does not have any significant variance with regard to altitude.

Next, we extend this simplified model of the PDRE to the PDRIME with a ‘Magnetic Piston’. In this extension, we assume that if the temperature is greater than 3000K; the conductivity is a constant non-zero value, in this particular case $\sigma = 1000mho/m$ in the nozzle and $\sigma = 500mho/m$ in the bypass tube. The nozzle impulse contribution is calculated the same way as the PDRE, while bypass tube impulse contribution is calculated by integrating the Lorentz force over the cycle duration, as follows:

$$I_{bypass} = \int_0^t (\mathbf{j} \times \mathbf{B})_x d\tau \approx \int_0^t \sigma u B_z (K_x - 1) d\tau \quad (5.2)$$

where all variables have been previously defined. We also assumed a constant magnetic field for both the nozzle and bypass section of the PDRIME, as illustrated in Figure 1.7. The configuration called ‘NG’ refers to the PDRE with energy extraction in the nozzle (for use of the ‘nozzle generator’), so, as expected there is a drop in impulse as shown in Figure 5.3. A promising concept postulated by Cambier[40] involving the PDRE with ‘Magnetic Piston’ was also simulated, but due to the lack of energy supplied to the ‘Magnetic Piston’ by the generator, this flight configuration could not be effectively utilized. In Chapter 7, the true energy ‘cost’ of the chamber piston will be investigated by exploring the nature of the ionized gas and chemical kinetics subjected to the Lorentz force. We will now explore other PDRE flight configurations which will build off of the PDRE with ‘NG’ concept in order to further optimize the PDRE.

5.1 PDRIME with Bypass Configurations

There were multiple flight configurations as well as different flight condition tested. Using the standard combustion chamber condition, nozzle, and nozzle generation configuration we were able to test various configurations of the Bypass Tube. Figure 5.3 shows the performance of the standard PDRIME configuration under various flight condition as they compare the performance of a PDRE, which we will refer to as the baseline. With this configuration, there are some marginal performance gains above the baseline case. The standard PDRIME utilizes a constant magnetic field, which is active only if the fluid temperature is greater than 3000K and the fluid is moving in the stream-wise direction. When activated, a constant magnetic field of 3T is applied to the applicable fluid.

5.2 Temporal/Temperature Controllers of the Magnetic Field

We performed component evaluations for the various flight configurations with different assumptions. This involved examining the net energy consumed compared to impulse gained or lost by a particular component of the flight configuration. During the course of component performance evaluation, it was determined that an MHD bypass accelerator, where a “piston” like acceleration was applied in the bypass section as done for the magnetic chamber piston, was under-performing relative to the nozzle which is shown in Figure 5.4. Zeineh[33] also saw the same under-performance in his 2-D simulations. The bypass available energy, ΔE_{gen} , is being applied to the bypass over approx 0.1 ms within a relatively small volume, dV , wherein most of the available energy is directed towards Joule heating rather than accelerating the fluid. This leads to large temperature spikes and little impulse increase.

From $E = \int c_v dT + \frac{1}{2}\rho v^2$ with introduction of Energy at constant volume

$$\Delta E_{\text{gen}} = c_v \Delta T + \frac{1}{2}\rho \Delta v^2 \quad (5.3)$$

We can see where and how the energy is being used in the bypass. ΔE_{gen} is a fixed amount of energy produced by the MHD generator in the nozzle. $c_v \Delta T$ represents the amount of energy that is converted to internal energy, which for our simplified model of constant heat capacity is represented by a rise in temperature. Lastly, $\frac{1}{2}\rho \Delta v^2 \propto \Delta KE$ represents the amount of kinetic energy which is imparted upon the fluid, and since energy is introduced at constant volume, ρ remains constant, so this change in kinetic energy is directly related to our change in impulse, $I \propto \Delta KE^{\frac{1}{2}}$. In order to reduce the temperature spikes and thus increase the impulse, when applying MHD to the bypass, one must regulate the ΔE_{gen} available for use by the bypass accelerator. To control this energy reintroduction, one must either control the conductivity of the

fluid, σ , or the strength of the magnetic field, B , acting on the bypass. Since it is impractical if not impossible to dynamically control the conductivity in the bypass, we chose the latter.

Our first approach is to scale the maximum magnetic field in the bypass with time, for which we prescribe a simple algorithm. First, the magnetic field is initially zero until the initiation time, t_0 , when at least one grid cell in the bypass meets the normal criteria for MHD accelerator: $T_i > 3000K$ and $u_i > 0$. The magnetic field is then scaled with the maximum field applied, B_0 . The magnetic field in the bypass is prescribed as follows:

$$B(t) = \begin{pmatrix} 0 & t < t_0 \\ \Pi(t) \cdot B_0 & t_0 < t < t_0 + \Delta t \\ B_0 & t > t_0 + \Delta t \end{pmatrix} \quad (5.4)$$

B_0 : Maximum Magnetic Field Strength

t_0 : time at which $T > 3000K$ and $u > 0$

Δt : ramp up time

$\Pi(t)$: Magnetic Field Scaling Factor

We ran a series of simulations incorporating this prescribed magnetic field, adjusting both $\Pi(t)$ and Δt as a means of “open loop” control. Our tests utilized three different magnetic field scaling factors:

$\Pi(t) = (\frac{t-t_0}{\Delta t})$ linear scaling where $B \propto t$

$\Pi(t) = (\frac{t-t_0}{\Delta t})^{\frac{1}{2}}$ energy scaling ($Energy \propto B^2$), where $B \propto t^{\frac{1}{2}}$

$\Pi(t) = (\frac{t-t_0}{\Delta t})^n$ power law scaling ($n = 3$) where $B \propto t^n$

Figure 5.5 compares the evolution of these magnetic field scaling factors with time. Figure 5.6 shows that the temporally varied bypass magnetic field with the “open loop” control shown in Equation 5.4 has the same marginal performance improvements performance as the standard bypass configuration. The optimal configuration of the bypass magnetic field is dictated by the flight conditions which include flight Mach number and altitude.

In our next approach, we return to the same problem of controlling the rate at which energy is consumed by the bypass. It was previously stated, that it was impractical to dynamically control the conductivity in the bypass, σ . When evaluating the nature of the conductivity of a fluid in the current regime, Equation 2.30 shows the conductivity’s strong dependency on the temperature, T . Rather than dynamically controlling the conductivity of the fluid, we modeled the behavior of an ‘ideally’ conductive fluid by prescribing its dependency to temperature, $\sigma = \sigma(T)$. We wish to implement this “closed loop” controller in the bypass in order to scale the magnetic field, B_i , with the sensible local temperature in the bypass, T_i . The normal criteria for MHD acceleration are still utilized. The bypass magnetic field “feedback” function is prescribed as follows:

$$B(T) = \begin{pmatrix} 0 & T < T_{min} \\ \Theta(T) \cdot B_0 & T_{min} < T < (T_{max} - T_{ref}) \\ B_0 & T > (T_{max} - T_{ref}) \end{pmatrix} \quad (5.5)$$

B_0 : Maximum Magnetic Field

T_{min} : Minimum Temperature (3000K)

$\Theta(T)$: Magnetic Field Scaling Factor

$$\Theta(T) = \left(\frac{T - T_{\text{ref}}}{T_{\text{max}} - T_{\text{ref}}} \right) \text{ linear scaling } B \propto T$$

T_{ref} and T_{max} are adjusted to optimize performance

The term “feedback” here is used in the sense that temperature is measured, and the magnetic field is adjusted according to Equation 5.5. Figures 5.7 through 5.10 show that the “closed-loop” controller in the bypass tube is able to match the performance of the standard configuration at a flight altitude of 25km and $T_{\text{max}} < 8 \times 10^3 K$. But at other flight altitudes, this “closed loop” controller falls short. The $B(T)$ model is much more feasible for implementing into a physical system because of the temperature dependency of many of the parameters that contribute to impulse from the bypass accelerator, e.g., $\sigma(T)$ and $B(T)$.

5.3 PDRIME with 2D Bypass Configuration

There was further examination of the PDRIME with various configurations performed in Zeineh[33] and Zeineh et al.[34]. In their study, Zeineh et al. found the flight configuration of the PDRIME at altitudes 20, 25, and 30 km at relatively low Mach numbers ($M \leq 5$) had significant performance increases over the baseline PDRE. Figures 5.11 through 5.13 show some of the performance gains of the PDRIME at different altitudes with the optimal bypass section lengths ($L_{\text{bypass}} = 3, 4, \text{ and } 6 \text{ m}$) demonstrated in [34]. While the results of Zeineh’s multidimensional simulations were quite promising, the effects of complex kinetics (i.e. hydrogen-air chemistry and ionization process) were not rigorously investigated. The constant conductivity assumption does not allow for the “closed loop” evolution of the conductivity (i.e. Joule heating further ionizing fluid), therefore in Chapter 7 we will

discuss and examine the effects of MHD when the conductivity is described more accurately via Equation 2.27.

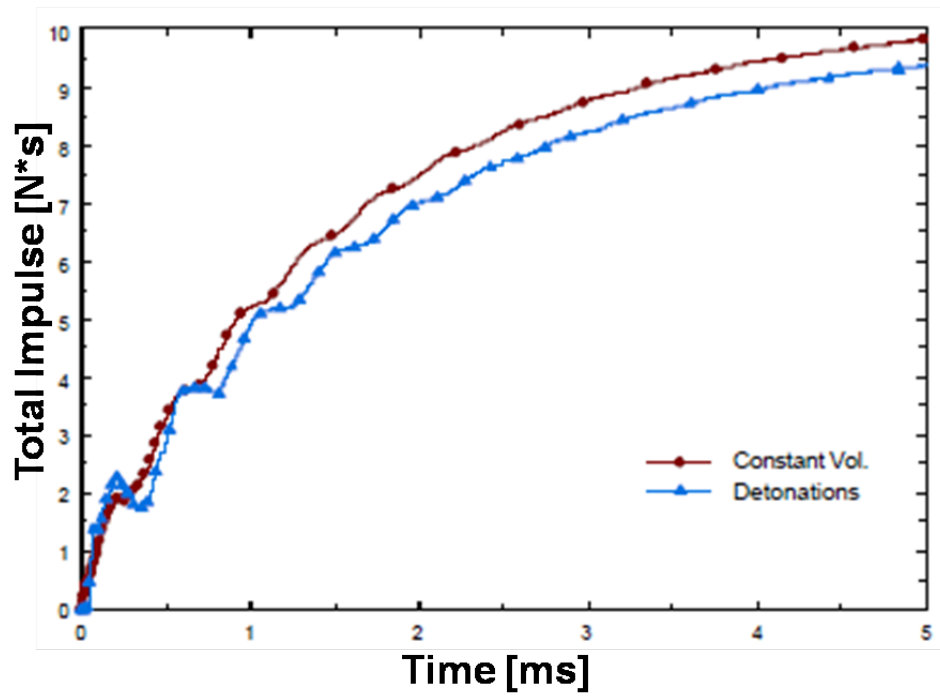


Figure 5.1: Variation in impulse for a PDRE. Results are shown from a full quasi-1D transient PDRE simulation and a cycle approximated by a constant volume reaction and a blow-down period(from Cambier[67])

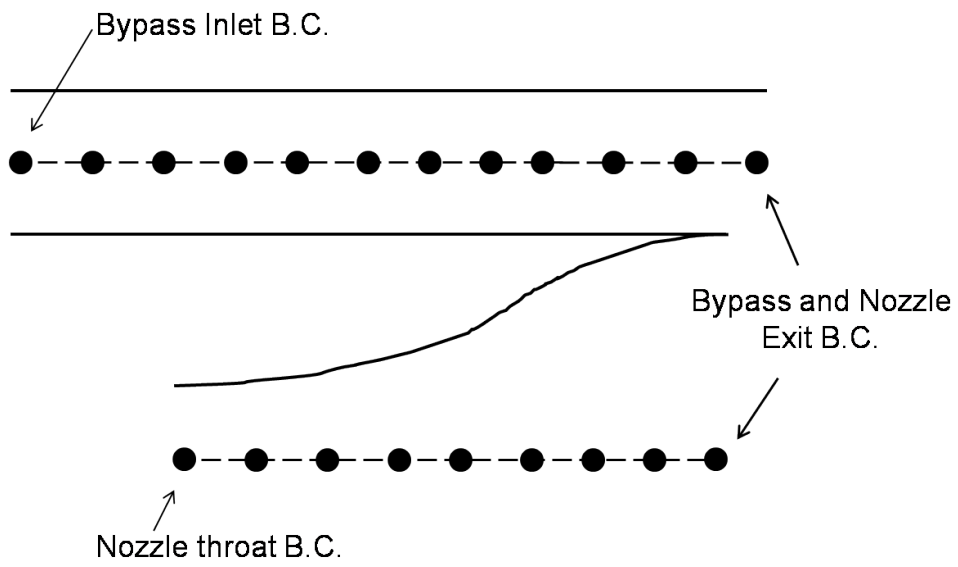


Figure 5.2: Quasi 1D Computational Domain, where the Bypass and Nozzle inlet and exit boundary conditions are shown

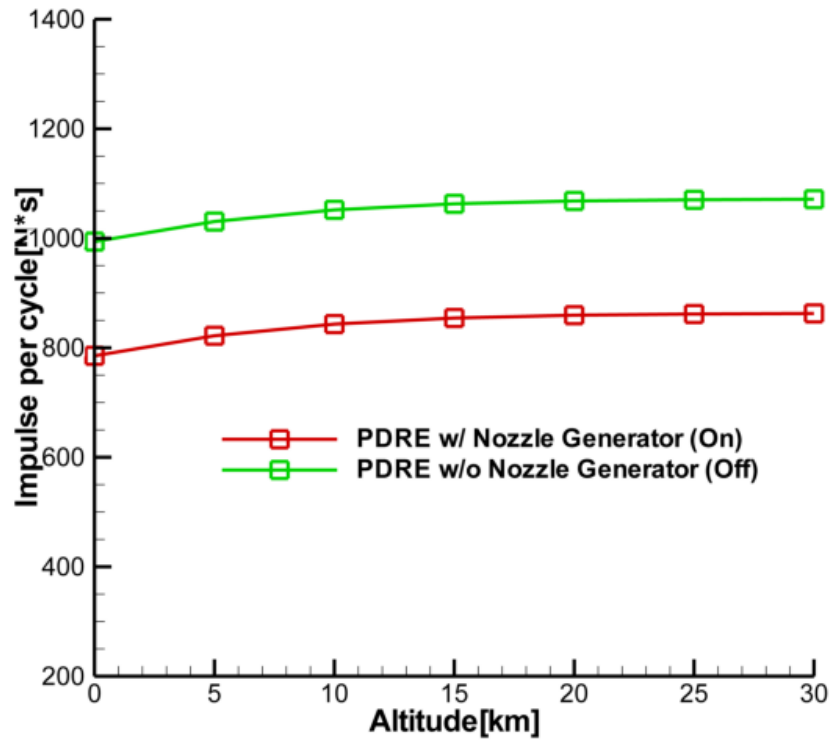


Figure 5.3: Quasi 1D Performance: Impulse Loss in Nozzle Energy Generation with H_2O product

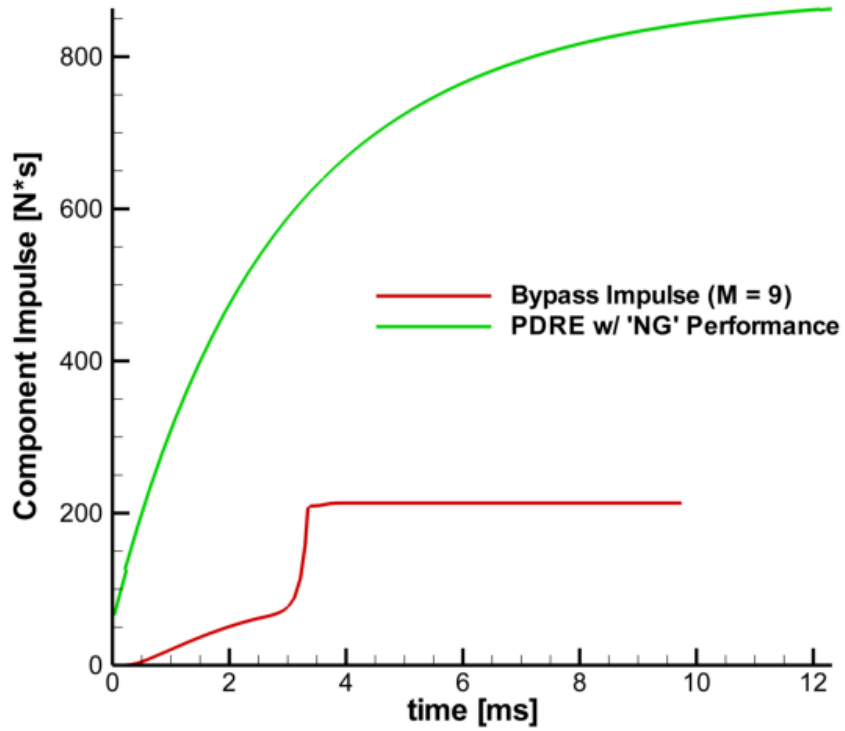


Figure 5.4: Quasi 1D Component Performance: Bypass vs. Nozzle Impulse at $M = 9$ and Alt: 25km with H_2O product

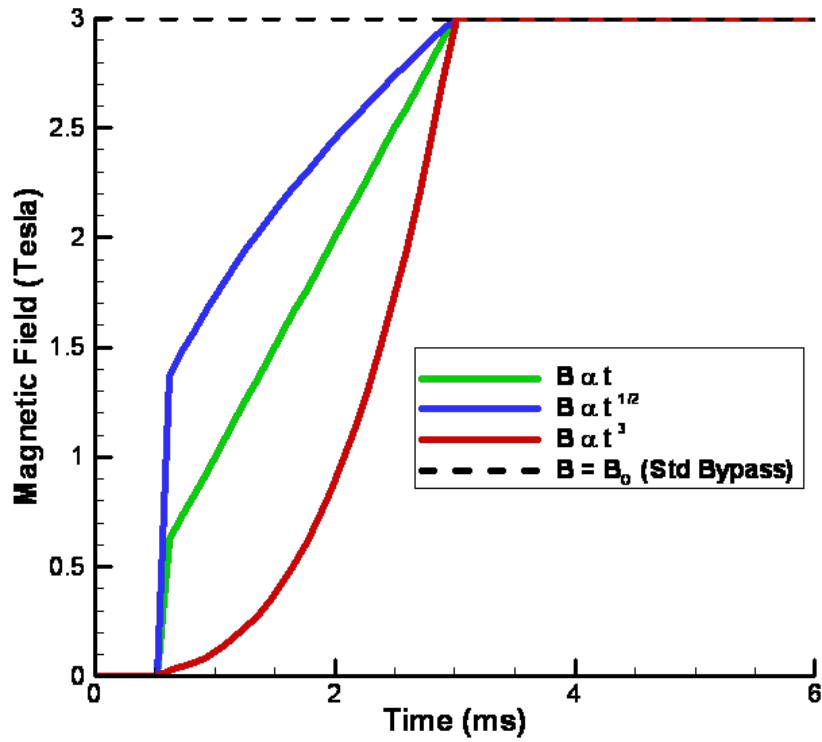


Figure 5.5: Magnetic Field Strength, B , as a function of time, using various Magnetic Field Strength functions, $\Pi(t)$

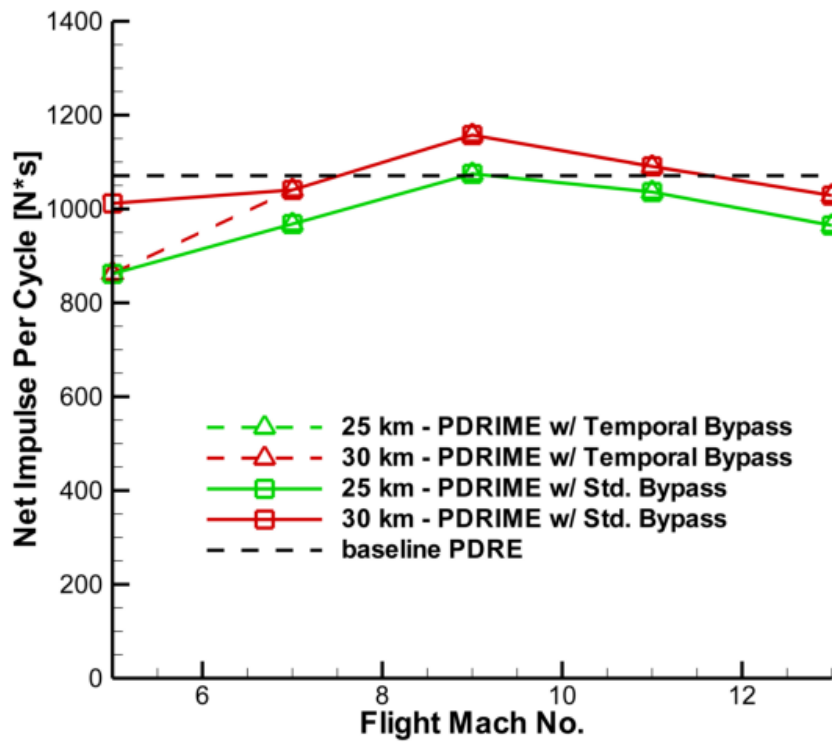


Figure 5.6: PDRIME: effects of flight Mach number. Magnetic Field, $B(t) \sim t^2$

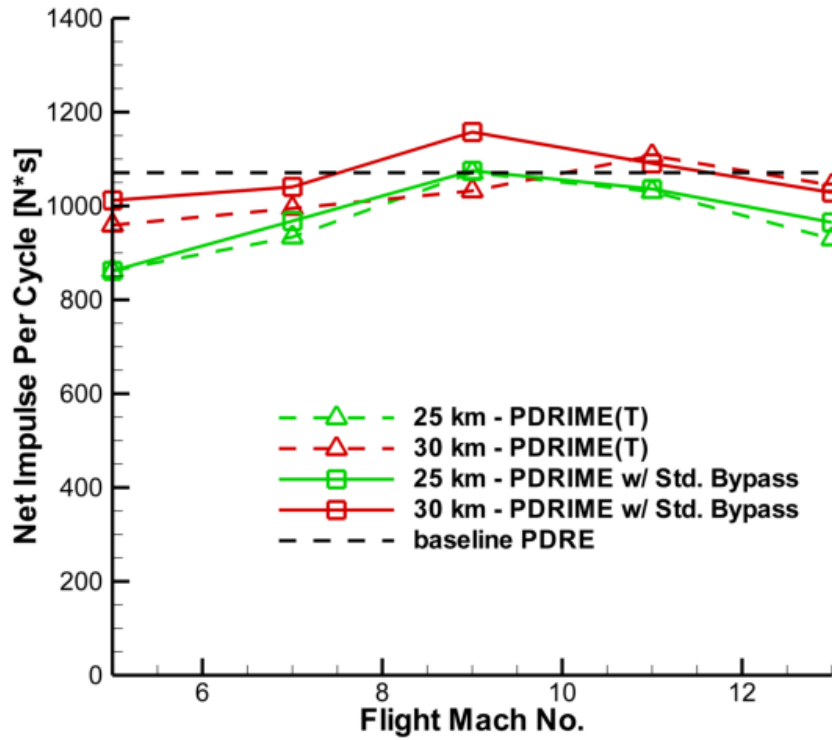


Figure 5.7: PDRIME with Chamber Piston: effects of flight mach number. Magnetic Field $B(T)$, $T_{\text{ref}} = 0K$ and $T_{\text{max}} = 6 \times 10^3 K$

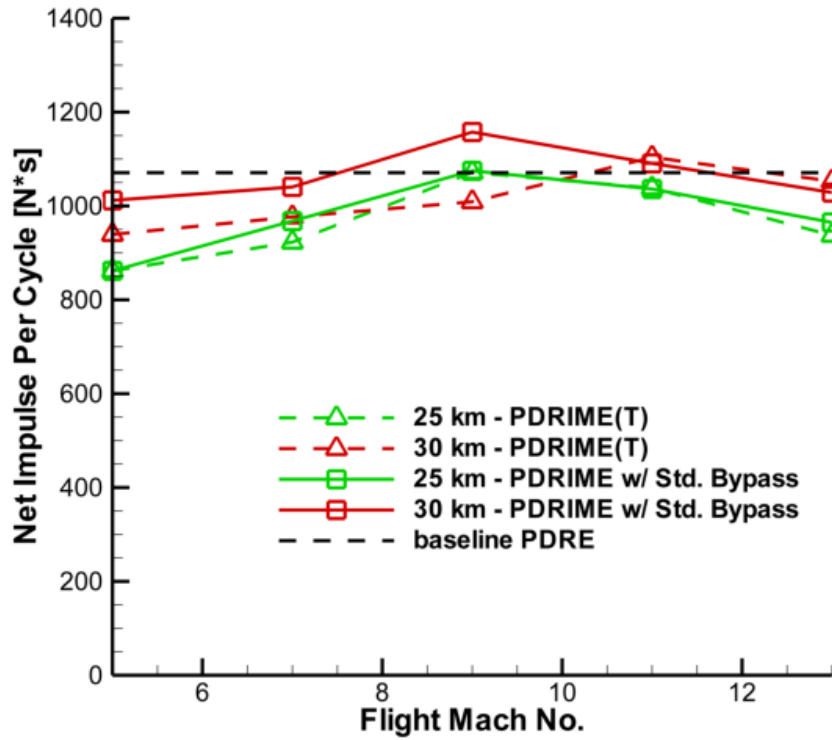


Figure 5.8: PDRIME: effects of flight mach number. Magnetic Field $B(T)$, $T_{\text{ref}} = 0K$ and $T_{\text{max}} = 7 \times 10^3 K$

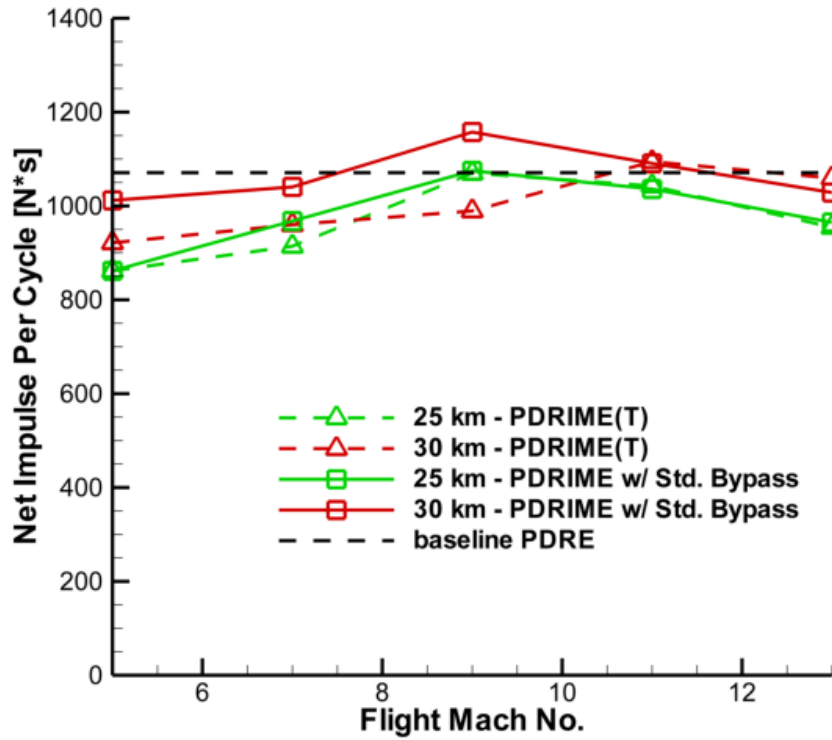


Figure 5.9: PDRIME: effects of flight mach number. Magnetic Field $B(T)$, $T_{\text{ref}} = 0K$ and $T_{\text{max}} = 8 \times 10^3 K$

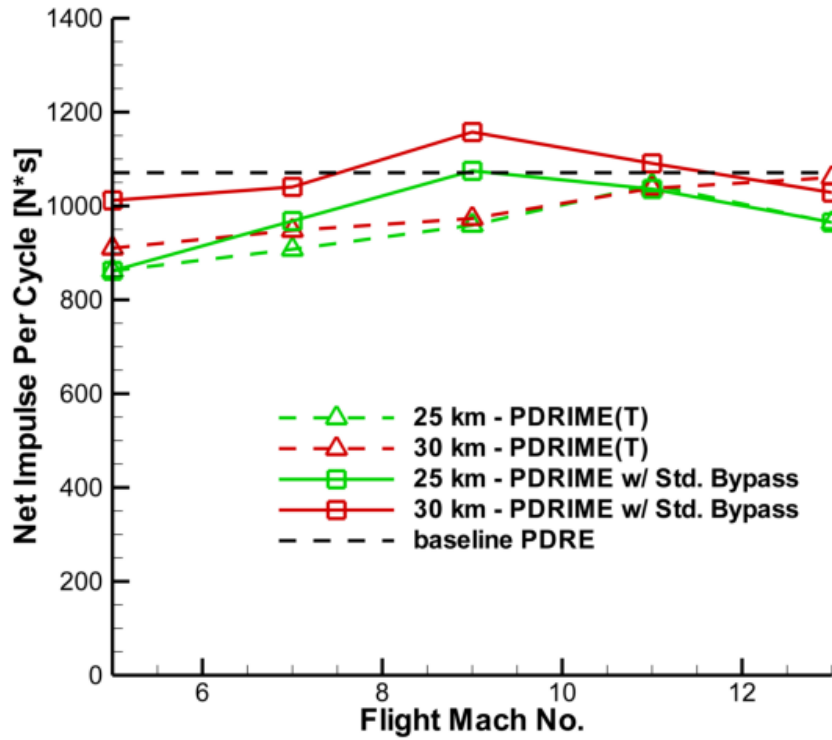


Figure 5.10: PDRIME: effects of flight mach number. Magnetic Field $B(T)$, $T_{\text{ref}} = 0K$ and $T_{\text{max}} = 9 \times 10^3K$

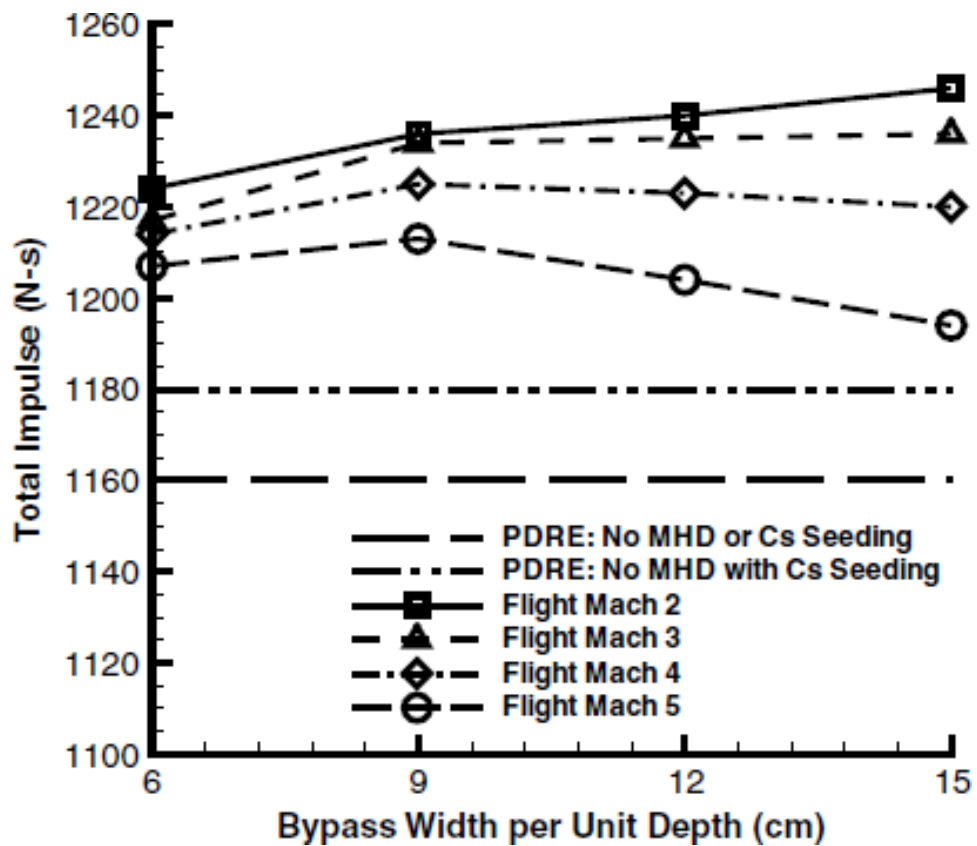


Figure 5.11: PDRIME impulse per cycle at 20 km plot against various Mach numbers and bypass area per unit depth. The chamber is initially seeded with 0.5% cesium by number at an initial temperature of 3000 K. The bypass length is $L_{bypass} = 3$ m and is seeded with 0.1% cesium by number. (from Zeineh et al.[34])

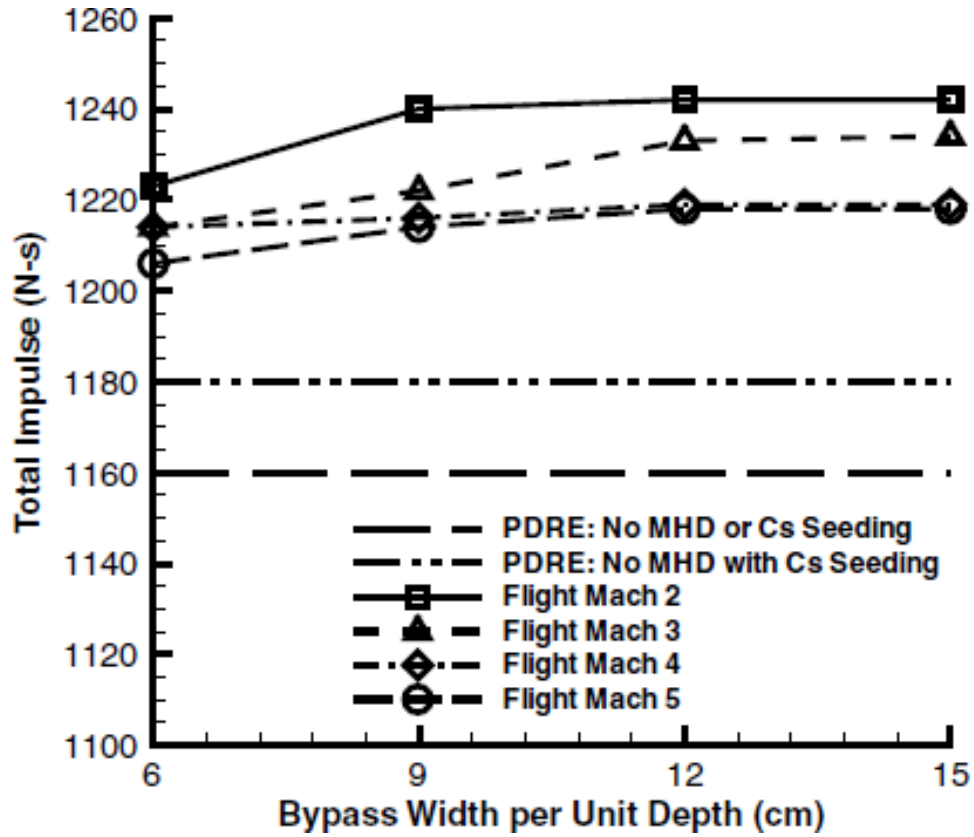


Figure 5.12: PDRIME impulse per cycle at 25 km plot against various Mach numbers and bypass area per unit depth. The chamber is initially seeded with 0.5% cesium by number at an initial temperature of 3000 K. The bypass length is $L_{bypass} = 4$ m and is seeded with 0.1% cesium by number. (from Zeineh et al.[34])

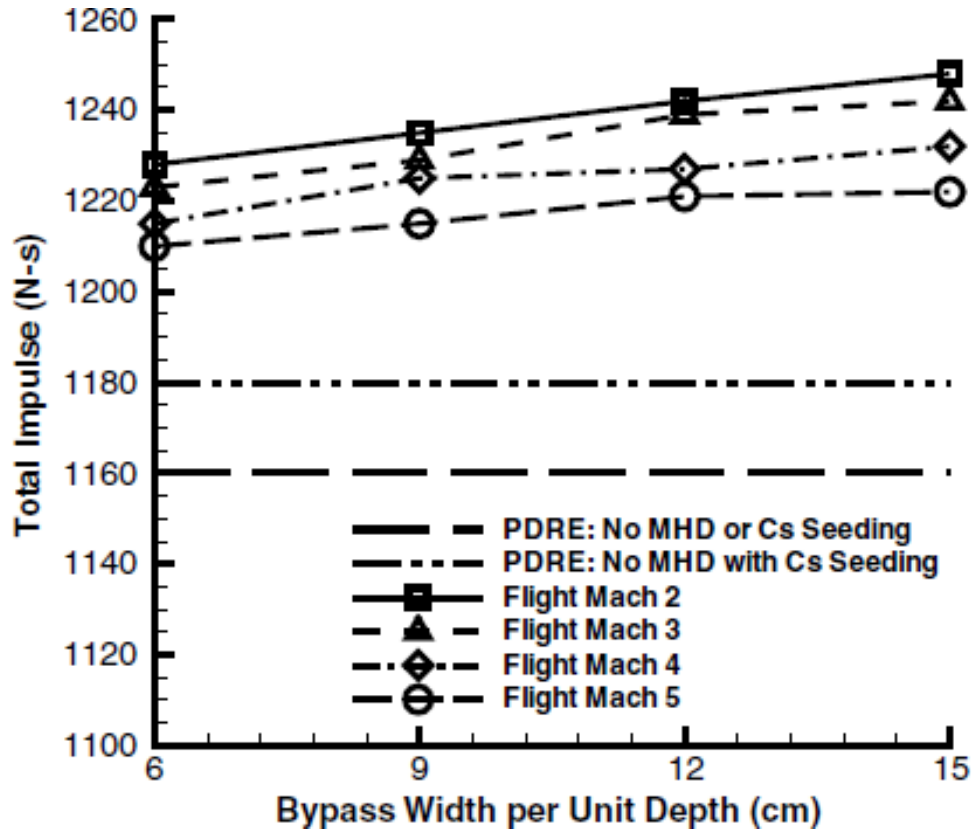


Figure 5.13: PDRIME impulse per cycle at 30 km plot against various Mach numbers and bypass area per unit depth. The chamber is initially seeded with 0.5% cesium by number at an initial temperature of 3000 K. The bypass length is $L_{bypass} = 6$ m and is seeded with 0.1% cesium by number. (from Zeineh et al.[34])

CHAPTER 6

Detonation Stability Phenomena

This chapter was taken with slight modification from the article “Stability of flame-shock coupling in detonation waves: 1D dynamics”, published in the journal Combustion Science and Technology [68].

6.1 Ignition and Instabilities

Direct initiation of the 1D detonation and the ensuing instabilities are now examined, in part for fundamental understanding but also to establish a baseline against which the effects of MHD may be compared in Chapter 7. In this study, a chamber is filled with a stoichiometric mixture of H_2 and air (temperature 300 K and pressure 1 atm), and ignition is achieved by setting a region adjacent to an end-wall of the simulated shock tube at high pressure (40 atm for most computations) and temperature (1500 K), as a simulated spark. This direct initiation is preferable to a deflagration-to detonation transition (DDT), since the latter is much more sensitive to initial conditions and grid resolution, it requires inclusion of species diffusion, and it requires a very long computational domain to reproduce both the DDT and the subsequent evolution of the detonation. Nevertheless, even direct initiation is sensitive to initial conditions and resolution. The requirements to achieve detonation

ignition with the MP5 scheme include a grid cell size Δx of less than $50 \mu\text{m}$ and a distributed simulated spark region (of length ℓ_{spark} ranging from 0.25 to 0.5 cm) with sufficiently high pressure. For example, Figure 6.1(a) is an x-t diagram illustrating the pressure contours of a spark-ignited mixture with initial pressure 20 atm, $\ell_{spark} = 0.25$ cm, and grid size $\Delta x = 50 \mu\text{m}$, which does not achieve detonation. In contrast, Figure 6.1(b) illustrates contours of the same mixture and grid resolution but with a higher spark pressure, 50 atm, and larger region ($\ell_{spark} = 0.5$ cm), which does achieve detonation. The constraints on initial spark conditions can be related to the concepts of minimum energy and kernel size for direct initiation [69]; similar studies by Eckett et al.[20] and He & Karagozian[70] indicate there are both pressure and temperature requirements for the spark. With an understanding of the range of satisfactory kernel/spark sizes and pressures, we fix the spark conditions to consistently achieve a rapid initiation, in order to remove the dependence of the long-term dynamics on the initial conditions. For the remainder of the studies in this chapter, the spark conditions are $\ell_{spark} = 0.25$ cm, $P_{spark} = 40$ atm, and $T_{spark} = 1500$ K.

The successful detonation initiation event proceeds in two phases. First, the gas in the spark region rapidly burns and increases the pressure, in a nearly constant-volume combustion process. This high pressure generates a strong shock which propagates into the unburnt mixture, which itself is ignited after a time delay and rapidly burns, starting from the region closest to the spark. In a scenario described as the SWACER mechanism [71], the combustion wave is amplified as it overtakes the leading shock, and the coalescence of the two fronts leads to extremely high peak pressures for a very short time. This event is easily identified in the trace of the peak pressure versus time as shown, for example, in Figure 6.2, and is referred to hereafter as the “re-explosion” event, the first explosion having taken place within the initial spark

region. Two different grid sizes are used in Figures 6.2(a) and 6.2(b), $\Delta x = 12.5 \mu\text{m}$ and $2.5 \mu\text{m}$, respectively, using the MP5 scheme. A more detailed examination of the dynamics for these two different grid sizes is shown in Figures 6.3 and 6.4, as will be discussed below.

The high pressure of this re-explosion event initiates another strong shock, which is followed, after an induction length (ℓ , measured in the reference frame of the shock) by the combustion zone. This flame is initially strongly coupled to the shock ($\ell \rightarrow 0$) and the wave is strongly over-driven, i.e., its speed exceeds that of the Chapman-Jouget (CJ) detonation. As the degree of overdrive decays and the detonation approaches the CJ limit, instabilities begin to appear, as shown in Figure 6.2(a) after about $35 \mu\text{s}$ and in Figure 6.2(b) after about $25 \mu\text{s}$.

These spark-ignited detonation simulations demonstrate the appearance of different instability modes. For both sets of results in Figure 6.2, instabilities appear when the detonation becomes close to the CJ condition, starting with a small-amplitude, but high-frequency mode – hereafter referred to as the ‘HF’ mode. For the low-resolution case in Figure 6.2(a), the transition to the high-frequency (HF) mode occurs at a time of the order of $30 - 35 \mu\text{s}$; this instability regime is shown in detail in Figure 6.3(a). For the high-resolution case, Figure 6.2(b), the transition occurs earlier, close to $25 \mu\text{s}$; this regime is shown in detail in Figure 6.3(b) for roughly the same time period as in Figure 6.3(a). For both grid sizes, we observe that at around $45 \mu\text{s}$, there is a transition towards a lower frequency but high-amplitude mode – referred to here as the ‘HA’ mode. This transition is more gradual in the high-resolution case, with both modes coexisting during a period of time (between approximately 44 and $48 \mu\text{s}$), as shown in more detail in Figure 6.4(b). In the low-resolution case of Figure 6.4(a), however, the behavior is less gradual and more

chaotic. The contrast between these two profiles is striking; while a periodic signal can still be detected in Figure 6.4(a), the characteristics and frequencies are both very different. Besides the smoothness of the temporal waveforms of the high amplitude instabilities, we also note that a period-doubling in the high resolution case, i.e., the HA signal has a dual oscillation (high-low pressures) which is not apparent at lower resolution¹. We note also that there are other manifest differences in the specific dynamical features of these instabilities, e.g., in the appearance of noise in the waveform after the re-explosion event (Figure 6.2(a)), which is eliminated for the higher resolution case in Figure 6.2(b). Thus, it is clear that there can be significant effects of the grid resolution on the dynamics of the instabilities. Furthermore, the appearance of sharp features in the traces also suggests that special care must be exercised in avoiding numerical procedures which can arbitrarily sharpen gradients, as mentioned earlier.

There is no obvious “very high frequency” mode that arises after the re-explosion event and before the initiation of the high frequency mode, as seen by Leung et al.[17], in the well-resolved result in Figure 6.2(b). But if one explores in detail the time regime after the re-explosion event, for grid sizes Δx of $2.5 \mu\text{m}$ and even smaller, as shown in Figure 6.5, one does observe relatively low amplitude and very high frequency oscillations, with frequencies and amplitudes dependent on the grid resolution. To examine the origin of these low amplitude oscillations, the variation in induction length as a function of time, determined from peaks in the concentration of H atoms, may be explored for these different resolutions. A plot of induction length as a function of time is shown in Figure 6.6(a), with an expanded view in Figure 6.6(b) corresponding to the same time period as shown in Figure 6.5. The

¹This was verified for longer time periods than shown; for clarity purposes, the extent of the simulation results shown in the figures has been truncated.

results in Figure 6.6 indicate that the amplitude of oscillations in induction length corresponds to the grid size Δx , and moreover, the frequency of oscillation corresponds to the ratio of the CFL number here (0.4) to the sampling period (1 nanosecond). Thus it appears that the very high frequency (and very low amplitude) oscillations seen using complex kinetics merely correspond to numerical uncertainties associated with the location of the peak pressure or peak in atomic hydrogen (mole fraction).

Because the re-explosion event is clearly identifiable, we can use this feature to conduct a more detailed study of the effect of grid resolution. For example, one can examine the variation of the measured time delay to this second explosion event, t_{exp} , for the specific initial spark conditions noted previously. Here the uniform grid spacing Δx is varied from $0.5 \mu m$ to $20 \mu m$. Figure 6.7 illustrates how the time to re-explosion for the MP5, AW5, and MW5 schemes varies with the grid resolution. Since the AW5 & MW5 schemes are more diffusive than MP5, it is not surprising that the AW5 & MW5 curves exhibit a shallower profile. The most striking feature here is the non-monotonic behavior, i.e. the presence of a maximum in the time to explosion, which delineates two regimes. The peak in t_{exp} for MP5 in Figure 6.7 occurs at approximately $\Delta x = 7 \mu m$, whereas the critical Δx value is slightly lower, at approximately $5.5 \mu m$, for AW5, and even lower for MW5 at $\Delta x \approx 4 \mu m$. For grid resolutions Δx below the critical value, the numerical simulation is in a “convectively” dominant regime, where the combination of the numerical scheme and fine grid resolution is sufficient to effectively mitigate the effects of numerical diffusion in the detonation formation. AW5 & MW5 produce similar values of t_{exp} for $\Delta x < 3 \mu m$, but for this complex kinetics scheme, time convergence for t_{exp} may not be reached except for $\Delta x < 0.5 \mu m$, consistent with findings by Powers & Paolucci[72]. In the case of AW5, grid convergence is observed at $\Delta x \approx 0.5 \mu m$.

For grid resolutions greater than the critical value of Δx in Figure 6.7, we enter the numerically dissipative regime, where coupling of the fluid mechanics and kinetics is enhanced due to numerical diffusion of temperature and chemical concentrations. The value of t_{exp} thus decreases with increasing Δx in this numerically dissipative regime.

To obtain results that are truly insensitive to the numerical effects, one requires $\Delta x \rightarrow 0$, since the two methods converge in that limit to a single value for t_{exp} , but of course this is a practical impossibility. The results in Figure 6.7 suggest that, to be able to reasonably resolve detonation propagation and shock-flame coupling dynamics, a grid spacing of $\Delta x = 2.5 \mu\text{m}$ or smaller may produce acceptable accuracy, given less than a 5% difference between the two different schemes. Yet the time to re-explosion is but one parameter that is affected by grid resolution, and calculations of the shock-flame instabilities at smaller grid spacings are needed to be able to explore other quantitative features.

A simple fast Fourier transform (FFT) can be used to find the spectral content of the two instability modes, HF and HA, which are observed in Figures 6.2 - 6.4. Figure 6.8 shows FFT results for the MP5 scheme and grid sizes $\Delta x = 2.5, 1.5,$ and $1.0 \mu\text{m}$. There is remarkable consistency in the dominant frequencies here; for both HA instabilities near a frequency of approximately 0.35 MHz and HF instabilities near 2.3 MHz, there is relatively little difference in results for $\Delta x \leq 2.5 \mu\text{m}$. This observation suggests that the spectral content of the resulting instability is relatively insensitive to the grid spacing, as long as Δx lies below the critical value for the start of numerical diffusion. At high frequencies, above 4 MHz, there is some grid dependency; in fact, frequencies above 4 MHz are not seen for $\Delta x = 1.5 \mu\text{m}$. The spectral content around 4.5 MHz is likely to be a harmonic of the strong 2.3 MHz

signal. Note that since the instabilities develop for a finite time only, the sampling statistics of the FFT are limited. The use of a wavelet decomposition did not provide improvements in the signal-to-noise ratio.

These results confirm earlier complex kinetics findings [16] which indicate that a detonation near the CJ limit has two physically distinct instability modes. The high frequency mode always appears first and marks the transition from a ‘stable’ CJ detonation, where a low frequency mode appears later in time. The overdriven detonation simulations by Leung et al.[17] with a two-step reaction mechanism also demonstrate multiple instability modes, but with distinct differences from those seen here, as noted above.

Our observed fluctuations in key properties (e.g., in species concentration, temperature, and pressure) of the fluid within the induction zone are described by Oran & Boris[73] as ‘hot spots’. The present study with complex reaction kinetics shows that these ‘hot spots’ contribute to an initial stage of the flame dynamics. In this regime, the induction length is very small ($\ell \ll \ell_{CJ}$), and acoustic waves generated by the perturbed chemistry are rapidly transmitted to the shock, i.e. leading to high-frequency modes. Because there is a very limited amount of fluid that can participate in the fluctuation of the heat release, only low-amplitude perturbations of the CJ peak pressure appear. As these acoustic waves reach the leading shock and strengthen it, their frequency can be measured as that of the fluctuations of the peak pressure. Eventually the average induction length continues to increase and the second mode appears, which directly couples the flame speed with the shock, resulting in fluctuations with lower frequency but much higher amplitude. This interpretation of our observations will be elaborated upon and verified in the next section.

6.2 Simplified Model

To better understand and interpret the coupling between reactive and fluid mechanical/acoustic phenomena that generates our observed results, a model for the induction zone may be constructed and explored. This model is composed of a leading shock, a heated, post-shock medium(fluid), and a flame front, all of which are illustrated in Figure 6.9. A single period of the detonation oscillation can be described, in the reference frame of the shock, in a manner similar to that of McVey & Toong[74], as follows. Fluctuations at the flame front create an acoustic (pressure) disturbance, which travels at the acoustic wave speed, λ_{ac} , through the induction zone until it reaches the leading shock; this process occurs between reference times t_a and t_b . Upon contact, the pressure fluctuation carried by the acoustic wave will accelerate the shock and alter the post-shock conditions, thus creating an entropy disturbance (temperature fluctuation). This entropy disturbance will propagate back into the induction zone at the entropy wave speed, λ_{en} , toward the flame front, this process occurring between times t_b and t_c . A resonant condition is achieved when, upon contact with the flame, the entropy wave creates a new acoustic disturbance in the flame, and the cycle repeats. Figure 6.9 illustrates this phenomenon, with relations for the entropy and acoustic wave speeds as follows, respectively:

$$\lambda_{en}(x, t) = \left. \frac{dx}{dt} \right|_{en} = u_2(x, t) \quad (6.1)$$

$$\lambda_{ac}(x, t) = \left. \frac{dx}{dt} \right|_{ac} = c(x, t) - u_2(x, t) \quad (6.2)$$

Here $u(x, t)$ is the fluid velocity, $c(x, t)$ is local speed of sound, $D(t)$ is the detonation velocity, and $u_2(x, t) = |u(x, t) - D(t)|$ is the post-shock fluid velocity in the

detonation reference frame. From these wave speeds the period of the cycle, τ , may be expressed by

$$\tau = \left| \int_{x_f}^{x_s} \frac{1}{\lambda_{ac}(x, t)} dx \right| + \left| \int_{x_s}^{x_f} \frac{1}{\lambda_{en}(x, t)} dx \right| \quad (6.3)$$

where $x_s = (t - t_0) \cdot D(t)$ is the position of the shock and x_f is the position of the flame.

At a zeroth-order approximation, the fluid properties in the induction region, $Q_2(x, t)$, are assumed to weakly vary with time for a given half cycle, $\frac{\partial Q_2(x, t)}{\partial t} \simeq 0$ & $\frac{\partial Q_2(x, t)}{\partial x} \simeq 0$. This also implies that the relative positions of the flame and shock front are approximately constant. From this approximation, the period can be determined

$$\tau = \frac{\bar{\ell}}{c_{ab} + u_{ab} - \bar{D}_{ab}} + \frac{\bar{\ell}}{u_{bc} - \bar{D}_{bc}} \quad (6.4)$$

where $\bar{\ell}$ is the period-averaged induction length, ab is the fluid state at the acoustic wave half-cycle, bc is the fluid state during the entropy wave half cycle, and u_α , c_α , and \bar{D}_α are the the fluid speed in the detonation reference frame, speed of sound, and average detonation speed, respectively, for half-cycle α . The model for acoustic and entropy half cycles are illustrated in Figure 6.10, corresponding to observed oscillations as indicated in the inset. From the period of the combined cycles, the frequency in oscillations of the peak pressure trace is $f = \tau^{-1}$.

Data may be extracted from the full kinetics results at different peak pressure cycles from the high frequency as well as high amplitude regime, and compared with the simplified model expressed in Equation 6.4. Figure 6.12 illustrates the evolution of the induction zone temperature profile in the detonation reference frame for a given period of the high amplitude mode, with data for the acoustic wave

propagation in (a) and for the entropy wave in (b). The density distributions for the corresponding HA mode are shown in Figure 6.14. Using the induction zone data and the period from Eq. (6.4), the frequency $f \approx 310 \text{ kHz}$ may be estimated for the HA mode, which is in excellent agreement with that obtained from the spectral analysis using the full simulation, $310 \pm 40 \text{ kHz}$, shown in Figure 6.8. Performing the same analysis on the high frequency (HF) mode, illustrated in the temperature profiles in Figure 6.11 and the density profiles in Figure 6.13, the frequency $f \approx 2.08 \text{ MHz}$ may be estimated, which is also in good agreement with that extracted from the spectral analysis ($2.29 \pm 0.4 \text{ MHz}$) in Figure 6.8. Hence this simple model appears to capture reasonably well the global processes that lead to the high- and low-frequency detonation instability modes.

We should point out that this simple model has been successfully applied to another case of shock-induced instability. For strong, ionizing shocks in a noble gas (specifically, argon), a similar structure of shock, induction zone and reaction front can be observed [75, 76, 77]. The instability in this case has lower amplitudes, due to the absence of exo-thermic reactions, but is also well explained by a resonant coupling between the shock front and reaction zone through the transmission and reflection of entropy and acoustic waves [75]. In fact, the 2D structure of that flow could be found to have features remarkably similar to detonations including, for example, artificial soot patterns [77]. This indicates that the model, despite its simplicity, provides a good insight into the true physical mechanisms involved and may have relevance to a universal class of instabilities in reactive shock systems.

6.3 Discussion

The ‘hot spot’ which appears in the high frequency mode temperature profiles (Figure 6.11) is of particular interest in interpreting the differences between modes. This hot spot burns only a fraction of the overall mixture and the heat release is not sufficient to significantly alter the characteristic speeds of the flow (especially since the speed of sound only varies with the square-root of the temperature). Examination of the temperature profiles in Figure 6.11, in particular panel (a), shows that the reaction zone fluctuates from a ‘hot-spot’ position without significant change in location; if at all, the perturbed region of accelerated burning is actually convected *downstream*. This pre-ignition effect does not allow the flame to accelerate, and in the case of the high frequency mode, the detonation is still slightly overdriven. The resonance between the perturbation of the chemical rates at the hot spot and the shock front still remains, though, and is the basis for the observed oscillation pattern, as indicated by the agreement between computed and measured frequencies.

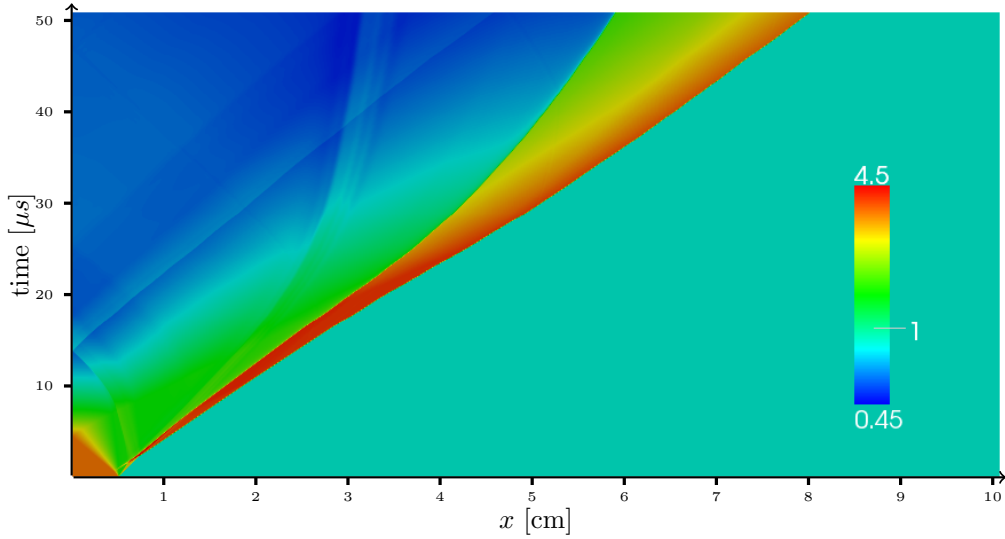
By contrast in the high amplitude mode’s temperature profiles, seen in Figure 6.12, there is no observed ‘hot spot’. More likely, the perturbation has moved to the flame region and any acceleration of the chemical rates in that region can enhance the rate of heat release much more significantly. This allows what is presumably a SWACER-like [71] mechanism to govern this high amplitude regime, starting from a flame at the furthest distance from the shock, $\bar{\ell}_{max}$, and accelerating towards the shock as it burns the fluid in the induction zone, releasing large amounts of energy up to the point of contact with the shock. This can be seen in Figure 6.12(a), where the temperature profiles for the HA mode clearly exhibit a dramatic reduction of the distance between the shock and flame fronts in time. Thus, the HA mode is very

much a SWACER-like mechanism, while the HF mode is not. This large change in shock-flame distance is not seen in the two-step model results of Leung et al.[17], thus highlighting another important feature of the true kinetics.

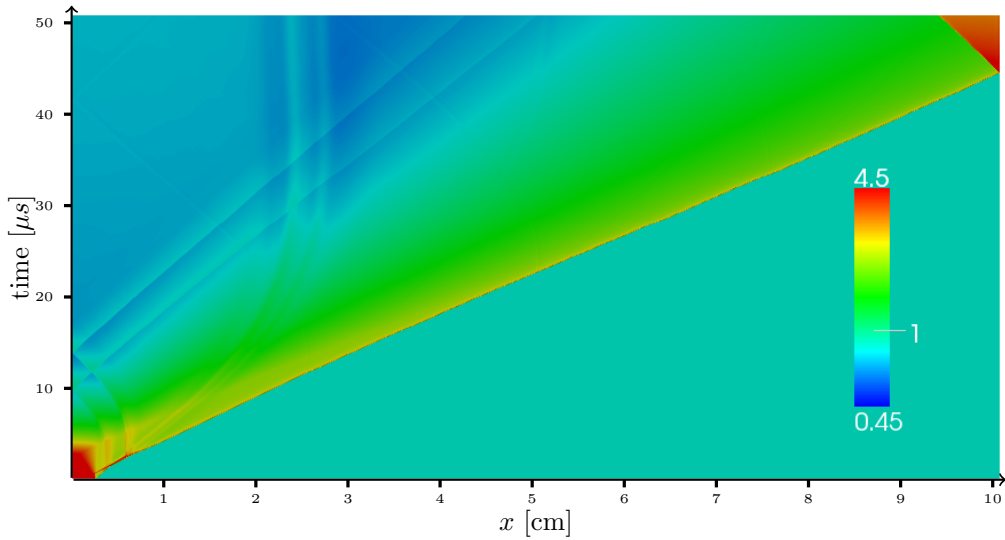
From the density profiles illustrated in Figures 6.13 and 6.14, it becomes quite apparent, even in the high-frequency regime, that there is a large variation of density within the induction zone throughout a given cycle. Neither single-step Arrhenius kinetics [12, 13, 14, 15] nor a two-step reaction model [17] account for these large density variations; their ZND approximation is only valid for a brief portion of the cycle in the HA regime. Therefore, more complex reaction kinetics than have been incorporated in the past should be utilized to capture the full quantitative features of the evolving detonation instabilities. The simple two-wave resonant model explored in Section 6.2 also depends on approximately constant flow properties within the induction zone, and thus the same limitations apply to this model, except that we have separated the cycle into two sections, each with different average flow properties and induction lengths. Hence a reasonable representation of global dynamical character is achieved with the simple model.

As the detonation relaxes toward the CJ condition prior to the onset of the instabilities, the post shock conditions can be used to determine the chemical time scale corresponding to the induction zone. For the present simulations this time scale is approximately $\tau_{hydr} = 300 \pm 10ns$. Using the same post shock conditions in a zero-dimensional reactive simulation produces time scale $\tau_{chem} = 215 \pm 5ns$. This level of disparity is to be expected, because the zero-dimensional calculations are performed at constant volume, and as the system approaches the peak of the H concentration (the criterion used to define the flame center), the energy liberated remains confined and leads to a more rapid rate of reaction. Using the τ_{hydr} value as a normalization

factor, the two modes observed in the present simulations, HF and HA, correspond to normalized periods of 1.6 and 10.75, respectively. This is within the range of instabilities observed by Leung et al.[17]; a more exact correspondence is difficult to obtain, since several parameters are being varied in their two-step model, with no direct relation to the actual chemical system. As noted in Section 6.1, in the present studies we do not observe the so-called “very-high frequency” mode seen by Leung et al.[17], except for very low amplitude oscillations that are shown to be a numerical artifact. In fact, a physical instability at very high frequency would correspond to an oscillation period that is *less* than the induction delay, implying that the “hot spot” be located very close to the shock. In that case, the extent of this perturbation (i.e., the reaction time) would need to be much smaller than the induction period. With realistic chemistry, this may not be possible. Thus, it is conjectured here that the very high frequency mode may be an artifice of the two-step model.

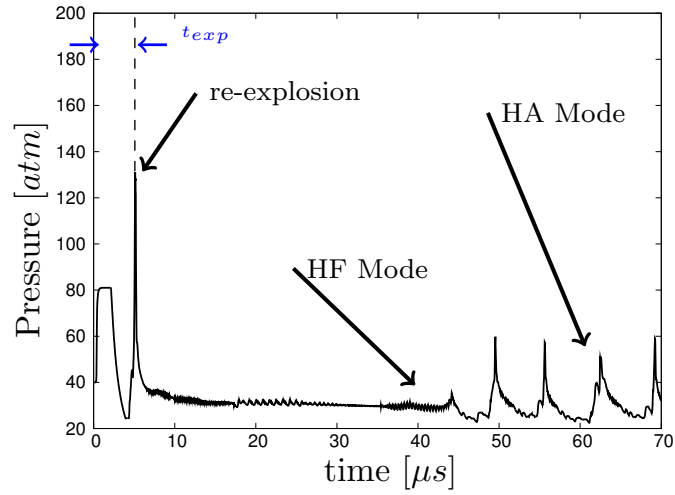


(a) $P_{spark} = 20 \text{ atm}$ with 0.25 cm spark length where detonation is not achieved

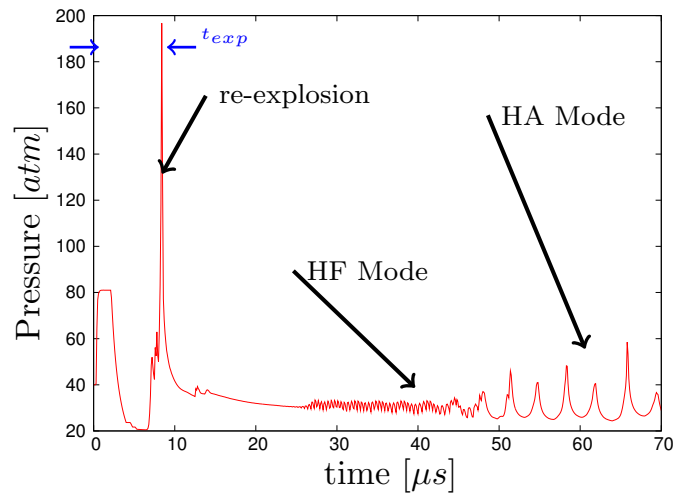


(b) $P_{spark} = 40 \text{ atm}$ with 0.25 cm spark length where detonation is achieved

Figure 6.1: Pressure contours on an x-t diagram for a spark ignited H_2 -Air mixture with $\Delta x = 50 \mu m$, computed using the MP5 scheme.

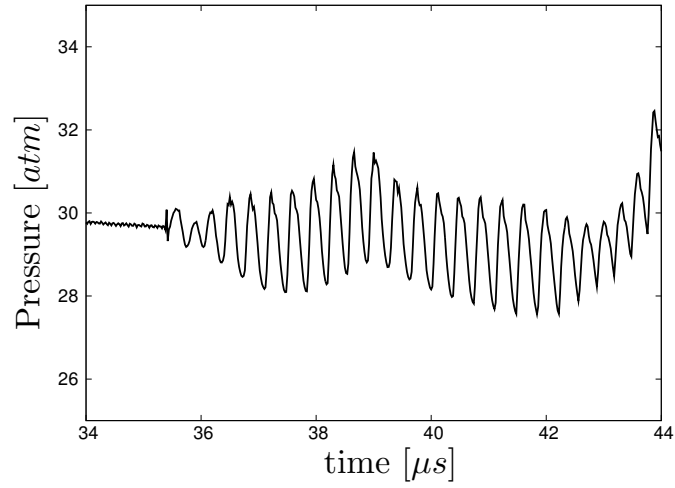


(a) $\Delta x = 12.5 \mu m$

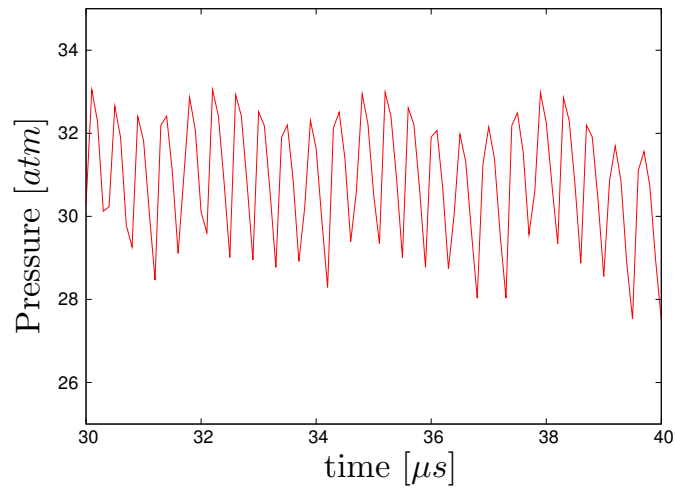


(b) $\Delta x = 2.5 \mu m$

Figure 6.2: Peak pressure-time history of a spark-ignited H_2 -air mixture simulated with two different grid cell sizes Δx using the MP5 scheme. The time to re-explosion, t_{exp} , high amplitude mode, HA, and high frequency mode, HF, are illustrated.

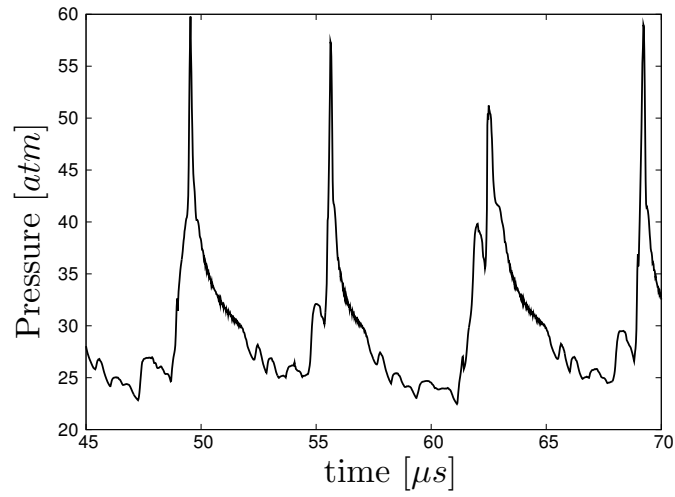


(a) $\Delta x = 12.5 \mu m$

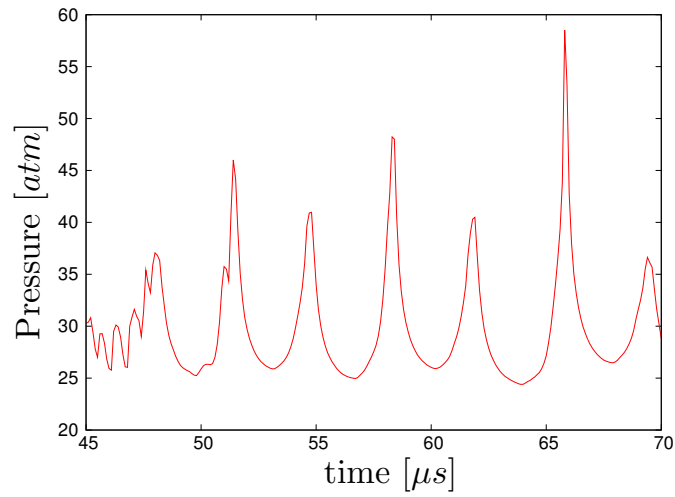


(b) $\Delta x = 2.5 \mu m$

Figure 6.3: High frequency portion of peak pressure time history as in Fig. 6.2, simulated with two different grid cell sizes Δx .



(a) $\Delta x = 12.5 \mu m$



(b) $\Delta x = 2.5 \mu m$

Figure 6.4: High amplitude portion of peak pressure time history as in Fig. 6.2, simulated with two different grid cell sizes Δx .

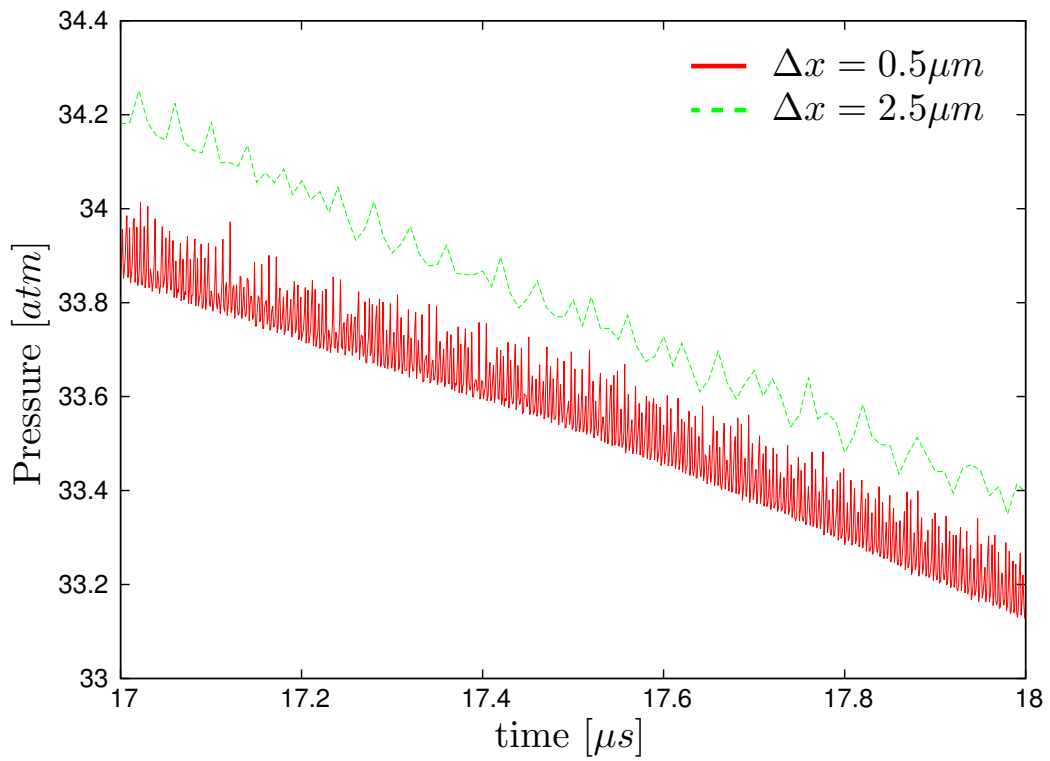
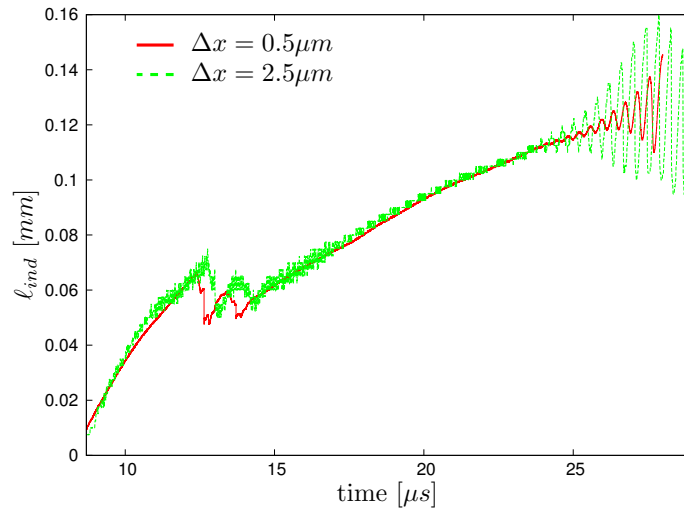
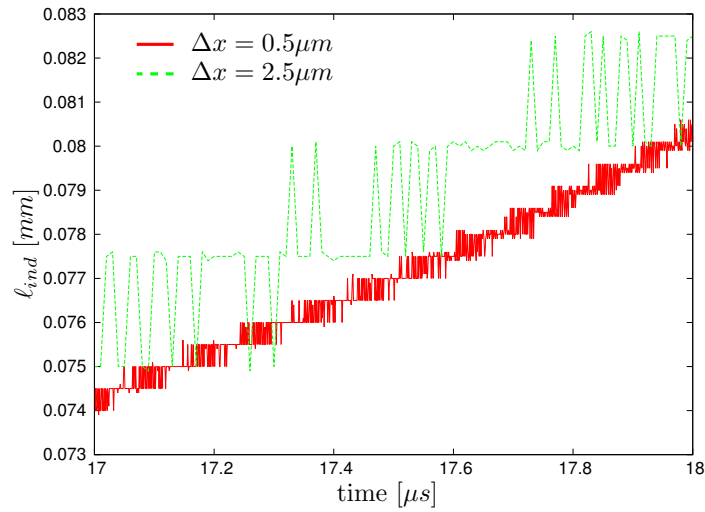


Figure 6.5: Early portion of peak pressure time history after re-explosion, simulated with two different grid cell sizes Δx .



(a) Induction length vs. time



(b) Induction length vs. time (zoom)

Figure 6.6: Early portion of induction length time history after re-explosion, simulated with two different grid cell sizes Δx .

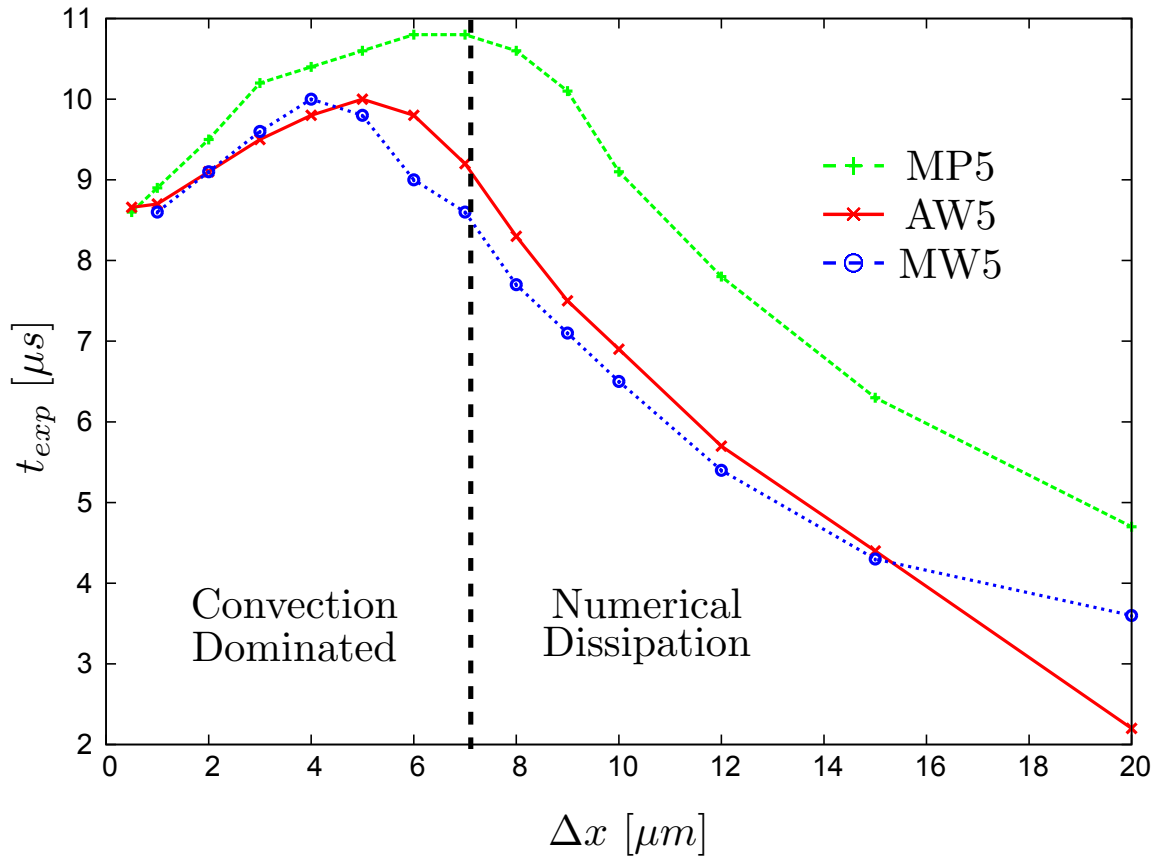


Figure 6.7: Time to re-explosion as a function of grid resolution size Δx for the MP5, AW5, and MW5 schemes.

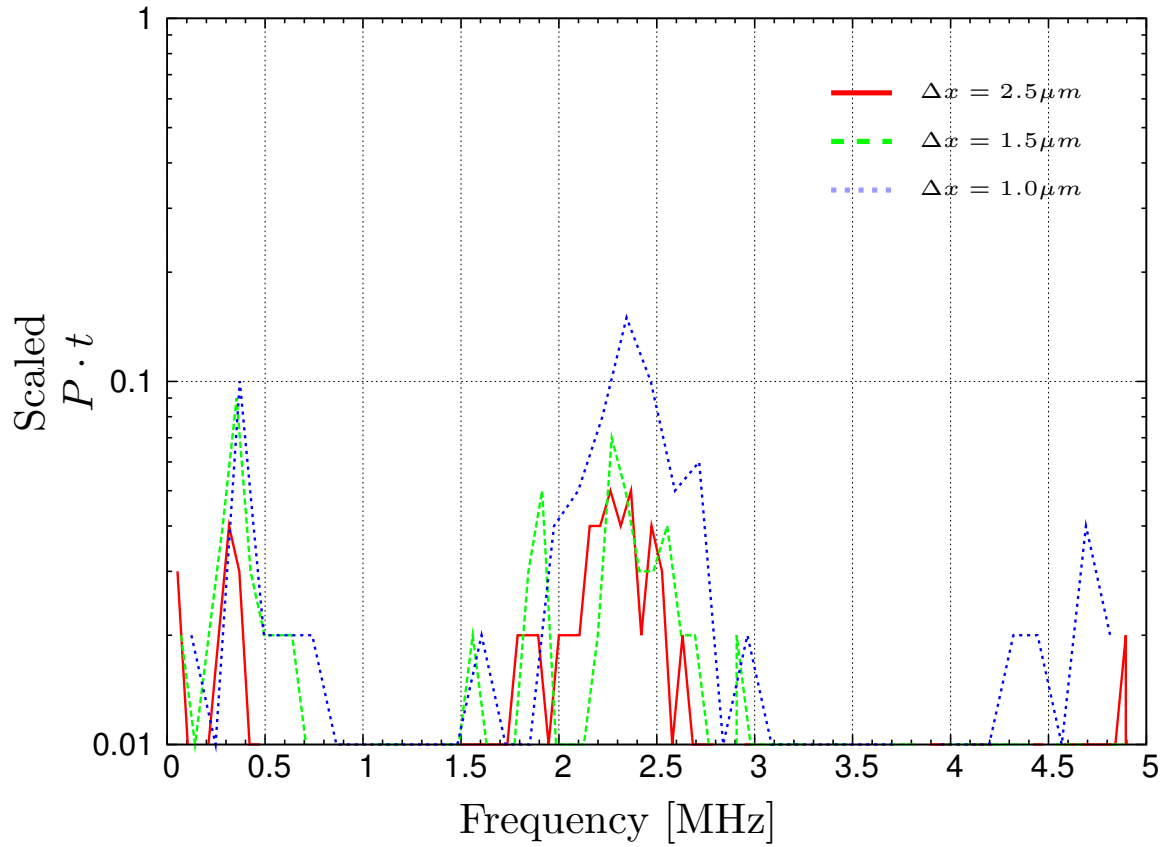


Figure 6.8: Fast Fourier transform of peak pressure traces for the unstable detonation with 3 different grid sizes Δx , simulated using the MP5 scheme.

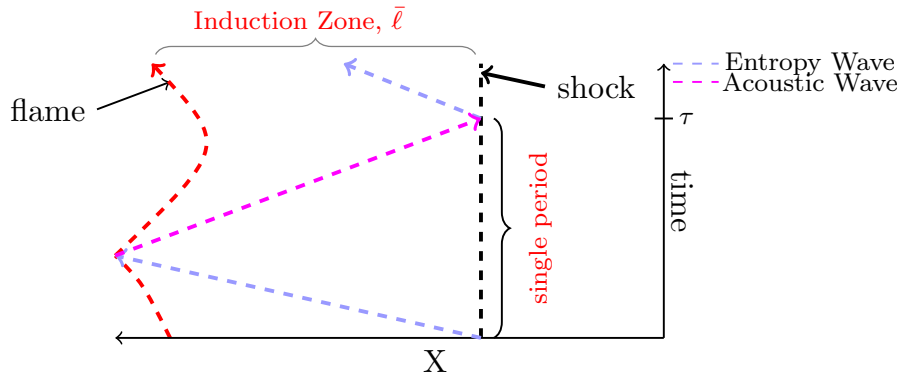


Figure 6.9: A simple model involving the shock, flame, induction zone, and transmission of entropy and acoustic waves to represent shock-flame coupling.

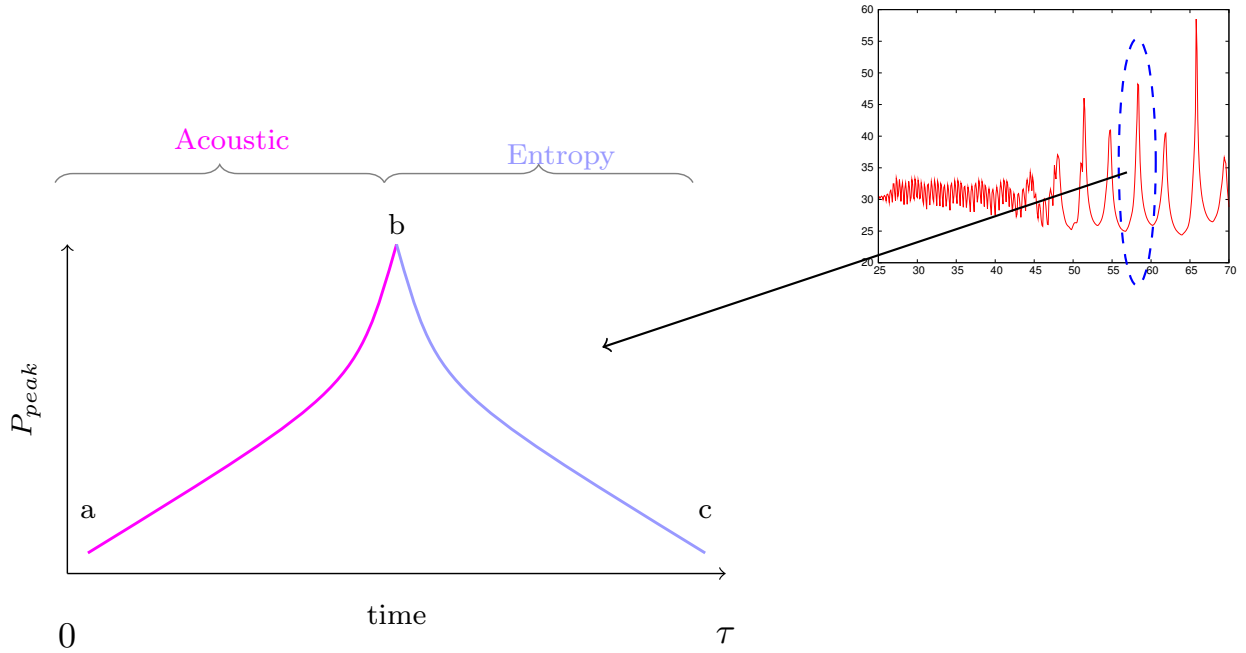
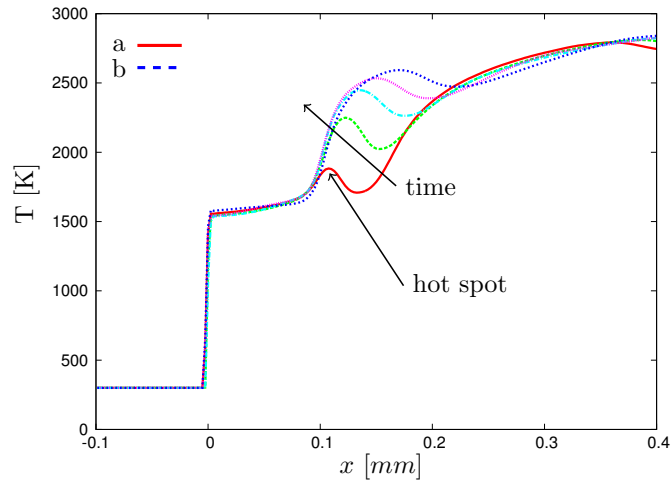
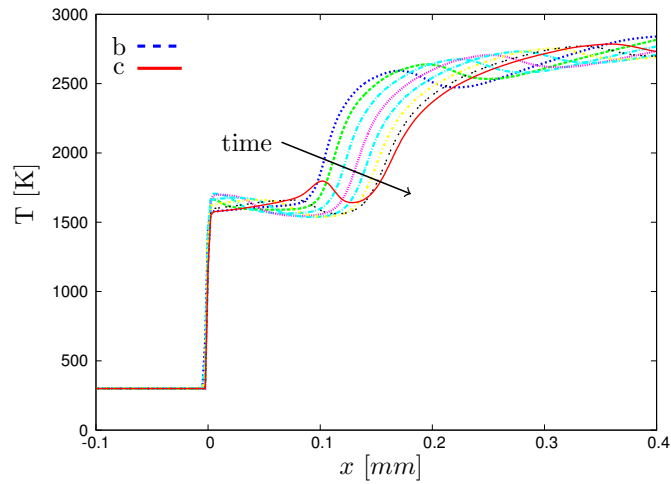


Figure 6.10: Simplified model of the peak pressure cycle (left) used to represent the numerically observed pulsations in peak pressure (right inset).

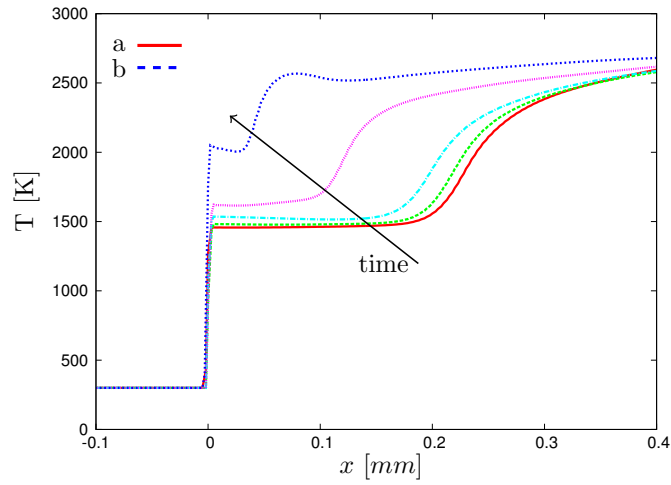


(a) acoustic wave cycle

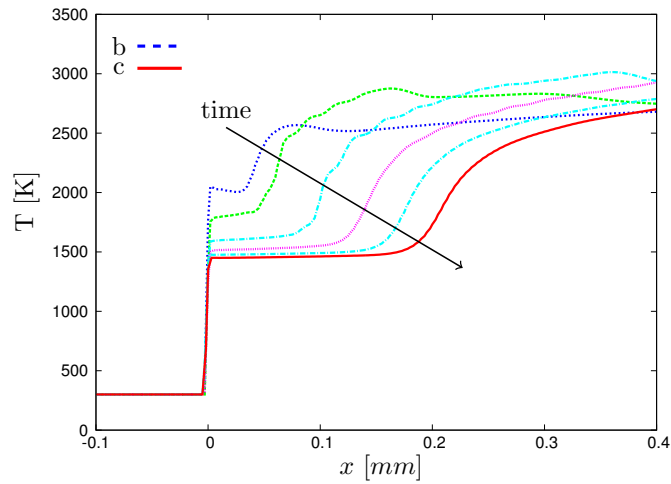


(b) entropy wave cycle

Figure 6.11: Temperature distribution in shock reference frame at different times within: (a) the acoustic wave cycle (times $a = 29.1 \mu s$ to $b = 29.3 \mu s$) and (b) the entropy wave cycle (times $b = 29.3 \mu s$ to $c = 29.5 \mu s$). Data are extracted from high frequency (HF) mode results.

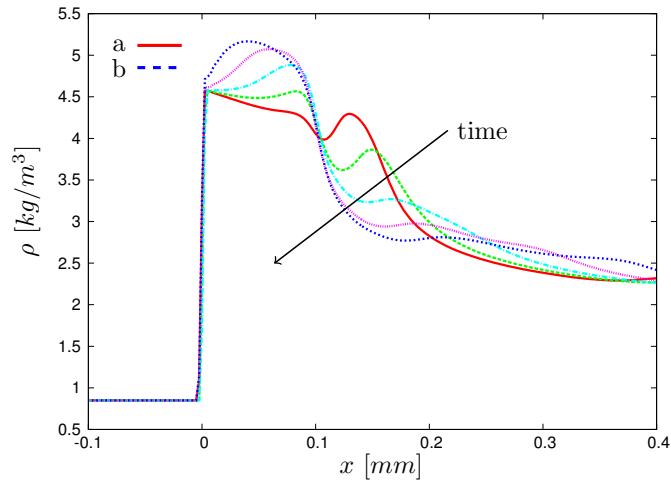


(a) acoustic wave cycle

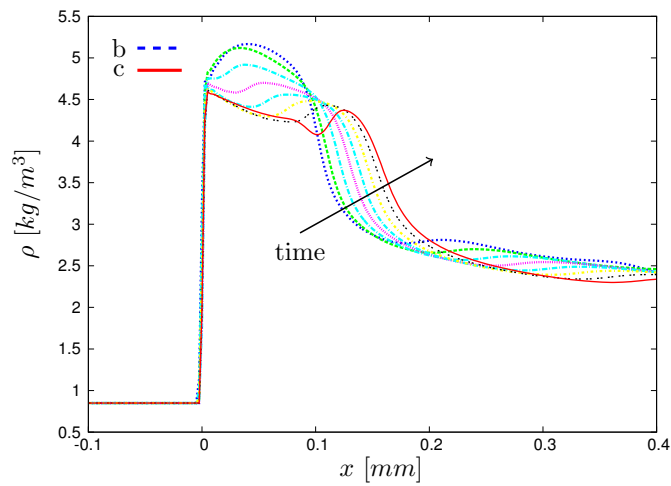


(b) entropy wave cycle

Figure 6.12: Temperature distribution in shock reference frame at different times within: (a) the acoustic wave cycle (times $a = 57.1 \mu s$ to $b = 58.3 \mu s$) and (b) the entropy wave cycle (times $b = 58.3 \mu s$ to $c = 60.7 \mu s$) Data are extracted from high amplitude (HA) mode results.

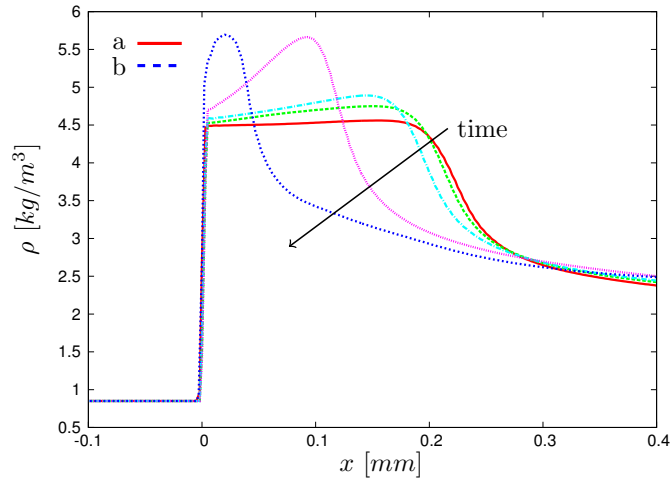


(a) acoustic wave cycle

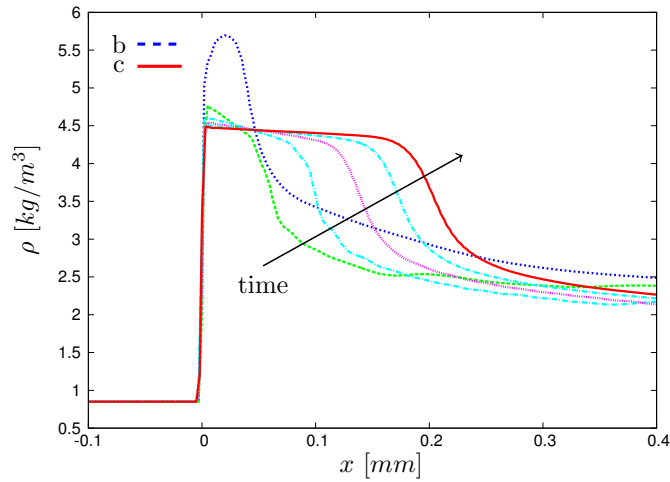


(b) entropy wave cycle

Figure 6.13: Density distribution in shock reference frame at different times within: (a) the acoustic wave cycle (times $a = 29.1 \mu s$ to $b = 29.3 \mu s$) and (b) the entropy wave cycle (times $b = 29.3 \mu s$ to $c = 29.5 \mu s$). Data are extracted from high frequency (HF) mode results.



(a) acoustic wave cycle



(b) entropy wave cycle

Figure 6.14: Density distribution in shock reference frame at different times within: (a) the acoustic wave cycle (times $a = 57.1 \mu s$ to $b = 58.3 \mu s$) and (b) the entropy wave cycle (times $b = 58.3 \mu s$ to $c = 60.7 \mu s$). Data are extracted from high amplitude (HA) mode results.

CHAPTER 7

Magnetic Field and Detonation Interactions

In evaluating the feasibility of the PDRIME configurations we must examine how a magnetic field will interact with a conducting, reacting flow such as the detonation as well as the amount of conductivity required in the fluid for sufficient interaction of the magnetic field and detonation. In Chapter 5, various PDRIME configurations have been evaluated using simplified combustion kinetics and the exploration of the effect of MHD to accelerate the reactive flow in the bypass section or magnetic chamber piston concept(CP) or decelerate the flow in the nozzle via nozzle generator concept(NG). In these prior calculations, the ability of MHD to affect combustion was modeled globally, but not in detail. The goal of the studies in this chapter is to determine if such MHD-based acceleration/deceleration is possible for detonation phenomena.

7.1 Detonation Instabilities with Applied Magnetic Fields

In Section 6.1, the stability of an unsupported detonation was evaluated. For the next simulations, we began with the same initial conditions used in the previous chapter and seeded the fluid with different amounts of cesium (1%, 5%, and 10% by mole). Because of the large molecular weight of cesium ($\frac{M_{Cs}}{M_{H_2}} \approx 70$, $\frac{M_{Cs}}{M_{Air}} \approx 5$), adding

upwards of 10% Cs can significantly affect the dynamics of the detonation (e.g., CJ detonation speed D_{CJ} , flame temperature T_f , post-leading shock pressure and temperature P^{vN}, T^{vN} , etc.) even without the presence of an applied magnetic field. Figure 7.1 illustrates the peak pressure traces of unmagnetized spark-ignited H_2 -air detonations with the addition of 0, 1, 5, & 10 % Cs. A grid resolution of $5\mu m$ and the MP5 scheme were used to perform the 1D detonation simulations in the remainder of this section. Figure 7.1(a), in the absence of Cs addition, shows the initiation of HF and HA instability modes, as observed in Figures 6.2(a) & (b) for different grid cell sizes. With a grid resolution of $5\mu m$ it is possible to capture the essential dynamics of the detonation, within the “convection” dominated regime (see Figure 6.7), although parameters such as time to re-explosion may not be as accurately determined. Nevertheless, $5\mu m$ resolution is sufficient to enable computation of additional ionization processes of Cs and their effect on instabilities.

From Figure 7.1 (a)-(d), one will notice the oscillations become less erratic and, at 5% and 10% molar addition, approaching consistent HA behavior, as more cesium is added. Extinction, where the peak pressure decays, is significantly delayed for higher Cs concentrations. This trend is consistent with the observations of Radulescu et al.[19] where argon was incrementally added to acetylene-oxygen mixture to stabilize the detonation. Heavy argon dilution in the mixture led to large-frequency, small amplitude regular oscillations of the shock front pressure. Radulescu et al. attributed the stabilizing effect of the diluent to the lower temperature in the reaction zone which leads to slower exothermic reaction rates. For the present calculations, regularization of both the HF and HA modes with Cs addition could result from the lowering of the reaction front temperature. The addition of Cs is also observed to reduce the effective 1D detonation speed, as also determined by the theoretical reduction in the

CJ speed (see Table 7.1). The results shown in Figure 7.1 will serve as the “baseline” case for the 1D dynamics as affected by an applied magnetic field.

Now that the “baseline” behavior has been established for cesium-seeded detonations, let us now examine how the behavior of these instabilities change when one gradually increases the strength of an applied magnetic field. A fixed magnetic field is used, per Equation 2.17, with a loading factor, $\mathbf{K} = 0$ (no applied electric field). The magnetic field configuration is illustrated in Figure 7.2 where a transverse magnetic field will be applied with strengths ranging from 0 to 8 Tesla. A spark-ignited detonation will propagate into the region of this magnetic field, as shown. Figures 7.3, 7.4, and 7.5 show the peak pressure traces of detonations seeded with 1%, 5%, and 10% Cs, respectively, under the influence of various applied magnetic field strengths. Without an applied magnetic field, the peak pressure trace of a detonation with a 1% Cs has an irregular periodicity (Figures 7.1(b) & 7.3(a)). As the magnetic field is strengthened (see Figures 7.3(b)-(f)) the detonation peak pressure trace shows more prolonged erratic behavior, with no clear trend in the time at which extinction (pressure decay) takes place. But Figure 7.4 shows that as the magnetic field strength is increased, the oscillations of the peak pressure trace are driven to become less regular at earlier times and extinguish sooner. Similarly findings are observed in Figure 7.5. There are a few qualitative assessments that can be made from these results. Figures 7.3(a), 7.4(d), & 7.5(e) illustrate peak pressure traces of detonations seeded with 1%, 5%, and 10% cesium under applied field strengths of $B_z = 0, 6,$ and 7 Tesla, respectively. These peak pressure traces demonstrate a general trend. It would appear as though the stabilizing effect of the presence of diluent, cesium, becomes less effective when the fluid at the flame has a greater conductivity and thus introduces an additional scale to the flame-shock dynamics. One

could attempt to find the modes that exist within the peak pressure trace to give some quantitative insight into the effects of these fields, but the data would prove unreliable due to the small time frame during which these large oscillations exist. The fact that the application of the magnetic field can degrade the cyclic stability of the 1D detonation at earlier times does indicate the ability of the \mathbf{B} field to alter the flame-detonation coupling as well as the combustion process itself.

7.2 Detonation Instabilities with MHD

The behavior of a detonation with an applied field using the MHD accelerator configuration will now be investigated. The study will begin with a fixed magnetic field, Equation 2.17, and the loading factors recommended by Cambier[4], $K_y = 1.5$ and 0.5 (i.e., the electric field scaled with $u_x \times B_z$), for the accelerator and generator, respectively. The remainder of the current detonation configuration is as specified in Section 7.1.

The previous section demonstrated that the H_2 -air, 1D spark-induced detonation under investigation is unstable under normal operating conditions with or without an applied magnetic field. Figures 7.6-7.8 show the peak pressure traces of detonation seeded with 1%, 5%, and 10% Cs, respectively, with an electric field in the accelerator configuration ($K_y = 1.5$) under the influence of various applied magnetic field strengths. In the 1% Cs test case, it becomes quite clear, when comparing Figures 7.6(b)-(f) with the unmagnetized case of Figure 7.6(a) that the MHD acceleration has the ability to regularize and sustain the oscillating detonation; the detonation does not extinguish, for the time period shown, as it does in Figure 7.6(a). When the amount of cesium is increased to 5%, as the magnetic field is increased as shown

in Figures 7.7(a)-(f) the detonation is cyclically stabilized and the peak pressure amplitude greatly reduced, by around 30%. When the amount of cesium is increased to 10%, as the magnetic field is increased from $B_z = 0T$, Figure 7.8(a), to $B_z = 8T$, Figure 7.8(f), the detonation goes from a cyclically stable galloping detonation to a nearly stable CJ detonation, with a slightly delayed onset of the initial instabilities.

Because of the strong effect the magnetic field had on the detonation stability and sustainment, in both the accelerator and generator configurations, we now examine these features side-by-side. Figures 7.9(a)(c)(e) illustrate the time dependent peak pressure, induction length, and detonation velocity, respectively, for a 10 % Cs in the accelerator configuration with applied magnetic field strengths of 0, 3, and 8 T. Figures 7.9(b)(d)(f) show the same thing for the generator configuration. Figure 7.9(a) & (c) show a significant decrease in amplitude of the peak pressure and induction length, respectively, as the magnetic field strength is increased for an accelerator, while figure 7.9(e) shows the detonation speed stabilizes near but above the Chapman-Jouguet velocity, with little propensity for extinction. In contrast, Figures 7.9(b) & (f) for the generator configuration show that peak pressure and detonation speed become erratic, with increasing magnetic field strength, and Figure 7.9(d) shows that the induction length oscillations becomes unbounded, leading to extinction for the 8 Tesla case. This contrast is quite striking, especially in the generator's influence on extinguishing the detonation. There appears to be some acceleration of the detonation, to a speed greater than CJ for the accelerator configuration (Figure 7.9(e), 8T), but overall there is no significant difference in the detonation velocities between accelerator and generator configurations.

7.3 2D Cellular Detonation in an Applied Magnetic Field

While the effects of MHD on the stability of the 1D detonation are interesting, the more realistic flow is that of a two-dimensional detonation structure. Before the effects of an applied magnetic field on a two-dimensional detonation are examined, however, one must first examine the effects of seeding cesium on the evolving cellular detonation. The detonation front as well as the underlying detonation structure may be found in the contours of the maximum pressure, P_{max} , at each point in space. These maximum pressure traces have been observed in experiments over decades in smoke-foil records[78]. The unmagnetized 2D detonation with various amounts of cesium will be examined first.

The 2D detonation initiated with a computational spark is illustrated in Figure 7.10. A grid resolution of $\Delta x = \Delta y = 50\mu m$ and the MW5 scheme are used to perform the 2D detonation simulations in the remainder of this chapter; much finer grid resolution becomes prohibitively expensive, yet this is found to be sufficient for the study of the overall detonation structure. Figure 7.11 shows that evolution of an H_2 -air detonation front (Schlieren-like plot and smoke-foil record) without the presence of an applied magnetic field and without Cs injection. From the series of figures, the Mach stem, transverse shocks, and incident shocks are well resolved. Figure 7.12 shows the detonation front and smoke-foil record after $75\mu s$ of the same detonation. At this resolution, it can be clearly seen in the smoke-foil record, Figure 7.12(b), that cellular detonation is achieved, and is consistent with the established literature for cellular detonations[78, 79, 80, 81]. The simulated detonation cellular length and width for this configuration are $\lambda_L = 2.7\pm 0.1mm$ and $\lambda_W = 1.67\pm 0.1mm$, respectively. It can also be demonstrated that an unmagnetized H_2 -air-Cs mixture

seeded with cesium ranging from 1-10% can achieve the same cellular detonation and detonation front resolution, shown in Figures 7.13 -7.15. The decreased detonation velocity as cesium is increased from 1% to 10% is consistent with the 1D simulations as well as the theoretical CJ velocity, which are tabulated in Table 7.1.

In the previous sections, 7.1 and 7.2, we demonstrated that an applied field can alter the cyclic stability of a 1D detonation. Now we will investigate if an applied field can affect the regularity or velocity of a 2D cellular detonation. Due to the large spatial variation of the longitudinal velocity, u_x , the static electric field should no longer be optimally tailored to u_x and B_z . In order to more accurately account for the static electric fields contribution to the MHD forces, while still keeping the loading factor concept for the accelerator and generator configurations, the static electric field is prescribed as $E_y = K_y U B_z$, where U is the mean velocity, and will not evolve with the flow. The optimal condition $U \approx 1000 \text{ m/s}$ is assumed. As performed with the one-dimensional test cases, 2D detonations in the both the accelerator and generator configurations were computed with varying amounts of cesium(1, 5, and 10%) using the highest magnetic field strength used previously in the 1D detonation simulations, $B_z = 8T$. From the X-t plots of the centerline of the 2D shock front, illustrated in Figures 7.16-7.18, there is no noticeable/significant altering of the detonation velocity in either generator or accelerator modes, as compared with the detonation in the absence of MHD. The peak pressure evolution in Figures 7.19-7.21 similarly do not show any noticeable change in the cyclic stability of these detonations. The differences in the two configurations can be seen in the centerline pressure and conductivity profiles, where the 10 % Cs and $B_z = 8T$ case at $t = 75\mu s$ case is illustrated in Figure 7.22. These differences in the profiles are seen further downstream, however, and do not play a role in the detonation dynamics. Hence even

at a very high magnetic field strength, 8T, and for 10% Cs, there does not appear to be a significant influence of the MHD on detonation dynamics. In an attempt to see if the two-dimensional detonation can be altered by MHD in some meaningful way, but under different conditions, two alternative approaches were taken. The first was to artificially enhance the kinetics of the cesium, (the original formulation of which is described in Appendix A). The second approach drastically increased the strengths of the applied magnetic and electric fields. For both cases, 10 % Cs was seeded because it allowed for more optimal levels of ionization as compared to 1 and 5% Cs addition.

7.3.1 Enhanced Kinetics

In the enhanced kinetics approach, the Arrhenius pre-factor of the cesium forward reaction mechanisms, A , was increased by factors of 10 and 100, respectively. Conductivity and Schlieren-type plots are shown in Figures 7.23 and 7.24 for the generator and accelerator configurations, respectively. One can see a significant increase in conductivity of the detonation close to the leading shock for both the accelerator and generator configurations, with an increase in the “enhanced kinetic factor”, EK , where the modified Arrhenius pre-factor in Equation 2.24 is $A' = EK \times A$. Slight deceleration and acceleration of the detonation front is observed, respectively, in Figures 7.23 & 7.24. The centerline peak pressure traces for the accelerator configuration, illustrated in Figure 7.25, show that as the EK is increased, the amplitude of the peak pressure decreases. In contrast, the centerline peak pressure traces for the generator configuration, illustrated in Figure 7.26, show that as EK is increased the amplitude of the peak pressure increases. These results are consistent with the

1D results from Section 7.2 for the accelerator and generator configurations, in that when there is sufficient conductivity, with a larger concentration of Cs for the 1D detonation, the applied magnetic and electric fields affect the amplitude of the peak pressure. But even with the large increase in conductivity shown in Figures 7.23 and 7.24 for $EK = 100$, the X-t diagram of the unmagnetized, accelerator, and generator configurations, illustrated in Figure 7.27, shows only a small alteration of the detonation velocity: $+30m/s$ (increase) and $-20m/s$ (decrease) for the accelerator and generator configurations, respectively.

7.3.2 Strong Applied Fields

Next, we subjected the 2D detonation to significantly stronger magnetic fields (16T and 32 T) without enhancing the cesium kinetics.¹ Figures 7.28 and 7.29 show the centerline peak pressure traces for $B_z = 8, 16,$ and 32 T in the accelerator and generator configurations, respectively. Even when the 2D detonation in the generator configuration is subjected to a strong field, the peak pressure amplitude, shown in Figure 7.29, is slightly increased. The X-t plot for the generator configuration, illustrated in Figure 7.30, shows only a marginal decrease in the detonation velocity. By comparing the profiles of the x-velocity, conductivity, pressure, and temperature for the generator, illustrated in Figures 7.31 - 7.34, respectively, one will see that the MHD effects are manifested significantly far downstream of ($\gg \lambda_W$) the leading shock.

The accelerator configuration with a strong field, on the other hand, has a more significant effect on the 2D detonation dynamics. From Figure 7.28 one can see a transition, from $B_z = 8T$ where the amplitude and frequency of oscillations are

¹Unrealistic but only interested in scaling and dynamics

regular, to $B_z = 16T$ where the amplitude begins to noticeably decrease at $t \approx 50\mu s$, and finally to $B_z = 32T$ where at $t = 40\mu s$ there is a significant decrease in amplitude and an increase in the mean peak pressure. Because of the significant change in the oscillation frequency, amplitude and mean of the centerline peak pressure, the associated smoke-foil record, illustrated in Figures 7.35 - 7.38, for field strengths $B_z = 0, 8T, 16T$ and $32T$, respectively, can be used to see the alteration of the underlying structure of the cellular detonation. In Figure 7.36, we see that for the $B_z = 8T$ case, cellular structure pattern remains regular, and from Figure 7.37 for the $B_z = 16T$ case, the cellular patterns become irregular at $x \approx 9.5cm$. The detonation case where $B_z = 32T$ (Figure 7.38) shows that there is a transition from a cellular structure to quasi-1D detonation at $x \approx 7.2cm$. The X-t plot for the accelerator configuration, illustrated in Figure 7.39, shows marginal increases in the detonation velocity of $+5m/s$ for the $B_z = 16$, but there is an increase of $338m/s$ for $B_z = 32T$, a 21% increase above the non-MHD case.

7.4 Conclusions

In this chapter, we examined the effects of a diluent (cesium) on the dynamics of a 1D spark-ignited detonation and confirmed the observation of Radulescu et al.[19] that the diluent had a regularizing effect on the oscillations of the 1D detonation. We also studied a cesium-seeded 1D spark-ignited detonation subjected to an applied magnetic field in both a accelerator and generator configurations and found that the accelerator mode had a regularizing effect on the detonation oscillations, while the generator mode had the opposite effect (see Figure 7.9). While it was demonstrated that the dynamics of a cesium-seeded 1D spark-ignited detonation can

be significantly altered when subjected to an applied magnetic field of reasonable strength ($B_z \leq 8T$), the same statement does not hold true for the two-dimensional case. When the enhanced kinetics factor EK for a cesium-seeded 2D spark-ignited detonation was increased ($EK = 1, 10, 100$), the conductivity behind the leading shock was significantly increased (see Figures 7.23 and 7.24), but there was no alteration to the detonation velocity (see Figures 7.30 and 7.31). The 2D spark-ignited detonation required a significantly stronger magnetic field ($32T$) than the 1D detonation to accelerate the detonation in the time ($75\mu s$) and length ($15cm$) scales of the problem (see Figure 7.39). These findings suggest that multidimensional effects play an important role in MHD acceleration. Perhaps a set of reactants/diluent with an increased flame temperature, for increased conductivity, and a lower density, for less inertia, would be more amenable for MHD acceleration.

%Cs	Theoretical CJ [m/s]	1-D [m/s]	2-D [m/s]
0	1967	1998	1938
1	1917	1950	1883
5	1754	1763	1714
10	1584	1600	1551

Table 7.1: The effects of the addition of Cesium on the detonation velocity of a 1D and 2D $H_2 - Air$ detonation. The theoretical Chapman-Jouguet(CJ) velocity is calculated with the initial conditions: $P_0 = 1 \text{ atm}$ and $T_0 = 300K$.

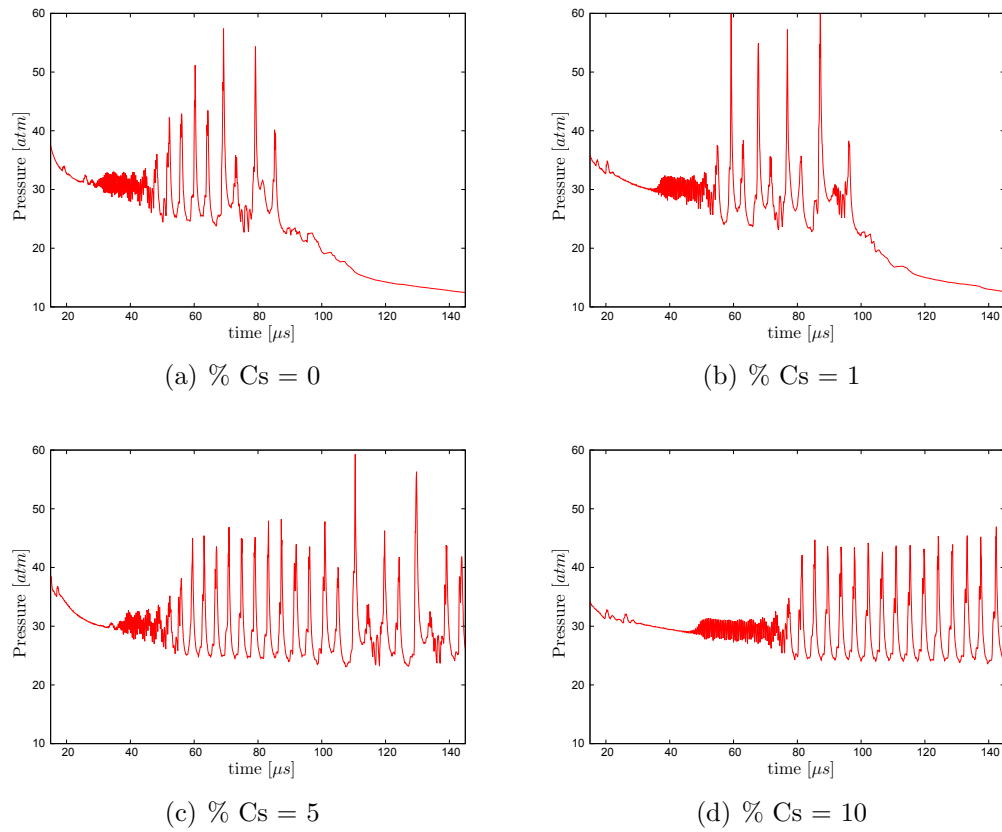


Figure 7.1: Peak pressure traces of spark-ignited H_2 -air detonations with different amounts of seeded cesium without an applied magnetic field ($\mathbf{B} = 0$). The MP5 scheme with $\Delta x = 5\mu m$ was used here.

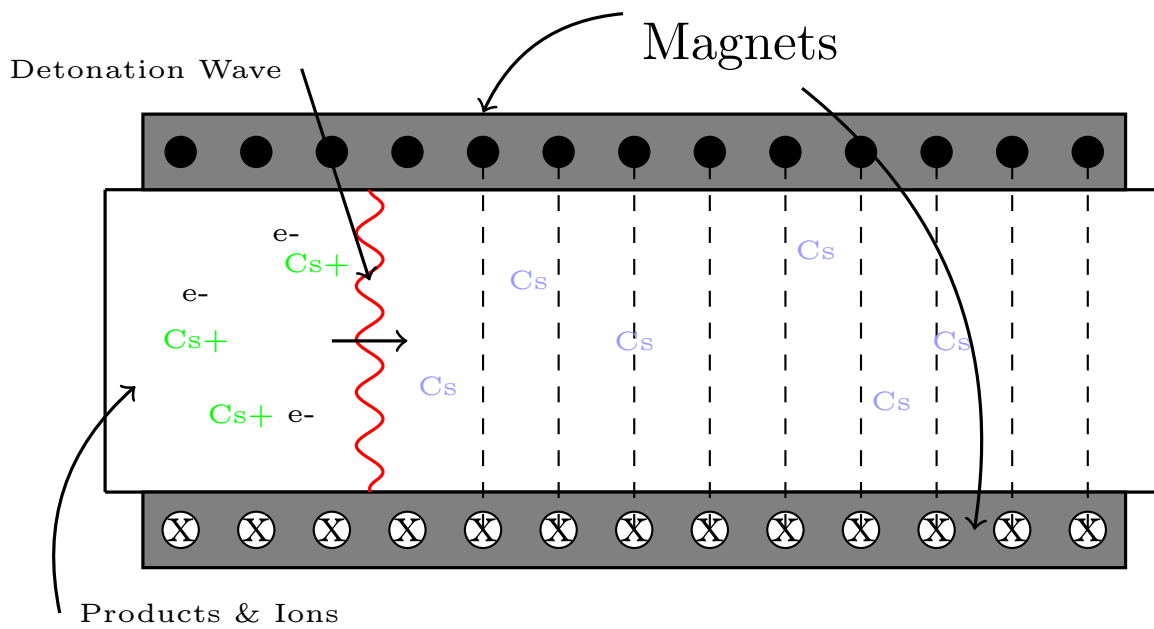


Figure 7.2: Configuration of spark-ignited detonation with an applied magnetic field.

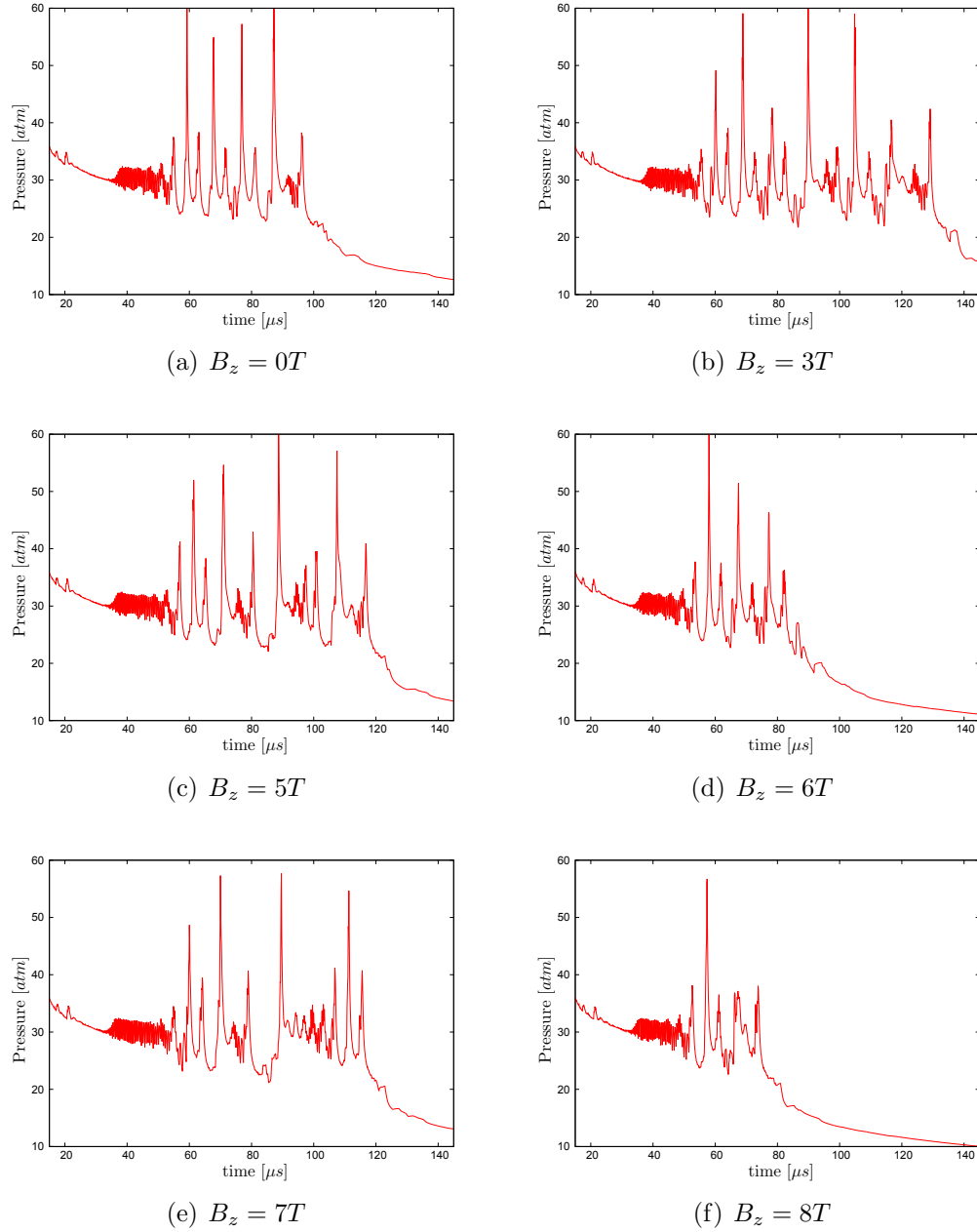


Figure 7.3: Peak pressure traces of detonations seeded with 1% cesium subjected to various magnetic field strengths B_z without an applied electric field ($\mathbf{K} = 0$). The MP5 scheme with $\Delta x = 5\mu m$ was used here.

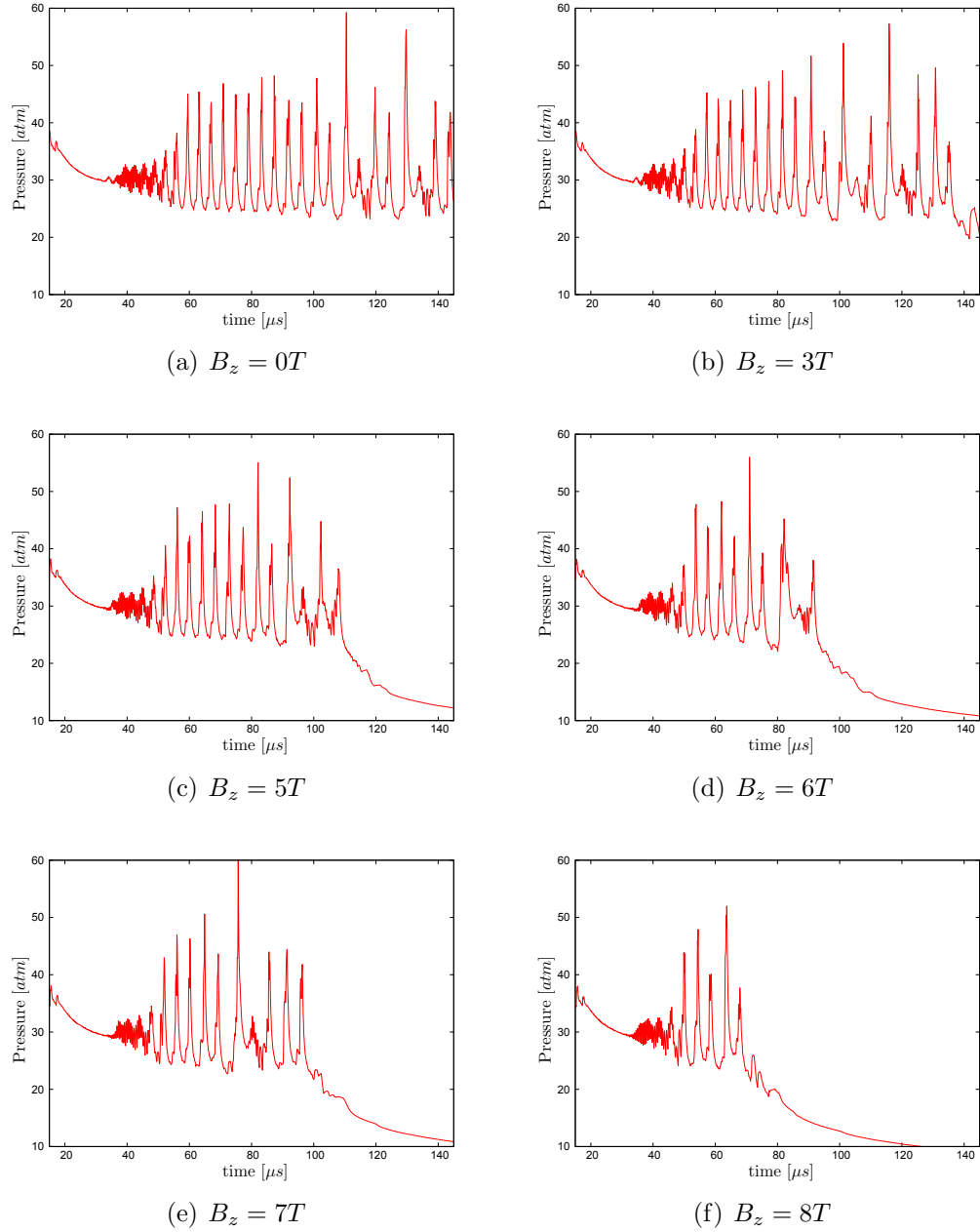


Figure 7.4: Peak pressure traces of detonations seeded with 5% cesium subjected to various magnetic field strengths, B_z without an applied electric field ($\mathbf{K} = 0$). The MP5 scheme with $\Delta x = 5\mu m$ was used here.

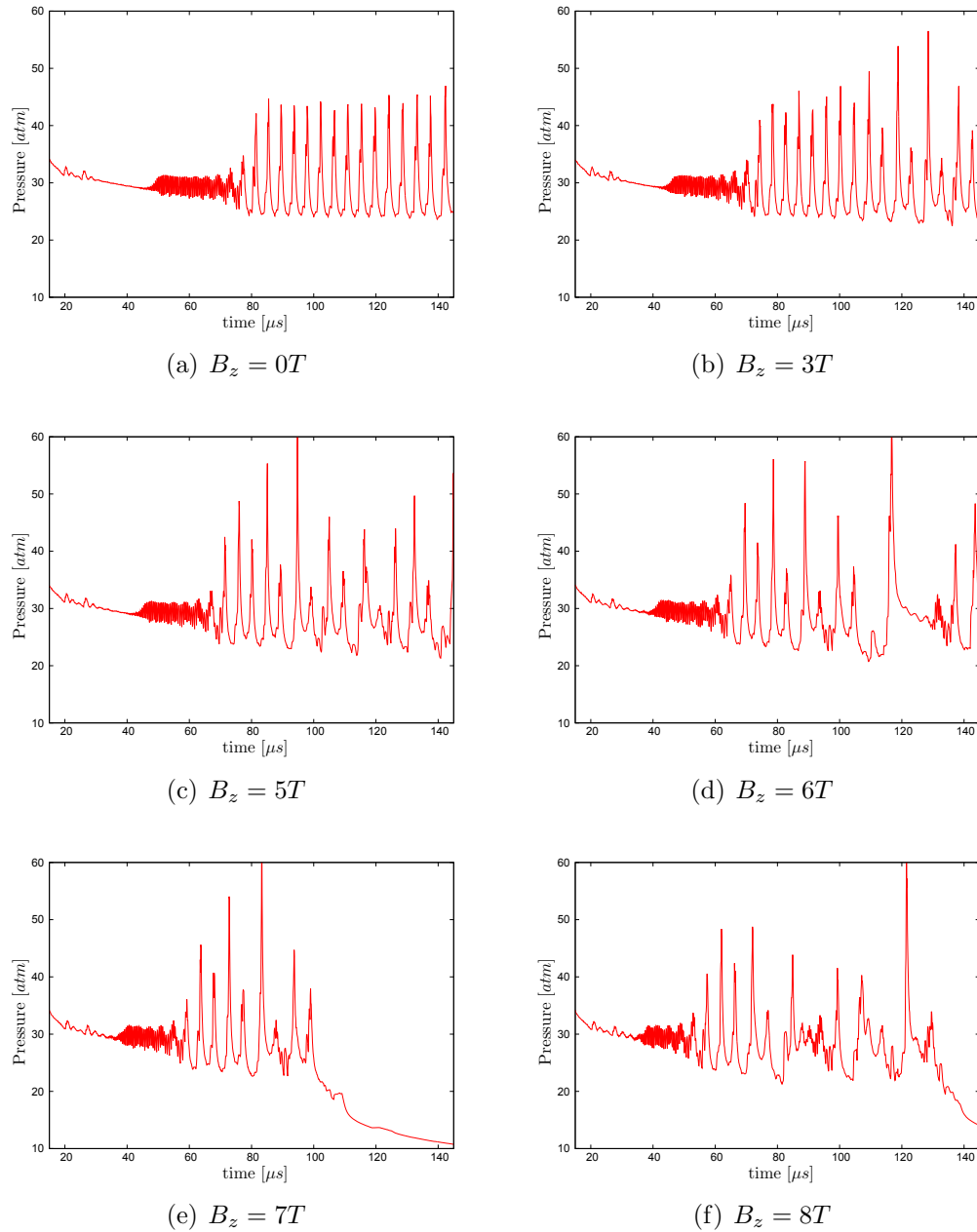


Figure 7.5: Peak pressure traces of detonations seeded with 10% cesium subjected to various magnetic field strengths B_z without an applied electric field ($\mathbf{K} = 0$). The MP5 scheme with $\Delta x = 5\mu m$ was used here.

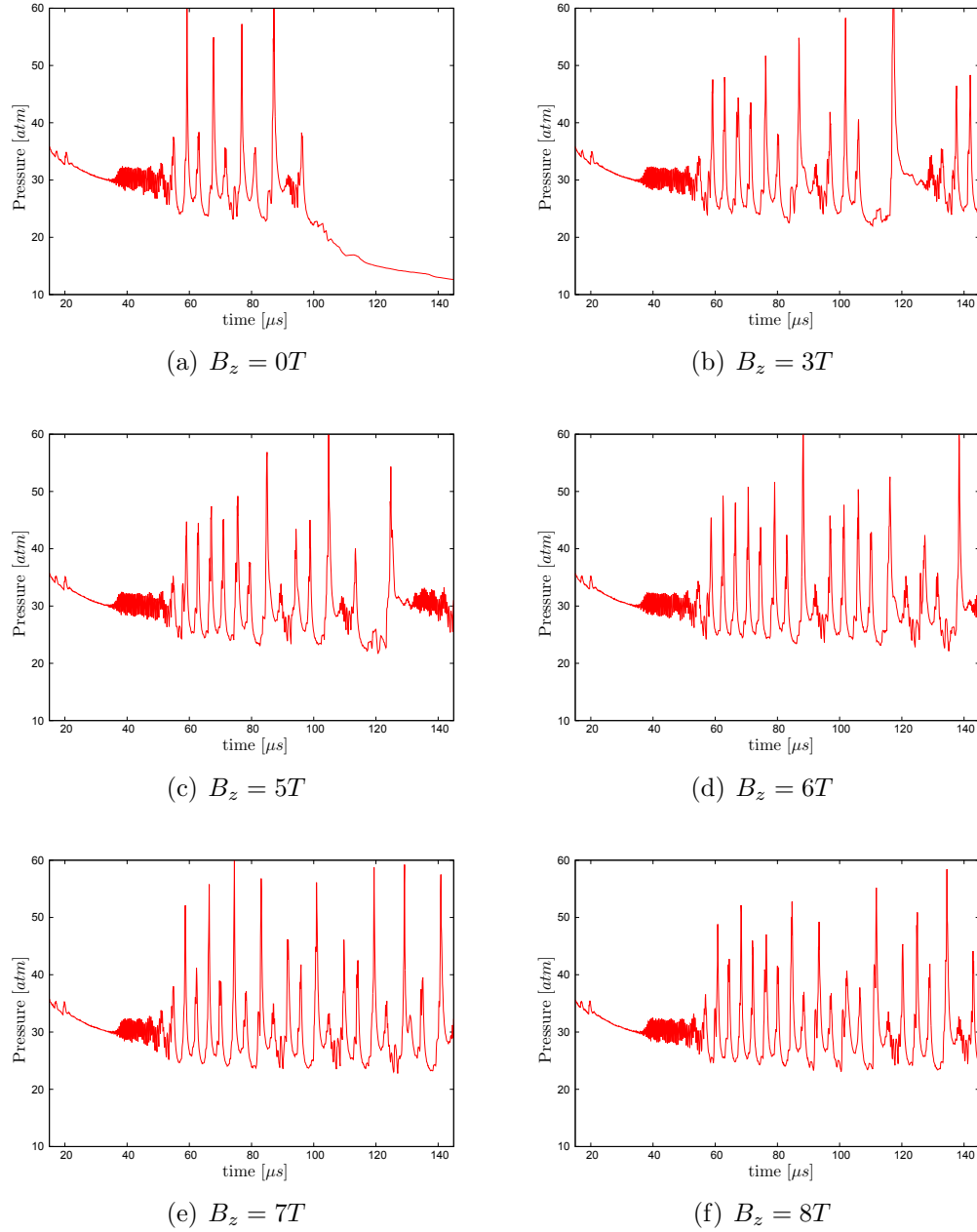


Figure 7.6: Peak pressure traces of detonations seeded with 1% cesium subjected to various magnetic field strengths B_z with an applied electric field ($K_y = 1.5$), for an “accelerator” configuration. The MP5 scheme with $\Delta x = 5\mu m$ was used here.

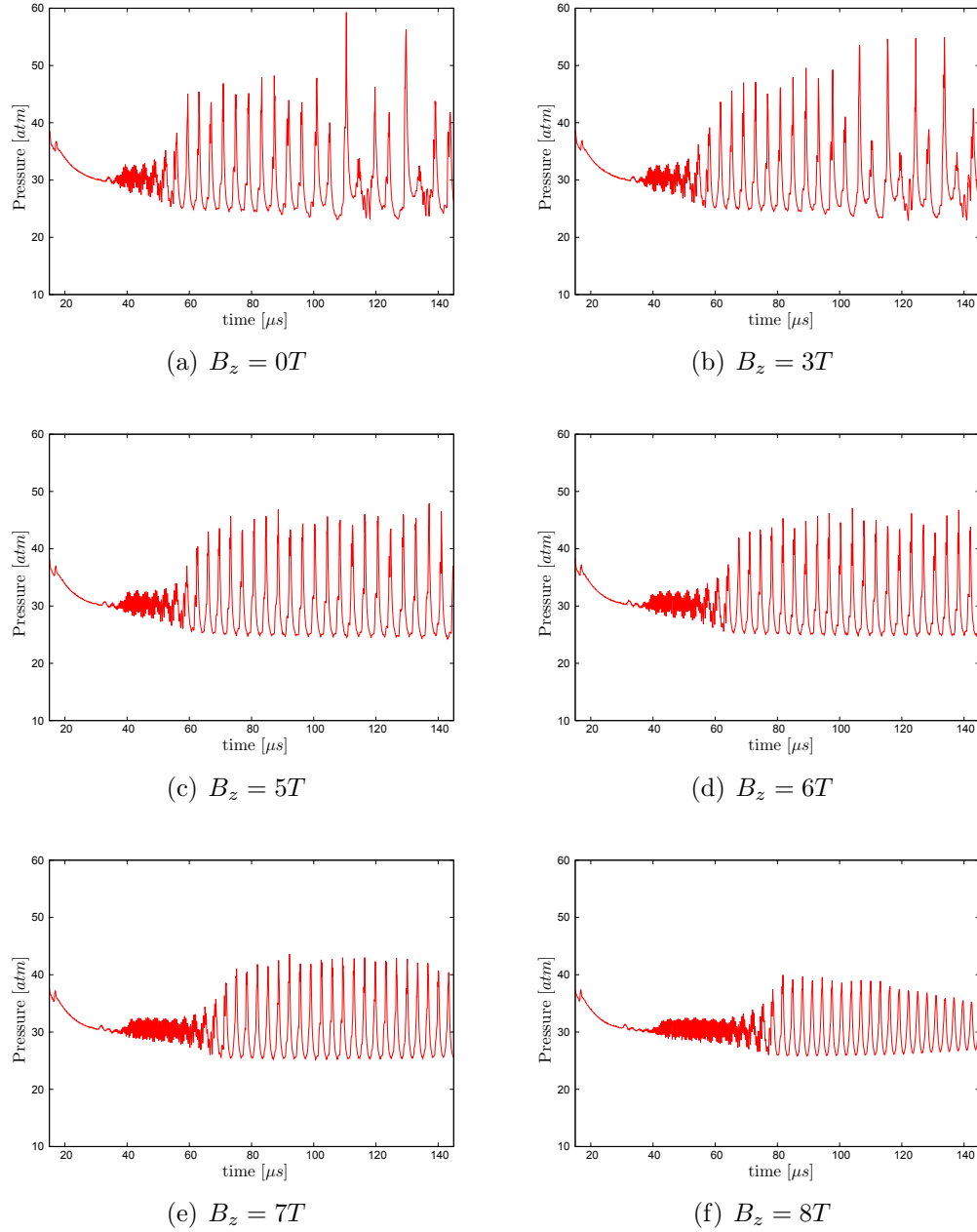


Figure 7.7: Peak pressure traces of detonations seeded with 5% cesium subjected to various magnetic field strengths B_z with an applied electric field ($K_y = 1.5$), for an “accelerator” configuration. The MP5 scheme with $\Delta x = 5\mu m$ was used here.

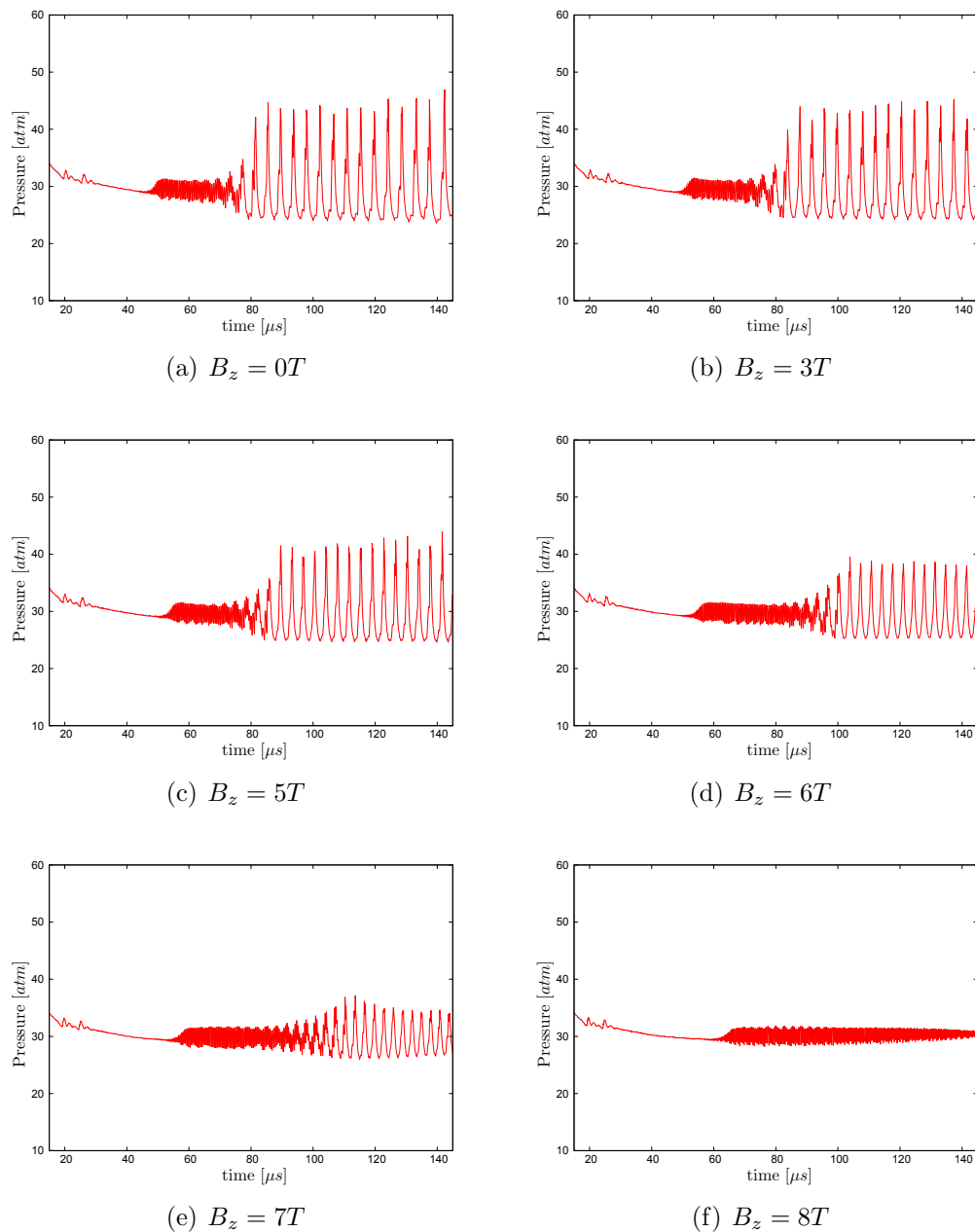
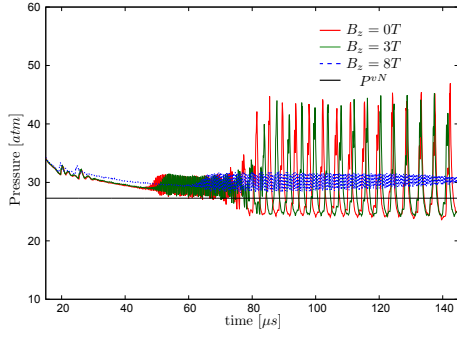
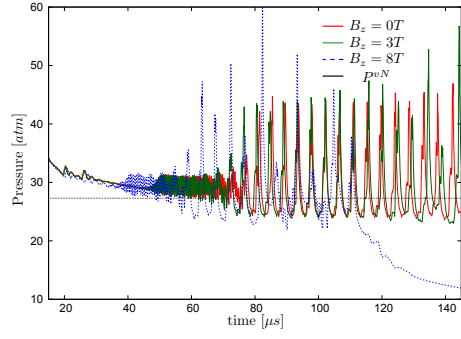


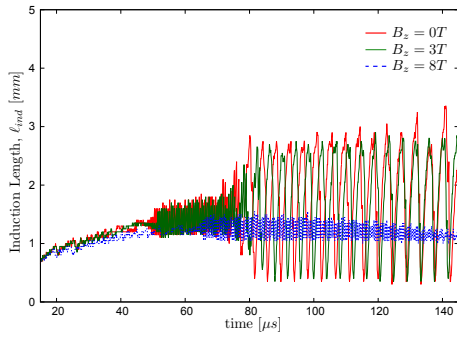
Figure 7.8: Peak pressure traces of detonations seeded with 10% cesium subjected to various magnetic field strengths B_z with an applied electric field ($K_y = 1.5$), for an “accelerator” configuration. The MP5 scheme with $\Delta x = 5\mu m$ was used here.



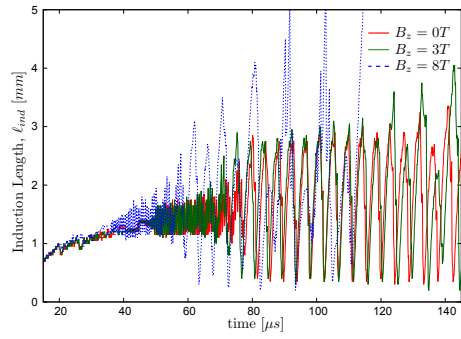
(a) Accelerator Peak pressure trace



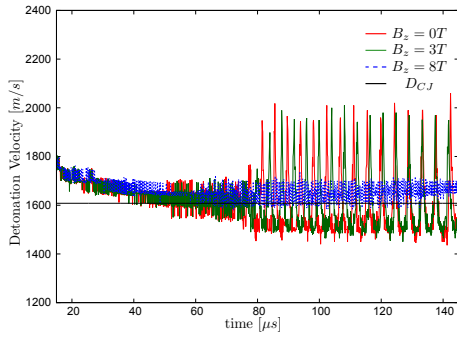
(b) Generator Peak pressure trace



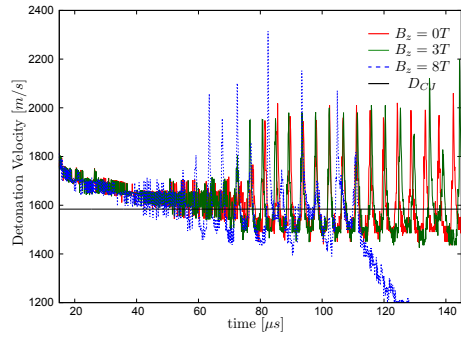
(c) Accelerator Induction Length



(d) Generator Induction Length



(e) Accelerator Detonation Velocity



(f) Generator Detonation Velocity

Figure 7.9: Time trace comparisons of $B_z = 0, 3,$ and $8T$ 1D detonations with 10% Cs in the accelerator configuration ($K_y = 1.5$) and generator configuration ($K_y = 0.5$) with $\Delta x = 5\mu m$.

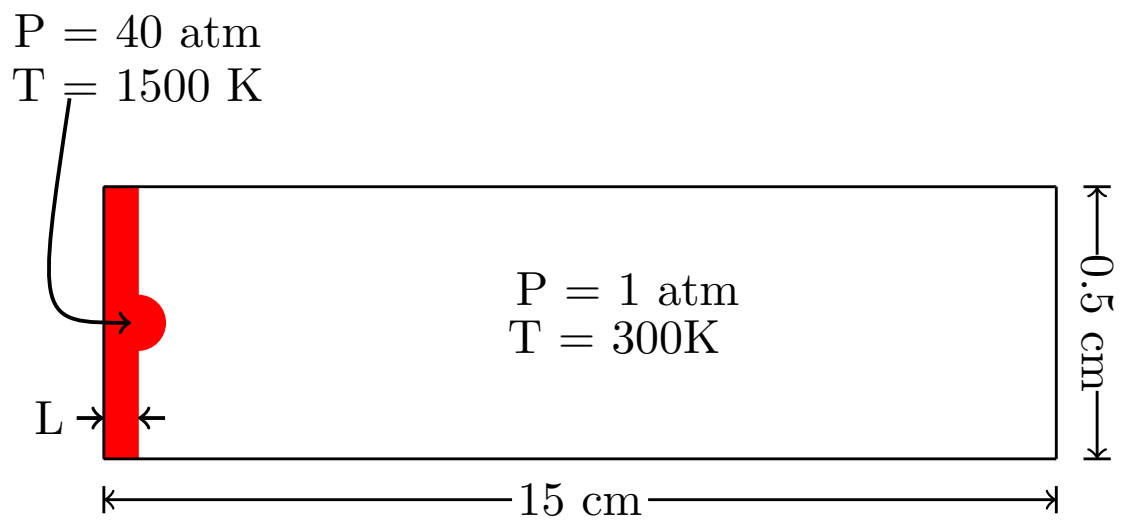


Figure 7.10: Computational setup for 2D detonation simulations, where the red region represents the computational spark.

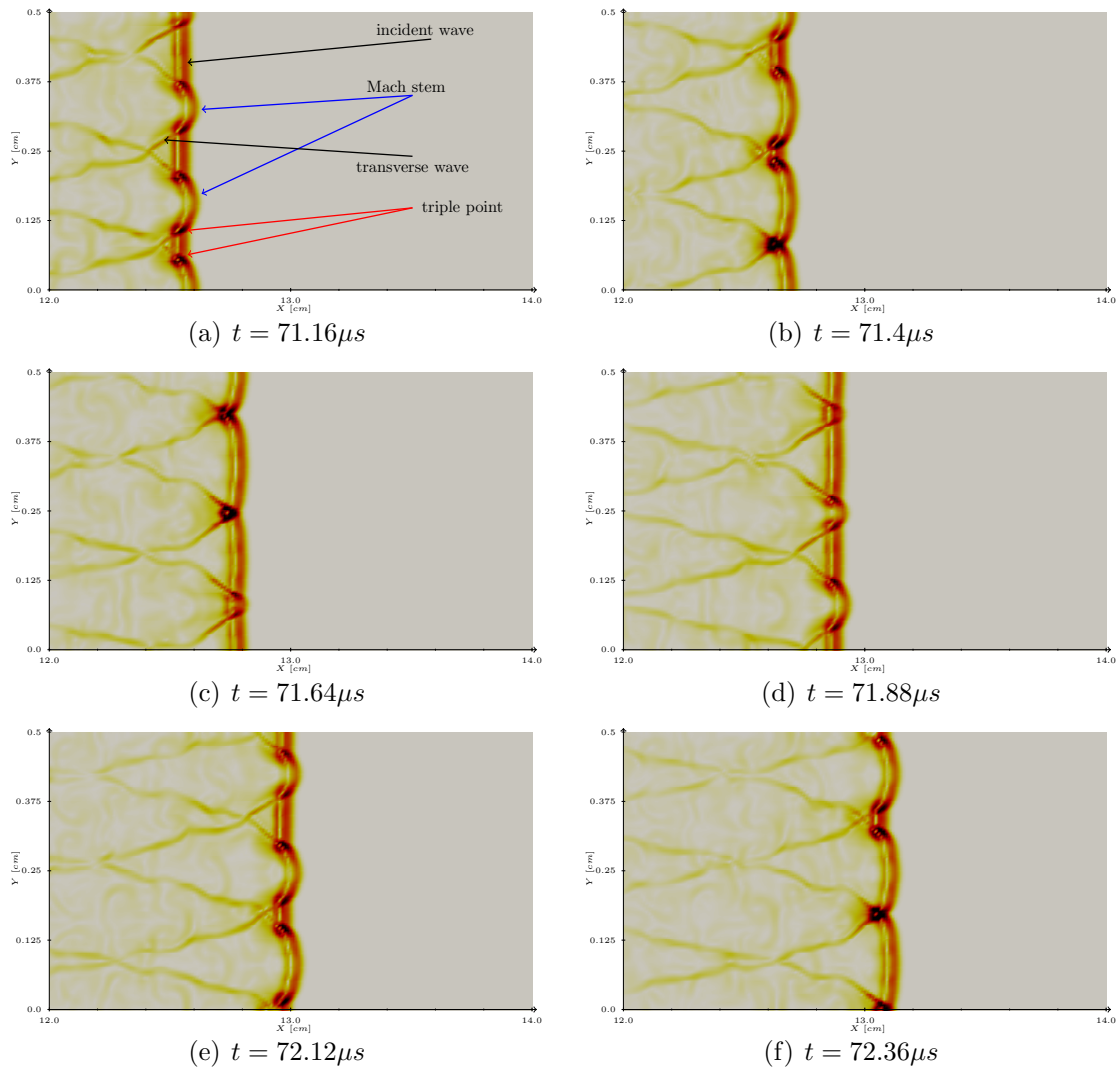
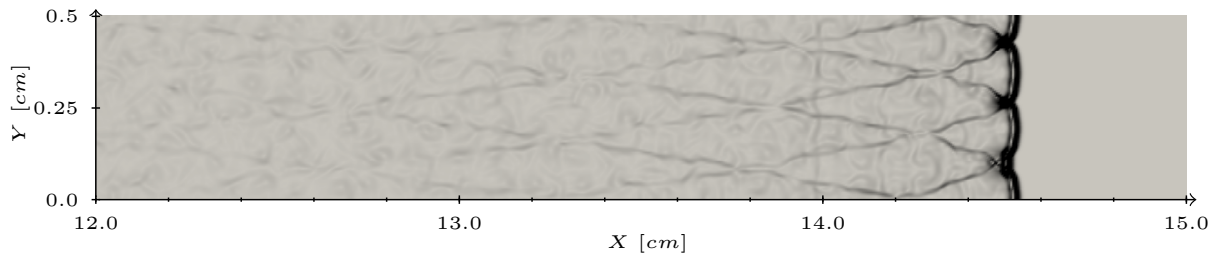
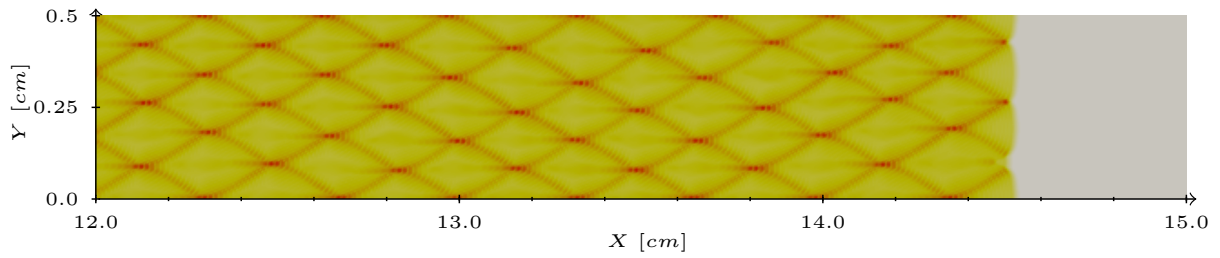


Figure 7.11: Schlieren-type plot using density gradients of the detonation front from time $71.16\mu s$ to $72.36\mu s$.



(a) Schlieren-type plot using density gradients of the detonation front




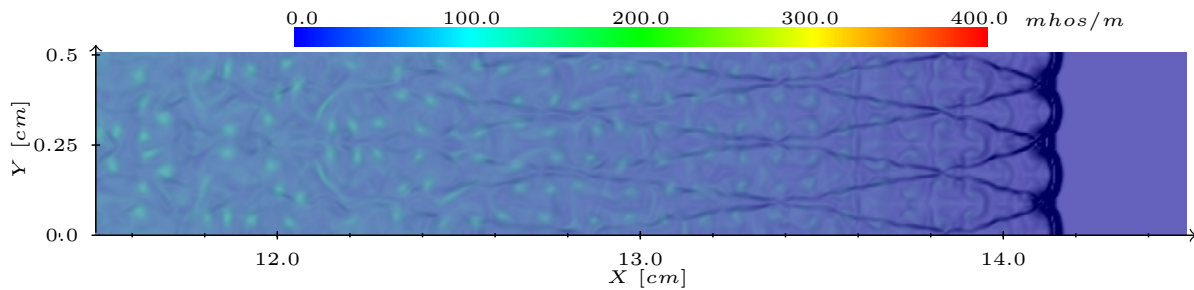
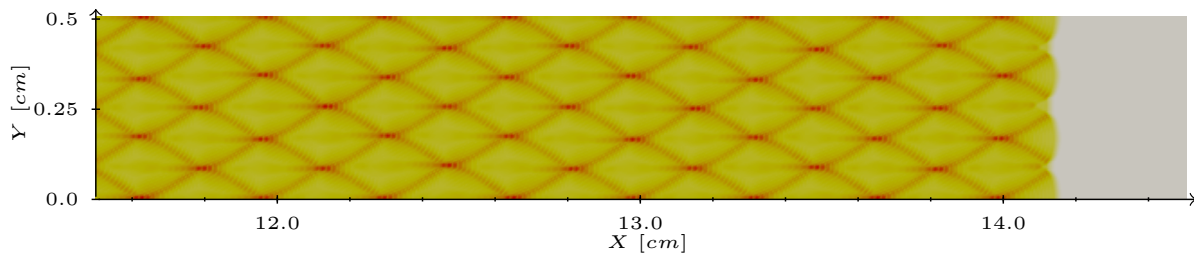
(b) Maximum pressure contour with linear color map (min  max)

Figure 7.12: Stoichiometric H_2 – Air detonation at $t = 75\mu s$ where $\Delta x = \Delta y = 50\mu m$ and $x : y \in [12, 15]cm : [0, 0.5]cm$.

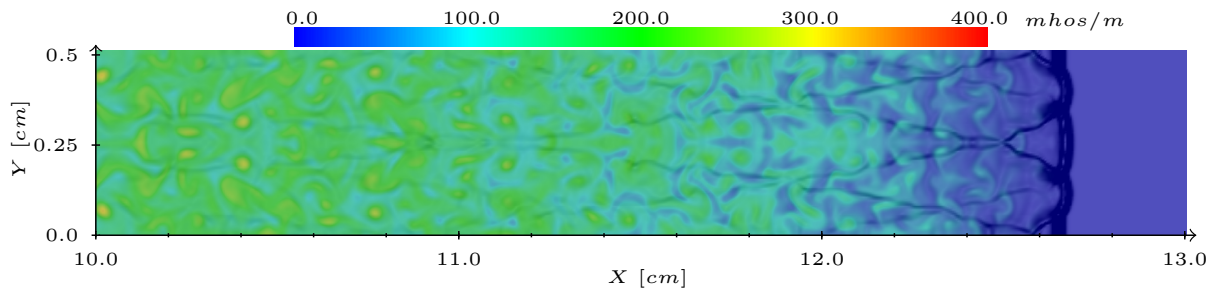


(a) Conductivity distribution with a linear color map overlaid on Schlieren-type plot using density gradients of the detonation front

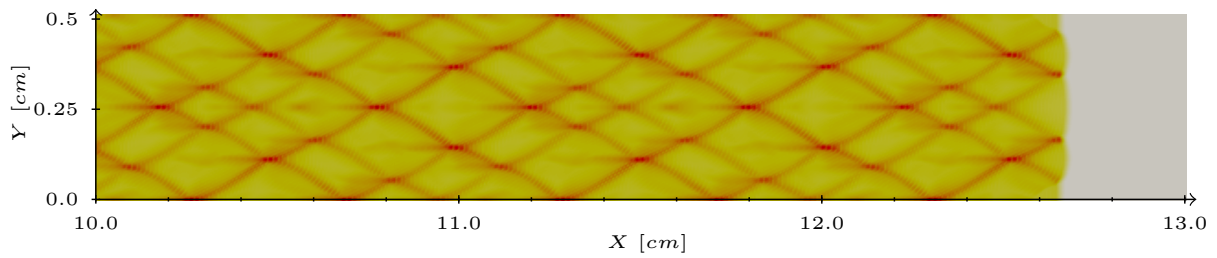


(b) Maximum pressure contour with linear color map (min to max)

Figure 7.13: Stoichiometric $H_2 - Air - 1\% Cs$ detonation at $t = 75 \mu s$ where $\Delta x = \Delta y = 50 \mu m$ and $x : y \in [11.5, 14.5] cm : [0, 0.5] cm$.



(a) Conductivity distribution with a linear color map overlaid on Schlieren-type plot using density gradients of the detonation front




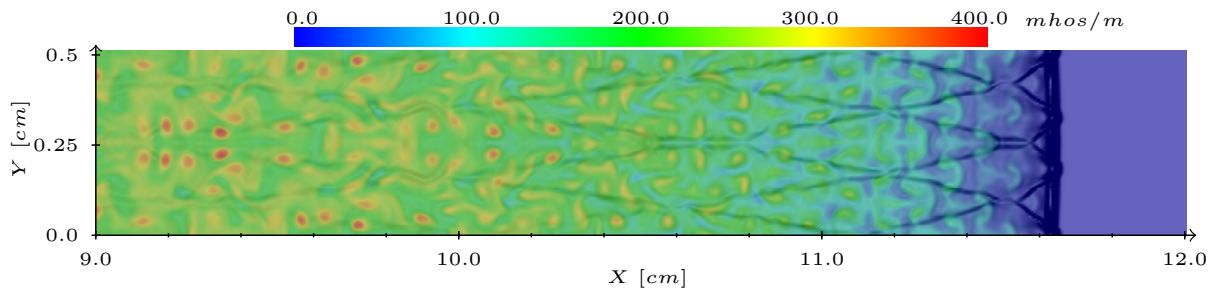
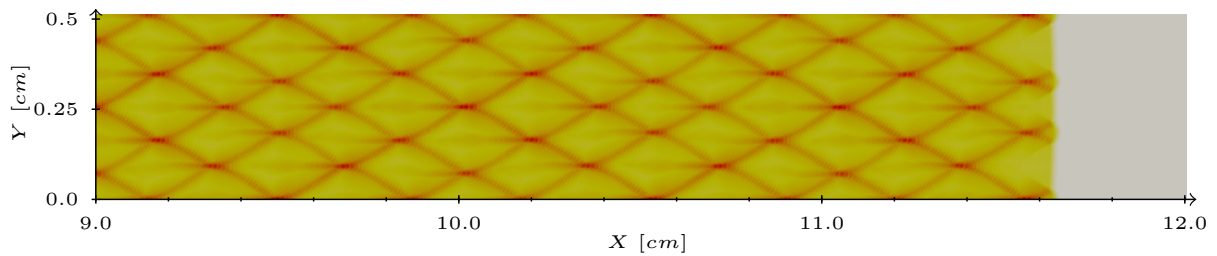
(b) Maximum pressure contour with linear color map (*min*  *max*)

Figure 7.14: Stoichiometric $H_2 - Air - 5\%Cs$ detonation at $t = 75\mu s$ where $\Delta x = \Delta y = 50\mu m$ and $x : y \in [10, 13]cm : [0, 0.5]cm$.



(a) Conductivity distribution with a linear color map overlaid on Schlieren-type plot using density gradients of the detonation front




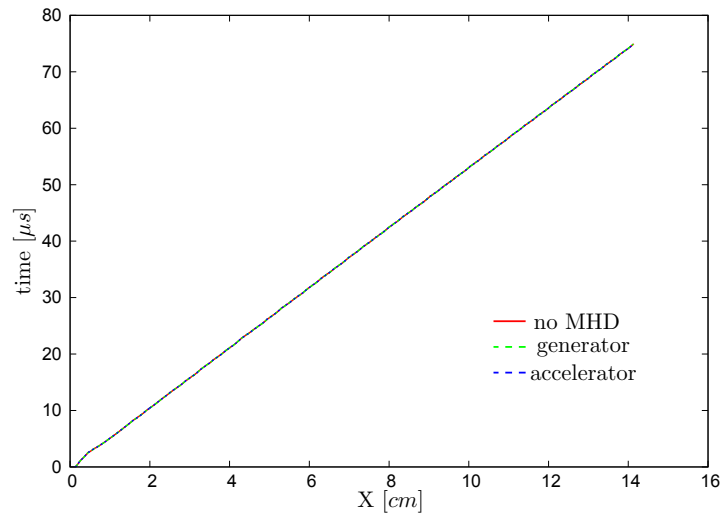
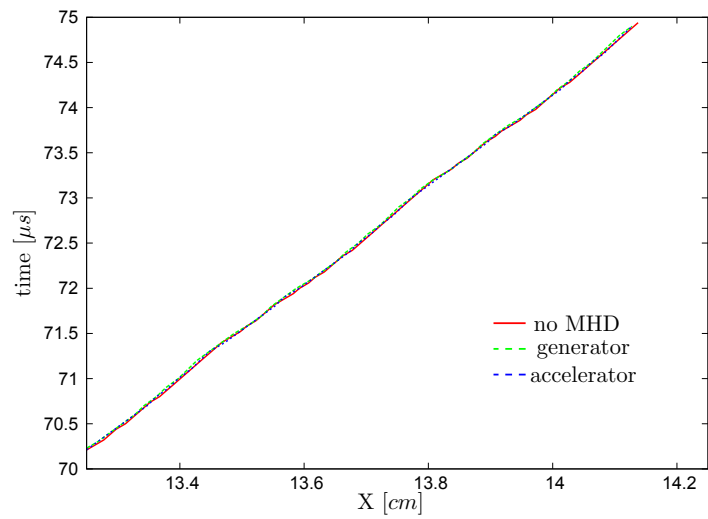
(b) Maximum pressure contour with linear color map (*min*  *max*)

Figure 7.15: Stoichiometric $H_2 - Air - 10\%Cs$ detonation at $t = 75\mu s$ where $\Delta x = \Delta y = 50\mu m$ and $x : y \in [9, 12]cm : [0, 0.5]cm$.

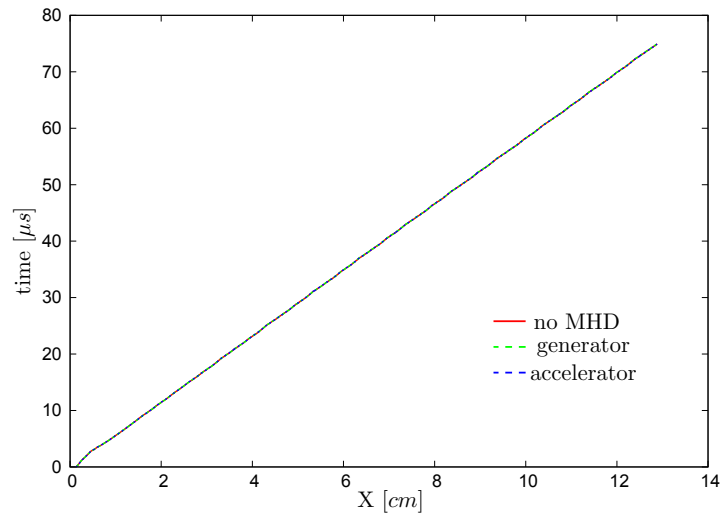


(a) Wide view

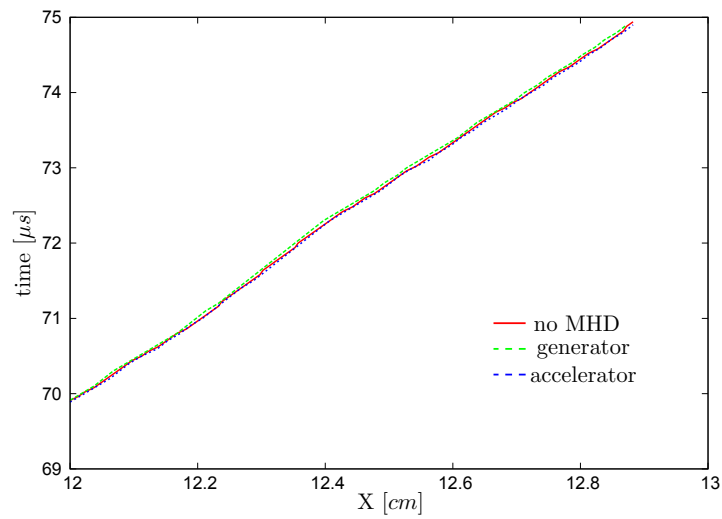


(b) Enlarged view

Figure 7.16: X-t plot comparing the progression of the leading shocks at the centerline of the 2D detonation with no MHD, generator, and accelerator configurations. Here the mixture has 1% Cs and $B_z = 8T$.

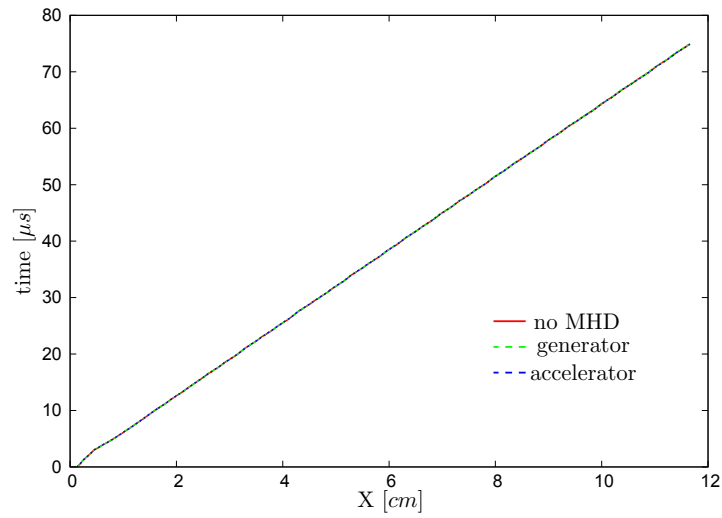


(a) Wide view

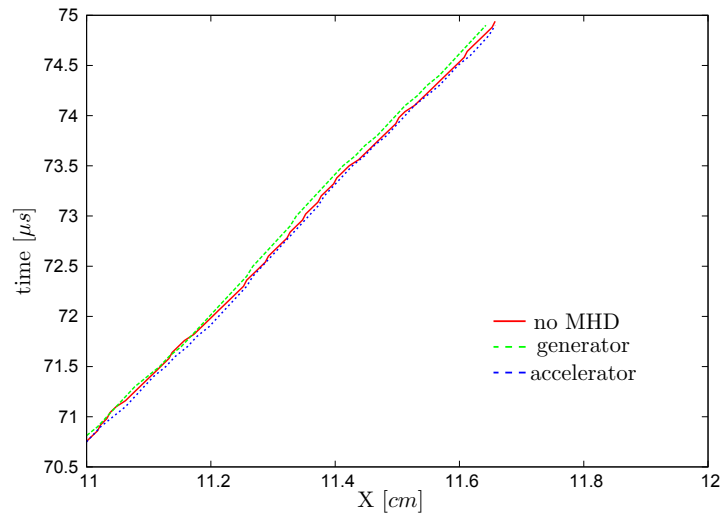


(b) Enlarged view

Figure 7.17: X-t plot comparing the progression of the leading shocks at the centerline of the 2D detonation with no MHD, generator, and accelerator configurations. Here the mixture has 5% Cs and $B_z = 8T$.

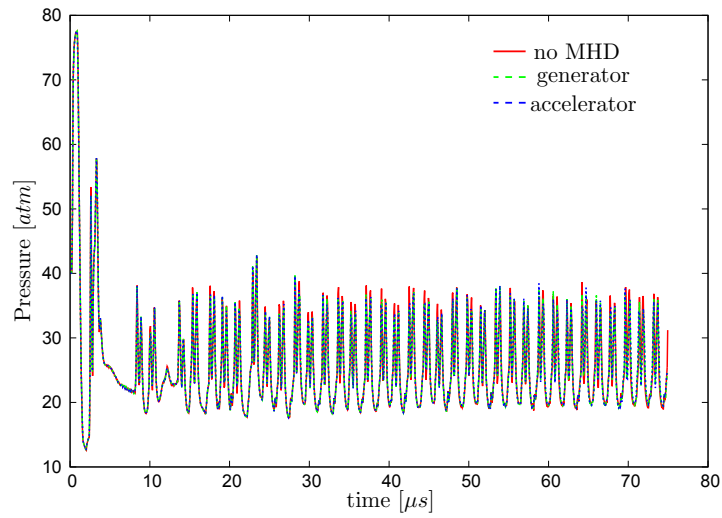


(a) Wide view

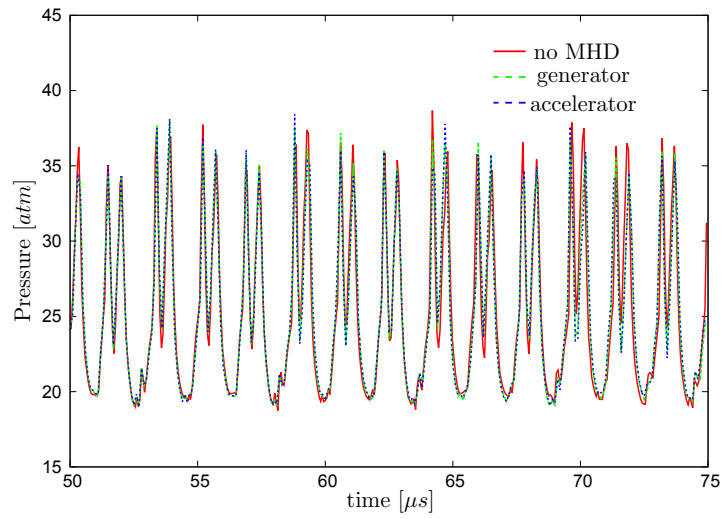


(b) Enlarged view

Figure 7.18: X-t plot comparing the progression of the leading shocks at the centerline of the 2D detonation with no MHD, generator, and accelerator configurations. Here the mixture has 10% Cs and $B_z = 8T$.

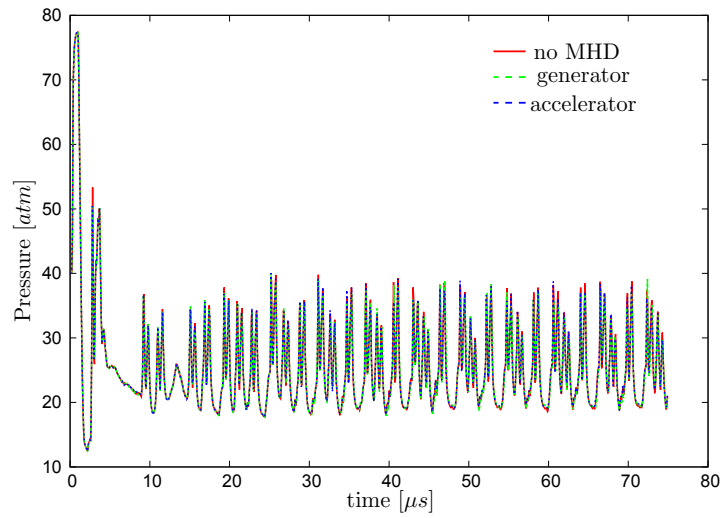


(a) Wide view

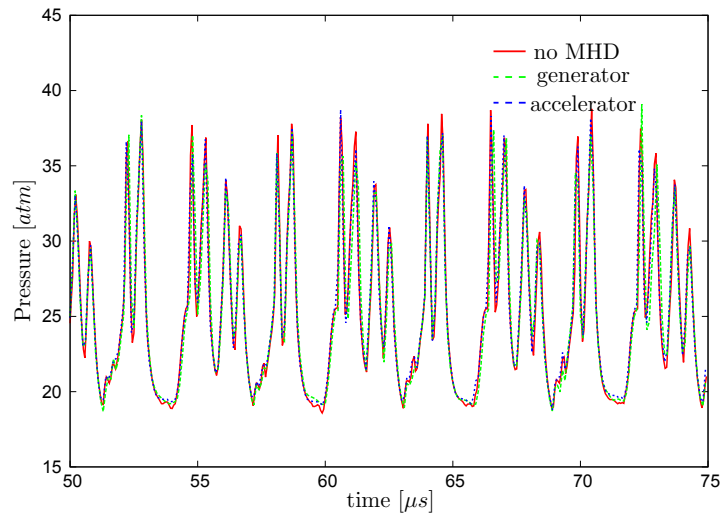


(b) Enlarged view

Figure 7.19: Peak pressure trace of the centerline of the leading shock of the 2D detonation with no MHD, generator, and accelerator configurations. Here the mixture has 1% Cs and $B_z = 8T$.

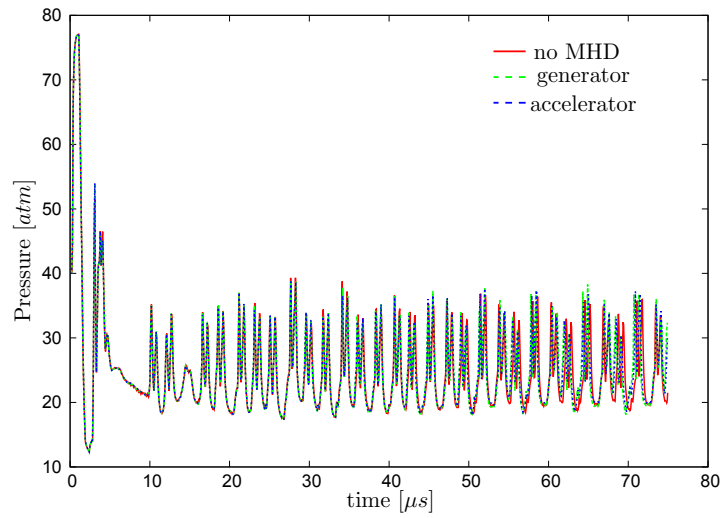


(a) Wide view

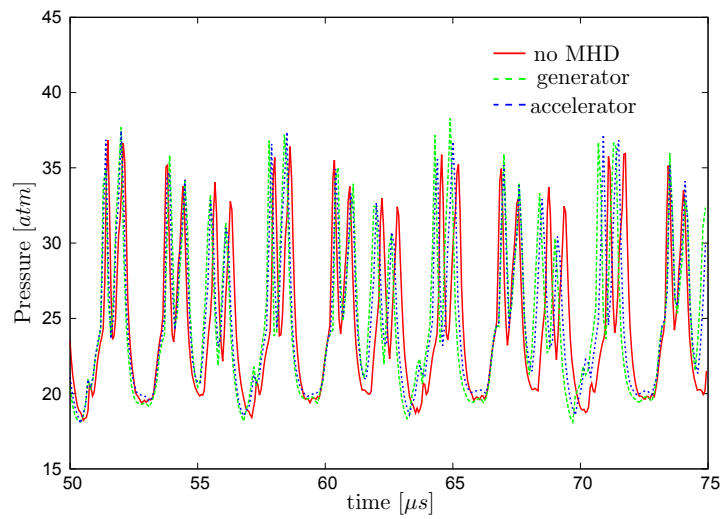


(b) Enlarged view

Figure 7.20: Peak pressure trace of the centerline of the leading shock of the 2D detonation with no MHD, generator, and accelerator configurations. Here the mixture has 5% Cs and $B_z = 8T$.



(a) Wide view



(b) Enlarged view

Figure 7.21: Peak pressure trace of the centerline of the leading shock of the 2D detonation with no MHD, generator, and accelerator configurations. Here the mixture has 10% Cs and $B_z = 8T$.

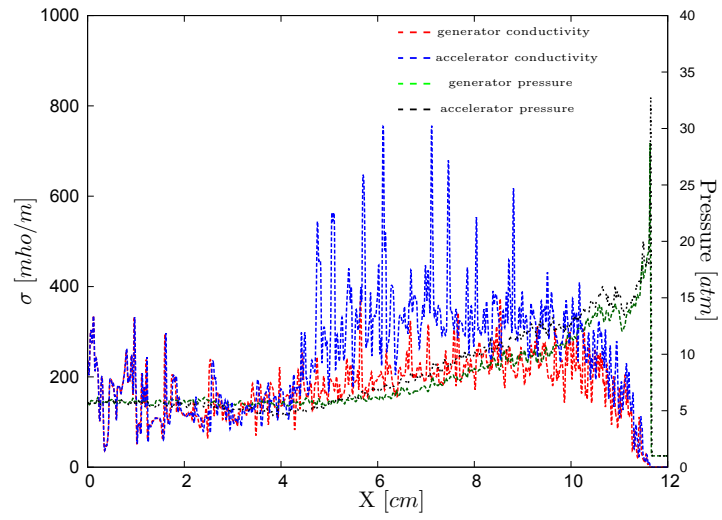


Figure 7.22: Centerline pressure and conductivity profiles for the accelerator and generator configurations with $B_z = 8T$ at $t = 75\mu s$.

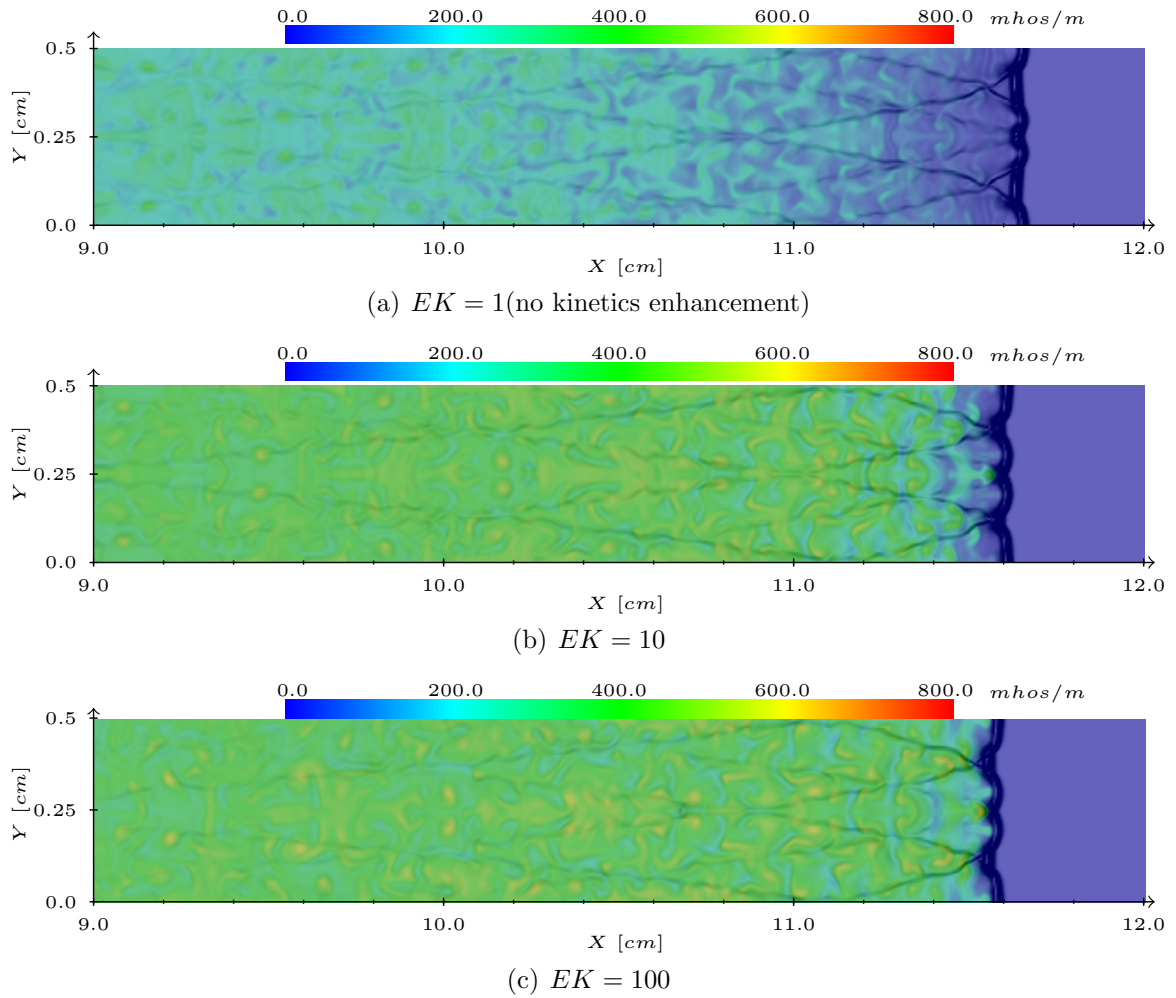


Figure 7.23: Conductivity distribution with a linear color map overlaid with Schlieren-type plot using density gradients of the detonation front in the generator configuration with 10% Cs and $B_z = 8T$, for different enhanced kinetic (EK) factors.

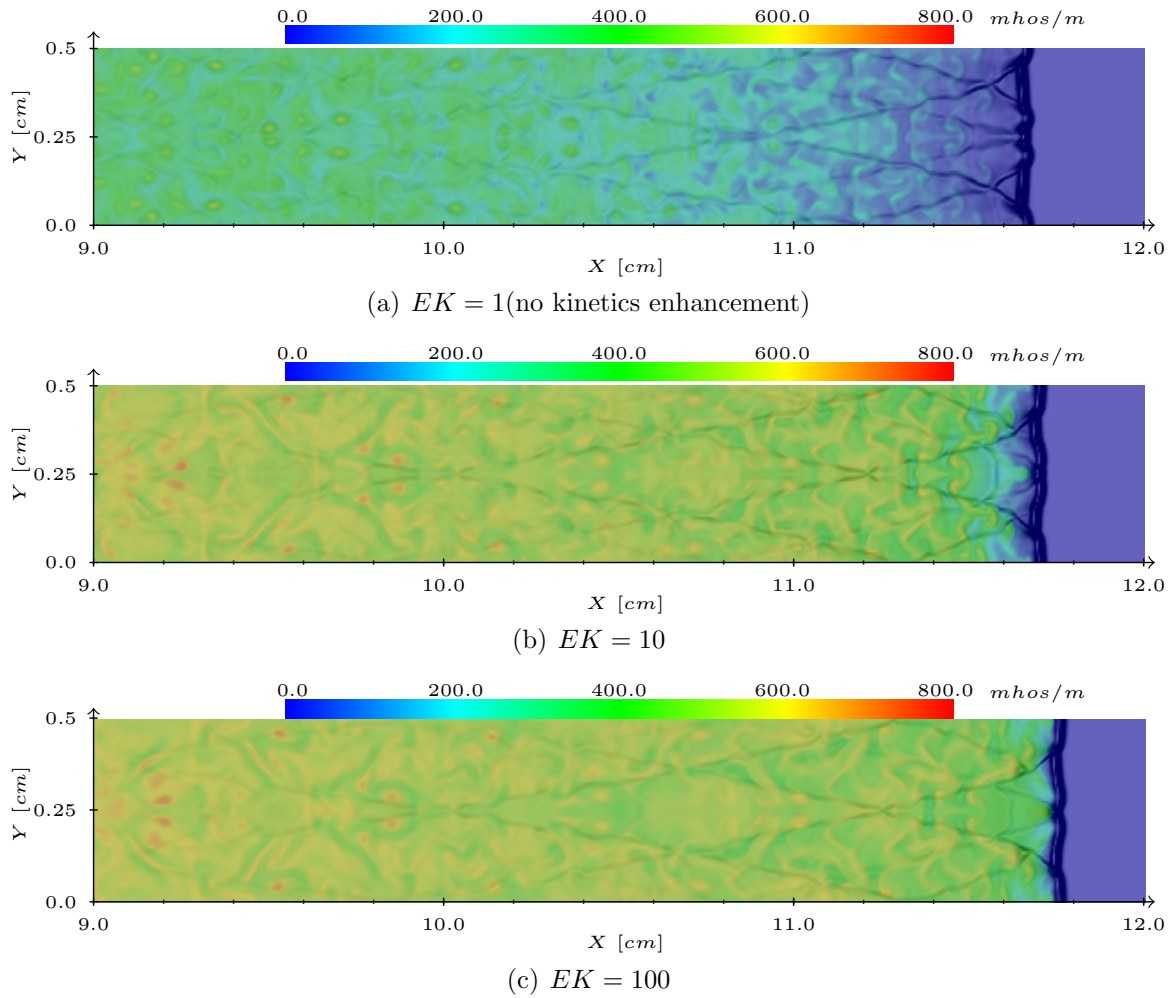
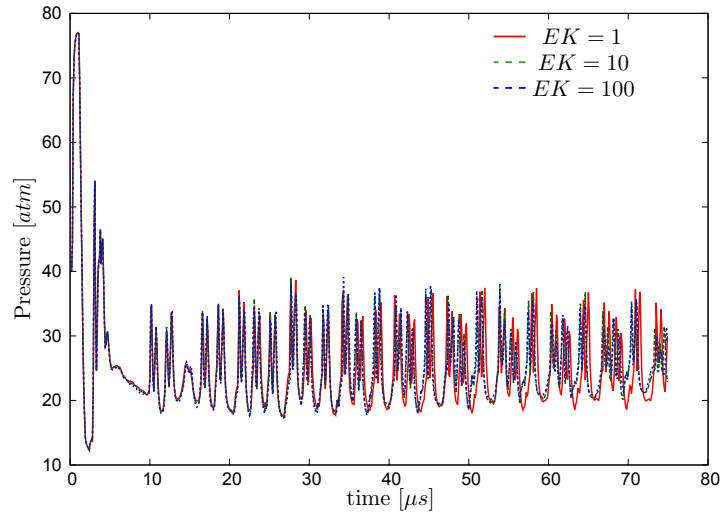
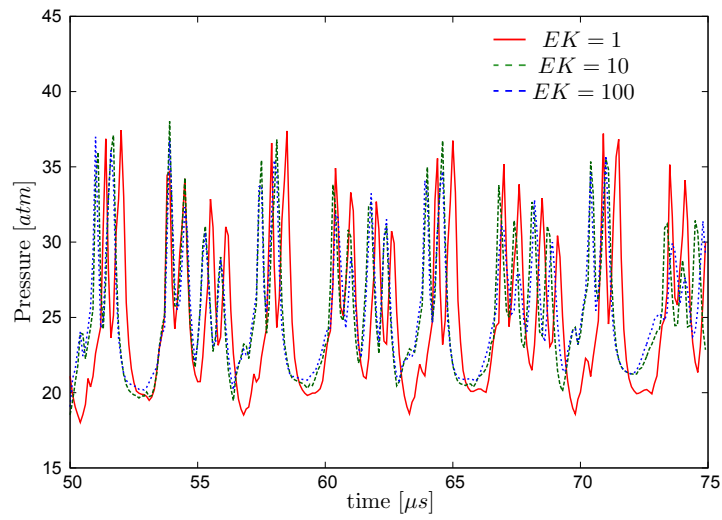


Figure 7.24: Conductivity distribution with a linear color map overlaid with Schlieren-type plot using density gradients of the detonation front in the accelerator configuration with 10% Cs and $B_z = 8T$, for different enhanced kinetic (EK) factors.

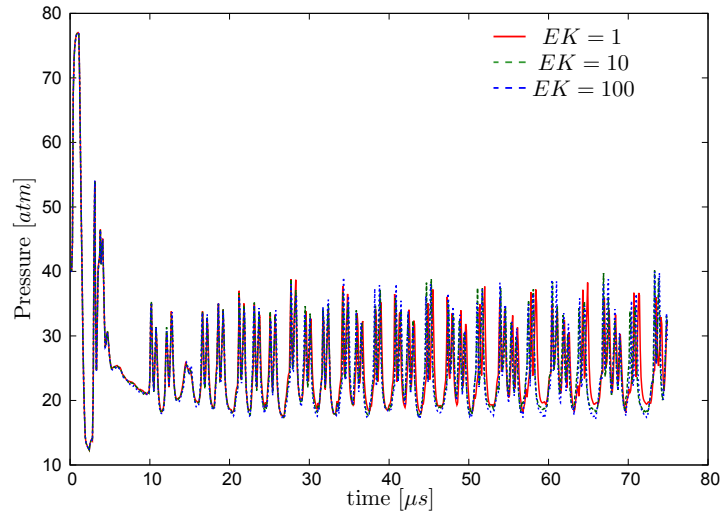


(a) Wide view

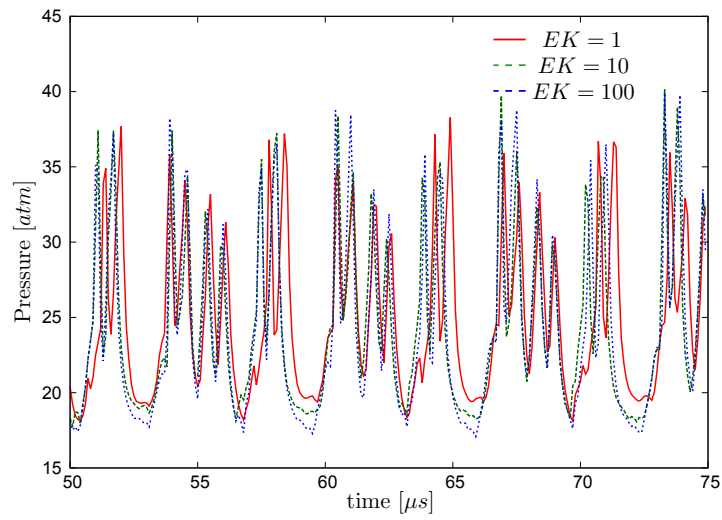


(b) Enlarged view

Figure 7.25: Centerline peak pressure trace of 2D detonation for the accelerator configurations with 10% Cs and $B_z = 8T$ with various enhanced kinetics values EK .

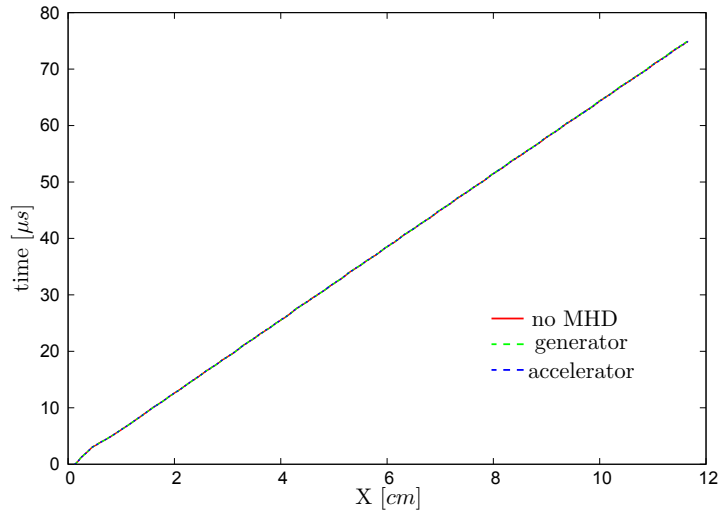


(a) Wide view

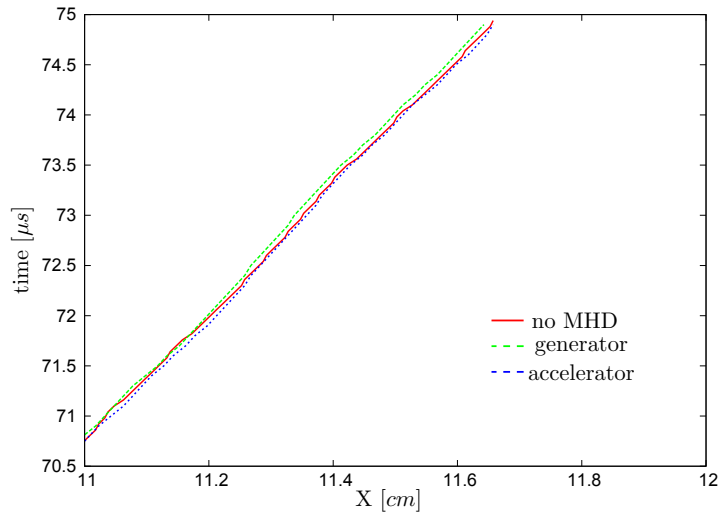


(b) Enlarged view

Figure 7.26: Centerline peak pressure trace of 2D detonation for the generator configurations with 10% Cs and $B_z = 8T$ with various enhanced kinetics values EK .

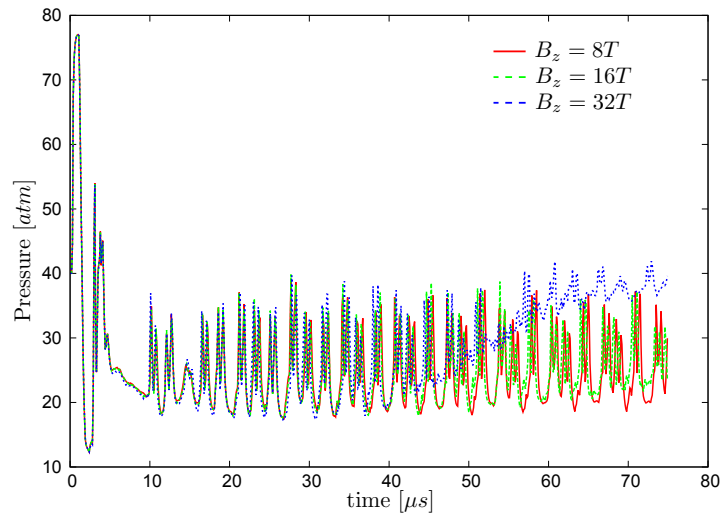


(a) Wide view

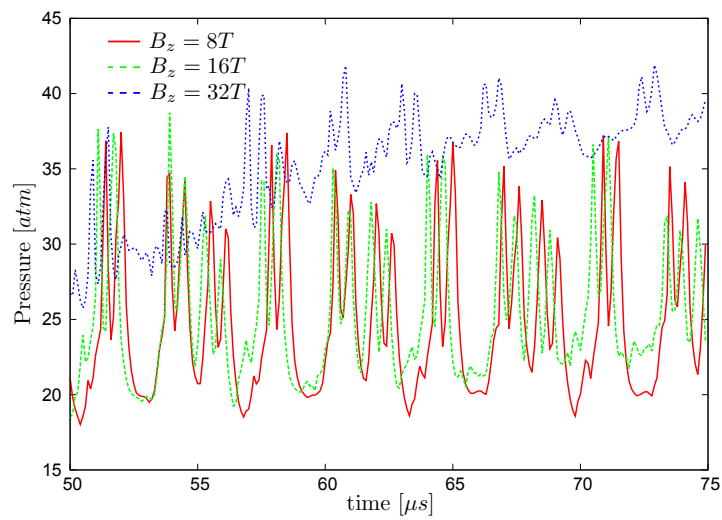


(b) Enlarged view

Figure 7.27: X-t plot of 2D detonation comparing the progression of the leading shocks at the centerline of the no MHD, generator, and accelerator configurations with $EK = 100$, 10% Cs and $B_z = 8T$.

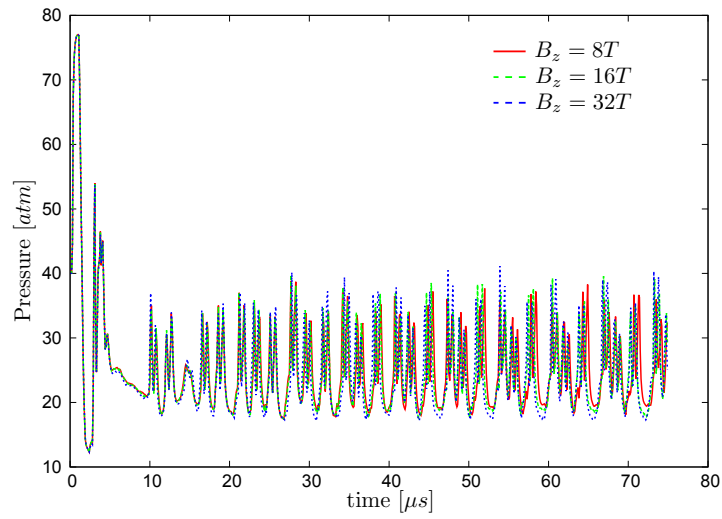


(a) Wide view

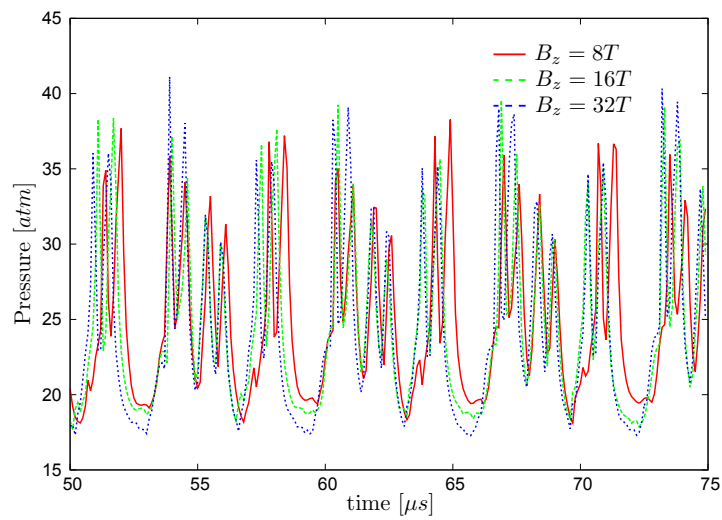


(b) Enlarged view

Figure 7.28: Centerline peak pressure trace of 2D detonation for the accelerator configuration with 10% Cs and various B_z values without enhanced kinetics.

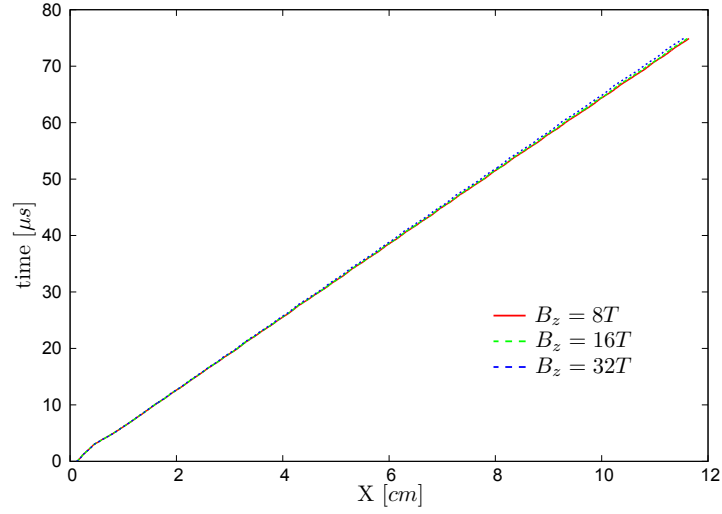


(a) Wide view

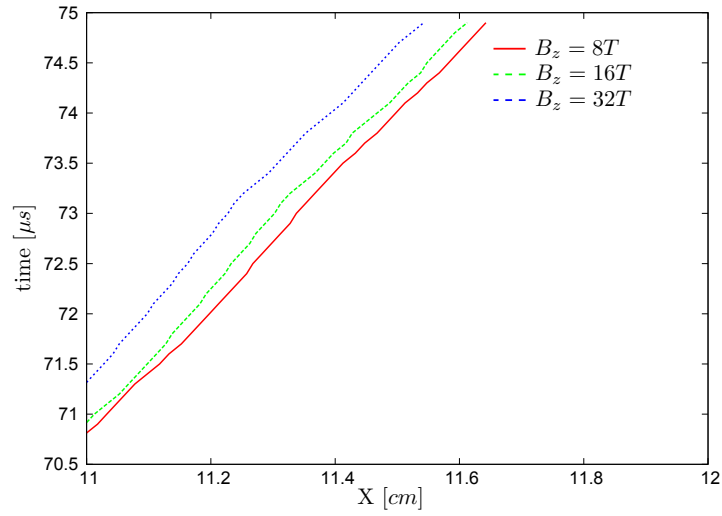


(b) Enlarged view

Figure 7.29: Centerline peak pressure trace of 2D detonation for the generator configuration with 10% Cs and various B_z values without enhanced kinetics.

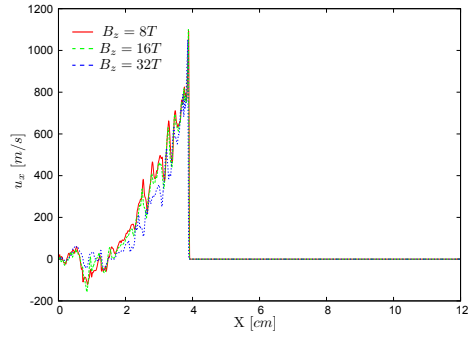


(a) Wide view

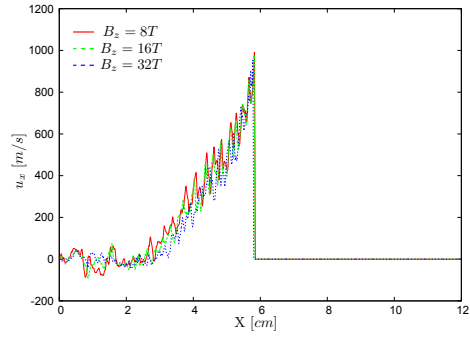


(b) Enlarged view

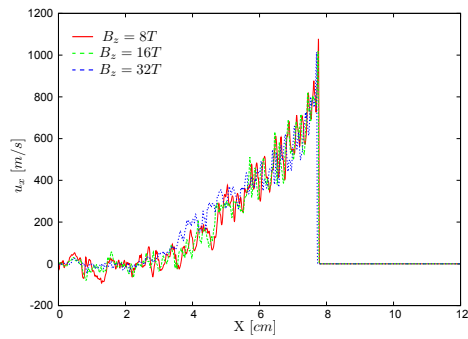
Figure 7.30: X-t plot of 2D detonation comparing the progression of the leading shocks at the centerline of the generator configuration with 10% Cs and various B_z values without enhanced kinetics.



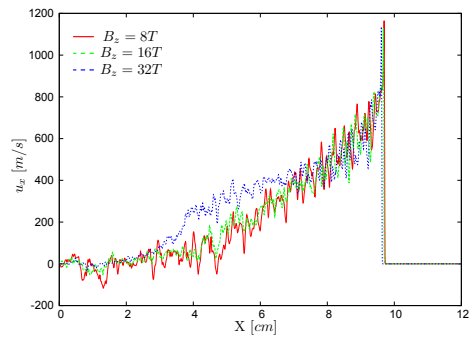
(a) $t = 25\mu s$



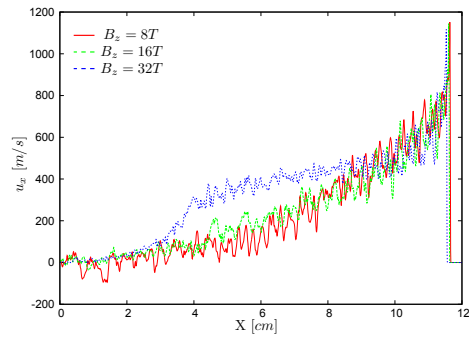
(b) $t = 37.5\mu s$



(c) $t = 50\mu s$



(d) $t = 62.5\mu s$



(e) $t = 75\mu s$

Figure 7.31: X-velocity profiles of 2D detonation at different times for the generator configuration with 10% Cs and various B_z values without enhanced kinetics.

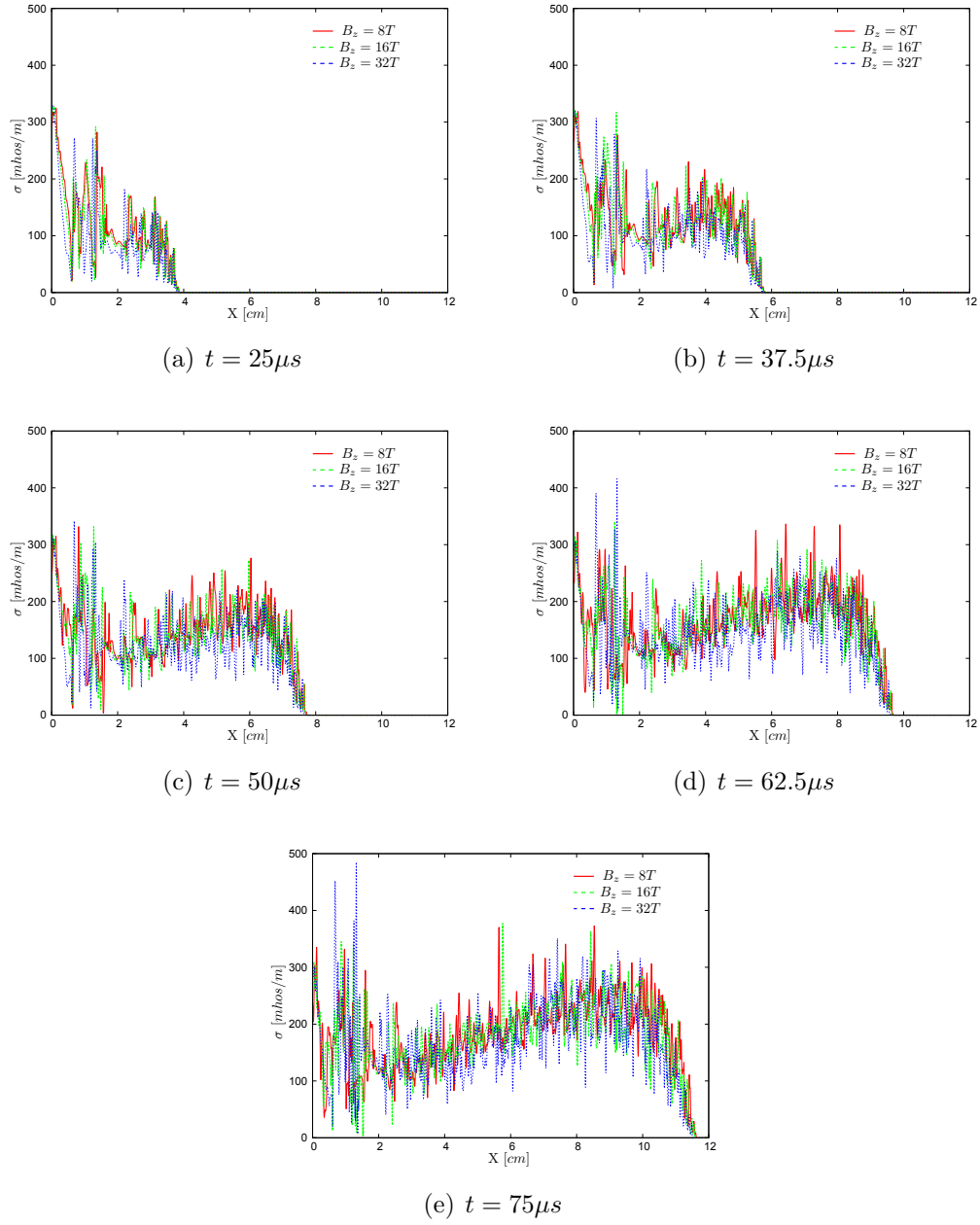
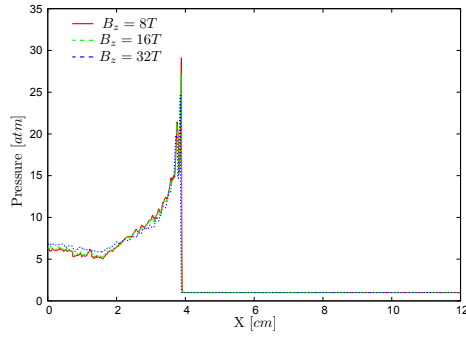
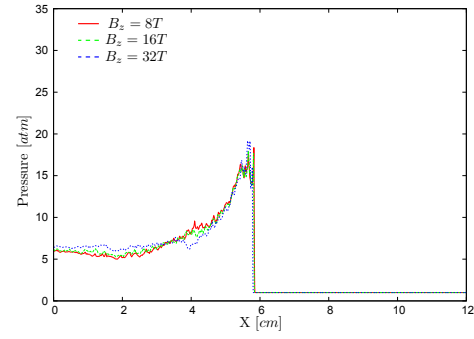


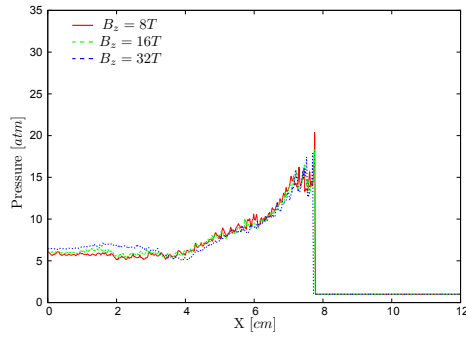
Figure 7.32: Conductivity profiles of 2D detonation at different times for the generator configuration with 10% Cs and various B_z values without enhanced kinetics.



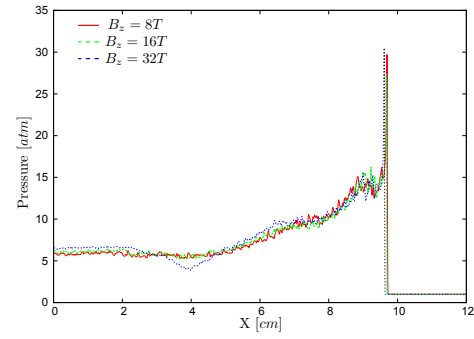
(a) $t = 25\mu s$



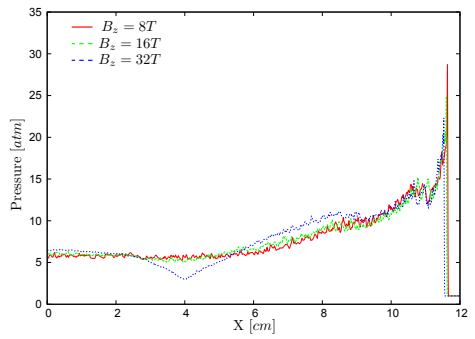
(b) $t = 37.5\mu s$



(c) $t = 50\mu s$

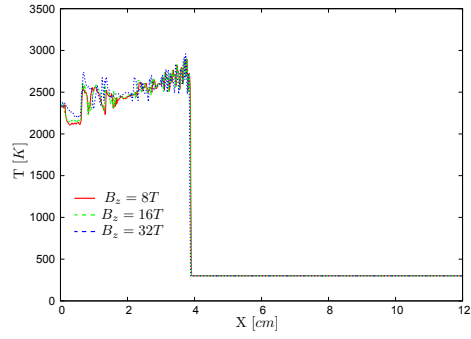


(d) $t = 62.5\mu s$

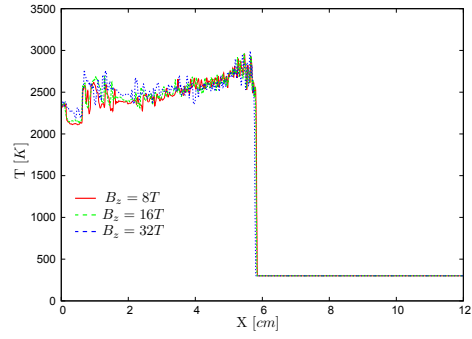


(e) $t = 75\mu s$

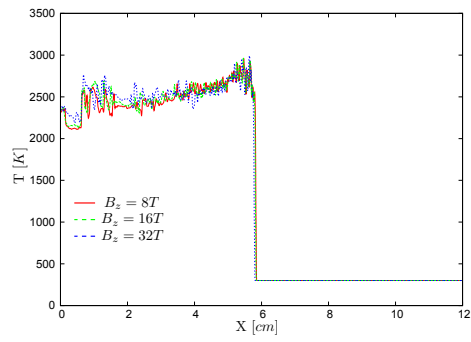
Figure 7.33: Pressure profiles of 2D detonation at different times for the generator configuration with 10% Cs and various B_z values without enhanced kinetics.



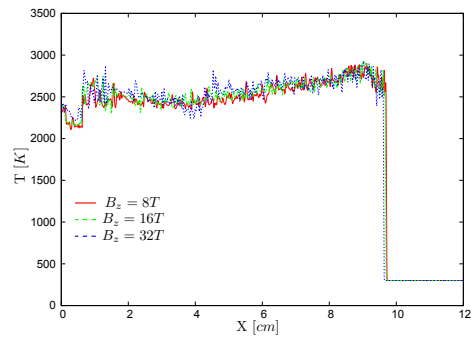
(a) $t = 25 \mu s$



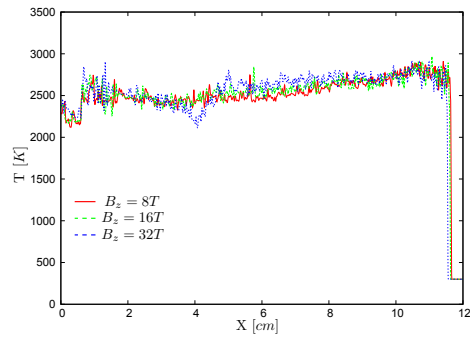
(b) $t = 37.5 \mu s$



(c) $t = 50 \mu s$



(d) $t = 62.5 \mu s$



(e) $t = 75 \mu s$

Figure 7.34: Temperature profiles of 2D detonation at different times for the generator configuration with 10% Cs and various B_z values without enhanced kinetics.

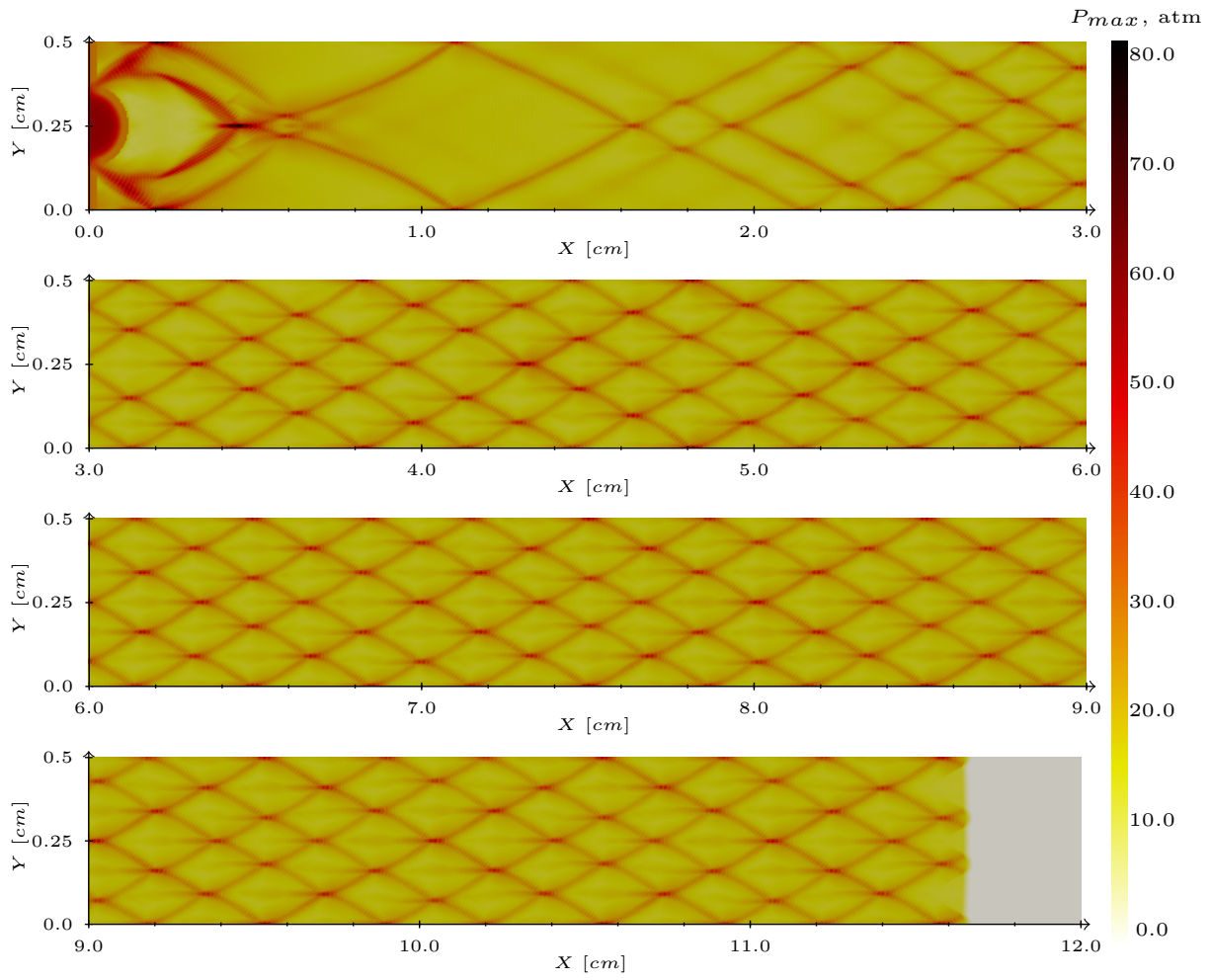


Figure 7.35: Detonation history presented by maximum pressure contours without MHD($B_z = 0T$) for 10% Cs.

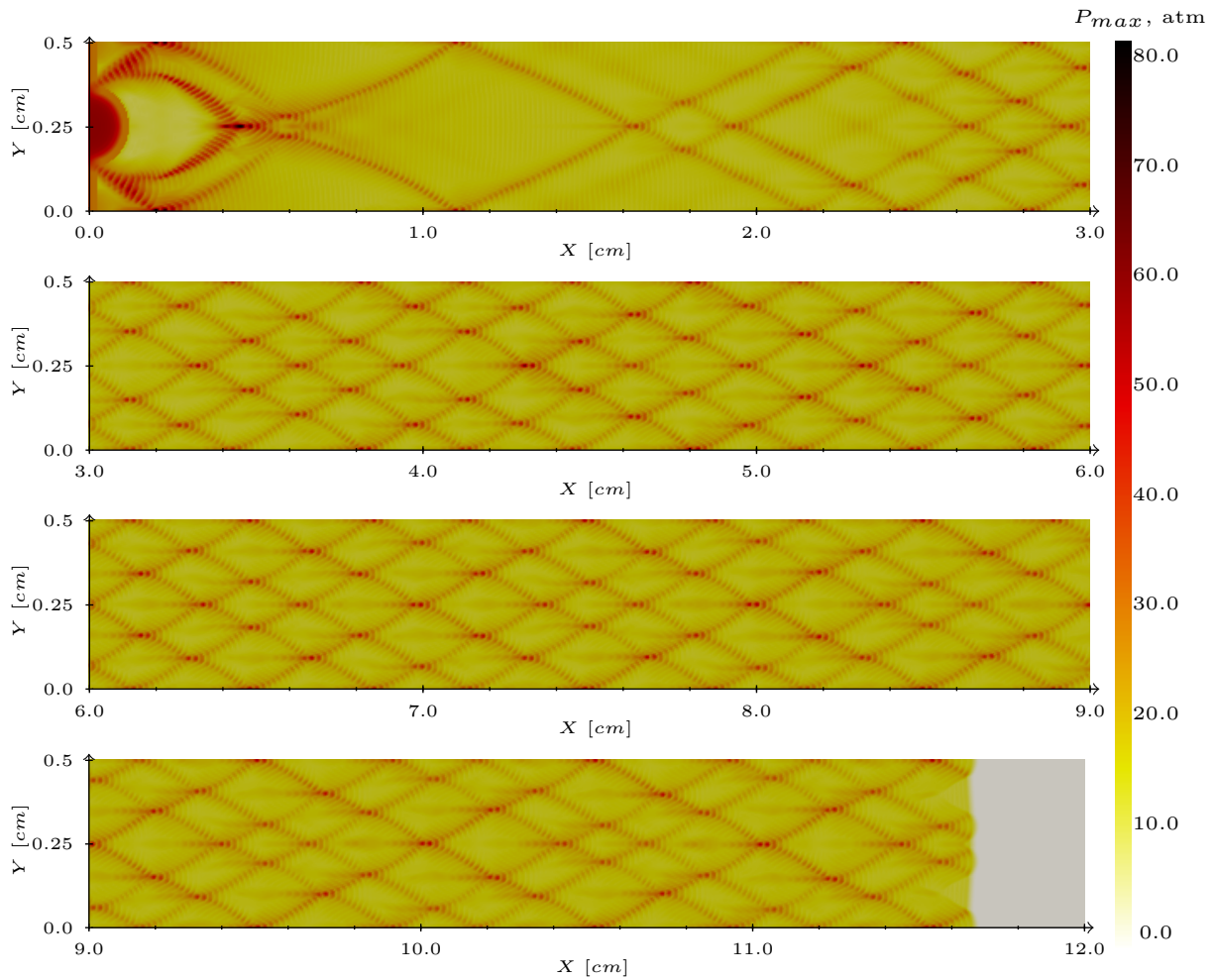


Figure 7.36: Detonation history presented by maximum pressure contours. Accelerator configuration with $B_z = 8T$ and 10% Cs.

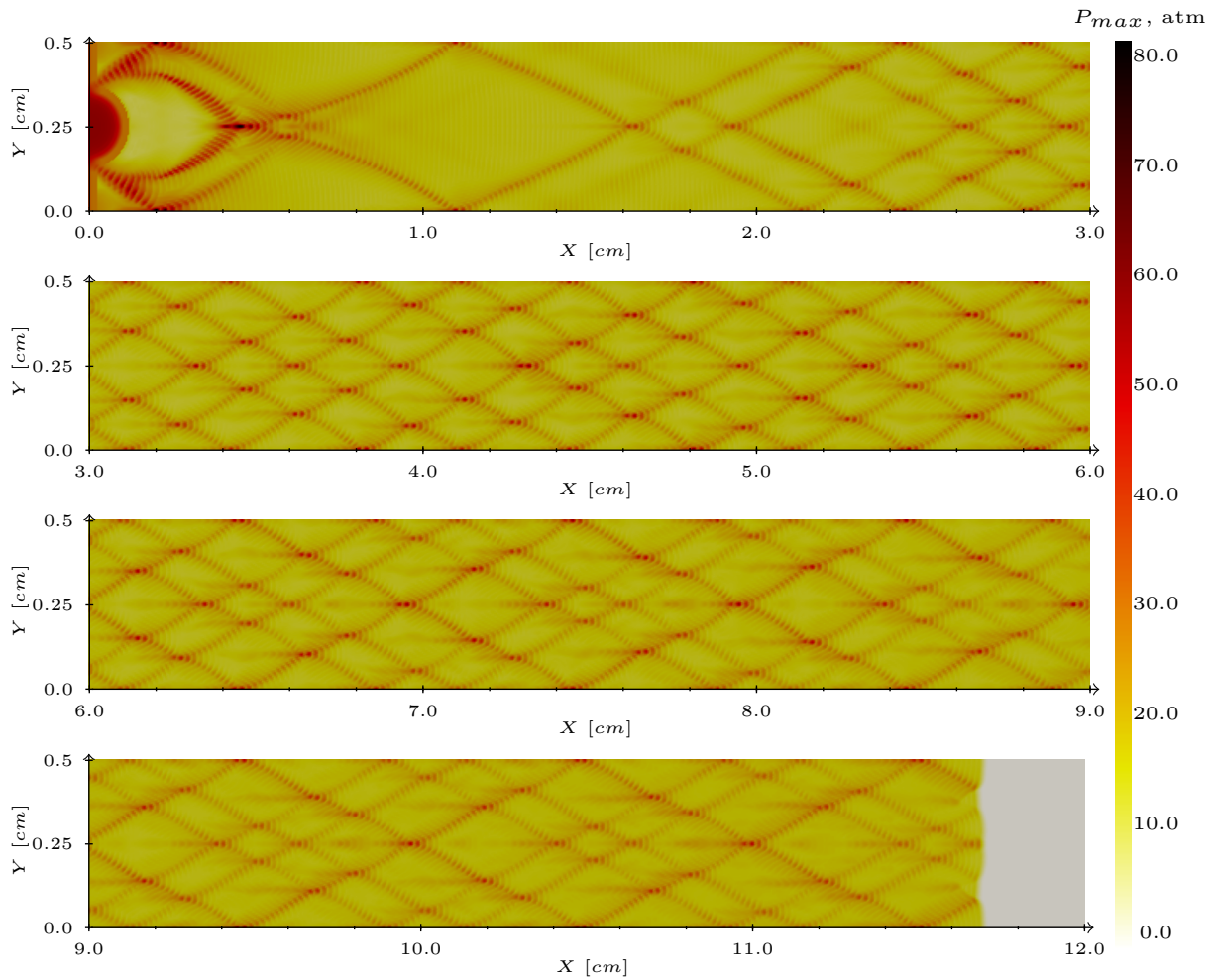


Figure 7.37: Detonation history presented by maximum pressure contours. Accelerator configuration with $B_z = 16T$ and 10% Cs.

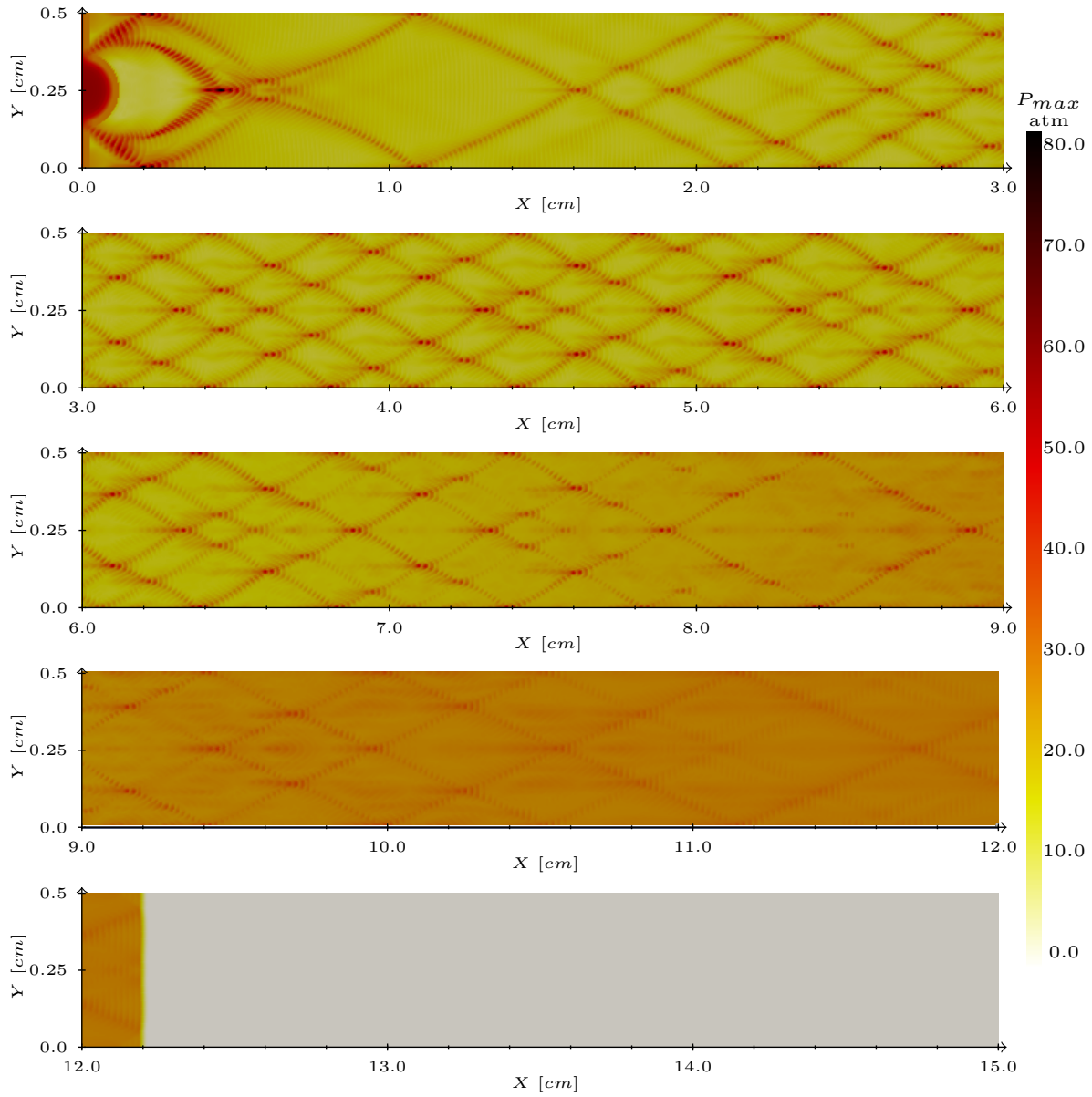
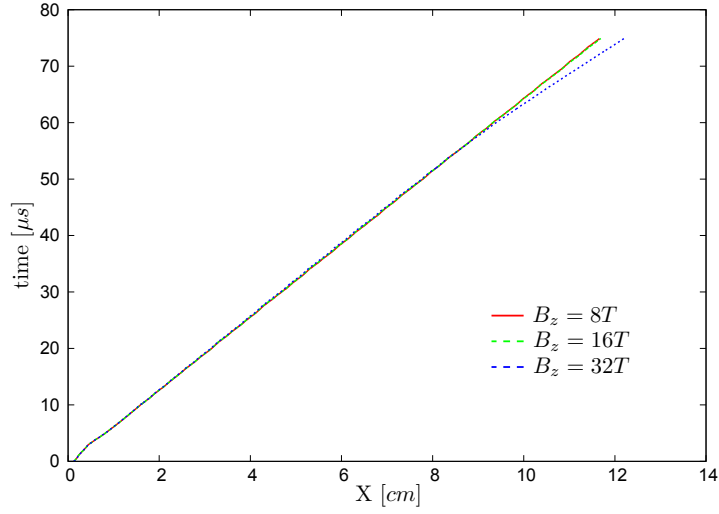
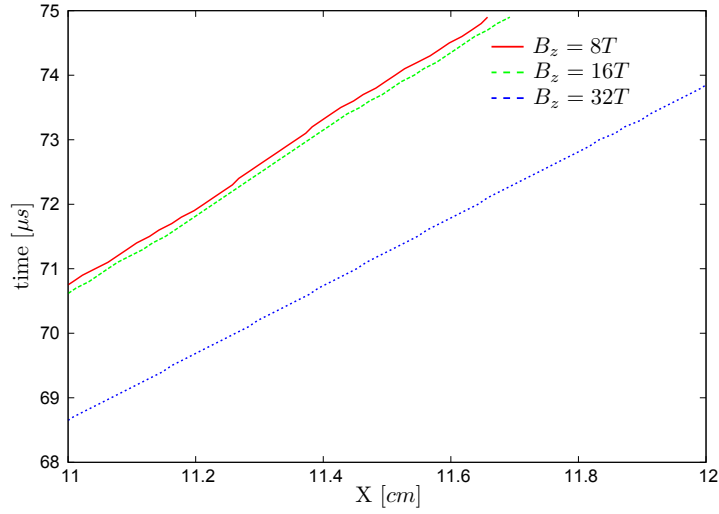


Figure 7.38: Detonation history presented by maximum pressure contours. Accelerator configuration with $B_z = 32T$ and 10% Cs.



(a) Wide view



(b) Enlarged view

Figure 7.39: X-t plot of 2D detonation comparing the progression of the leading shocks at the centerline of the accelerator configuration with 10% Cs and various B_z values without enhanced kinetics.

CHAPTER 8

Conclusions and Future Work

The present computational studies have enabled both a global exploration of PDRIME concepts for propulsive devices, as well as a detailed exploration of the underlying physics of detonation-MHD interactions.

For the standard PDRIME utilizing a constant magnetic field, there was marginal gains in performance over the baseline PDRE configuration using simplified modelling approaches. We investigated closed and open loop control of the magnetic field utilizing, temporal and temperature controllers, respectively. We found that these methods of control had marginal performance gains, at best. When the flight Mach number was significantly lowered ($M \leq 5$), we found significant performance increases without the use of controllers.

The stability and dynamics of a 1D spark-ignited detonation with complex kinetics were also investigated. We developed a model to understand and interpret the coupling between the reactive and fluid mechanical/acoustic phenomena. We found that the frequency in oscillations of the peak pressure trace is inversely related to the time it takes for an acoustic wave to propagate from the flame to the leading shock and the entropy wave generated from the perturbed shock to travel back to the flame. We verified the model by finding out it was in agreement with the peak pressure cycles extracted from the 1D complex kinetics detonation simulation.

After gaining insight into the stability of the 1D detonation, we investigated the stability of a cesium-seeded detonation. We confirmed previous findings by Radulescu et al.[19] that the diluent had a regularizing effect on the 1D detonation. We then applied MHD using a loading factor, K_y , to the 1D cesium-seeded detonation with both the generator and accelerator configurations at various magnetic field strengths, B_z , and concentrations of cesium. We found that for a given concentration of cesium and applied field strength the accelerator had a regularizing effect, while the generator had the opposite effect. We then investigated the effect the applied fields had on the 2D cesium-seeded spark-ignited detonation with the same parameters used for the 1D simulations (i.e., B_z and cesium concentration) and found that the MHD had little to no effect on the detonation dynamics, i.e., cellular structure and detonation velocity. Next, we increased the Arrhenius pre-factor of the cesium forward reaction mechanism by factors of 10 and 100. We observed a significant increase of conductivity near the leading shock of the 2D detonation, but little change in the detonation velocity in either the accelerator or generator configurations. Lastly, we significantly increased the strength of the magnetic field ($16T$ and $32T$) without enhancing the cesium kinetics. The generator mode had little effect on the detonation dynamics, while the accelerator mode significantly altered the detonation velocity.

In Chapter 7, the conductivity of the fluid played an important role in the MHD acceleration of the detonation. But in order to properly calculate the conductivity, the number density of electrons as well as the electron temperature, T_e , must be determined (per Equation 2.27). Section 2.3.3 describes how the electron energy is coupled to the bulk fluid via a two-temperature model. One future direction of this research is to investigate the dynamics of the detonation in 1D and 2D simulations using the two-temperature model to more accurately characterize the thermal non-

equilibrium effects of the bulk fluid. Additionally, the kinetics of excitation and ionization of the gas can be further investigated by means of a collisional radiative model[75, 76], commonly used in the study of gas discharges[82, 83], which allow for a more accurate representation of the atomic state distribution function.

The simulations performed in this dissertation utilized high-order accurate methods which significantly reduced numerical dissipation. The high-order accuracy allowed for the capturing of sharp flow features (i.e., shocks and contact discontinuities). Oran et al.[84] demonstrated that the viscous effects did not change the dynamics of the leading shock, thus did not have a significant effect on the detonation cellular structure. But unlike, previous works[68, 84, 85] with detonations, the downstream effects play an important role in the overall dynamics of the detonation with MHD acceleration. Future studies involving full ionization kinetics, including collisional-radiative processes, will be used to examine these processes in further detail. In addition, a more physically accurate model based on the Navier-Stokes equations and including species diffusion is needed to correctly model the transport of the fluid. In addition, precursor effects[86] might play a role in heating the upstream fluid, which then alters the flame temperature. It might also be interesting to investigate the thermal losses to the wall as well as the interactions of the boundary layer with the shock[87].

APPENDIX A

Reaction Mechanism

A.1 H_2 -Air Reaction Mechanism

The H_2 -air reaction mechanism and Arrhenius coefficients used in the present study contains 19 reversible elementary mechanisms composed of 9 species[37].

	Elementary Mech.	A	η	E_A
1.)	$H + O_2 \rightleftharpoons O + OH$	$2.60E14$	0.000	8400
2.)	$O + H_2 \rightleftharpoons H + OH$	$1.80E10$	1.000	4450
3.)	$H_2 + OH \rightleftharpoons H + H_2O$	$2.20E13$	0.000	2575
4.)	$2OH \rightleftharpoons H_2O + O$	$6.30E12$	0.000	545
5.)	$H + OH + M \rightleftharpoons H_2O + M$	$2.20E22$	-2.00	0.000
6.)	$2H + M \rightleftharpoons H_2 + M$	$6.40E17$	-1.000	0.000
7.)	$H + O + M \rightleftharpoons OH + M$	$6.00E16$	-0.600	0.000
8.)	$2O + M \rightleftharpoons O_2 + M$	$6.00E13$	0.000	-900
9.)	$H_2 + O_2 \rightleftharpoons HO_2 + H$	$1.00E14$	0.000	28000
10.)	$H + O_2 + M \rightleftharpoons HO_2 + M$	$2.10E15$	0.000	-500
11.)	$H + HO_2 \rightleftharpoons 2OH$	$1.40E14$	0.000	540
12.)	$H + HO_2 \rightleftharpoons O + H_2O$	$1.00E13$	0.000	540
13.)	$O + HO_2 \rightleftharpoons O_2 + OH$	$1.50E13$	0.000	475

14.)	$OH + HO_2 \rightleftharpoons O_2 + H_2O$	$8.00E12$	0.000	0.000
15.)	$H_2O_2 + M \rightleftharpoons 2OH + M$	$1.20E17$	0.000	22750
16.)	$2HO_2 + M \rightleftharpoons H_2O_2 + O_2$	$2.00E12$	0.000	0.000
17.)	$H + H_2O_2 \rightleftharpoons H_2 + HO_2$	$1.40E12$	0.000	1800
18.)	$O + H_2O_2 \rightleftharpoons OH + HO_2$	$1.40E13$	0.000	3200
19.)	$OH + H_2O_2 \rightleftharpoons H_2O + HO_2$	$6.10E12$	0.000	715

(A.1)

A.2 Cesium Reaction Mechanism

The cesium reaction mechanism and Arrhenius coefficients used in the present study contains 2 reversible elementary mechanisms composed of Cs , Cs^+ , and e^- .

	Elementary Mech.	A	η	E_A
1.)	$Cs + e^- \rightleftharpoons Cs^+ + e^- + e^-$	$2.48E14$	0.500	45900
2.)	$Cs + M \rightleftharpoons Cs + e^- + M$	$2.48E11$	0.500	45900

(A.2)

APPENDIX B

Eigenvector Matrices

The following was derived for a multi-species, two-temperature eigen-system[35, 88].

B.1 Governing Equation

The governing equation for a non-reactive multi-species, multi-temperature three-dimensional flow without LHS is:

$$\mathbf{Q}_t + \nabla_n \mathbf{F} = 0 \quad (\text{B.1})$$

Here the vector containing the conserved variables, \mathbf{Q} , and the flux normal to control volume surface , \mathbf{F} , are:

$$\mathbf{Q} = \begin{pmatrix} \rho_s \\ \rho \mathbf{u} \\ \mathbf{B} \\ E^* \\ S_e \end{pmatrix} \quad \mathbf{F} = \begin{pmatrix} \rho_s u_n \\ \rho \mathbf{u} u_n + P^* \mathbf{n} - \frac{1}{\mu_0} B_n \mathbf{B} \\ u_n \mathbf{B} - \mathbf{u} B_n \\ (E^* + P^*) u_n - \frac{1}{\mu_0} B_n \mathbf{u} \cdot \mathbf{B} \\ S_e u_n \end{pmatrix} \quad (\text{B.2})$$

B.2 Roe Averaged Weighting

Before the eigensystem can be determined, the Roe Averaged variables[46], i.e., mass fraction, spatial components of velocity and enthalpy, must first be determined on a flux interface, $i + \frac{1}{2}$. First the primitive variables are calculated for i and $i + 1$ as:

$$\mathbf{V} = \begin{pmatrix} c_s \\ \mathbf{u} \\ \mathbf{b} \\ h \\ \hat{s}_e \end{pmatrix} \quad (\text{B.3})$$

$$h = \frac{1}{\rho} \left(E + P - \frac{\mathbf{B}^2}{2\mu_0} - E_e \right), \quad c_s = \frac{\rho_s}{\rho}, \quad \mathbf{b} = [b_n, b_t]^T / \sqrt{\rho\mu_0}, \quad \text{and} \quad \hat{s}_e = \frac{S_e}{\rho}$$

where c_s represents the mass fraction of the s^{th} species, h represents the specific enthalpy, and \hat{s}_e represents the specific electron entropy. Next, by using the densities at i and $i + 1$, the Roe-averaged variables at the face, $i + \frac{1}{2}$, are determined by:

$$\mathbf{V}_{i+\frac{1}{2}} = \frac{\mathbf{V}_i\sqrt{\rho_i} + \mathbf{V}_{i+1}\sqrt{\rho_{i+1}}}{\sqrt{\rho_i} + \sqrt{\rho_{i+1}}} \quad (\text{B.4})$$

B.3 Eigensystem and Flux Jacobian Matrix

The flux Jacobian represents the relation $\tilde{A} = \frac{\partial \mathbf{F}}{\partial \mathbf{Q}}$. From here we diagonalize the flux Jacobian to get a formulation involving the Jacobian, left and right eigenvector matrices, and the eigen-matrix.

$$\tilde{A} = \frac{\partial \mathbf{F}}{\partial \mathbf{Q}} = \mathbf{R}\mathbf{A}\mathbf{L} \quad (\text{B.5})$$

The eigen-matrix is defined as the following,

$$\Lambda = \begin{pmatrix} u_n & 0 & 0 & 0 & 0 & 0 & 0 & 0 & 0 & 0 \\ 0 & \ddots & 0 & 0 & 0 & 0 & 0 & 0 & 0 & 0 \\ 0 & 0 & u_n + c_f & 0 & 0 & 0 & 0 & 0 & 0 & 0 \\ 0 & 0 & 0 & u_n - c_f & 0 & 0 & 0 & 0 & 0 & 0 \\ 0 & 0 & 0 & 0 & u_n + c_s & 0 & 0 & 0 & 0 & 0 \\ 0 & 0 & 0 & 0 & 0 & u_n & 0 & 0 & 0 & 0 \\ 0 & 0 & 0 & 0 & 0 & 0 & u_n - c_s & 0 & 0 & 0 \\ 0 & 0 & 0 & 0 & 0 & 0 & 0 & u_n + c_A & 0 & 0 \\ 0 & 0 & 0 & 0 & 0 & 0 & 0 & 0 & u_n - c_A & 0 \\ 0 & 0 & 0 & 0 & 0 & 0 & 0 & 0 & 0 & u_n \end{pmatrix} \quad (\text{B.6})$$

Where the diagonal entries are the eigen-values of the system. The definitions of the fast(slow) magneto-acoustic, $c_{f(s)}$, and the Alfvén, c_A , wave speeds can be found in [88]. The similarity transformation matrices \mathbf{R} and \mathbf{L} are defined in the next sections.

B.3.1 Right Eigenvectors

The system satisfies $\Delta Q = \mathbf{R} \cdot \tilde{\alpha}$ where

$$\mathbf{R} = \begin{pmatrix} 1 & r_f & r_f & r_s & 0 & r_s & 0 & 0 & 0 \\ u_x & \Theta_{f,x}^+ & \Theta_{f,x}^- & \Theta_{s,x}^+ & 0 & \Theta_{s,x}^- & \sqrt{\rho}s_x & \sqrt{\rho}s_x & 0 \\ u_y & \Theta_{f,y}^+ & \Theta_{f,y}^- & \Theta_{s,y}^+ & 0 & \Theta_{s,y}^- & \sqrt{\rho}s_y & \sqrt{\rho}s_y & 0 \\ u_z & \Theta_{f,z}^+ & \Theta_{f,z}^- & \Theta_{s,z}^+ & 0 & \Theta_{s,z}^- & \sqrt{\rho}s_z & \sqrt{\rho}s_z & 0 \\ 0 & \tilde{\Delta}_f t_x & \tilde{\Delta}_f t_x & \tilde{\Delta}_s t_x & n_x & \tilde{\Delta}_s t_x & -s_B s_x \sqrt{\mu_0} & s_B s_x \sqrt{\mu_0} & 0 \\ 0 & \tilde{\Delta}_f t_y & \tilde{\Delta}_f t_y & \tilde{\Delta}_s t_y & n_y & \tilde{\Delta}_s t_y & -s_B s_y \sqrt{\mu_0} & s_B s_y \sqrt{\mu_0} & 0 \\ 0 & \tilde{\Delta}_f t_z & \tilde{\Delta}_f t_z & \tilde{\Delta}_s t_z & n_z & \tilde{\Delta}_s t_z & -s_B s_z \sqrt{\mu_0} & s_B s_z \sqrt{\mu_0} & 0 \\ \frac{\tilde{u}^2}{2} & \mathcal{H}_f^+ & \mathcal{H}_f^- & \mathcal{H}_s^+ & 0 & \mathcal{H}_s^- & u_s \sqrt{\rho} & u_s \sqrt{\rho} & \mathcal{H}_e \\ 0 & r_f \hat{s}_e & r_f \hat{s}_e & r_s \hat{s}_e & 0 & r_s \hat{s}_e & 0 & 0 & 1 \end{pmatrix} \quad (\text{B.7})$$

where s_B is the sign of the normal component of the magnetic field and for the purpose of a compact expression of \mathbf{R} , the following variables are defined,

$$\tilde{\Delta}_f = r_s \frac{c_f}{\sqrt{\rho}} \quad (\text{B.8a})$$

$$\tilde{\Delta}_s = -r_f \frac{a^2}{c_f^2} \frac{c_f}{\sqrt{\rho}} \quad (\text{B.8b})$$

$$\tilde{\Gamma}_f = -s_B b_n r_s \quad (\text{B.8c})$$

$$\tilde{\Gamma}_s = +s_B a r_f \quad (\text{B.8d})$$

$$\mathcal{H}_e = \frac{\zeta_e}{\gamma_e - 1} \rho^{\gamma_e - 1} \quad (\text{B.8e})$$

$$\mathcal{H}_{f(s)}^\pm = r_{f(s)} h \pm r_{f(s)} u_n c_{f(s)} \pm u_t \tilde{\Gamma}_{f(s)} + \frac{B_t}{\mu_0} \tilde{\Delta}_{f(s)} \quad (\text{B.8f})$$

$$\Theta_{f(s),x}^\pm = r_{f(s)} u_x \pm r_{f(s)} c_{f(s)} n_x \pm \tilde{\Gamma}_{f(s)} t_x \quad (\text{B.8g})$$

similarly for the y, z components and $\zeta_e = 1 - \frac{\gamma_e - 1}{\gamma_h - 1}$. As noted by Brio & Wu[60], renormalization factors, r_f and r_s , are needed to avoid singular solutions when the magnetic field vanishes. Their definitions and identities are as follows¹,

¹Identities computed with $\epsilon_t = \frac{b_t^2}{a^2 + b_n^2} > \epsilon_t^* \sim 10^{-6}$

$$r_f = \sqrt{\frac{c_f^2 - b_n^2}{c_f^2 - c_s^2}} \quad (\text{B.9a})$$

$$r_s = \sqrt{\frac{c_f^2 - a^2}{c_f^2 - c_s^2}} = \frac{c_f}{b_n} \sqrt{\frac{b_n^2 - c_s^2}{c_f^2 - c_s^2}} \quad (\text{B.9b})$$

$$r_f r_s = \frac{c_f b_t}{c_f^2 - c_s^2} \quad (\text{B.9c})$$

$$r_s^2 + r_f^2 \frac{a^2}{c_f^2} = 1 \quad (\text{B.9d})$$

$$r_f^2 + r_s^2 \frac{c_s^2}{a^2} = 1 \quad (\text{B.9e})$$

B.3.2 Left Eigenvectors

The systems satisfies $\mathbf{L} = \mathbf{R}^{-1}$, where

$$\mathbf{L} = \begin{pmatrix} L_c \\ L_f^+ \\ L_f^- \\ L_s^+ \\ L_{pseudo} \\ L_s^- \\ L_A^+ \\ L_A^- \\ L_e \end{pmatrix} \quad (\text{B.10})$$

$$\begin{aligned}
L_c = \frac{1}{a^2} & \begin{pmatrix} a^2 - \beta \frac{\bar{u}^2}{2} \\ \beta u_x \\ \beta u_y \\ \beta u_z \\ \beta \frac{B_t}{\mu_0} t_x \\ \beta \frac{B_t}{\mu_0} t_y \\ \beta \frac{B_t}{\mu_0} t_z \\ -\beta \\ \beta \mathcal{H}_e \end{pmatrix}^T, \quad L_f^\pm = \frac{1}{2c_f^2} \begin{pmatrix} r_f \beta \frac{\bar{u}^2}{2} \mp r_f u_n c_f \pm r_s s_B b_n u_t \\ -r_f \beta u_x \pm r_f c_f n_x \mp r_s s_B t_x \\ -r_f \beta u_y \pm r_f c_f n_y \mp r_s s_B t_y \\ -r_f \beta u_z \pm r_f c_f n_z \mp r_s s_B t_z \\ -r_f \beta \frac{B_t}{\mu_0} t_x + r_s \sqrt{\frac{\rho}{\mu_0}} c_f t_x \\ -r_f \beta \frac{B_t}{\mu_0} t_y + r_s \sqrt{\frac{\rho}{\mu_0}} c_f t_y \\ -r_f \beta \frac{B_t}{\mu_0} t_z + r_s \sqrt{\frac{\rho}{\mu_0}} c_f t_z \\ \beta r_f \\ -\beta r_f \mathcal{H}_e \end{pmatrix}^T \\
L_A^\pm = \frac{1}{2\sqrt{\rho}} & \begin{pmatrix} -u_s \\ s_x \\ s_y \\ s_z \\ \mp s_B \sqrt{\frac{\rho}{\mu_0}} s_x \\ \mp s_B \sqrt{\frac{\rho}{\mu_0}} s_y \\ \mp s_B \sqrt{\frac{\rho}{\mu_0}} s_z \\ 0 \\ 0 \end{pmatrix}^T, \quad L_s^\pm = \frac{1}{2a^2} \begin{pmatrix} r_s \beta \frac{\bar{u}^2}{2} \mp r_s u_n c_s \mp r_f s_B u_t a \\ -r_s \beta u_x \pm r_s c_s n_x \pm r_f s_B a t_x \\ -r_s \beta u_y \pm r_s c_s n_y \pm r_f s_B a t_y \\ -r_s \beta u_z \pm r_s c_s n_z \pm r_f s_B a t_z \\ -r_s \beta \frac{B_t}{\mu_0} t_x - r_f \sqrt{\frac{\rho}{\mu_0}} \frac{a^2}{c_f} t_x \\ -r_s \beta \frac{B_t}{\mu_0} t_y - r_f \sqrt{\frac{\rho}{\mu_0}} \frac{a^2}{c_f} t_y \\ -r_s \beta \frac{B_t}{\mu_0} t_z - r_f \sqrt{\frac{\rho}{\mu_0}} \frac{a^2}{c_f} t_z \\ \beta r_s \\ -\beta r_s \mathcal{H}_e \end{pmatrix}^T,
\end{aligned}$$

$$L_e = \frac{1}{a^2} \begin{pmatrix} -\hat{s}_e \beta \frac{\vec{u}^2}{2} \\ \beta u_x \hat{s}_e \\ \beta u_y \hat{s}_e \\ \beta u_z \hat{s}_e \\ \beta \frac{B_t}{\mu_0} \hat{s}_e t_x \\ \beta \frac{B_t}{\mu_0} \hat{s}_e t_y \\ \beta \frac{B_t}{\mu_0} \hat{s}_e t_z \\ -\beta \hat{s}_e \\ 1 + \beta \mathcal{H}_e \hat{s}_e \end{pmatrix}^T, \quad L_{pseudo} = \begin{pmatrix} 0 \\ 0 \\ 0 \\ 0 \\ n_x \\ n_y \\ n_z \\ 0 \\ 0 \end{pmatrix}^T$$

B.3.3 Riemann ‘Jump’ conditions

The ‘jump’ conditions satisfy $\tilde{\alpha} = \mathbf{L} \cdot \Delta \mathbf{Q}$ and is defined,

$$\tilde{\alpha} = \begin{pmatrix} \tilde{\alpha}_c \\ \tilde{\alpha}_f^+ \\ \tilde{\alpha}_f^- \\ \tilde{\alpha}_s^+ \\ \tilde{\alpha}_s^- \\ \tilde{\alpha}_A^+ \\ \tilde{\alpha}_A^- \\ \tilde{\alpha}_e \end{pmatrix} \quad (\text{B.11})$$

where,

$$\tilde{\alpha}_c = \left(1 - \beta \frac{\vec{u}^2}{2a^2}\right) \Delta \rho + \frac{\beta \vec{u}}{a^2} \Delta(\rho \vec{u}) + \beta \frac{B_t}{a^2} \Delta B_t - \frac{\beta}{a^2} \Delta E^* \quad (\text{B.12a})$$

$$\text{or... } \tilde{\alpha}_c = \Delta\rho - \frac{\Delta P}{a^2}$$

$$\tilde{\alpha}_f^\pm = \frac{r_f}{2c_f^2} [\Delta P \pm \rho c_f \Delta u_n] + r_s \frac{\sqrt{\rho}}{2c_f} \left[\Delta B_t \mp s_B \sqrt{\rho} \frac{b_n}{c_f} \Delta u_t \right] \quad (\text{B.12b})$$

$$\tilde{\alpha}_s^\pm = \frac{r_s}{2a^2} [\Delta P \pm \rho c_s \Delta u_n] - r_f \frac{\sqrt{\rho}}{2c_f} \left[\Delta B_t \mp s_B \sqrt{\rho} \frac{c_f}{a} \Delta u_t \right] \quad (\text{B.12c})$$

$$\tilde{\alpha}_A^\pm = \frac{1}{2} [\sqrt{\rho} \Delta u_s \mp s_B \Delta B_s] \quad (\text{B.12d})$$

$$\tilde{\alpha}_e = \Delta \hat{s}_e - \frac{E_e}{\rho} \frac{\Delta P}{a^2} \quad (\text{B.12e})$$

APPENDIX C

MHD Divergence Cleaning for General Coordinate Systems

The pseudo electric field is defines as $\Omega = \mathbf{u} \times \mathbf{B}$. From Maxwell's Equations the temporal evolution can be described by

$$\frac{\partial \mathbf{B}}{\partial t} = -\nabla \times \Omega \quad (\text{C.1})$$

For a cartesian coordinate system with x , y , and z dependants $\frac{\partial \mathbf{B}}{\partial t}$ is described as:

$$\begin{aligned} \frac{\partial B_x}{\partial t} &= \frac{\partial}{\partial y} \Omega_z - \frac{\partial}{\partial z} \Omega_y \\ \frac{\partial B_y}{\partial t} &= \frac{\partial}{\partial z} \Omega_x - \frac{\partial}{\partial x} \Omega_z \\ \frac{\partial B_z}{\partial t} &= \frac{\partial}{\partial x} \Omega_y - \frac{\partial}{\partial y} \Omega_x \end{aligned} \quad (\text{C.2})$$

For a coordinate system with a $r - z$ dependants $\frac{\partial \mathbf{B}}{\partial t}$ is described as:

$$\begin{aligned} \frac{\partial B_r}{\partial t} &= -\frac{1}{r} \frac{\partial}{\partial z} (r \Omega_\theta) \\ \frac{\partial B_z}{\partial t} &= \frac{1}{r} \frac{\partial}{\partial r} (r \Omega_\theta) \\ \frac{\partial B_\theta}{\partial t} &= -\frac{\partial}{\partial r} \Omega_z + \frac{\partial}{\partial z} \Omega_r \end{aligned} \quad (\text{C.3})$$

For a coordinate system with a $r - \theta$ dependants $\frac{\partial \mathbf{B}}{\partial t}$ is described as:

$$\begin{aligned} \frac{\partial B_r}{\partial t} &= \frac{1}{r} \frac{\partial}{\partial \theta} \Omega_z \\ \frac{\partial B_z}{\partial t} &= -\frac{1}{r} \frac{\partial}{\partial \theta} \Omega_r + \frac{1}{r} \frac{\partial}{\partial r} (r \Omega_\theta) \\ \frac{\partial B_\theta}{\partial t} &= -\frac{\partial}{\partial r} \Omega_z \end{aligned} \quad (\text{C.4})$$

APPENDIX D

Jacobians and Transforms

D.1 Chemical Jacobian

We first start out with the model ordinary differential equation for the kinetics:

$$\frac{d\mathbf{Q}}{dt} = \dot{\mathbf{\Omega}} \quad (\text{D.1})$$

where

$$\mathbf{Q} = \begin{pmatrix} n_s \\ E \end{pmatrix} \quad \dot{\mathbf{\Omega}} = \begin{pmatrix} \dot{\omega}_s \\ \dot{\omega}_E \end{pmatrix} \quad (\text{D.2})$$

n_s is the number density of the s^{th} species, and $\dot{\omega}_s$ and $\dot{\omega}_E$ are the species and energy production terms, respectively. The number density, n_s , was used in lieu of mass density, ρ_s , out of convenience and can be easily transformed, $\frac{\partial \rho_l}{\partial n_k} = M_k \delta_{kl}$. The implicit 1st order numerical formulation of Equation D.1 is carried out with the following steps:

$$\begin{aligned} \frac{\Delta \mathbf{Q}}{\Delta t} &= \dot{\mathbf{\Omega}}^{n+1} \\ \frac{\Delta \mathbf{Q}}{\Delta t} &= \dot{\mathbf{\Omega}}^n + \frac{\partial \dot{\mathbf{\Omega}}}{\partial t} \Delta t \\ \frac{\Delta \mathbf{Q}}{\Delta t} &= \dot{\mathbf{\Omega}}^n + \frac{\partial \dot{\mathbf{\Omega}}}{\partial \mathbf{Q}} \frac{\Delta \mathbf{Q}}{\Delta t} \Delta t \\ \frac{\Delta \mathbf{Q}}{\Delta t} &= \dot{\mathbf{\Omega}}^n + \frac{\partial \dot{\mathbf{\Omega}}}{\partial \mathbf{Q}} \Delta \mathbf{Q} \\ \left(\mathbf{I} - \frac{\partial \dot{\mathbf{\Omega}}}{\partial \mathbf{Q}} \Delta t \right) \Delta \mathbf{Q} &= \dot{\mathbf{\Omega}}^n \Delta t \\ \Delta \mathbf{Q} &= \left(\mathbf{I} - \frac{\partial \dot{\mathbf{\Omega}}}{\partial \mathbf{Q}} \Delta t \right)^{-1} \dot{\mathbf{\Omega}}^n \Delta t \end{aligned} \quad (\text{D.3})$$

D.2 Chemical Jacobian($\frac{\partial \dot{\Omega}}{\partial Q}$) Derivation

$$\frac{\partial \dot{\omega}_s}{\partial n_k} = \sum_r \nu_{rs} \frac{\nu'_{rk}}{n_k} \prod_j n_j^{\nu'_{rj}} \quad (\text{D.4})$$

$$\frac{\partial \dot{\omega}_s}{\partial E} = \frac{\partial \dot{\omega}_s}{\partial T} \frac{\partial T}{\partial E} = \frac{\partial \dot{\omega}_s}{\partial T} \frac{1}{C_v}$$

$$\frac{\partial \dot{\omega}_s}{\partial T} = \sum_r \nu_{rs} \frac{dk_r}{dT} \prod_k n_k^{\nu'_{rk}}$$

$$\frac{\partial k_r}{\partial T} = \frac{\eta_r}{T} A_r T^{\eta_r} \exp\left(\frac{-\theta_r}{T}\right) + \frac{\theta_r}{T^2} A_r T^{\eta_r} \exp\left(\frac{-\theta_r}{T}\right)$$

$$\frac{\partial k_r}{\partial T} = \left(\frac{\eta_r}{T} + \frac{\theta_r}{T^2}\right) k_r$$

$$\frac{\partial \dot{\omega}_s}{\partial E} = \frac{1}{C_v} \sum_r \nu_{rs} \left(\frac{\eta_r}{T} + \frac{\theta_r}{T^2}\right) k_r \prod_k n_k^{\nu'_{rk}} \quad (\text{D.5})$$

$$\dot{\omega}_E = \sum_s \omega_s e_{0s} = \sum_s e_{0s} \sum_r \nu_{rs} k_r \prod_k n_k^{\nu'_{rk}}$$

$$\frac{\partial \dot{\omega}_E}{\partial n_k} = \sum_s \frac{\partial \dot{\omega}_s}{\partial n_k} e_{0s} \quad (\text{D.6})$$

$$\frac{\partial \dot{\omega}_E}{\partial E} = \sum_s \frac{\partial \dot{\omega}_s}{\partial E} e_{0s} \quad (\text{D.7})$$

APPENDIX E

Steady State Detonation

We will first begin with our model equation with the steady state approximation:

$$\cancel{\frac{\partial \mathbf{Q}}{\partial t}} + \frac{\partial \mathbf{F}}{\partial x} = \dot{\mathbf{\Omega}} \quad (\text{E.1a})$$

$$\mathbf{A} \frac{\partial \mathbf{Q}}{\partial x} = \dot{\mathbf{\Omega}} \quad (\text{E.1b})$$

$$\frac{\partial \mathbf{Q}}{\partial x} = \mathbf{A}^{-1} \dot{\mathbf{\Omega}} \quad (\text{E.1c})$$

From Equation E.1c, the explicit space-marching formulation is defined as:

$$\frac{\Delta \mathbf{Q}}{\Delta x} = \mathbf{A}^{-1} \dot{\mathbf{\Omega}}_i \quad (\text{E.2})$$

The implicit space-marching formulation is also defined,

$$\frac{\Delta \mathbf{Q}}{\Delta x} = \mathbf{A}^{-1} \dot{\mathbf{\Omega}}_{i+1} \quad (\text{E.3a})$$

$$\frac{\Delta \mathbf{Q}}{\Delta x} = \mathbf{A}^{-1} \left(\dot{\mathbf{\Omega}}_i + \frac{\partial \dot{\mathbf{\Omega}}}{\partial \mathbf{Q}} \Delta \mathbf{Q} \right) \quad (\text{E.3b})$$

$$\frac{\Delta \mathbf{Q}}{\Delta x} - \mathbf{A}^{-1} \frac{\partial \dot{\mathbf{\Omega}}}{\partial \mathbf{Q}} \Delta \mathbf{Q} = \mathbf{A}^{-1} \dot{\mathbf{\Omega}}_i \quad (\text{E.3c})$$

Now by solving for $\Delta \mathbf{Q}$ the final form is expressed as:

$$\Delta \mathbf{Q} = \left(\mathbf{A} - \Delta x \frac{\partial \dot{\mathbf{\Omega}}}{\partial \mathbf{Q}} \right)^{-1} \dot{\mathbf{\Omega}}_i \Delta x \quad (\text{E.4})$$

APPENDIX F

Iterative & Direct Solvers

F.1 Thomas' Algorithm

The triadiagonal matrix algorithm, commonly referred to as Thomas' algorithm, is a simplified form of Gaussian elimination used to solve triadiagonal system of equation.

These systems of equations take on the following form:

$$a_i x_{i-1} + b_i x_i + c_i x_{i+1} = d_i \quad (\text{F.1})$$

where $a_0 = 0$ and $c_N = 0$. And represented in the matrix form as:

$$\begin{bmatrix} b_1 & c_1 & & & 0 \\ a_2 & b_2 & c_2 & & \\ & a_3 & b_3 & \cdot & \\ & & \cdot & \cdot & c_{N-1} \\ 0 & & & a_N & b_N \end{bmatrix} \begin{bmatrix} x_1 \\ x_2 \\ \cdot \\ \cdot \\ x_N \end{bmatrix} = \begin{bmatrix} d_1 \\ d_2 \\ \cdot \\ \cdot \\ d_N \end{bmatrix} \quad (\text{F.2})$$

Just as in Gaussian elimination, Thomas' algorithm consist of a forward elimination and backward substitution to solve the system as follows:

Forward Elimination

for $k = 2$ loop through N

$$\begin{aligned} m &= \frac{a_k}{b_{k-1}} \\ b_k &= b_k - mc_{k-1} \\ d_k &= d_k - md_{k-1} \end{aligned}$$

Backward Substitution

$$x_N = \frac{d_N}{b_N}$$

for $k = N - 1$ loop through 1

$$x_k = \frac{d_k - c_k x_{k+1}}{b_k}$$

This algorithm is applicable for diagonally dominant matrices, where

$$|b_i| > |a_i| + |c_i| \quad i \in 1, \dots, N \quad (\text{F.3})$$

F.2 Black-Red Gauss-Seidel

Gauss-Seidel is an iterative method used to solve problems of the general form:

$$\mathbf{U} = f(\vec{\mathbf{U}}) \quad (\text{F.4})$$

If one were to solve this equation explicitly, it would simply take the form,

$$\mathbf{U}^{n+1} = f(\vec{\mathbf{U}}^n) \quad (\text{F.5})$$

If $\vec{\mathbf{U}}$ is the spatially distribution of \mathbf{U} , Equation F.4 can be solved implicitly using Gauss-Seidel. In this procedure, one would begin with an initial solution at $t = t^{n+1}$, $\mathbf{U}^{(s)}$, where $s=0$ initially. The solution at $\mathbf{U}^{(s)}$ is used to determine $\mathbf{U}^{(s+1)}$ until convergence which is as follows:

$$\begin{aligned}
\mathbf{U}_{i,j}^{(s+1)} &= f(\vec{\mathbf{U}}^{(s)}) \\
\text{error} &= \max \|\mathbf{U}_{i,j}^{(s+1)} - \mathbf{U}_{i,j}^{(s)}\| \\
&\text{continue until ...} \\
\text{error} < \epsilon &\rightarrow \mathbf{U}^{n+1} = \mathbf{U}^{(s+1)} \text{ (convergence!)}
\end{aligned} \tag{F.6}$$

Using this procedure, the update solution, $\mathbf{U}^{(s+1)}$, is solved for using the latest solution. In order to speed up this process, instead of sweeping through all of the cells (i & j for 2D), one can first sweep through and solve for the computational grid cells colored red in Figure F.1, then using the updated solutions, $\mathbf{U}_{red}^{(s+1)}$, sweep through and solve for the black grid cells, $\mathbf{U}_{black}^{(s+1)}$. The procedure would be as follows:

$$\begin{aligned}
\mathbf{U}_{red}^{(s+1)} &= f(\vec{\mathbf{U}}_{black}^{(s)}) \\
\mathbf{U}_{black}^{(s+1)} &= f(\vec{\mathbf{U}}_{red}^{(s+1)}) \\
\text{error} &= \max \|\mathbf{U}_{i,j}^{(s+1)} - \mathbf{U}_{i,j}^{(s)}\| \\
&\text{continue until ...} \\
\text{error} < \epsilon &\rightarrow \mathbf{U}^{n+1} = \mathbf{U}^{(s+1)} \text{ (convergence!)}
\end{aligned} \tag{F.7}$$

The procedure shown above is referred to as *Red-Black Gauss-Seidel*.

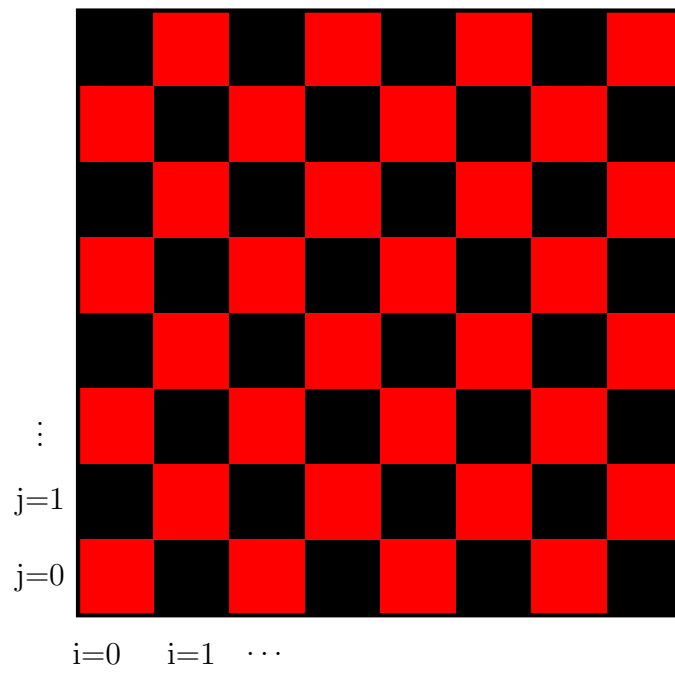


Figure F.1: Computational domain split into red and black computational cells.

APPENDIX G

Message Passing Interface (MPI) Implementation

G.1 Grid Connectivity

A three dimensional computational domain can be broken up into rectangular cuboid subdomains; each containing 6 rectangular faces. A face can connect with one or more faces from adjacent domain(s), which is illustrated in Figure G.1. This illustration also shows that domain p0 is connected with 2 domains(p1 & p2), domain p1 is connected with 3 domains(p1,p2,p3), and domain p3 is connected with 2 domains (p1 & p2). The red numbers in the figure represent unique domain-to-domain connection of which there are 5. Domains p0 & p2 of Figure G.1 are illustrated with there associated ghost layers iin Figure G.2. For this connection, labeled 1 in Figure G.1, p0 would pass information of its interior cells to the ghost layer of p1 and p1 would in turn information of its interior to p2. This example shows that for each connection, there are two receive buffers required, which will be refered to as memory windows without explanation for the moment. From the 5 connections in Figure G.1, a list of 10 memory windows and its associated domains are created in Table G.1.

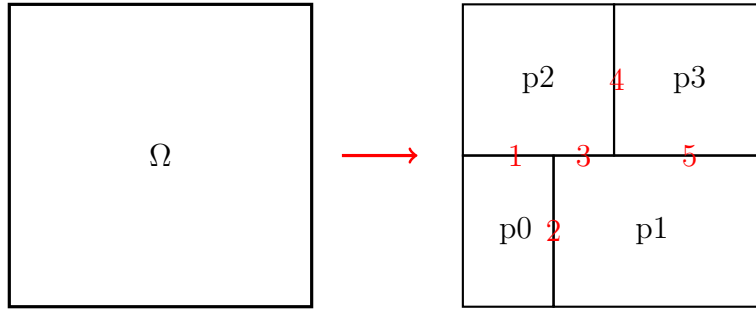


Figure G.1: The computational domain, Ω is decomposed into 4 subdomains.

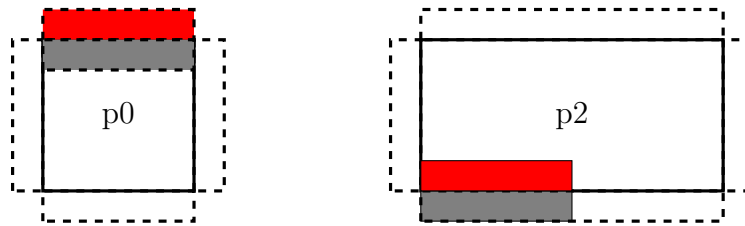


Figure G.2: Domain-to-domain connection example where the red shaded area is a p0 ghost to p2 physical window and the grey shaded area is a p2 ghost to p0 physical window.

window	0	1	2	3	4	5	6	7	8	9
local	0	2	0	1	2	1	2	3	3	1
remote	2	0	1	0	1	2	3	2	1	3

Table G.1: Generic memory window list generated from Figure G.1 domain connections where ‘local’ is the domain sending its physical cell data to the ghost cell of the ‘remote’ domain.

REFERENCES

- [1] K. Ziolkovsky. The investigation of outer space by means of reaction apparatus. *Science Survey*, 1903.
- [2] Robert H. Goddard. A method of reaching extreme altitudes. *The Smithsonian Institute*, 1919.
- [3] P. Hill and C. Peterson. *Mechanics and Thermodynamics of Propulsion*. Addison-Wesley Publishing Company, 2nd edition, 1992.
- [4] Jean-Luc Cambier. A thermodynamic study of MHD ejectors. *AIAA*, 1998.
- [5] Jean-Luc Cambier. MHD augmentation of pulse detonation rocket engines. Technical Report 2001-1782, *AIAA*, 2001.
- [6] D. L. Chapman. On the rate of explosion in gases. *Philos. Mag.*, 47:90104, 1899.
- [7] E. Jouguet. On the propagation of chemical reactions in gases. *J. de mathematiques Pures et Appliquees*, 1:347425, 1905.
- [8] Ja. B. Zel'dovich. On the theory of the propagation of detonation in gaseous systems. *Zh. Eksp. Teor. Fiz.*, 10:542568, 1940.
- [9] J. von Neumann. Theory of detonation waves. *Von Neumann, Collected Works*, 1:347425, 1942.
- [10] W. Döring. On detonation processes in gases. *Ann. Phys.*, 43:421436, 1943.
- [11] John H. S. Lee. *The Detonation Phenomenon*. Cambridge University Press, 2008.
- [12] A. Bourlioux and A. J. Majda. Theoretical and numerical structure for unstable two-dimensional detonations. *Combustion and Flame*, 90:211–229, 1992.
- [13] Peter Hwang, B. Merriman, Ann R. Karagozian, and S. J. Osher. Numerical resolution of pulsating detonation waves. *Combustion Theory & Modeling*, 4(3):217240, 2000.
- [14] Y. Daimon and A. Matsuo. Detailed features of one-dimensional detonations. *Phys. Fluids*, 15:112–122, 2003.

- [15] H. D. Ng, A. J. Higgins, C. B. Kiyanda, M. I. Radulescu, J. H. S. Lee, K. R. Bates, and N. Nikiforakis. Nonlinear dynamics and chaos analysis of one-dimensional pulsating detonations. *Combustion Theory and Modeling*, 9:159170, 2005.
- [16] Jean-Luc Cambier. Development of numerical tools for pulse detonation engine studies. Technical report, Aero. Research Inst. of Sweden, 1996. Flygtekniska Försökstantalten FFA TN 1996-50.
- [17] C. Leung, M. I. Radulescu, and G. J. Sharpe. Characteristics analysis of the one-dimensional detonations. *Phys. Fluids*, 22:126101–1 126101–15, 2010.
- [18] M. Short and G. J. Sharpe. Pulsating instability of detonations with a two-step chain-branching reaction model: Theory and numerics. *Combustion Theory and Modeling*, 7:401–416, 2003.
- [19] M. I. Radulescu, H. D. Ng, J. H. S. Lee, and B. Varatharajan. The effects of argon dilution on the stability of Acetylene/Oxygen detonations. In *Proceedings of the Combustion Institute*, volume 29, page 28252831, 2002.
- [20] C. A. Eckett, J. J. Quirk, and J. E. Shepherd. The role of unsteadiness in direct initiation of gaseous detonations. *Journal of Fluid Mechanics*, 421:147–183, 2000.
- [21] J. E. Shepherd and J. H. S. Lee. On the transition from deflagration to detonation. In *Major topics in Combustion*. Springer-Verlag, 1992.
- [22] E. Schultz, E. Wintenberger, and J. Shepherd. Investigation of deflagration to detonation transition for application to pulse detonation engine ignition systems. In *Proceedings of the 16th JANNAF Propulsion Symposium*, Chemical Propulsion Information Agency, 1999.
- [23] Elaine S. Oran and Vadim N. Gamezo. Origins of the deflagration-to-detonation transition in gas-phase combustion. *Combustion and Flame*, 148:4–47, 2007.
- [24] L. Barr. Pulse detonation engine flies into history. *Air Force Print News Today*, May 2008.
- [25] J. Cole, J. Campbell, and A. Robertson. Rocket induced magnetohydrodynamic ejector - a single-state-to-orbit propulsion concept. Technical Report 95-4079, AIAA, 1995.

- [26] C. Bruno and P. Czysz. An electro-magnetic-chemical hypersonic propulsion system. Technical Report 98-1582, AIAA, 1998.
- [27] N. Krall and A. Trivelpiece. *Principles of Plasma Physics*. McGraw-Hill, New York, 1973.
- [28] R.J. Rosa. *Magnetohydrodynamic Energy Conversion*. Hemisphere Publishing Corporation, Washington, D.C, 1987.
- [29] G. Pollack and D. Stump. *Electromagnetism*. Addison-Wesley Publishing Company, 2002.
- [30] Jean-Luc Cambier. MHD power extraction from a pulse detonation engine. In *34th AIAA/ASME/SAE/ASEE Joint Propulsion Conference and Exhibit*, Albuquerque, New Mexico, June 1998. AIAA.
- [31] Jean-Luc Cambier. Preliminary modeling of pulse detonation rocket engines. Technical Report 99-2659, AIAA, 1999.
- [32] A.C. Kolb. Production of high-energy plasmas by magnetically driven shockwaves. *Physical Review*, 107:345350, 1957.
- [33] Christopher Zeineh. *Numerical Simulations of Pulse Detonation Rocket Engines with Magnetohydrodynamic Thrust Augmentation*. PhD thesis, University of California, Los Angeles, 2010.
- [34] Christopher Zeineh, Lord K. Cole, Timothy Roth, Ann R. Karagozian, and Jean-Luc Cambier. Magnetohydrodynamic augmentation of pulse detonation rocket engines. *Journal of Propulsion and Power*, 28(1):146159, January 2012.
- [35] Jean-Luc Cambier, M. Carroll, and Michael Kapper. Development of a hybrid model for non-equilibrium high-energy plasmas. In *35th AIAA Plasmadynamics and Lasers Conference*, Portland, Oregon, June 2004.
- [36] William C. Gardiner. *Combustion Chemistry*. Springer-Verlag, 1984.
- [37] Casimir J. Jachimowski. An analysis of combustion studies in shock expansion tunnels and reflected shock tunnels. Technical Report NASA TP-3224, 1992.
- [38] M. Short and G. J. Sharpe. Pulsating instability of detonations with a two-step chain-branching reaction model: Theory and numerics. *Combustion Theory and Modeling*, 7:401–416, 2003.

- [39] C. Leung, M. I. Radulescu, and G. J. Sharpe. Characteristics analysis of the one-dimensional detonations. *Phys. Fluids*, 22:126101–1 – 126101–15, 2010.
- [40] Jean-Luc Cambier. Mhd augmentation of pulse detonation rocket engines. Technical Report 2001-1782, AIAA, 2001.
- [41] W. Lotz. Electron-impact ionization cross-sections and ionization rate coefficients for atoms and ions. *The Astrophysical Journal Supplement Series*, 14:207, 1967.
- [42] IUri Petrovich Razer. *Gas discharge physics*. Springer-Verlag, 1991.
- [43] R.J. Rosa. *Magnetohydrodynamic Energy Conversion*. Hemisphere Publishing Corporation, Washington, D.C, 1987.
- [44] J. C. Strikwerda. *Finite Difference Schemes and Partial Differential Equations*. Wadsworth and Brooks, 1989.
- [45] G.-S. Jiang and C.-W. Shu. Efficient implementation of weighted ENO schemes. *Journal of Computational Physics*, 126:202228, 1996.
- [46] P. L Roe. Approximate riemann solvers, parameter vectors, and difference schemes. *Journal of computational physics*, 43(2):357372, 1981.
- [47] B. Einfeldt. On godunov-type methods for gas dynamics. *SIAM Journal on Numerical Analysis*, pages 294–318, 1988.
- [48] X.-D. Liu, S. J. Osher, and T. Chan. Weighted essentially non-oscillatory schemes. *Journal of Computational Physics*, 115:200 – 212, 1994.
- [49] A. Harten, B. Engquist, S. Osher, and S. R Chakravarthy. Uniformly high order accurate essentially non-oscillatory schemes, III. *Journal of Computational Physics*, 71(2):231–303, 1987.
- [50] A. Suresh and H. T. Huynh. Accurate monotonicity-preserving schemes with runge-kutta time stepping. *Journal of Computational Physics*, 136:8399, 1997.
- [51] Dinshaw S. Balsara and Chi-Wang Shu. Monotonicity preserving weighted essentially non-oscillatory schemes with increasingly high order of accuracy. *Journal of Computational Physics*, 160(2):405–452, May 2000.
- [52] V. A. Titarev and E. F. Toro. ADER: arbitrary high order godunov approach. *Journal of Computation Physics*, 17:609–618, 2002.

- [53] Dinshaw S Balsara, Tobias Rumpf, Michael Dumbser, and Claus-Dieter Munz. Efficient, high accuracy ADER-WENO schemes for hydrodynamics and divergence-free magnetohydrodynamics. *arXiv:0811.2200*, November 2008.
- [54] Gary A Sod. A survey of several finite difference methods for systems of nonlinear hyperbolic conservation laws. *Journal of Computational Physics*, 27(1):1–31, April 1978.
- [55] P. Woodward and P. Colella. The numerical simulation of two-dimensional fluid flow with strong shocks. *Journal of Computational Physics*, 54:115–173, 1984.
- [56] C.-W. Shu and S. J. Osher. Efficient implementation of essentially non-oscillatory shock-capturing schemes, II. *Journal of Computational Physics*, 83:3278, 1989.
- [57] Milton Van Dyke. *An Album of Fluid Motion*. The Parabolic Press, Stanford, California, 1982.
- [58] James J. Quirk. A contribution to the great riemann solver debate. *International Journal for Numerical Methods in Fluids*, 18(6):555574, 1994.
- [59] S. Chandrasekhar. *Hydrodynamic and Hydromagnetic Stability*. Oxford University Press, 1961.
- [60] M Brio and C.C Wu. An upwind differencing scheme for the equations of ideal magnetohydrodynamics. *Journal of Computational Physics*, 75(2):400–422, April 1988.
- [61] Guang-Shan Jiang and Cheng-chin Wu. A high-order WENO finite difference scheme for the equations of ideal magnetohydrodynamics. *Journal of Computational Physics*, 150(2):561–594, April 1999.
- [62] Steven A. Orszag and Cha-Mei Tang. Small-scale structure of two-dimensional magnetohydrodynamic turbulence. *Journal of Fluid Mechanics*, 90(01):129–143, 1979.
- [63] Dinshaw S Balsara and Daniel S Spicer. A staggered mesh algorithm using high order godunov fluxes to ensure solenoidal magnetic fields in magnetohydrodynamic simulations. *Journal of Computational Physics*, 149(2):270–292, March 1999.

- [64] J. F. Remacle, J. E. Flaherty, and M. S. Shephard. An adaptive discontinuous galerkin technique with an orthogonal basis applied to compressible flow problems. *SIAM review*, page 5372, 2003.
- [65] Byung-II Jun, Michael L. Norman, and James M. Stone. A numerical study of rayleigh-taylor instability in magnetic fluids. *The Astrophysical Journal*, 453:332–349, November 1995.
- [66] Gábor Tóth. The $\nabla \cdot B = 0$ constraint in shock-capturing magnetohydrodynamics codes. *Journal of Computational Physics*, 161(2):605–652, July 2000.
- [67] Jean-Luc Cambier. Preliminary Modeling of Pulse Detonation Rocket Engines. Technical Report 99-2659, AIAA, 1999.
- [68] Lord K. Cole, A. R. Karagozian, and J.-L. Cambier. Stability of flame-shock coupling in detonation waves: 1D dynamics. *Combustion Science and Technology*, 184(10-11):1502–1525, 2012.
- [69] J. H. S. Lee. Initiation of gaseous detonations. *Ann. Rev. of Phys. Chem.*, 28:75104, 1977. DOI: 10.1146/annurev.pc.28.100177.000451.
- [70] Xing He and Ann R. Karagozian. Pulse-detonation-engine simulations with alternative geometries and reaction kinetics. *Journal of Propulsion and Power*, 22:852–861, 2006.
- [71] J. H. S. Lee, R. Knystaustas, and N. Yoshikawa. Photochemical initiation of gaseous detonations. *Acta Astronautica*, 5:971–982, 1978.
- [72] Joseph M. Powers and S. Paolucci. Accurate spatial resolution estimates for reactive supersonic flow with detailed chemistry. *AIAA*, 43:10881099, May 2005.
- [73] Elaine S. Oran and J. P. Boris. *Numerical Simulation of Reactive Flow*. Elsevier Science, 1987.
- [74] J. B. McVey and T. Y. Toong. Mechanism of instabilities of exothermic hypersonic blunt-body flows. *Combustion Science and Technology*, 3:63 – 76, 1971.
- [75] J.-L. Cambier. Numerical simulations of a nonequilibrium argon plasma in a shock-tube experiment. *22nd AIAA Fluid Dynamics, Plasma Dynamics and Lasers Conference*, AIAA paper 91-1464, July 1991.
- [76] M. G. Kapper and J.-L. Cambier. Ionizing shocks in argon part i: Collisional-radiative model and steady-state structure. *J. Appl. Phys.*, 109:113308, 2011.

- [77] M. G. Kapper and J.-L. Cambier. Ionizing shocks in argon part II: transient and multi-dimensional effects. *J. Appl. Phys.*, 109:113309, 2011.
- [78] V. N. Gamezo, D. Desbordes, and E. S. Oran. Formation and evolution of two-dimensional cellular detonations. *Combustion and Flame*, 116(1):154165, 1999.
- [79] V. N. Gamezo, D. Desbordes, and E. S. Oran. Two-dimensional reactive flow dynamics in cellular detonation waves. *Shock Waves*, 9(1):1117, 1999.
- [80] D. N. Williams, L. Bauwens, and E. S. Oran. A numerical study of the mechanisms of self-reignition in low-overdrive detonations. *Shock Waves*, 6(2):93110, 1996.
- [81] D. Scott Stewart, Tariq D. Aslam, and Jin Yao. On the evolution of cellular detonation. *Symposium (International) on Combustion*, 26(2):2981–2989, 1996.
- [82] A. Bogaerts, R. Gijbels, and J. Vlcek. Collisional-radiative model for an argon glow discharge. *Journal of applied physics*, 84(1):121136, 1998.
- [83] C. O. Laux, L. Pierrot, and R. J. Gessman. State-to-state modeling of a recombining nitrogen plasma experiment. *Chemical Physics*, 2011.
- [84] Elaine S. Oran, James W. Weber Jr., Eliza I. Stefaniw, Michel H. Lefebvre, and John D. Anderson Jr. A numerical study of a two-dimensional h₂-o₂-ar detonation using a detailed chemical reaction model. *Combustion and Flame*, 113(12):147–163, April 1998.
- [85] K. Inaba, A. Matsuo, and J. E. Shepherd. Soot track formation by shock waves and detonations. In *Proceedings of the 20th International Colloquium of Dynamics of Explosion and Reactive Systems, Montreal*, 2005.
- [86] Y. B. Zel'Dovich and Y. P. Raizer. *Physics of shock waves and high-temperature hydrodynamic phenomena*. Dover Publications, 2002.
- [87] J. Damazo, J. Ziegler, J. Karnesky, and J. E. Shepherd. Investigating shock WaveBoundary layer interaction caused by reflecting detonations. In *Proceedings of the 8th ISPHMIE Conference, Sep*, page 510, September 2010.
- [88] Jean-Luc Cambier. Numerical methods for TVD transport and coupled relaxing processes in gases and plasmas. volume 90-1574, Seattle, WA, June 1990.